

ON THE ELASTIC INTERACTION OF PLATE-SHAPED
PRECIPITATES

By



VUKO PEROVIC, DIPL. ENG., M.ENG.

A Thesis

Submitted to the School of Graduate Studies

in Partial Fulfilment of the Requirements

for the Degree

Doctor of Philosophy

McMaster University

June 1980

ON THE ELASTIC INTERACTION OF PLATE-SHAPED
PRECIPITATES

To my parents

DOCTOR OF PHILOSOPHY
(Metallurgy and Materials Science)

McMASTER UNIVERSITY
Hamilton, Ontario

TITLE: On the elastic interaction of plate-shaped
precipitates

AUTHOR: Nuko Perovic, Dipl. Eng.

(University of Belgrade,
Yugoslavia)

M. Eng.

(McMaster University,
Hamilton, Ontario)

SUPERVISOR: Professor G. R. Purdy

NUMBER OF PAGES: xxiv, 189

ABSTRACT

The influence of the elastic interaction energy of plate-shaped precipitates causing tetragonal distortion on nucleation, growth and coarsening is considered.

The analysis shows that the elastic interaction energy may be minimized by the formation of regular three-dimensional arrays, which emphasize the "edge-face" configuration. Algebraic conditions of stability against coarsening are developed, and the results of the detailed numerical test of stability against coarsening for a particularly simple and symmetric array are reported. Experimental observations on θ' (Al-3%Cu alloy) microstructures show strong evidence of short-range ordering, with two characteristic configurations (edge-face and "parallel-step"), both energetically favourable.

It is shown that the elastic interaction energy may have a decisive role in the nucleation stage of θ' precipitates. The θ' microstructure, in a relatively early stage of development, is often inhomogeneous and consists mainly of linear (parallel inclined and cross-like) stacks.

Numerical calculations of the elastic interaction energy show that the experimentally observed stacks are energetically favourable, and can be generated in an autocatalytic way. Numerical and preliminary experimental results on the stability against growth and coarsening of elastically-locked linear arrays are reported.

Finally, the chemical driving force and elastic retarding force acting on moving ledges on a planar interphase boundary are considered. It is shown that elastic interaction may cause a departure from the local equilibrium at a moving growth ledge, and may dictate the location of "homogeneous" nucleation of growth ledges. Some experimental results concerning ledge nucleation and ledge interaction are reported.

ACKNOWLEDGEMENTS

I wish to express my gratitude to my supervisor, Dr. G. R. Purdy and to Dr. L. M. Brown for suggesting the topic of research treated here and for their continuing guidance, help and encouragement throughout the course of this work. It is a pleasure to express my sincere gratitude to Dr. J. S. Kirkaldy and Dr. C. V. Stager for serving on my Ph. D. Committee.

I am also grateful to Mrs. H. Kennelly for rapidly and accurately typing this thesis and to Mr. T. Bryner for his work on the photographs.

Thanks are also extended to many of the faculty, technical staff and graduate students.

The financial support of the National Research Council of Canada is gratefully acknowledged.

TABLE OF CONTENTS

| | <u>PAGE</u> |
|---|-------------|
| INTRODUCTION AND SCOPE | xxiv |
| CHAPTER 1 LITERATURE SURVEY | 1 |
| 1.1 The role of elastic energy in phase transformations in solid state | 1 |
| 1.1a Introduction | 1 |
| 1.1b Basic equations of the general theory of elasticity | 3 |
| 1.1c The optimal form and relationship of the coherent inclusions of the new phase | 7 |
| 1.1d The distribution of coherent inclusions | 18 |
| 1.2 Previous work on Al(rich)-Cu alloys | 34 |
| 1.3 An approximation for the strain field of a disc-shaped G.P. zone | 37 |
| 1.4 Elastic interaction between pairs of dislocation loops - the infinitesimal approximation | 44 |
| 1.5 Diffraction contrast of the θ'' and θ' precipitates and optical diffraction of electron micrographs | 45 |
| 1.5a Introduction | 45 |
| 1.5b Electron diffraction contrast from ledges at the interface of faceted θ' precipitates | 46 |
| 1.5c Elastic strain effects | 48 |
| 1.5d On the origin of "tweed" contrast | 49 |
| 1.5e Optical diffraction of electron micrographs | 55 |

| | <u>PAGE</u> | |
|-----------|---|----|
| CHAPTER 2 | EXPERIMENTAL PROCEDURES | 57 |
| 2.a | Preparation of single crystals | 57 |
| 2.b | Specimen preparation | 58 |
| 2.c | Precipitation heat treatment | 58 |
| 2.d | Thin foil preparation | 58 |
| 2.e | Electron microscopy operation | 59 |
| 2.f | Optical diffraction | 59 |
| CHAPTER 3 | RESULTS AND DISCUSSION | 61 |
| 3.a | Prologue | 61 |
| 3.1 | On the stability of arrays of precipitates | 61 |
| 3.1.1 | Elastic properties of three-dimensional arrays of plate shaped precipitates | 62 |
| 3.1.1.1 | Elastic self energy | 62 |
| 3.1.1.2 | The interaction energy | 63 |
| 3.1.1.3 | The energetics of the $\langle 1230 \rangle$ array | 64 |
| 3.1.1.4 | Numerical test of the mechanical stability of the $\langle 1230 \rangle$ array | 77 |
| 3.1.1.5 | Experimental results | 82 |
| 3.1.1.6 | Discussion | 84 |
| 3.1.2 | Elastic stabilization of three-dimensional arrays against Ostwald ripening | 87 |
| 3.1.2.a | Introduction | 87 |
| 3.1.2.1 | Conditions for stability against Ostwald ripening | 88 |
| 3.1.2.2 | Algebraic conditions for stability | 92 |
| 3.1.2.2a | The interfacial energy | 92 |

| | <u>PAGE</u> |
|---|-------------|
| 3.1.2.2b The equilibrium shape | 93 |
| 3.1.2.3 Numerical test of the stability of the <1230> array against coarsening | 95 |
| 3.1.2.4 Numerical test of the stability of arrays of precipitates against co-ordinated diffusion | 100 |
| 3.1.2.5 Discussion | 106 |
| 3.2 Autocatalytic nucleation and elastic stabilization of linear arrays of plate- shaped precipitates | 110 |
| 3.2a Introduction | 110 |
| 3.2.1 Nucleation and morphology of stacks | 112 |
| 3.2.1a Results | 112 |
| 3.2.1b Nucleation of θ' | 117 |
| 3.2.1c Numerical estimation of the elastic interaction energy | 118 |
| 3.2.2 The stability against growth of particles in stacks | 139 |
| 3.2.2a Results | 139 |
| 3.2.2b Numerical estimations of stability | 141 |
| 3.2.3 Discussion | 149 |
| 3.3 The elastic interaction of the ledges on plate-shaped precipitates | 151 |
| 3.3a Introduction | 151 |
| 3.3.1 Thermal nucleation of growth ledges | 152 |

| | <u>PAGE</u> |
|--|-------------|
| 3.3.2 The strain field of plate-like precipitates and steps at the interphase interfaces | 153 |
| 3.3.3 The elastic interaction energy | 153 |
| 3.3.4 Numerical estimation of the elastic interaction energy | 154 |
| 3.3.5 The chemical force | 157 |
| 3.3.6 Experimental observations | 169 |
| 3.3.7 Discussion | 171 |
| SUMMARY | 173 |
| APPENDIX I | 177 |
| APPENDIX II | 180 |
| REFERENCES | 182 |

LIST OF FIGURES

| <u>Fig. No.</u> | | <u>Page</u> |
|-----------------|--|-------------|
| 1 | Schematic representation of a set of five imaginary operations in order to find the elastic field (after (18)). | 10 |
| 2 | A section of a solid solution with unit edge lengths. Lattice parameter a has to be subjected to strains $\delta = (a-a_0)/a$ in both x and y directions if it is to be coherent when added to material having a lattice parameter a_0 in the xy plane (after (45)). | 25 |
| 3 | The relationship between Helmholtz free energy $[f'(c)]$ and the coherent free-energy function $\Phi(C, C_0)$. Coexisting coherent phase compositions in a system of average composition C_0 are seen to lie within the coexisting incoherent phase compositions (after (46)). | 29 |
| 4 | Typical morphology of G.P. zones and γ' precipitates in Cu-2% Be alloys. Notice in a incipient alignment of G.P. zones; b, shows the γ'' phase with $\{100\}$ habit plane, but aligned along the traces of the $\{110\}_\alpha$ planes (after (33)). | |
| 5 | Dark field micrographs of a Ni-19% V alloy aged $\frac{1}{2}$ minute to 6.3 hours at 780°C. a) 1 minute, g $[010]$. Note a random distribution of θ precipitates. (b) 18 minutes g $[010]$ and $[001]$. Notice a larger distribution of one variant of θ precipitates in the right-hand side micrograph. (c) 6.3 hours, g $[001]$ and $[010]$. Notice two completely different distributions of θ precipitates on a given region (after (33)). | |
| 6 | Microstructures and diffraction pattern obtained via computer simulation. Figures (a), (b) and (c) are in order of increasing "ageing" in the computer. Notice the alignment of tetragonal precipitates along the $\{110\}$ planes and the preferred development of one variant of precipitates (after (48)). | 33 |
| 7 | Crystal lattices of θ'' , θ' and θ in the Al-4% Cu alloys. The misfit in the c direction is taken by elastic displacement in the matrix. | 36 |

| <u>Fig. No.</u> | | <u>Page</u> |
|-----------------|---|-------------|
| 8 | Phase diagram for Al(rich)-Cu alloys showing the solvus lines of θ , θ' , θ'' and G.P. zones (after (58)). | 38 |
| 9 | Transformation of a plate-like inclusion (a) is formed by displacement by $-b$ of the upper side (b). | 39 |
| 10 | Pure prismatic infinitesimal dislocation loop. | 43 |
| 11 | a) The geometry of the thin foil used by Weatherly and Sargent (72) to compute images of ledges in precipitates in Al-4wt% Cu. b) A CDF image obtained with a (111) matrix reflection showing particles with ledges. c) Schematic diagrams showing images of growth and dissolution steps. The position of the step is given by the dashed line, the heavy line being black contrast and the shaded region bright. d) A BF image with a (200) reflection showing the ledges as faint double images. e) Displacement fringes visible in BF, $\vec{g}(111)$. | |
| 12 | Schematic representation of streaks produced by strain field effects along $\langle 111 \rangle$ for G. P. zones on {100} in Cu-Be alloys for three different reflections (after (30)). | 50 |
| 13 | (a) Disposition of plates in a b.c.c. lattice of edge length L . The arrows indicate the direction of the particular plate normal. (b) Projection of the arrangement of (a) onto a (001) plane. Plates depicted by dashed line lie at $L/2$ above and below the plane of the projection. (c) Schematic tweed contrast from overlapping black-white images, $\vec{g} = 200$, beam direction [001]. (d) Schematic tweed contrast $\vec{g} = 110$, beam direction [001] (after (35)). | 52 |
| 14 | (a) Schematic pattern of distortions due to projection of strain centres in Fig. 13 onto (001). Two orthogonal transverse waves with wave vectors parallel to $[110]$ and $[1\bar{1}0]$ are produced, with $\lambda = L/\sqrt{2}$. (b) Diffraction pattern associated with lattice disturbed by single transverse wave of wavelength λ (after (77)). | 54 |
| 15 | Arrays of circular rings ranging from perfect square alignment (a) to complete disorder (3). Optical diffraction patterns made from negative copies of these arrays are shown in Fig. 16 (after (81)). | 56 |

| <u>Fig. No.</u> | | <u>Page</u> |
|-----------------|--|-------------|
| 16 | Optical diffraction patterns made from negative copies of the arrays of rings in Fig. 15. Note that the diffraction pattern of the regular square array (a) gradually disappears and is replaced by an approximation to the diffraction pattern for a single ring (d). Note also that the first order diffraction spots in (a) fall within the limits of the rings in (d) (after (81)). | |
| 17 | Simple optical diffractometer. The diagram shows the arrangement of the components used to construct a simple optical diffractometer. A, laser; B, beam expanding lens; D, pinhole; E, adjustable diaphragm; F ₃ , diffraction lens; G, electron micrograph; and H, viewing screen or camera (81). | 60 |
| 18 | The <1230> array. | 66 |
| 19 | Interaction energy of two square shaped particles when they are mutually parallel (face-face configuration) as a function of separation. The broken line indicates the interaction of infinitesimal precipitates of the same strength. D is the centre-to-centre distance; each unit represents the edge-length of the particles (D has the same meaning, r/ℓ , in all other figures in which it appears. | 68 |
| 20 | Interaction energy of two square shaped particles when they are mutually parallel (edge-edge configuration) as a function of separation. The broken line indicates the interaction of infinitesimal precipitates of the same strength. | 69 |
| 21 | Interaction energy of two square shaped particles when they are mutually perpendicular (edge-edge configurations) as a function of separation. The broken line indicates the interaction of infinitesimal precipitates of the same strength. | 70 |
| 22 | Interaction energy of two square shaped particles when they are mutually perpendicular (edge-face configuration) as a function of separation. The broken line indicates the interaction of infinitesimal precipitates of the same strength. | 71 |
| 23 | The total elastic energy of the <1230> array per plate vs the distance between the plates enclosed by the sphere of radius of 6.4, 7.5 and 10.0 times the plate-length. | 73 |

| <u>Fig. No.</u> | | <u>Page</u> |
|-----------------|--|-------------|
| 24 | The total elastic energy per plate of the $\langle 1230 \rangle$ array vs the number of precipitates, N (or R), the radius of the sphere which includes that number of precipitates). The distance between the particles is 1.2 times the plate-length. | 75 |
| 25 | The total elastic energy per plate of the $\langle 1230 \rangle$ array vs the distance between the plates (infinitesimal approximation). The energy was calculated between the central plate and the plates enclosed by the sphere of radius of 10.0 plate edge-lengths. | 76 |
| 26 | The elastic energy change per plate of the $\langle 1230 \rangle$ array in the infinitesimal approximation as a function of the displacement of the central plate along the x-direction (each division is 1/10 plate edge-length). The radius of the sphere is 10.0 times the plate edge-length and the distance between the particles (centre-centre) is 1.2 plate edge-lengths. | 78 |
| 27 | The elastic energy change per plate of the $\langle 1230 \rangle$ array in the infinitesimal approximation as a function of the displacement of the central plate along the z-direction (each division is 1/10 plate edge-length). The radius of the sphere is 10.0 times the plate edge-length and the distance between the particles (centre-centre) is 1.2 plate edge-lengths. | 79 |
| 28 | The elastic energy change per plate of the $\langle 1230 \rangle$ array in the fininitesimal approximation as a function of the displacement of the central plate along the y-direction (each division is 1/10 plate edge-length). The radius of the sphere is 10.0 times the plate edge-length and the distance is 10.0 times the plate edge-length and the distance between the particles (centre-centre) is 1.2 plate edge-lengths. | 80 |
| 29 | The elastic energy change per plate of the $\langle 1230 \rangle$ array in the 'large precipitate' approximation as a function of the displacement of the central plate along the y-direction (each division is 1/10 plate edge-length). The radius of the sphere is 7.5 times the plate-length and the distance between the particles (centre-centre) is 1.2 plate edge-lengths. | 81 |
| 30 | Al-3% Cu crystal with (001) orientation, solution-treated and aged 6 hours at 160°C. Bright-field conditions show tweed contrast. θ " particles are not clearly seen (94500 \times). | |

| <u>Fig. No.</u> | | <u>Page</u> |
|-----------------|--|-------------|
| 31 | Bright field microtraphs of Al-3% Cu crystal with (001) orientation, solution-treated and aged 24 hours at 160°C, showing strain fields of the individual θ " particles. The particles are now revealed as about 400 Å in diameter (94500×). | |
| 32 | Al-3% Cu crystal with (001) orientation, solution-treated and aged 95 hours at 160°C. a) Bright field micrograph shows coarse tweed-like contrast (27500×); b) Corresponding selected-area electron diffraction pattern. | |
| 33 | Optical diffraction patterns corresponding: a) to the model lattices of different degrees of ordering and b) to the series of micrographs of the type shown in Fig. 32. | |
| 34 | Bright field micrographs of Al-3% Cu crystal with (001) orientation, solution-treated and aged 95 hours at 160°C. Both micrographs show that the energetically favoured edge-face and "parallel step" orientations are well represented, clearly showing evidence of short-range ordering. (a) 55000×; (b) 33000×. | |
| 35 | The change of elastic energy due to volume exchange between a pair of 'large' precipitates in the face-face configuration. The distance between the precipitates is 2.6, 3.2 and 4.0 times the plate edge-length. | 96 |
| 36 | The change of elastic energy due to volume exchanges between a pair of 'large' precipitates in the edge-face configuration. The distance between the particles is 0.8, 1.0, 1.2 and 2.0 times the plate-edge-length. | 97 |
| 37 | The elastic energy change per plate of the $\langle 1230 \rangle$ array due to volume exchanges between a pair of 'large' precipitates in the edge-face configuration. The distance between the first neighbours is 0.8, 1.6 and 2.0 plate edge-lengths. The radius of the sphere is 6.4 times the plate edge-length. The ordinate represents the even part of the variation of E_{11} with V_1 and so clearly shows the positive curvature and the array stability. | 99 |

| <u>Fig. No.</u> | | <u>Page</u> |
|-----------------|---|-------------|
| 38 | The variation of $K(f,p)$ function vs the volume fraction f (or D , the distance between the precipitates). The arrow indicates the D value at which the interaction energy is a minimum; see Fig. 23. The aspect ratio l/d is kept constant at a value of 10. | 101 |
| 39 | The elastic energy change of the $\langle 1230 \rangle$ array due to co-ordinated volume exchanges among the nearest neighbours in the $[010]$ direction (full line). The broken line represents the volume exchange between the single pair labelled (2) and (5). The distance between the first neighbours is 1.5 plate edge-lengths, and the cut-off radius of the sphere is 7.5 times the plate edge-length. The ordinate represents the even part of the variation of E with V and so clearly shows the positive curvature of the stability of the array. | 104 |
| 40 | The elastic energy change of the $\langle 1230 \rangle$ array due to co-ordinated volume exchanges among the third nearest neighbours in the $[100]$ direction. The distance between the first neighbours is 1.5 plate edge-lengths, and the cut-off radius of the sphere is 7.5 times the plate edge-length. The ordinate represents the even part of the variation of E with V and clearly shows the positive curvature and the stability of the array. | 105 |
| 41 | Al-3% Cu crystal with (001) orientation, solution-treated and aged 1 hour at 240°C. Bright field conditions show inclined stacks of parallel θ' particles, containing only one $\{100\}$ variant (24750 \times). | |
| 42 | Bright field micrographs of Al-3% Cu crystal with (001) orientation, solution-treated and aged 1 hour at 240°C, show inclined stacks of parallel θ' particles. The inclination angle with $\{100\}$ habit plane is much smaller than that of Fig. 41. (a) 53250 \times ; (b) 33000 \times . | |
| 43 | Al-3% Cu crystal with (001) orientation, solution-treated and aged 1-3 hours at 240°C. This series of micrographs shows non-parallel stacks containing more than one $\{001\}$ variant. (a) and (b) contain two $\{100\}$ variants and (c) and (d) contain three $\{100\}$ variants. Note much smaller θ' particles between larger θ' plates, and also larger θ' particles on the ends of the stacks. (a) aged 3 hours, 12450 \times , (b) aged 1 hour, 25000 \times , (c) aged 1 hour, 55000 \times , (d) aged 1 hour, 41250 \times . | |

- 44 A series of micrographs similar to Fig. 43 but with different proportions of the respective habit plane variants. Note, again, smaller θ' precipitates between larger θ' particles. (a) aged 3 hours at 240°C; 41250× (b) aged 1 hour at 240°C; 14250× (c) aged 3 hours at 240°C; 65250× (d) aged 9 hours at 240°C; 41250×.
- 45 Al-3% Cu crystal with (001) orientation, solution-treated and aged 1 hour at 240°C. Bright field micrographs show overall structure of θ' precipitates in their relatively early stage of development. Both micrographs contain different kinds of stacks, already described in Figs. 43 and 44. (a) high strain field around stacks is very visible. (b) only particles are imaged by tilting the foil from the Bragg condition (bright field weak beam condition).
(a) 15000× (b) 25000×.
- 46 Al-3% Cu crystal with (001) orientation solution-treated and aged 1 hour at 240°C. The series of micrographs show stacks in dark field. (a) and (b) stacks imaged in dark field using matrix reflections, show strain field around particles; Note also the stack in (a) imaged by differential absorption. (c) and (d) show stacks in dark field using precipitate reflections.
(a) 42000×, (b) 14250×, (c) 33000×, (d) 14250×.
- 47 Al-3% Cu crystal, solution-treated and aged 1 hour at 240°C. Bright field micrograph showing stacks in the foil of approximately (111) orientation (28000×).
- 48 Solution-treated and water-quenched Al-3% Cu crystal with (001) orientation. (a) dark field micrograph shows punching of dislocation loops from an inclusion (14250×). (b) Bright field micrograph shows the matrix with only a few defects; small defects could not be resolved (53250×).
- 49 Al-3% Cu crystal with (001) orientation, plastically deformed during cutting, solution treated and aged 1 hour at 240°C. Dark field micrograph shows repeated nucleation on moving dislocation; note the leading dislocation (42500×).

- 50 Al-3% Cu crystal with (001) orientation, solution-treated and aged 15 minutes at 240°C. This series of bright field micrographs shows small clusters of only a few particles, all in energetically favourable orientations. Note possible spreading of θ' precipitates from the cluster on the top (a) and small particles very close to the large ones (c) and (d). Two particles, large and small, in very favourable orientation (face-face and edge-face) are seen in (3) and (f). Also note in (c) and (d) how the strain field can obscure visibility of small particles.
 (a) 27500 \times , (b) 43500 \times , (c) 27500 \times ,
 (d) 27500 \times , (e) 79500 \times , (f) 94500 \times .
- 51 Bright field micrographs of Al-2% Cu crystal with (001) orientation, solution-treated and aged 1 hour at 240°C, show clusters of a few particles in the energetically favoured, edge-face orientation. Note how diffusion and strain interaction fields have influenced the particle shape.
 (a) 16000 \times , (b) 16000 \times .
- 52 Al-3% Cu crystal with (001) orientation, solution-treated and double-aged (1 hour at 240°C and 23 hours at 160°C) to show the solute fields around the original θ' particles by well defined θ'' precipitates.
 (a) 53250 \times , (b) 31500 \times .
- 53 Al-3% Cu crystal with (001) orientation, solution-treated, aged 15 minutes at 240°C followed by in situ hot stage ageing at 240-300°C. Matrix dark-field micrograph shows a dislocation network on the semicoherent θ' particles (42000 \times).
- 54 Interaction energy of two square shaped particles when they are mutually parallel (face-face configuration) as a function of separation. The broken line indicates the interaction of infinitesimal precipitates of the same strength. 119
- 55 Interaction energy of two square shaped particles when they are mutually perpendicular (edge-face configuration) as a function of separation. The broken line indicates the interaction of infinitesimal precipitates of the same strength. 120

| <u>Fig. No.</u> | | <u>Page</u> |
|-----------------|---|-------------|
| 56 | Interaction energy of two equal size square-shaped particles, when they are mutually perpendicular (edge-face orientation) as a function of inclination angle ψ , keeping the centre-to-centre distance constant (1.2 times the plate length, which corresponds to the minimum in Fig. 55). | 122 |
| 57 | Interaction energy of two equal size square-shaped particles, when they are mutually parallel (face-face configuration) as a function of translation (parallel to the plate plane) of one particle. The effect of variation in the initial separation is also shown. | 123 |
| 58 | Interaction energy of two equal size square-shaped particles when they are mutually perpendicular (edge-edge configuration) as a function of translation along the y-axis. | 124 |
| 59 | Schematic representation of some linear arrays. | 126 |
| 60 | The total elastic interaction energy of the linear array of equal size parallel particles (per central plate) as a function of the inclination angle and distance between the plates. The energy was calculated between the central plate and 9 particles equally spaced along the z axis. | |
| 61 | The total elastic interaction energy of the linear array of equal size particles (per central plate) vs distance between the plates. The array is made up of parallel plates (the inclination angle $\psi = 45^\circ$) and of perpendicular particles (edge-face configuration). | 129 |
| 62 | The total elastic interaction energy of the linear array of equal size particles (per pair of central precipitates) vs the distance between the plates. The array is formed from parallel plates (with inclination angle $\psi = 0^\circ$) and from perpendicular plates (edge-face configuration); r is the centre to centre distance between the particles in edge-face configuration. | 130 |
| 63 | Interaction energy between large and small particles when they are mutually perpendicular (edge-face configuration) as a function of separation. (The size ratio in this and all similar calculations was 1/10). | 132 |

| <u>Fig. No.</u> | | <u>Page</u> |
|-----------------|--|-------------|
| 64 | The change of elastic interaction energy (for a pair initially at the minimum in the potential curve of Fig. 63) as a function of the displacement of the small particle along the z-axis. | 133 |
| 65 | The change of elastic interaction energy between large and small particles when they are mutually parallel (face-face configuration) as a function of the displacement of the small particle along the y-axis. | 134 |
| 66 | Interaction energy between large and small particles when they are mutually perpendicular (edge-edge configuration) as a function of the displacement of the small particle along the y-axis. | 136 |
| 67 | Interaction energy between large and small particles when they are mutually parallel (face-face configuration; inclination angle $\psi = 0^\circ$) as a function of separation. | 137 |
| 68 | The change of elastic interaction energy which corresponds to the minimum in the potential curve given in Fig. 67 as a function of displacement of the small particles along the z-axis. | 138 |
| 69 | Al-3% Cu crystal with (001) orientation, solution-treated and aged 1 hour at 240°C. Bright field micrograph shows stack development in relatively early stage. Note supersaturated matrix around the stack (53250×). | |
| 70 | Al-3% Cu crystal with (001) orientation, solution-treated and aged 3 hours at 240°C. Bright field micrograph shows development of new θ' particles in the stack and around the stack (41250×). | |
| 71 | Al-3% crystal with (001) orientation, solution-treated and aged 9 hours at 240°C. The θ' particles are much smaller than the θ' plates in the surrounding matrix. Particles on the ends of the stack are much longer than those within the stack (53250×). | |

Figure No.

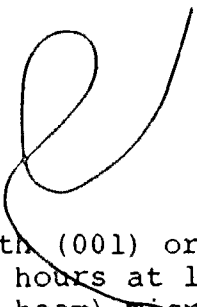
Page

- 72 Al-3% Cu crystal with (001) orientation, solution-treated and aged 23 hours at 240°C. Bright field micrograph shows the attack possible elastically stabilized against growth. Note much longer θ' particles in the surrounding matrix (18750 \times).
- 73 The change of elastic interaction energy of the linear array of parallel plates (inclination angle $\psi = 45^\circ$, and vertical separation 1.2 times the plate length) due to lengthening of the central plate into the matrix. The rest of the particles in the array have equal dimensions. The central particle was allowed to increase to length in one direction as indicated by the arrow. 142
- 74 The change of elastic interaction energy of the linear array of parallel particles (inclination angle $\psi = 45^\circ$, the vertical separation is 1.2 times the plate length) due to lengthening of the central particle into matrix. The central particle was allowed to increase its length in two directions. 143
- 75 The change of elastic interaction energy of the linear array of parallel particles (inclination angle $\psi = 16^\circ$, vertical separation 0.3 times the plate length) due to lengthening of the central plate. The central plate was allowed to increase its length in one direction only. 144
- 76 The change of elastic interaction energy of the linear array due to lengthening of the central plate into the matrix. The central plate was allowed to increase its length in one direction. The array is formed from parallel plates (face-face configuration, $\psi = 45^\circ$, vertical separation 1.2 times the plate length) and perpendicular plates (edge-face configuration with the centre-to-centre distance 1.2 times the plate length. 145
- 77 The change of elastic interaction energy of the linear array of parallel particles (face-face configuration, $\psi = 45^\circ$, vertical separation 1.2 plate lengths) due to lengthening of the last particle in the array. The particle was allowed to grow in one direction. 147

| <u>Figure No.</u> | | <u>Page</u> |
|-------------------|---|-------------|
| 78 | The change of elastic interaction energy of the 11- near array of the parallel particles (face-face configuration, $\psi = 16^\circ$, vertical separation 0.3 times the plate length) due to volume exchanges between the central plate and its first neighbour. | 148 |
| 79 | Elastic interaction energy between large and small parallel plates as a function of the position of the small plate along the y-axis. The small plate lies on the large one. | 155 |
| 80 | Elastic interaction energy between two parallel and coaxial ledges as a function of size of the smaller ledge. | 157 |
| 81 | The Gibbs-Wulff construction of the θ' precipitate. | 162 |
| 82 | Variation of the elastic misfit obtained by matching integral number of half θ' unit cells and matrix unit cells. | 163 |
| 83 | The free energy change as a function of the nucleus size expressed in terms of integral number of half θ' unit cells. | 165 |
| 84 | The total force acting on the interface of the gro- wing ledge as a function of the ledge size. | 168 |
| 85 | Al-3% Cu crystal with (001) orientation, solution- treated and aged 5 hours at 240°C. This series of dark field micrographs show very complex ledges morphology of the particles. At arrowed regions in (a) and (b) it appears that the ledges on upper and lower surface interact. Heterogeneous nuclea- tion of the ledges at points of precipitate impinge- ment is evident in (c). (a) 87000 \times ; (b) 62500 \times ; (c) 42000 \times . | |
| 86 | Al-3% Cu crystal with (111) orientation, solution- treated and aged 1 hour at 240°C. Dark field condition shows high density of equally spaced growth ledges (71000 \times). | |

Figure No.

Page

- 
- 87 Al-3% Cu crystal with (001) orientation, solution-treated and aged 92 hours at 160°C. This series of dark field (weak beam) micrographs shows very regular shapes of θ' particles and ledges. Ledges are nucleated as pill-boxes in the middle of the plates. In many cases it seems that the edges clearly lead the ledges.
(a) 55000 \times ; (b) 42000 \times .
- 88 Al-3% Cu crystal with (001) orientation, solution-treated and in situ aged at 240-300°C. Bright field micrograph shows high density of equally spaced dissolution ledges (11250 \times).
- 89 Al-3% Cu crystal with (001) orientation, solution-treated and aged 30 minutes at 390°C. Heterogeneous nucleation of the equilibrium θ phase on the θ' interfaces. Dissolution ledges on the θ' interfaces are clearly seen (11250 \times).

LIST OF TABLES

| <u>Table No.</u> | | <u>Page</u> |
|------------------|--|-------------|
| 1 | The total number of precipitates enclosed by sphere of radius 6.4 to 10 units for near-neighbour separations of 0.8, 1.0, 1.6 and 2.0 units. | 74 |
| 2 | The estimated misfits and the corresponding elastic self energies, obtained by matching integral number of half θ' unit cells and driving forces as a function of the ledge radius. | 164 |
| 3 | The constrained concentrations, $C_i^{r_2}$, at the ledge interface and the corresponding chemical driving forces as a function of the ledge radius. | 167 |

INTRODUCTION AND SCOPE

Certain phase transitions in the solid state are accompanied by considerable elastic deformation of the parent crystal. At the same time the phase transition occurs in such a manner that, at each step, the loss of free energy of the system due to the deformation turns out to be minimal.

While the chemical free energies of the matrix and precipitate phases generally provide the bulk of the driving force for precipitation, the elastic strain energy may affect significantly the kinetic path along which ageing occurs. That is, the elastic strain energy is generally believed to exert a major influence upon the distribution and shape of precipitates which are coherently bound to the matrix.

The aim of this work is the investigation of the role of elastic interaction energy of plate shaped precipitates on their spatial distribution, nucleation, growth and coarsening.

CHAPTER 1

LITERATURE SURVEY

1.1 THE ROLE OF ELASTIC ENERGY IN PHASE TRANSFORMATIONS IN SOLID STATE

1.1.a INTRODUCTION

In solid-solid transformations the difference in specific volumes of the matrix and precipitate phases introduces an extra energy term, the strain energy, because in this case the volume change of the transformation cannot easily be accommodated by the matrix material. We find that in general the shape factors are not those of simple spherical nucleus, but both surface and strain energy terms are anisotropic. Furthermore, these terms are composition dependent. The characteristics of solid-solid transformation processes therefore vary widely depending upon the particular compositions, crystal structures and elastic constants of the matrix and precipitate phases.

The minimization of elastic energy is possible because of the existence of an optimal form and distribution of the inclusions of the new phase which are coherently bonded to the matrix.

The (self) strain energy of an inclusion has been shown to depend on the shape of the inclusion both in the case where

the precipitate-matrix interface is incoherent (1,2) and when it is coherent (3,4). In addition, periodic arrays of coherent precipitates have been shown (5-12) to be energetically preferred over a random distribution owing to the interaction of the strain fields of the precipitates.

In the investigation of the coherent stage the following important questions arise:

1. What is the optimal shape of the new-phase particles to ensure minimum free-energy?
2. What is the orientation of the new-phase particles relative to the crystallographic axes of the matrix?
3. What is the orientation relationship between the lattices of the new and parent phases?
4. What is the mutual spatial distribution of the inclusions?

A complete answer to these questions may be obtained in principle by considering the elastic properties of the matrix and the precipitate, the crystal geometry of the transformation and the surface tension (free energy).

The present review concerning the optimal form and distribution of the inclusions of the new phase is based chiefly on the work of Khachaturyan and co-workers (11,6).

1.1.b BASIC EQUATIONS OF THE GENERAL THEORY OF ELASTICITY

The components of the displacement will be denoted by u_i . The spatial derivatives of u_i will be written $u_{i,j}$ so that,

$$u_{i,j} = \frac{\partial u_i}{\partial x_j}, \quad (1)$$

The components of the strain tensor are defined as follows,

$$e_{ij} = \frac{1}{2} (u_{i,j} + u_{j,i}) \quad (2)$$

The components of the stress are denoted by σ_{ij} , and the components of the body force per unit volume are f_i .

The conditions for translational equilibrium can now be written as

$$\sigma_{ij,j} + f_i = 0 \quad ; \quad (i,j = 1,2,3) \quad (3)$$

or, when written out in full,

$$\frac{\partial \sigma_{11}}{\partial X_1} + \frac{\partial \sigma_{12}}{\partial X_2} + \frac{\partial \sigma_{13}}{\partial X_3} + f_1 = 0$$

$$\frac{\partial \sigma_{21}}{\partial X_1} + \frac{\partial \sigma_{22}}{\partial X_2} + \frac{\partial \sigma_{23}}{\partial X_3} + f_2 = 0$$

$$\frac{\partial \sigma_{31}}{\partial X_1} + \frac{\partial \sigma_{32}}{\partial X_2} + \frac{\partial \sigma_{33}}{\partial X_3} + f_3 = 0$$

The e_{ij} and σ_{ij} are symmetric.

The relations between stress and strain are taken to be the generalized Hooke's law of proportionality of stress and strain (14).

$$\sigma_{ij} = C_{ijkl} e_{kl} \quad (4)$$

These relations restrict us to the linear theory of elasticity. They may break down when the elastic strain becomes large, e.g. in the region close to a dislocation. (In a more rigorous treatment, we might consider either a nonlinear theory of elasticity, a detailed atomic theory or a plastic deformation theory.)

In general, the elastic constants C_{ijkl} in the foregoing will vary from point to point in a medium. They are constant, however, in an elastically homogeneous continuum, which is the best macroscopic approximation to a chemically homogeneous single crystal.

It follows from the symmetry of σ_{ij} and e_{ij} that

$$C_{ijkl} = C_{jikl} = C_{ijlk}. \quad (5)$$

Therefore it follows from eq. (4) and eq. (2) that

$$\sigma_{ij} = C_{ijkl} U_{k,l} \quad (6)$$

so that the equilibrium conditions, eqs. (3) can also be written as follows:

$$C_{ijkl} U_{k,lj} + f_i = 0 \quad (7)$$

It can be shown that, in the case of an isotropic medium, the set of elastic constants C_{ijkl} reduces to two independent constants. Introducing Lamé's constant λ and the modulus of rigidity μ , Hooke's law reduces to,

$$\sigma_{ij} = \lambda \epsilon_{kk} \delta_{ij} + 2\mu e_{ij} . \quad (8)$$

It can be shown that it is possible to represent the unknown functions - the displacements, u_i , entering the equilibrium equations (7) in terms of three harmonic functions B_x , B_y , B_z . In other words, the displacement vector u can be represented by an harmonic vector B , whose Laplacian vanishes:

$$\Delta B = \nabla \cdot \nabla B = 0 . \quad (9)$$

The projections of this vector on the axes of a cartesian coordinates system satisfy Laplace's equation.

$$\Delta B_x = 0 ; \quad \Delta B_y = 0 ; \quad \Delta B_z = 0 . \quad (10)$$

The general expression for the displacement vector, for three dimensional elasticity theory, in terms of the harmonic vector B and the harmonic scalar β , given by Popkovich and Neuber (8, 14) is,

$$u = U_0 + B - \frac{1}{4(1-\nu)} (R \cdot B + \beta) \quad (11)$$

where the vector U_0 is an arbitrary particular solution of the equilibrium equations which accounts for the action of body forces, and R is the radius vector from the origin. In a cartesian system of coordinates, the displacements in the absence of body forces are given by,

$$U_i = B_i - \frac{1}{4(1-\nu)} \frac{\partial}{\partial X_i} (X_1 B_1 + X_2 B_2 + X_3 B_3 + \beta) \quad (12)$$

with

$$\nabla^2 B_i = \nabla^2 \beta = 0$$

where $i = 1, 2, 3$ and $X_i = x, y, z$.

The solution of the problem of the effect of a concentrated force, f , in an infinite elastic medium gives an example of a state of stress which arises in the presence of the simplest point singularity; with the aid of this solution one can construct states of stress which are produced by singularities of a more complicated nature. Given the solution of the equations of elasticity, corresponding to a concentrated force, one can derive by means of summation the solution for any distribution of forces throughout a volume, over a surface or along a line in an infinite elastic body.

A powerful method for the solution of problems in the continuum theory of elasticity (in particular for the continuum theory of dislocations) derives from a consideration of point forces. The problem is similar to that of finding the electrostatic potential caused by a distribution of charge. Solutions are derived by the Green's function method of electrostatics.

To integrate the differential equations of elasticity e.g. (7), it is useful to introduce Green's tensor function, analogous to Green's function of electrostatic theory. In electrostatics, Green's function represents the potential arising from a point charge. Similarly, Green's tensor function represents the displacement $u_i(r)$ at a point r arising from a point force at the origin in the x_j direction.

The displacement due to the force f applied at the point, assuming the classical isotropic theory of elasticity is given by (e.g. 15).

$$u_i = U_{ij} \cdot f_j \quad (13)$$

where

$$U_{ij} = \frac{1}{16\pi\mu(1-\nu)} \left[\delta_{ij} \frac{1}{r} (3-4\nu) + \frac{r_i r_j}{r^3} \right] \quad (14)$$

U_{ij} is the Green's tensor function for the elastic displacements; it denotes displacement in the i -direction from a unit point force acting in the j -direction (it is symmetrical in the i and j indices). An exact derivation of eq. (14) can be found in (16) and (17). There are several ways of finding Green's tensor function. The method of Fourier transforms seems to be the most straightforward.

1.1.c THE OPTIMAL FORM AND RELATIONSHIP OF THE COHERENT INCLUSIONS OF THE NEW PHASE

As a result of fluctuations in concentration and order parameters, inhomogeneities bearing a more or less random character arise in the crystal. If the lattice parameters depend strongly on composition, then from the macroscopic point of view the inhomogeneities of composition will lead to concentration stresses, inhomogeneous strains associated with these, and static displacements of the atoms in the crystal. As a result of the superposition of the fields of the displacements created by different atoms, a complex distribution of static displacements develops in the solution.

It is clear that the determination of the stresses and static displacement as a function of the coordinates of the atoms in the crystal in the above mentioned case of a complex and not completely symmetrical fluctuation of stresses sources constitutes an extremely difficult problem. The problem is

greatly simplified, however, if we use the method of fluctuation waves and transform from the displacements of the atoms to their Fourier components.

In the case of long-wave fluctuation waves we may carry out a macroscopic calculation of the static displacement waves, based on the use of equations taken from elastic theory and not on any specific model of the crystal. The amplitudes of the displacement waves are expressed in terms of crystal characteristics which may be determined experimentally. In the case of short wave fluctuations, the macroscopic approach becomes inapplicable.

For a wave-like change in concentration;

$$\delta c(r) = C_k \exp(-ikr) . \quad (15)$$

Corresponding to the k-th fluctuation wave, the displacements and strains also vary in a wave-like manner:

$$\begin{aligned} e_{\ell m} &= \frac{1}{2} \left[\frac{\partial(\delta U_\ell)}{\partial X_m} + \frac{\partial(\delta U_m)}{\partial X_\ell} \right] \\ &= \frac{1}{2} [K(n_m A_{k\ell} + n_\ell A_{km})] C_k \exp(-ikr) \end{aligned} \quad (16)$$

where n_ℓ are the components of the unit vector $n = k/k$ parallel to the wave vector k , $A(k)$ are the proportionality factors between the amplitudes of the static-displacement and concentration waves. Because of the presence of the matrix, internal stresses exist both inside and outside the inclusion.

To obtain a general solution for the elastic state of an inclusion and the matrix when the inclusion undergoes a change of shape and size (optimal form and orientation of the inclusions of the new phase) one must answer the question: What is the energy of a non-simply-connected anisotropic continuum with arbitrary configurations of the domains of non-simply-connectedness?

The problem in such a general formulation does not seem to have a solution in closed form. However, such a solution can be found if one assumes that the elastic moduli of the inclusions and of the matrix are identical, and that the interphase boundaries are coherent.

In order to find the elastic field*, following Khachaturyan (11), a set of five imaginary operations can be used as shown in Fig. 1.

* The strain energy associated with a coherent particle in an infinite homogeneous isotropic elastic medium, has been analyzed by Eshelby (4). Eshelby provides formulae for calculating the total strain energy, referred to unit volume of inclusion, for an ellipsoidal particle of arbitrary transformation strain, and arbitrary, but isotropic, elastic constants in the inclusion and matrix.

The elastic field of a dislocation loop derived by Kroupa (69) using Eshelby's theory (4) will be given in the section 1.3

Cahn's treatment of the coherent strain energy (44) (again for isotropic elastic medium) and the effect of the coherent strain energy on nucleation in a binary solid solution (46) will be given at the end of this section).

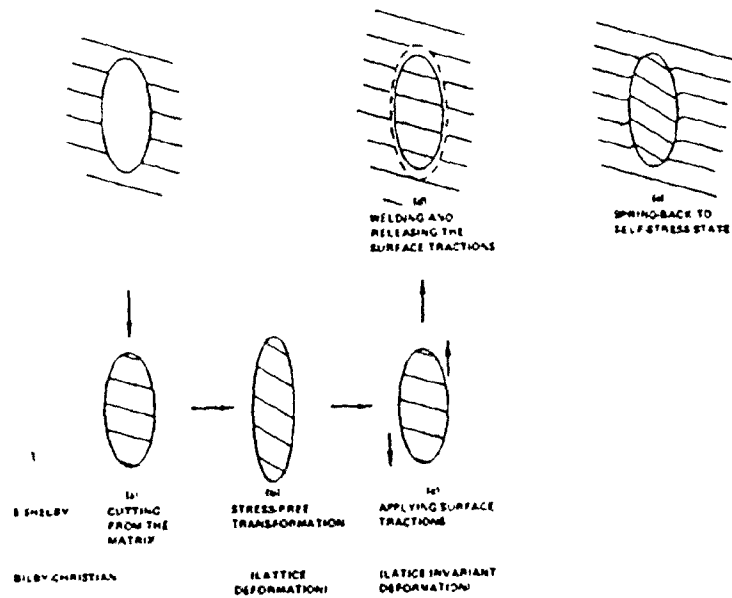


Fig. 1 Schematic representation of a set of five imaginary operations in order to find the elastic field (after (18)).

- a) Cut around the inclusion which is going to transform and remove it from the matrix.
- b) Allow the transformation to proceed without the constraint; i.e. stress free transformation, ϵ_{ij}^0 , which is directly connected with crystallographic transformation.

- c) Apply surface tractions to restore the original shape of the inclusion.
- d) Replace the inclusion into the hole in the matrix and rejoin the material across the cut.
- e) Allow spring-back to the self stressed state by the release of the surface tractions.

The surface traction in (c) can be written as;

$$F_i = \sigma_{ij}^0 n_j = \lambda_{ijkl} \varepsilon_{lm}^0 n_j \quad (17)$$

where n_j is the normal to the surface and λ_{ijkl} are the elastic constants of the new phase.

Applying operation (d) no strain is produced in the system, but there is the stress in the inclusion,

$$\sigma_{ij}^0 = \lambda_{ijkl} \varepsilon_{lm}^0 \quad (18)$$

The surface force has now become a layer of body force spread over the whole surface, s .

In order to cancel the force f_i inside the inclusion, a further force ($-f_i$) must be applied. This force produces displacements u_i at every point in the matrix and the inclusion. The body is now free of external force but in a state of self-stress because of the transformation of the region. The total elastic energy in the matrix and inclusion is given by (e.g. 19).

$$E = -\frac{1}{2} \epsilon_{ij}^0 \int_V \sigma_{ij} dV \quad (19)$$

where σ_{ij} is the stress in the inclusion, V is the volume of the inclusion and ϵ_{ij}^0 is the stress-free strain which the inclusion would undergo in the absence of the matrix.

The stress in the inclusion is given by;

$$\sigma_{ij} = \sigma_{ij}(f_1) - \sigma_{ij}^0 \quad (20)$$

where

$$\sigma_{ij}(f_1) = C_{ijkl} \epsilon_{kl} = C_{ijkl} U_{k,m} \quad (21)$$

is the elastic stress, caused by the force $(-f_1)$.

Introducing the function $\bar{\theta}(r)$, which is equal to one inside the inclusion and zero outside, eq. (19) can be integrated over the whole body,

$$E = -\frac{1}{2} \epsilon_{ij}^0 \int \sigma_{ij} \bar{\theta}(r) d^3r \quad (22)$$

The displacement component u_i at a point x , due to the component f_j of a point force acting at a point r , is known from the theory of elasticity (e.g. 15). It is given by,

$$u_i = U_{ij} f_j \quad (23)$$

U_{ij} denotes the displacement in the i -direction from a point acting in the j -direction.

The displacement field u_i from a surface distribution of forces $(\sigma_{ij}^0 n_j)$ is given by a surface integral (the force on a surface element dS is $df_j = \sigma_{ij}^0 dS_i$)

$$u_i = \int_S U_{ij} f_j dS \quad (24)$$

or using the Gauss theorem,

$$u_i = \int_{V'} \sigma_{kj}^o U_{ij,k} dV' \quad (25)$$

As already mentioned, in order to integrate the differential equations of elasticity (eq. 7) it is useful to introduce Green's tensor function G_{ij} , analogous to Green's function of electrostatic theory. After introducing the function $\bar{\theta}(r)$, eq. 25 can be written as

$$u_i(r) = \int \sigma_{kj}^o \frac{\partial G_{ij}(r-r')}{\partial X_k} \bar{\theta}(r') d^3 r' \quad (26)$$

with the condition that the Green's tensor function in an infinite elastic continuum satisfies the equation:

$$\lambda_{iklm} \frac{\partial^2 G_{mj}(r-r')}{\partial X_k \partial X_l} + \delta_{ij} \delta(r-r') = 0 \quad (27)$$

together with boundary condition that G_{ij} vanish at infinity.

δ_{ij} is the Kroneker delta and $\delta(r-r')$ is Dirac's delta function. Expressing eq. 20 in terms of eq. 26, eq. 22 becomes,

$$E = \frac{1}{2} \epsilon_{ij}^o \sigma_{ij}^o V - \frac{1}{2} \sigma_{lm}^o \sigma_{st}^o \int \bar{\theta}(r) d^3 r \int \bar{\theta}(r') \frac{\partial^2 G_{ls}(r-r')}{\partial X_m \partial X_t} d^3 r' \quad (28)$$

Finding Green's tensor function using Fourier transforms eq. 28 can be written as,

$$E = \frac{1}{2} \epsilon_{ij}^o \sigma_{ij}^o V - \frac{1}{2} \int A\left(\frac{k}{k}\right) |\theta(k)|^2 \frac{d^3 k}{(2\pi)^3} \quad (29)$$

where

$A(\frac{k}{k}) = \sigma_{lm}^o k_m G_{ls}(k) \sigma_{st}^o k_t$ is the function which depends only on the direction but not on the magnitude of the vector k , ($G_{ls} \sim 1/k^2$).

$$\theta(k) = \int \bar{\theta}(r) \exp(-ikr) d^3r$$

$G_{ls}(k) = \int G_{ls}(r) \exp(-ikr) d^3r$ is the Fourier transform of Green's function which can be obtained from the eq. 27.

Equation 28 expresses the elastic energy in terms of the coefficients σ_{ij}^o and $(G^{-1})^{ij}$ which characterize the elastic properties of the anisotropic medium and crystal geometry of the transformation, and also in terms of the function $|\theta(k)|^2$, which characterizes the shape of the particle. It gives a connection between the elastic energy of the system (precipitates of the new phase and perfect matrix) and the elastic properties of the system, the crystallography of the transformation, the shape of the precipitates and their crystallographic relationship with the matrix. Eq. 28 is valid if elastic constants of the inclusion and the matrix are equal.

To elucidate the orientation relationship between the lattices of the phases it is necessary to find the angle of rotation of the new-phase particle relative to the matrix. The vector of local rotation, ϕ , at a point is expressed in terms of the displacement at this point by the equation:

$$\langle \phi \rangle = \frac{1}{V} \int |\theta(k)|^2 [k, \hat{G}^{-1}(k) \hat{\sigma}_o(k)] \frac{d^3k}{(2\pi)^3} \quad (30)$$

From the structure of eq. 30 it follows that the orientation of the invariant plane depends, generally speaking, on the shape of the crystal of the new phase.

The formation of a single inclusion of the new phase in an infinite anisotropic continuum is accompanied by a minimum value of the elastic energy if the inclusion has the form of a thin extended plate, the normal unit vector k_0 of which is determined by the condition of maximum for the quantity $A(k|k)$. The answer to the questions posed can now be formulated:

1. The optimum shape of a new-phase particle to ensure minimum elastic energy is that of a thin plate, with length and width much greater than its thickness.
2. The plane of this plate is perpendicular to one of the k_0 vectors, thus bringing about a maximum $A(k|k)$.
3. The direction and magnitude of the angle of rotation of the crystallographic axis of this plate are given by eq. 30. The invariant plane is perpendicular to the vector $\langle\phi\rangle$.

For the case where the crystal geometry of the transformation is described by tensor ϵ_{ij}^0 , which has a tetragonal character, while the matrix for a cubic lattice, $\epsilon_{11}^0 = \epsilon_{22}^0 = \Delta a/a$, $\epsilon_{33}^0 = \Delta c/c$, $\epsilon_{ij}^0 = 0$ when $i \neq j$. In that case we have:

$$\sigma_{ij}^0 = \sigma_0 \begin{vmatrix} 1 & 0 & 0 \\ 0 & 1 & 0 \\ 0 & 0 & 1 \end{vmatrix} + \hat{\sigma}_0 \begin{vmatrix} -\frac{1}{2} & 0 & 0 \\ 0 & -\frac{1}{2} & 0 \\ 0 & 0 & -1 \end{vmatrix} \quad (31)$$

where

$$\sigma_o = \frac{C_{11}+2C_{12}}{3} \epsilon_{11}^o = \frac{C_{11}+2C_{12}}{3} \left(-2 \frac{\Delta a}{a} + \frac{\Delta c}{c}\right)$$

$$\hat{\sigma}_o = \frac{2(C_{11}-C_{12})}{3} \left(\frac{\Delta c}{c} + \frac{\Delta a}{a}\right)$$

$$\lambda_{1111} = C_{11} \quad ; \quad \lambda_{1112} = C_{12} \quad ; \quad \lambda_{1212} = C_{44}$$

For the case of a cubic lattice the matrix $(\hat{G}^{-1})^{ij}$ has the following form:

$$\begin{aligned} [G^{-1}(k)]^{11} &= \frac{1}{k^2} \frac{C_{11} - (C_{11} - C_{44})n_1^2 + \Delta(C_{11} + C_{12})n_2^2 n_3^2}{C_{44} D(n)} \\ [G^{-1}(k)]^{12} &= -\frac{1}{k^2} \frac{(C_{12} + C_{44})(1 + \Delta n_3^2)n_1 n_2}{C_{44} D(n)} \end{aligned} \quad (32)$$

where

$$\begin{aligned} D(n) &= C_{11} + \Delta(C_{11} + C_{12})(n_1^2 n_2^2 + n_1^2 n_3^2 + n_2^2 n_3^2) + \\ &\quad + \Delta^2(C_{11} + 2C_{12} + C_{44})n_1^2 n_2^2 n_3^2 \\ n &= k/k \quad ; \quad \Delta = \frac{C_{11} - C_{12} - 2C_{44}}{C_{44}} \end{aligned}$$

The other components of the tensor $[G^{-1}(k)]^{ij}$ are obtained by cyclic permutation of the cartesian indices. The elastic energy is given as:

$$E_1 = \frac{(\sigma_o + \hat{\sigma}_o)^2}{2D(n)} [\gamma + n_1^2 A - n_1^4 B + \Delta C n_1^2 n_2^2 n_3^2 + 2\Delta \gamma^2 n_2^2 n_3^2] \quad (33)$$

where

$$\gamma = \frac{\sigma_o - \frac{\hat{\sigma}_o}{2}}{\sigma_o + \hat{\sigma}_o}$$

$$A = \frac{C_{11}}{C_{44}} + \left(\frac{C_{11}}{C_{44}} - 2 \right) \gamma^2 - 2\gamma \left(\frac{C_{12}}{C_{44}} + 1 \right)$$

$$B = \frac{C_{11}}{C_{44}} - 1 + \gamma^2 \left(\frac{C_{11}}{C_{44}} - 1 \right) - 2\gamma \left(\frac{C_{12}}{C_{44}} + 1 \right)$$

$$C = \frac{C_{11}}{C_{44}} + \frac{C_{12}}{C_{44}} + 2\gamma^2 \left(\frac{C_{12}}{C_{44}} - 1 \right) .$$

From eq. 33 it follows that the elastic energy of the crystal takes on its least value when the normal to the new-phase plate, $n = k_o/k_o$, is oriented in such a way that the right-hand side of eq. 33 is a minimum.

On analyzing eq. 33 it can be shown that, depending on the relationship between the elastic constants C_{ij} and the value of the numerical factor γ , the energy is a minimum when the vector n lies either in the plane (100) or in (110). This means that the Miller indices of the plane of the crystal form (the plane of the plate) may either have the form (h0l) or (hhl).

To find the invariant plane (the orientational relationship) it is necessary to find the direction of the axis of rotation. For this we must know the direction of the vector $\hat{\sigma}_o^{-1} \hat{\sigma}_o k_o$. As the tensor $\hat{\sigma}_{ij}^o$ has tetragonal symmetry, then both the vector k_o and $\hat{\sigma}_o^{-1}(k_o) \hat{\sigma}_o k_o$ lie either in the plane (100) or in (110). Since the vector $\langle \phi \rangle$ is the vector product of the vector k_o and $\hat{\sigma}_o^{-1}(k_o) \hat{\sigma}_o k_o$, then the axis of rotation lies perpendicular to these planes. Thus when tetragonal deformations are present the invariant planes are either (100) or (110).

All the results derived above are valid as long as it is possible to neglect the contribution made by surface tension. The effect of surface tension will be to prevent the "expansion" of the new-phase particle into an infinitely thin, infinitely wide plate. In the general case the equilibrium shape of the inclusion will be determined by competition between the elastic deformation energy, which is minimal for an inclusion in the form of an infinitely thin, infinitely wide plate, and surface tension (energy), which conversely, is minimal for an inclusion of equiaxial form, if energy is isotropic. (It should be noted that besides the important role of the surface tension in determining the equilibrium shape, it is very important in controlling shapes formed on initial growth; however a clear distinction between kinetic and equilibrium shapes should be maintained.)

1.1.d THE DISTRIBUTION OF COHERENT INCLUSIONS

The so-called modulated, periodic or tweed structures have been observed in numerous systems.

Present X-ray and electron microscopical studies show that in a number of cubic solid solutions, a periodic distribution of coherent inclusions of a cubic precipitate phase arise at an early stage of decomposition. This phenomenon was observed in Cu-Ni-Co (20-22), Cu-Ni-Fe (20-23), in a group of nickel-based alloys (24-27), Au-Pt (28), Fe-Be (29).

This kind of structure is not only restricted to cubic precipitate phases. One of the characteristic modes of trans-

formation associated with strain relief twinning are the kinetic ordering reactions that are characterized by plate-like morphology and by specific crystallographic features which comply with the crystallography of martensitic transformation; e.g. Cu-AuII (40) and TaO_y (41).

Finally a phase transformation from a cubic to a tetragonal one associated with a periodic distribution of strain relief twinning is martensite transformation. The martensitic transformation in steels is only one example of a class of similar transformations that are found in a number of physical systems. Materials known to exhibit martensitic transformation include a variety of metal alloy systems, ferro-electric materials such as barium titanate, ceramic materials such as zirconium oxide, superconducting phases, and many others.

This observation has instigated theoretical work on the elastic interaction between individual inclusions (4,6). It is well known that there is no elastic interaction among centres of dilatation in an elastically isotropic medium (4, 42,43). Sometimes particles of a separated phase have an "equiaxial" form which is nearly spherical. Eshelby (5) has calculated the interaction potential of two spherical inclusions under the assumption that the interaction is due to the differences in elastic moduli of the inclusions and matrices, and that the tensor ϵ_{ij}^0 described a pure dilation. In this case the potential goes as $1/r^6$ and decreases rapidly.

However, defects or precipitates which give rise to

tetragonal distortions can interact quite strongly (6). The presence of a strong interaction must lead to correlations in the relative positions of the inclusions (short range and possible long-range order) during their formation in the field of already formed inclusions and also in their subsequent growth.

In a theoretical study of the elastic interaction of tetragonally distorted spheres Khachatryan and Shatalov (6) showed that the existence of strain fields which differ from purely dilatation fields, leads to a complicated angular dependence in the potential even for the isotropic continuum. Following Khachatryan and Shatalov (6), the elastic energy of the medium with the inclusion of the new phase relative to the undeformed state is (if the elastic moduli of both phases are equal)

$$E_{el} = \sum_{p=1}^z \int [\sigma_{ij}^0(p) \epsilon_{ij}(r) \bar{\theta}_p(r) + \frac{1}{2} \lambda_{ijlm} \epsilon_{ij}(r) \epsilon_{lm}(r)] d^3r \quad (34)$$

where: $\sigma_{ij}^0(p) = \lambda_{ijlm} \epsilon_{lm}^0(p)$; λ_{ijlm} is the elastic moduli tensor; $\epsilon_{ij}(r)$ is the strain tensor; $\bar{\theta}(r)$ is a function which is one inside the inclusion p and zero outside; z is the number of inclusion types.

Transforming to Fourier components eq. 34 becomes:

$$E_{el} = - \frac{1}{2} \sum_{p,q}^z \int (n, \hat{\sigma}^0(p) G(n) \hat{\sigma}^0(p) n) \theta_p^+(k) \theta_q^+(k) \frac{d^3k}{(2\pi)^3} \quad (35)$$

where k is the wave vector of the Fourier transformation;
 $n = k/k$; the symbol (\dots, \dots) indicates the scalar product;
 $\hat{\sigma}^0(p)$ and $G(k)$ are operators whose elements are $\hat{\sigma}_{ij}^0(p)$ and
 $G_{ij}(k)$, where $G_{ij}(k)$ is the Fourier component of the Green's
 tensor for the elastic problem.

The function $\theta_p(k)$ can be multiply connected. For
 simplicity it will be considered a medium in which there are
 only two inclusions altogether. Then, if the origin is put
 at the center of mass of one inclusion at type p designating
 the form factor of this simply connected inclusion by $\theta_p(k)$,
 the form factor of the other simply connected inclusion of
 type q , located at a distance r from the origin, has the
 form $\theta_q(k)\exp(ikr)$, where $\theta_q(k)$ is calculated in a coordinate
 system with origin at r .

It follows from eq. 35 that the interaction of these
 two inclusions is given by the expression:

$$E_{\text{int}}^{pq} = -\frac{1}{2} \int A_{pq}(n) \theta_p(k) \theta_q^\dagger e^{-ikr} \frac{d^3k}{(2\pi)^3} \quad (36)$$

where: $A_{pq}(n) = (n, \hat{\sigma}^0(p) G(n) \hat{\sigma}^0(q) n)$. The quantity
 $A_{pq}(n) \theta_p(k) \theta_q^\dagger(k)$ is the Fourier component of the pair interac-
 tion potential.

Using the isotropic continuum model to solve $A_{pq}(n)$, the
 interaction of two inclusions is given by the expression:

$$E_{\text{int.}}^{\text{pq}} = \frac{V_1 V_2}{16} \left[\frac{2D_2^{\text{pq}}}{r^3} + \frac{(R_1^2 + R_2^2) D_4^{\text{pq}}}{5r^5} \right] \quad (37)$$

where D_2^{pq} and D_4^{pq} are complicated terms depending on the orientation of the particles relative to the radius vector which connects the two particles. The first term in eq. 37 is the interaction for distances much greater than the inclusion dimension, and the second term is connected with the inhomogeneity of the deformation field of one inclusion at the limits of the region occupied by the other inclusion.

The expressions for the total energy of the elastic stresses of the system of coherent inclusion may be written in the general form:

$$E = E_o + E_{\text{int.}} \quad (38)$$

The first term in eq. 38 does not depend on the mutual arrangement of the inclusions; it is the sum of the elastic self-energies of inclusions. The second term in eq. 38, on the contrary, depends on the relative spatial orientation of the inclusions. Consequently it represents the stress-induced interaction caused by the interference of the stress fields associated with each inclusion. One of the most interesting aspects of the potential in eq. 38 is that it can have the form of a potential with a minimum, $\partial E_{\text{int.}} / \partial r = 0$. It has been shown that the resulting potentials can be monotonically attractive, monotonically repulsive, or can have a minimum at a specific value of the interparticle spacing.

Since $E_{int.} \sim V_1 V_2$, $E_{int.}$ is maximal when $V_1 = V_2$, other conditions being equal. This means that the inclusions "try" to have the same dimensions if $E_{int.}$ is negative, for then $E_{int.}$ is minimal. Thus, the elastic interaction energy appears as a factor which stabilizes the dimensions of the particles if this interaction is attractive.

The theoretical treatment has been extended to multi-particle arrays (7,8). It was shown that three types of periodic arrays are possible: a one-dimensional system of parallel lamellae; a two-dimensional distribution which may be viewed as a planar square macro-lattice formed by rods of the second phase; a three-dimensional primitive cubic macrolattice which is equivalent to the macro CsCl array connected with spinodal decomposition.

Next we will turn to Cahn's treatment of coherent dilatation strains (44) (the derivation of the coherent strain energy is based on Hilliard's review paper (45)).

For most crystalline solid solutions there is a variation of lattice parameter with composition. If the lattice of such a solution is to remain coherent in the presence of composition modulation, work has to be performed in straining the lattice. The maintenance of coherency thus affects the driving force for diffusion.

Consider an infinite crystal containing an arbitrary composition fluctuation which is one dimensional and parallel to the axis of a set of orthogonal axes x, y, z . The composi-

tion will be uniform across any xy plane in the crystal and there will be no tendency for any variation of lattice spacing within the plane. Because of the composition variation along the z axis one might expect a corresponding variation in the lattice spacing in an xy plane as it is moved along the z axis. However, it is the basic premise of Cahn's calculation that no such variation is allowable if the lattice is to remain coherent. The reason for this restriction is evident if we consider the consequences of a difference in lattice parameter between two adjacent xy atomic planes. As we move away from the region where there is a matching of atoms between the planes there will be an increasing relative displacement between corresponding atoms in the planes, and this displacement must eventually reach a value equal to half the atomic spacing. In such a region, the lattice will no longer be coherent in the z direction.

Having established the foregoing principle, the work required to maintain coherency in the presence of a composition fluctuation can be now calculated. Consider a slab of the solid solution (Fig. 2) having a unit cross-section area in the xy plane. Let the lattice parameter in this plane be a_0 . To this slab we wish to add a slice of thickness w which in the unstressed state has a lattice parameter a . The slice is supposed thin enough for there to be no appreciable variation in composition along the z direction.

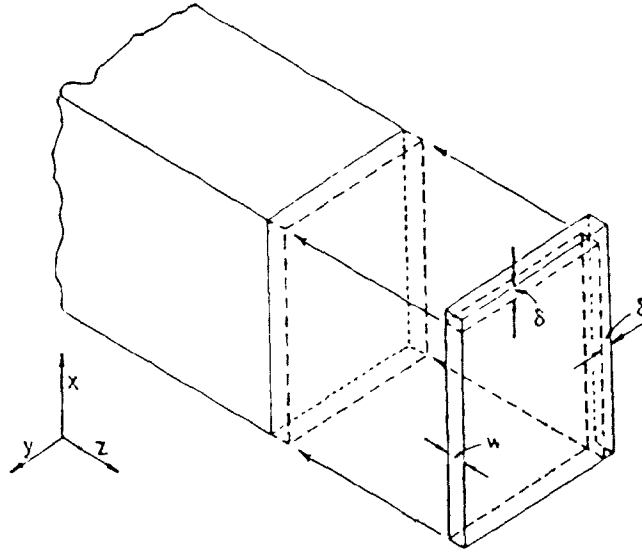


Fig. 2 A section of a solid solution with unit edge lengths. Lattice parameter a has to be subjected to strains $\delta = (a-a_0)/a$ in both x and y directions if it is to be coherent when added to material having a lattice parameter a_0 in the xy plane (after (45)).

If this slice is to be coherent with the slab after its addition it must be subject to a strain δ in the x and y directions given by

$$\delta = (a-a_0)/a. \quad (39)$$

Assume that the solid is elastically isotropic (which is never strictly true for a crystal); then stresses σ_x and σ_y required to produce this deformation in the absence of any stress in the z direction are given by the solution of

$$\delta = \epsilon_x = S_{11}\sigma_x + S_{12}\sigma_y \quad (40)$$

$$\delta = \epsilon_y = S_{12}\sigma_x + S_{11}\sigma_y \quad (41)$$

in which the S's are the elastic compliances. Thus,

$$\sigma_x = \sigma_y = \delta / (S_{11} + S_{12}) \quad (42)$$

The reversible work, W of deformation is given by

$$W = \frac{1}{2} (\epsilon_x \sigma_x + \epsilon_y \sigma_y) \quad (43)$$

and hence, from Eq. 42, is

$$W = \omega \delta^2 / (S_{11} + S_{12}) \quad (44)$$

Inasmuch as Young's modulus $E = 1/S_{11}$ and Poisson's ratio $\nu = -S_{12}/S_{11}$, Equation (44) can be rewritten in the form

$$W = \omega Y \delta^2 \quad (45)$$

in which $Y = E/(1-\nu)$. If a solid of length L is made up of a large number of such slices, then the work done per unit volume, W_v , in achieving coherency is given by

$$W_v = (1/L) \int_0^L Y \delta^2 dz \quad (46)$$

The next step is to relate δ to the composition variation.

Denoting the average composition by C_0 and the lattice parameter of the unstressed solid of this composition by a_0 , then a Taylor's expansion about C_0 yields

$$a = a_0 [1 + \eta (C - C_0) + \dots] \quad (47)$$

in which $\eta = (1/a_0) (da/dc)$ evaluated at C_0 . Thus,

$$\delta = (a - a_0) / a \approx \eta (C - C_0) \quad (48)$$

which, on substitution into equation (46), yields

$$W_V = \left(\frac{1}{L}\right) \int_0^L \eta^2 Y (C - C_0)^2 dz . \quad (49)$$

This then is the coherency strain energy for any arbitrary one-dimensional composition fluctuation in an isotropic solid of infinite cross section. If Y can be assumed independent of composition and the higher-order terms in Eq. (47) are likewise negligible, the additional stresses required to maintain coherency are unaffected by the composition variation in the z direction. In other words, there is no interaction between the fluctuations in two directions. The strain energy will therefore be the sum of the energies of the individual fluctuations. Thus, for any arbitrary three-dimensional composition variation in a volume V ,

$$W_V = \frac{1}{V} \eta^2 Y \int_V (C - C_0)^2 dv . \quad (50)$$

This result applies strictly only to isotropic systems and to the case where the amplitudes of the fluctuations are small enough to justify neglecting the composition dependence

of η and the elastic constants. Thus, it is applicable to the early stages of spinodal decomposition in isotropic solids, but may be a poor approximation in nucleation because the nucleus can differ appreciably in composition from the surrounding phase.

Cahn (46) modified the equation for the free energy of an inhomogeneous fluid to include strain energy to give

$$F = \int [f'(c) + \frac{\xi^2 E}{1-\nu} (C-C_0)^2 + k(\nabla C)^2] dV. \quad (51)$$

Combining Helmholtz free energy and strain energy Cahn defined a new free-energy function,

$$\phi(C, C_0) = f'(c) + \frac{\xi^2 E}{(1-\nu)} (C-C_0)^2 \quad (52)$$

which has the same properties for coherent systems that $f'(c)$ has in incoherent systems. A system is stable with respect to small coherent fluctuations as long as $\partial^2 \phi / \partial c^2 > 0$, just as $\partial^2 f'(c) / \partial c^2 > 0$ insures the stability of fluid systems. The barrier to coherent nucleation is $\Delta \phi$ for critical nucleus formation, so strain energy is automatically included with the chemical free energy.

Fig. 3 shows the relation between $\phi(C, C_0)$ and $f'(c)$ and between the coherent and incoherent miscibility gaps in a hypothetical system.

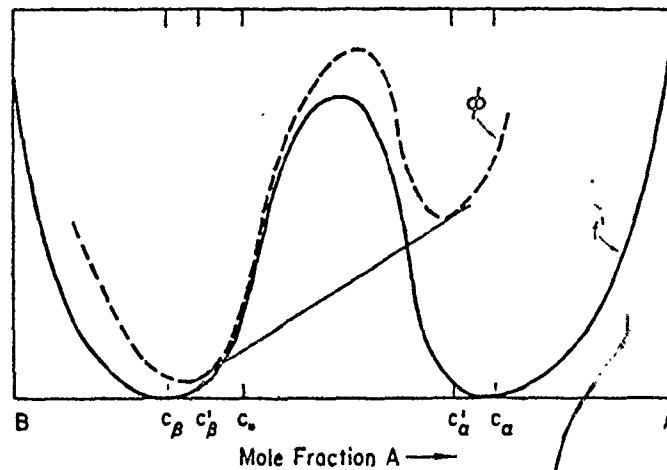


Fig. 3 The relationship between Helmholtz free energy $[f'(c)]$ and the coherent free-energy function $\phi(C, C_0)$. Coexisting coherent phase compositions in a system of average composition C_0 are seen to lie within the coexisting incoherent phase compositions (after (46)).

It can be seen that $\phi(C, C_0) > f'(c)$ for all compositions but $C = C_0$. The common tangent rule applies (as shown) for coherent equilibrium between phases.

Cahn (47) has also considered the interaction of dilatational strains in elastically anisotropic cubic crystals. The strain energy associated with an infinitesimal volume now depends not only on the strain at that point (as in eq. 52) but also on the strains due to all other particles in the system

as well as strains in other parts of the same particle. Cahn gives the strain energy per unit volume strained region in a cubic crystal as

$$W(r) = \bar{Y} [e_{11}^T(r)]^2 - \int_V g(r, r') dV' \quad (53)$$

where $g(r, r')$ is a complicated expression involving transformation strains and elastic constants, and r, r' are position vectors. The integral over the volume contains anisotropic contributions. \bar{Y} is the average over all orientations of an elastic constant $\bar{Y}(r)$. Equation (53) gives only the strain energy associated with an infinitesimal volume at r , and must be integrated again over all space to give the total strain energy. Cahn draws some interesting qualitative conclusions without evaluating the integral in eq. (53). Nucleation of a second particle in the presence of a pre-existing precipitate particle is easier in a "soft" direction, a direction where $\bar{Y}(r)$ is a minimum. For most metals, $\langle 100 \rangle$ directions are favored (47).

Next consider a particle with two neighbours of equal size at equal distances, but with one neighbor in a hard direction and the other in a soft direction. The particle in the soft direction has a lower solubility and hence is more stable than the other particle of the same size. Therefore, even if particles nucleate and initially grew at random, the enhanced stability would favor the development of an ordered array, a

simple cubic pattern if $\langle 100 \rangle$ directions are soft. Random nucleation followed by growth could give the same kind of array of particles that is produced by spinodal decomposition (47).

To summarize this discussion on the spatial distribution of coherent inclusions it can be seen that the most common and most controversial microstructures of coherent phase mixtures are the so-called modulated, periodic, or tweed structures. As already mentioned they have been observed in numerous alloy systems. The only transformation process of coherent phases which leads inherently to phase separation with a given spacing (λ_m) is spinodal decomposition. However, periodically modulated microstructures are not only observed in systems with miscibility gaps but also in systems where ordered phases precipitate from solid solutions; i.e. where $\partial^2 f / \partial c^2 > 0$ for both phase at all compositions and temperatures and, therefore, no spinodal occurs. However, modulated structures can develop from initial arrays which are not modulated at all (26,27). Modulated structures do not seem to occur when the volume fraction is small.

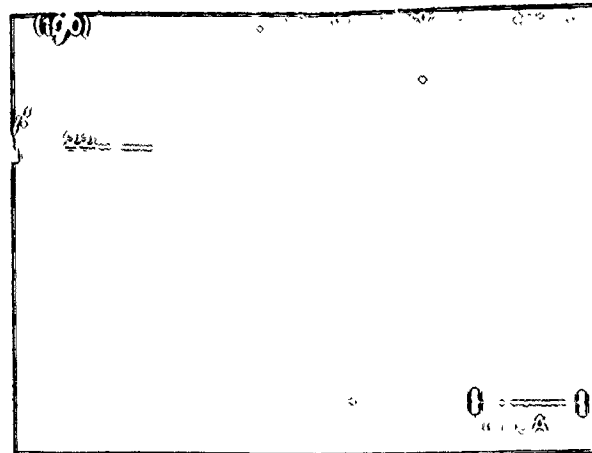
All modulated structures, including those produced by spinodal decomposition, involve to some extent the minimization of strain energy of the array. In the preceding paragraphs we have seen that elastic interactions between individual particles play a role. All modulated or tweed structures thus far observed can be referred to one of the three types

of periodic arrays described above (see p. 23). Their development in an ordinary precipitating system will begin with randomly distributed supercritical nuclei which produce increasing displacements as they grow (and coarsen) until the stresses become sufficiently high that they affect the diffusional processes. These will then become anisotropic in such a way as to favour the growth of periodic arrays whose elastic energy is minimum-completely analogous to those produced by spinodal decomposition when the misfit is significant (47). Providing that the chemical driving force for overall homogeneous nucleation is small, the elastic interaction energy may also be a controlling factor during nucleation.

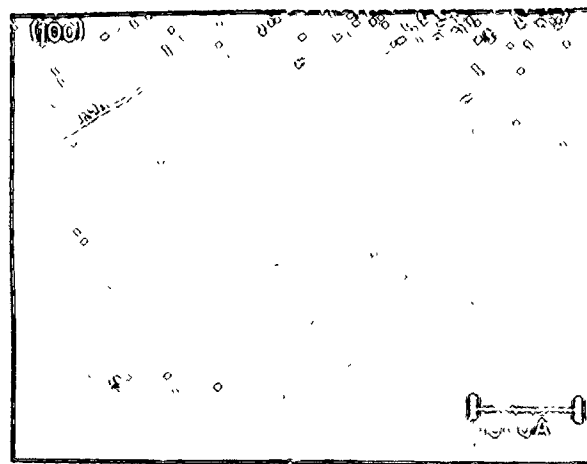
Thus, coherent precipitation associated with coherency strains and higher volume fractions of precipitates will always result in quasi-periodic wave-like arrays of matrix and particles which are similar to spinoidally decomposed structures with composition-waves.

It can be seen that spinodal decomposition cannot simply be distinguished by the resulting microstructure: the origin of periodically modulated, coherent arrays is a minimization of elastic strain energy by anisotropically stress affected diffusion in all cases.

An illustration of development of alignment structure Cu-2% Be and Ni-19% V alloys is shown in Figs. 4 and 5 (after 33).



a



b

Fig. 4 Typical morphology of G.P. zones and γ'' precipitates in Cu-2% Be alloys. Notice in a incipient alignment of G.P. zones; b, shows the γ'' phase with $\{100\}$ habit plane, but aligned along the traces of the $\{110\}_{\alpha}$ planes (after (33)).

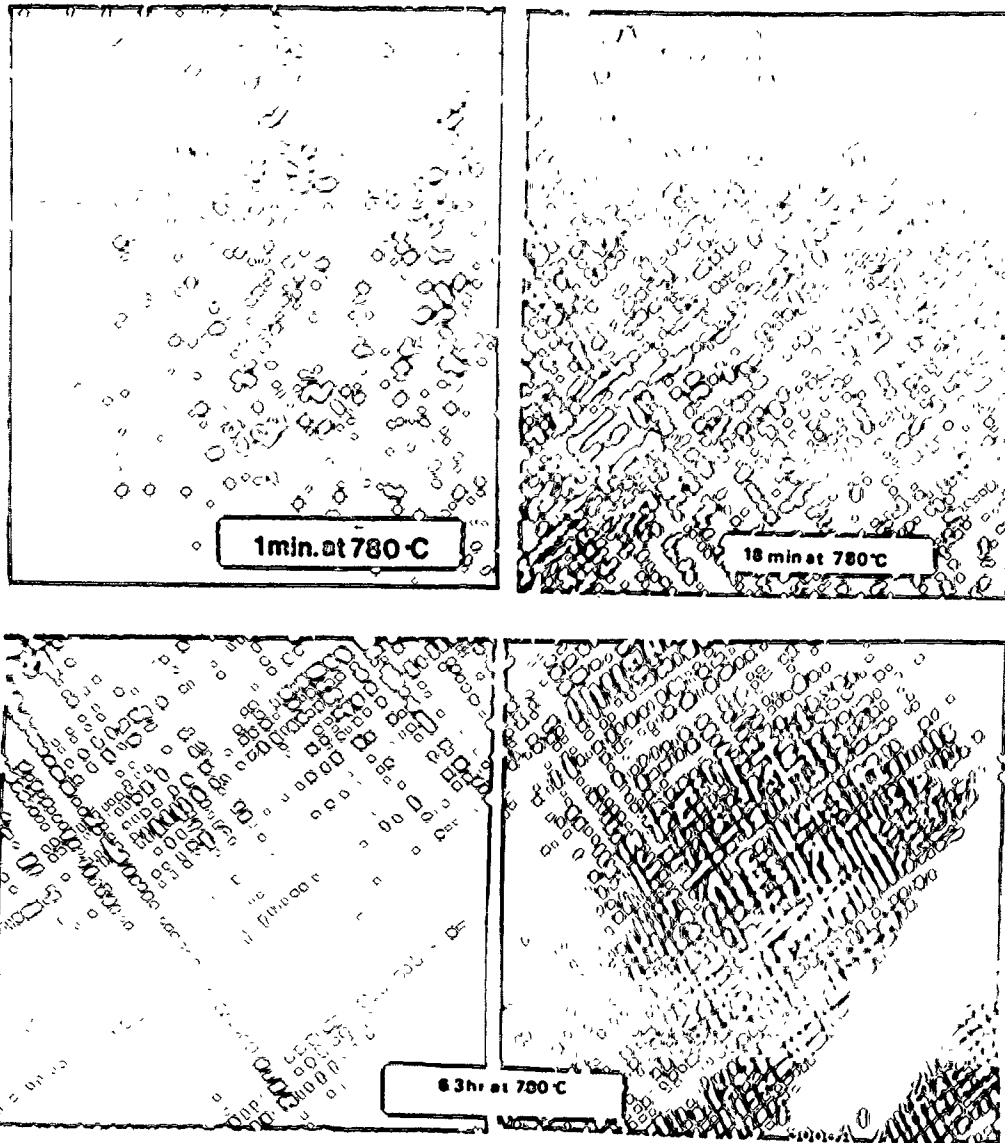


Fig. 5 Dark field micrographs of a Ni-19% V alloy aged 1 minute to 6.3 hours at 780°C. a) 1 minute, \bar{g} [010]. Note a random distribution of θ precipitates. (b) 18 minutes g [010] and [001]. Notice a larger distribution of one variant of θ precipitates in the right-hand side micrograph. (c) 6.3 hours, \bar{g} [001] and [010]. Notice two completely different distributions of θ precipitates on a given region (after (33)).

Chen et al. (48) have also performed computer simulations of the microstructures that develop during phase separation when the elastic energy is a major contribution to the free energy of the system. Their results for tetragonal precipitates are shown in Fig. 6. Notice the alignment of tetragonal precipitates along the $[110]$ direction.

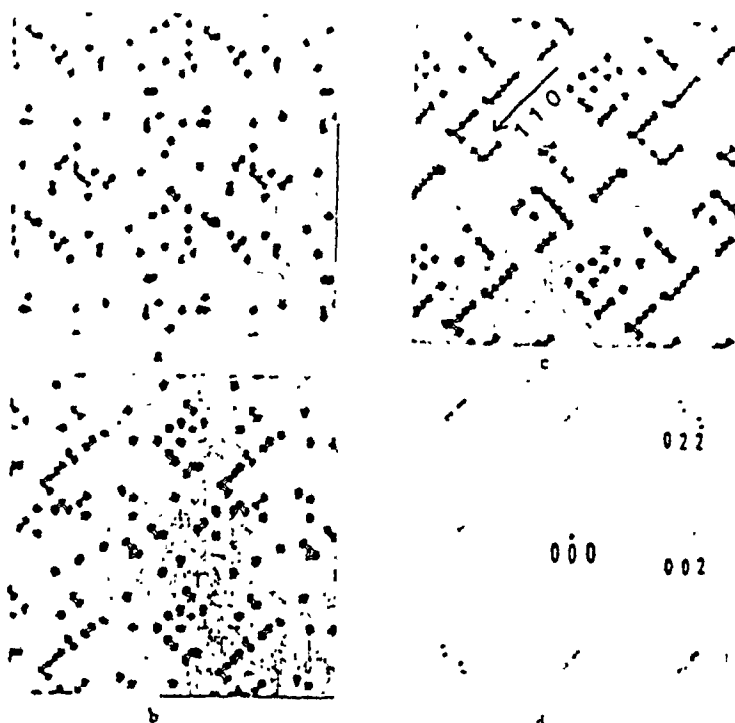


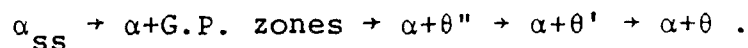
Fig. 6 Microstructures and diffraction pattern obtained via computer simulation. Figures (a), (b) and (c) are in order of increasing "ageing" in the computer. Notice the alignment of tetragonal precipitates along the $\{110\}$ planes and the preferred development of one variant of precipitates (after (48)).

1.2 PREVIOUS WORK ON Al(RICH)-Cu ALLOYS

A tremendous amount of research has been performed on Al(riCh)-Cu alloys. The number of contributions to the literature concerning these binary alloys is so large that it is impractical to report on all of them. Therefore, only the most relevant references will be mentioned*.

The precipitation processes in aluminum-copper alloys have been studied by a variety of techniques over the past fifty years. The extensive X-ray investigations have been reviewed by Hardy and Heal (49). The more recent electron microscopy and electrical resistivity observations have been discussed by Kelly and Nicholson (50) and Phillips (51,52). These investigations have demonstrated the existence of several metastable phases in addition to the equilibrium $\text{CuAl}_2(\theta)$ phase.

The generally accepted sequence of precipitation in supersaturated solid solution aged at 130°C and above is (50, 51).



Using X-ray techniques, Guinier (53), Preston (54) and Gerold (55) deduced that G.P. zones are thin copper rich platelets, probably one or two atom planes thick, lying in $\{100\}$ planes of the aluminum matrix. Both θ'' and θ' are ordered arrangements of copper and aluminum atoms with tetra-

* Further references will be mentioned in chapter 3.

gonal unit cells. The precipitates are thin discs with the c axis perpendicular to the habit plane, and the orientational relationship is (56):

$$\{100\}_{\theta''} \parallel \theta' \parallel \{100\}_{\alpha}$$

The θ'' plane can be envisioned as $\{100\}$ planes of pure copper separated by the three planes of pure aluminium, Fig. 7(a).

It has been shown that a minimum in the elastic energy at four atomic planes from an existing G.P zone enhances the formation of the θ'' phase.

Silcock et al. (56) have pointed out that when θ'' forms from G.P zones, the c parameter changes from 8.0 to 7.6 Å as the θ'' precipitate grows. Because the maximum misfit between the θ'' and matrix lattice planes is about 5 percent, θ'' is coherent across all interfaces.

The misfit in the c direction is taken up by elastic displacements in the matrix as shown in Fig. 7(b).

The structure of θ'^* , as determined by Silcock et al. (56) is shown in Fig. 7(c). θ' is coherent across the interface parallel to the habit plane, but owing to the large misfit

* It should be noted that the exact structure of θ' is still unknown. No one of the proposed models matches exactly with X-ray intensity distributions, displacement field measurements and lattice images. This is also true for many coherent metastable phases in substitutional alloys and intermediate phases, e.g. in Fe(-Au,Be,Cu,Mo,W) alloys and many others.

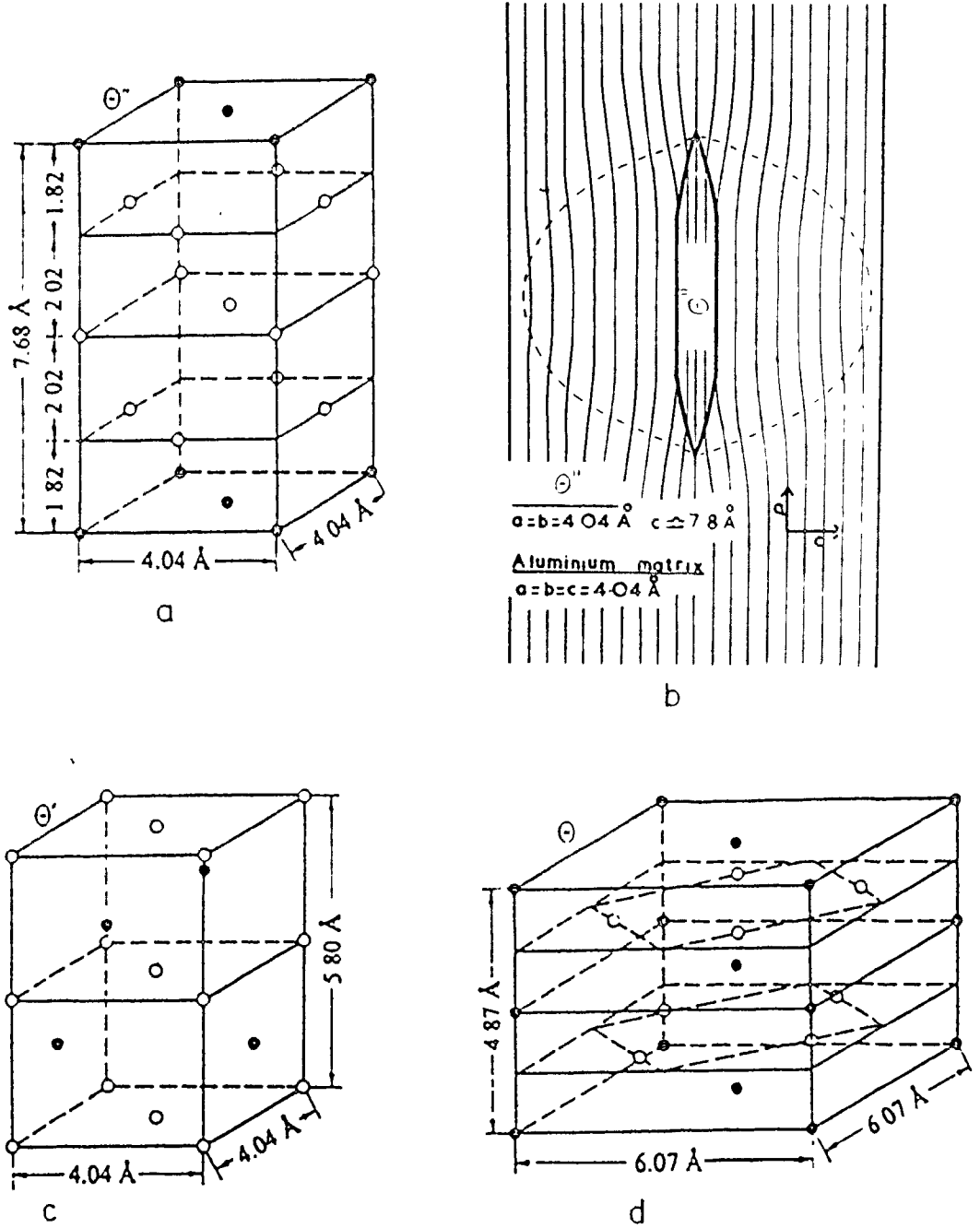


Fig. 7 Crystal lattices of θ'' , θ' and θ in the Al-4% Cu alloys. The misfit in the c direction is taken by elastic displacement in the matrix.

in the c direction, it is non-coherent across the interface of the periphery of the disc. The chemical composition of this phase is about CuAl_2 .

The equilibrium phase $\theta(\text{CuAl}_2)$ is also tetragonal, Fig. 7(d). This phase is incoherent or semicoherent. θ precipitates nucleated preferentially at grain boundaries, dislocations and at the θ' parent interface.

The metastable phase diagram as compiled by Aaronson and Russell (58) is shown in Fig. 8.

1.3 AN APPROXIMATION FOR THE STRAIN FIELD OF A DISC-SHAPED G.P. ZONE

Several models have been proposed for the strain field of disc-shaped zones. Guinier (53,59) based his model on the Fourier transform of intensity distributions observed from low-angle diffuse X-ray scattering, while others (60-64) calculated intensities from assumed strain fields, and compared these with intensities observed in diffuse X-ray scattering experiments.

Nabarro (65) noted that a collapsed disc of vacancies may be regarded essentially as a prismatic dislocation loop. Franz and Kroner (66) showed that the strain field of a G.P. zone, as modelled, for example, by Gerold (60,61) may be approximated by that of a prismatic dislocation loop, with Burgers vector proportional to the difference between the size of solute and solvent atoms. The calculation of finite prismatic loops has been carried out in detail by Bullough

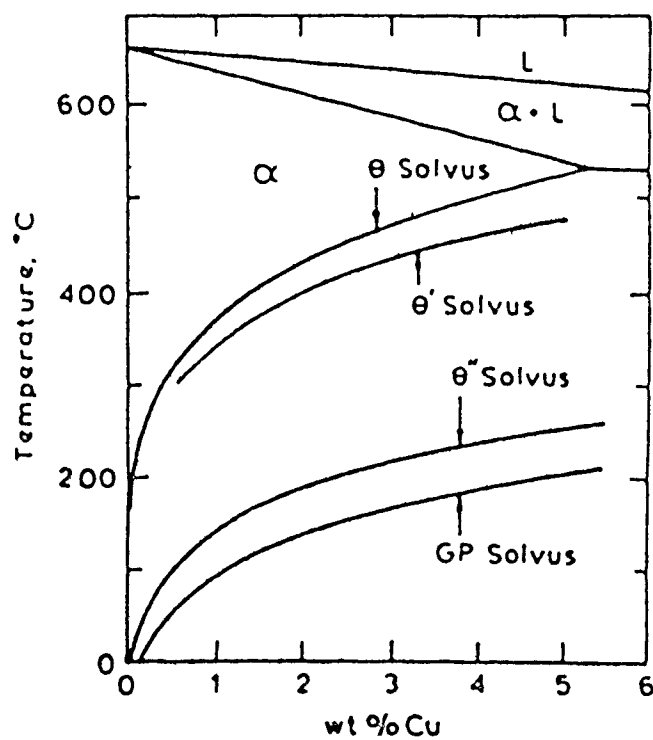


Fig. 8 Phase diagram for Al(rich)-Cu alloys showing the solvus lines of θ , θ' , θ'' and G.P. zones (after (58)).

and Newman (69) and Kroupa (68).

When the diameter of the loop is small compared to the detail required, it is possible to treat a prismatic loop as a point singularity in an elastic continuum (69). Kroupa (69) specialized the derivation used by Eshelby (4) for the more general case of an ellipsoidal inclusion. We will show the derivation of the formulae for the displacement and stress field around it, following Kroupa (69).

Consider a plate-like region T with an area δA and thickness h (Fig. 10(a)) in an infinite body with the same elastic constants as the region T and perform the same operation as described on pages 10 and 11.

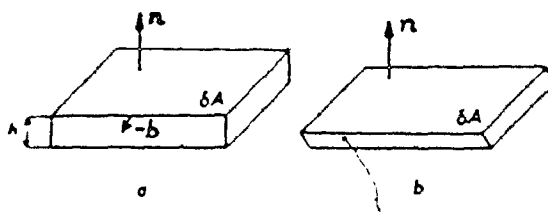


Fig. 9 Transformation of a plate-like inclusion (a) is formed by displacement by $-b$ of the upper side (b).

The region T taken out of the body is transformed in such a way that the face on the positive side of the normal ("upper side") displaced by a vector $-b$ while the face on the negative side of the normal ("lower side") does not move at all (Fig. 9(b)).

The plastic displacements u_k in the region are,

$$u_k = -\frac{b}{h} (x_i' - x_i^{o'}) n_i \quad (54)$$

where x_i' are the coordinates of a point of the region T, $x_i^{o'}$ the coordinates of a point on the lower side.

The tensor of the plastic deformation $e_{kj}^T = \frac{1}{2} (\partial u_k / \partial X_j + \partial u_j / \partial X_k)$ is constant in the region T and given by,

$$e_{kj}^T = -\frac{1}{2h} (b_k n_j + b_j n_k) \quad (55)$$

Stresses in the region T are equal to zero during this operation. Assuming that the elastic constants of the region have not changed during the plastic deformation the stress tensor σ_{kj}^T can be calculated from Hooke's (eq. 8) using e_{kj}^T as strain tensor.

The displacement and stress field outside the region T can be calculated as the result of forces $(\sigma_{kj}^T n_k)$ spread over the surface T.

The displacement component u_i at a point X, due to the component f_j of a point force acting at a point X', as already discussed on p. 7 is given by,

$$u_i = U_{ij} f_j \quad (56)$$

where

$$U_{ij} = \frac{1}{16\pi\mu(1-\nu)} \left[\delta_{ij} \frac{1}{r} (3-4\nu) + \frac{r_i r_j}{r^3} \right] \quad (57)$$

U_{ij} denotes the displacement in the i-direction from a point force acting in the j-direction (it is symmetrical in the i and j indices). The displacement field u_i from a surface

distribution of forces is given by a surface integral (eq. 18). For the displacements at a large distance from the region T (i.e. at a distance much larger than the dimensions of the region T), the integral in eq. (25) can be replaced by the product.

$$u_i = U_{ij,k} \sigma_{kj}^T V' \quad (58)$$

where

$$V' = \delta A \cdot h \quad (59)$$

The derivation $U_{ij,k}$ in eq. (58) is taken in respect to the coordinate X_k' of an internal point of the region T. Denoting this point X_k' as the "centre" of the region T, or, according to reality, that the distance r is much larger than the dimensions of T, as the point at which the region T is placed.

From eqs. (58), (59), (8), (55) and (57) (after differentiation with respect to X_k') and using the relations between λ , μ and ν , u_i can be written as,

$$u_i = \frac{k_0}{r^2} \left\{ \frac{1-2\nu}{r} [n_i b_k r_k + b_i n_k r_k - r_i b_k n_k] + \frac{3r_i b_k r_k n_k}{r^3} \right\} \delta A \quad (60)$$

where

$$k_0 = - \frac{1}{8\pi(1-\nu)} \cdot$$

Equation (60) does not depend on the thickness h of the region T and also gives the limit for $h \rightarrow 0$ for which the transformed region T represents a dislocation loop with an area δA , normal n and Burgers vector b . Eq. (60) also gives

displacements at a large distance from a (finite) dislocation loop (described by δA , n , b). They depend only on the area of the loop and not on the form of the loop.

For an infinitesimal area δA the loop can be called infinitesimal. Then we can write dA instead of δA and du_i instead of u_i ,

$$du_i = \frac{k_o}{r^2} \{ \dots \} dA. \quad (60')$$

The stress tensor σ_{ij} at a larger distance from a finite loop or $d\sigma_{ij}$ around an infinitesimal loop can be calculated from eq. (60) or (60') using Hooke's law, thus

$$\begin{aligned} \sigma_{ij} = & \frac{2k_o \mu}{r^3} \left[\frac{3(1-2\nu)}{r^2} b_k r_k n_\ell r_\ell + (4\nu-1) b_k n_k \right] \delta_{ij} + (1-2\nu) (b_i n_j + n_i b_j) + \\ & + \frac{3\nu}{r^2} [b_k r_k (n_i r_j + r_i n_j) + n_k r_k (b_i r_j + r_i b_j)] + \\ & + \frac{3(1-2\nu)}{r^2} b_k n_k r_i r_j - \frac{15}{4} b_k r_k n_\ell r_\ell r_i r_j \} \delta A \end{aligned} \quad (61)$$

or

$$d\sigma_{ij} = \frac{2k_o \mu}{r^3} \{ \dots \} dA \quad (61')$$

it is apparent that the displacements decrease with distance r or $1/r^2$ and stresses as $1/r^3$.

Equations (60') and (61') can be simplified by using a special coordinate system, Fig. 10.

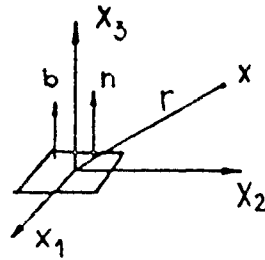


Fig. 10. Pure prismatic infinitesimal dislocation loop.

The loop is at the origin of the coordinate system in the X_1X_2 plane ($n_1 = n_2 = 0$, $n_3 = 1$) and separately introduces displacements and stress for a pure prismatic infinitesimal dislocation loop ($b_1 = b_2 = 0$, $b_3 = b$) which are:

$$u_1 = \frac{KX_1}{6r^3} \left[-(1-2\nu) + \frac{3X_3^2}{r^2} \right]$$

$$u_2 = \frac{KX_2}{6r^3} \left[-(1-2\nu) + \frac{3X_3^2}{r^2} \right] \quad (62)$$

$$u_3 = \frac{KX_3}{6r^3} \left[1-2\nu + \frac{3X_3^2}{r^2} \right]$$

$$\sigma_{11} = \frac{K\mu}{r^3} \left[\frac{4\nu-1}{3} + (1-2\nu) \frac{X_1^2+X_3^2}{r^2} - \frac{5X_1^2X_3^2}{r^4} \right]$$

$$\sigma_{22} = \frac{K\mu}{r^3} \left[\frac{4\nu-1}{3} + (1-2\nu) \frac{X_2^2+X_3^2}{r^2} - \frac{5X_2^2X_3^2}{r^4} \right]$$

$$\sigma_{33} = \frac{K\mu}{r^3} \left[\frac{1}{3} + \frac{2X_3^2}{r^2} - \frac{5X_3^4}{r^4} \right] \quad (63)$$

$$\sigma_{12} = K\mu \frac{X_1X_2}{r^5} \left[1-2\nu - \frac{5X_3^2}{r^2} \right]$$

(continued next page)

$$\sigma_{13} = K\mu \frac{x_1 x_2}{r^5} \left[1 - 5 \frac{x_3^2}{r^2}\right]$$

$$\sigma_{23} = K\mu \frac{x_2 x_3}{r^5} \left[1 - 5 \frac{x_3^2}{r^2}\right]$$

where

$$K = - \frac{3b_3}{4\pi(1-\nu)} dA ,$$

b is Burgers vector, dA is the area of the loop, $r^2 = x_1^2 + x_2^2 + x_3^2$,
 μ is shear modulus and ν is the Poisson ratio (assumed 1/3).

1.4 ELASTIC INTERACTION BETWEEN PAIRS OF DISLOCATION LOOPS - THE INFINITESIMAL APPROXIMATION

The total energy of a pair of dislocation loops is the self energy of each loop plus the interaction energy between the two. This interaction energy may be defined as the energy required to create one loop in the stress field of the other: For infinitesimal loops, it can be written as,

$$E_{\text{int}} = n_i^{(2)} \sigma_{ij}^{(1)} b_j^{(2)} \delta A^{(2)} \quad (64)$$

where: $n_i^{(2)}$ is the unit normal at loop 2,
 $\sigma_{ij}^{(1)}$ is the stress tensor from loop 1 at loop 2;
 σ_{ij} of course depends upon r_i , the vector defining the relative positions of the loops
 $b_j^{(2)}$ is the Burgers vector of loop 2,
 $\delta A^{(2)}$ is the area of loop 2.

Examples of this kind of interaction for various relative

orientations of precipitates are given by Eurin et.al. (10). It has been shown that, depending on the configuration, interaction can be strongly attractive, strongly repulsive and other configurations which are intermediate between these extremes. For example, the edge-face configuration is strongly attractive and the face-face configuration is strongly repulsive.

From these interaction energies (and derivative forces) one can proceed to larger numbers of loops in different configurations; a balance may be obtained between the repulsion of two parallel coaxial loops and a loop placed midway perpendicular to both, etc.

Fillingham et al. (70) have also used the infinitesimal loop approximation to calculate energies of several ordered arrays of disc shaped zones in order to describe "tweed" structures and to model the diffraction contrast they yield in the transmission electron microscope.

1.5 DIFFRACTION CONTRAST FROM THE θ'' AND θ' PRECIPITATES AND OPTICAL DIFFRACTION FROM ELECTRON MICROGRAPHS

1.5.a INTRODUCTION

A description of the Howie-Whelan two-beam dynamical theory has been published (71). The following equations represent both the wave amplitudes, ϕ_0 (transmitted) and ϕ_g (diffracted), obtained by the dynamical theory for the general case of the imperfect crystal with varying atomic displacements.

$$\frac{d\phi_0}{dz} = -\frac{\pi l}{\xi_0} \phi_0 + \left(\frac{1}{\xi_g} - \frac{1}{\xi'_g}\right) \phi_g \quad (65)$$

and

$$\frac{d\phi_g}{dz} = \pi \left(\frac{i}{\xi_g} - \frac{1}{\xi'_g}\right) \phi_0'' + \left(-\frac{\pi}{\xi_0} + 2\pi l s + 2\pi l g \cdot \frac{dR}{dz}\right) \phi_g \quad (66)$$

where ξ_g is the extinction distance; ξ_0' and ξ_g' are the absorption parameters, s is the deviation from Bragg diffraction condition, g is the reciprocal lattice vector and R is the displacement which leads to a phase shift between the two parts of the matrix lattice.

It will be observed in the above equations that the amplitudes of contrast intensity of the image in thin foils are dependent on $g \cdot dR/dz$ and consequently, provided that $dR/dz \neq 0$ when $g \cdot R \neq 0$, phase contrast is obtained.

1.5.b ELECTRON DIFFRACTION CONTRAST FROM LEDGES AT THE INTERFACES OF FACETED θ' PRECIPITATES

For a sessile ledge, which can only move by diffusion, the strain field (if the length is much greater than the thickness) is almost identical to that of prismatic dislocation loop of Burger's vector $b = \epsilon d$; where ϵ is the elastic mismatch and d is the thickness of the precipitate.

The contrast arising from such ledges has been studied in detail by Weatherly and Sargent (72) using the geometry shown in Fig. 11(a). The ledge is treated as a dislocation $b = \frac{1}{2}[001]_{\theta}$, and the following features were charac-

16 a

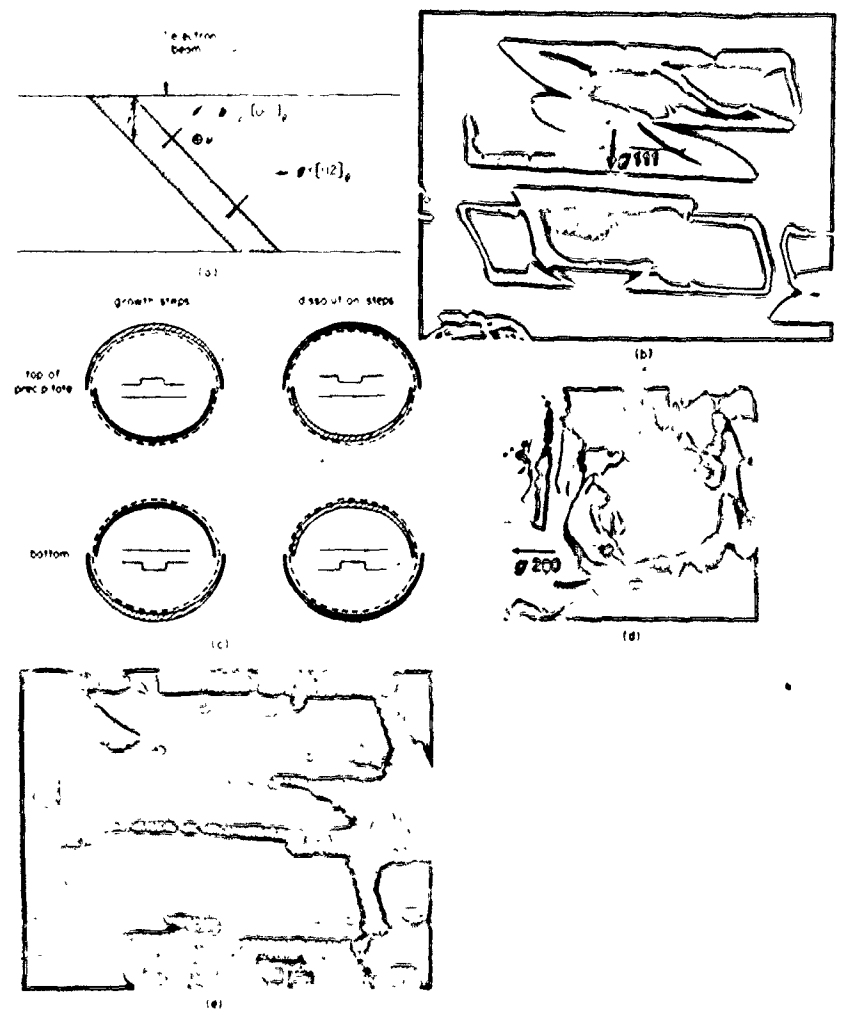


Fig. 11 a) The geometry of the thin foil used by Weatherly and Sargent (72) to compute images of ledges in precipitates in Al-4wt% Cu. b) A CDF image obtained with a (111) matrix reflection showing particles with ledges. c) Schematic diagrams showing images of growth and dissolution steps. The position of the step is given by the dashed line, the heavy line being black contrast and the shaded region bright. d) A BF image with a (200) reflection showing the ledges as faint double images. e) Displacement fringes visible in BF, $g(111)$.

terized for precipitates $\sim 150 \text{ \AA}$ thick.

- a) The precipitate dark field images are often wide ($\sim 300 \text{ \AA}$), Fig. 11(b).
- b) In two-beam precipitate dark-field with no significant excitation of the matrix reflection, (that is, only the precipitate diffracts), continuous ledges in the interface (like a circular dislocation loop) have a line of no contrast approximately perpendicular to \vec{g} . On one side of the line of no contrast the image of the ledge on a positive print is a black line whereas in the other it is a white line (see Fig. 11(b), provided that $w = 1.0-1.5$. For a given \vec{g} and type of step (that is, either growth or dissolution) the black and white image reverses depending upon whether or not the ledge lies on the top or bottom surface of the precipitate (see the schematic diagrams, Fig. 11(c)). For a given ledge the black/white contrast reverses across the line of no contrast when \vec{g} or w reverse sign.
- c) When a matrix reflection is excited in bright field with \vec{g} in the habit plane a faint double image is observed, Fig. 11(d), like $g \cdot b = 0$ and $g \cdot b \wedge u \geq 0.64$ for a dislocation.
- d) When a matrix reflection with \vec{g} not in the habit plane is excited displacement fringes are observed in bright

field at the interface, Fig. 11(e). These fringes are displaced at the ledges and the magnitude of the displacement is related to ledge height (73).

1.5.c ELASTIC STRAIN EFFECTS

Guinier (59) has shown that elastic distortion of the matrix arising from a coherent misfitting precipitate produces diffuse scattering in reciprocal space in the direction of the distortion. Often, the diffuse scattering arises simultaneously with shape effects (Al-Cu, Ni-Al alloys) and these are difficult to separate because they often occur in the same direction. However, Tanner (30) showed that it was possible to do so for G.P zones in Cu-2% Be alloys. In this case, G.P zones are plates on {100} matrix planes producing shape streaks in reciprocal space in $\langle 100 \rangle$. However, the coherency strains are shear strains in $\langle 100 \rangle^*$ (31) and produce streaks parallel to $\langle 110 \rangle$ in reciprocal space.

The main characteristics of elastic strain effects were described by Guinier (59) and obtained for Cu-Be alloys by Tanner (30). These are as follows.

- 1) The size of the streak increases with increasing order of \vec{g} (this is difficult to observe because s increases with increasing order of \vec{g} and the specimen must be tilted to $s=0$ for each reflection).

* More about the origin of this contrast will be given in section 1.5.d.

- 2) There are no streaks on the transmitted spot.
- 3) There are no streaks present along the distortion directions that lie in the reflecting plane. Thus, for $\langle 110 \rangle$ strain fields, all $\langle 110 \rangle$ distortions will be represented within the selected area operator. Each reciprocal lattice point will have some streak missing, that is $\{111\}$ types will have three out of six missing, $\{200\}$ types will have two out of six missing, and $\{220\}$ types one of six missing, see Fig. 12.

It is important to realize that the occurrence of double diffraction effects whereby a diffracted beam contacts as an incident beam can complicate the above effects.

1.5.d ON THE ORIGIN OF "TWEED" CONTRAST

The reason for the occurrence of shear coherency strains in Cu-Be alloys but not in the Al-Cu alloys is not at present clear. Initially it was attributed to elastic anisotropy of the Cu-rich matrix (30) but more recently this has been rejected in favour of complex strain field interactions from the very closely spaced particles (74,70,75).

Phillips and Tanner (75) applied high resolution electron microscopy techniques and for the first time they have clearly revealed the monolayer G.P zones that are formed parallel to $\{100\}$ matrix planes during the ageing of a Cu \sim 2.0 wt % Be alloy at 100 and 198°C. Ageing at 100 and 198°C produced abutting stair-step arrangements of zones.

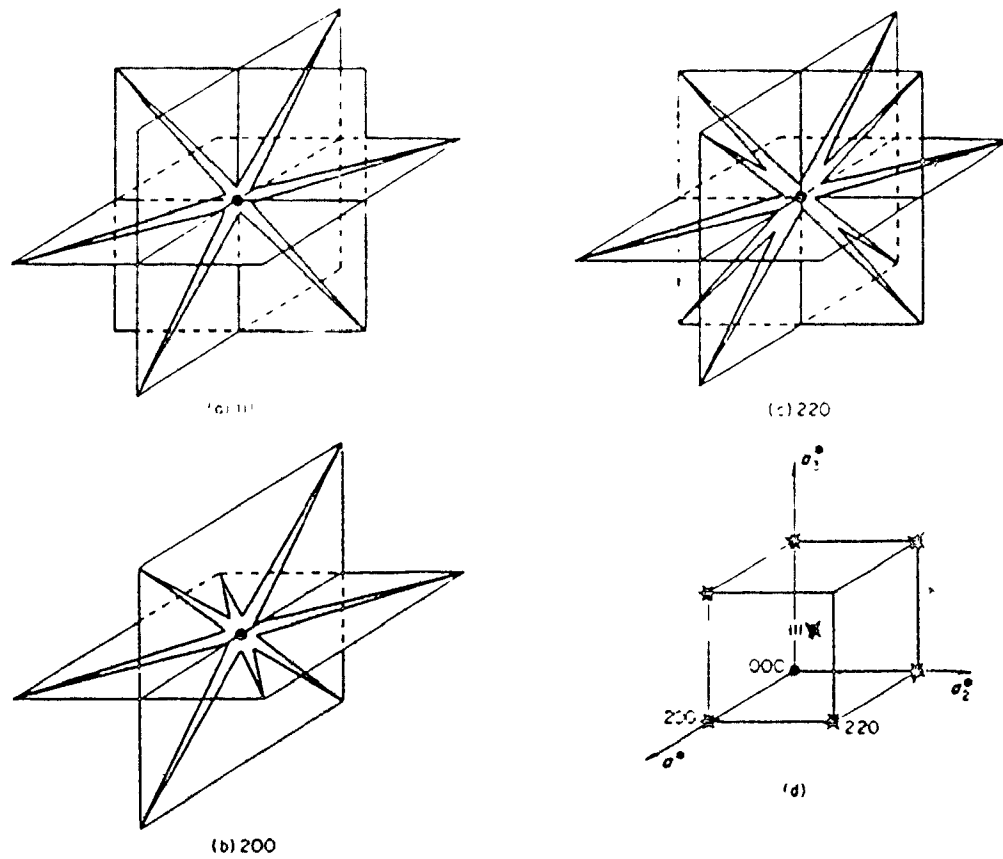


Fig. 12 Schematic representation of streaks produced by strain field effects along $\langle 111 \rangle$ for G.P. zones on $\{100\}$ in Cu-Be alloys for three different reflections (after (30)).

Computer simulations have shown that "tweed" contrast can arise from a two-dimensional array of two mutually perpendicular loops (the "stair-step" array) which produce overlapping black-white strain contrast (70). The three-dimensional arrays have also been proposed (70,76) to account for the tweed structure but neither give simulated "tweed" contrast compatible with that observed.

Eurin et al. (10) have considered the elastic interaction between precipitates which cause tetragonal distortions and conclude that they arrange themselves in a pseudo-periodic array to maximize the number of "edge-face" configurations,

Jack (35) used one of their arrays to demonstrate how "tweed" contrast may arise from a three-dimensional periodic array of tetragonal strain centres acting in $\langle 001 \rangle$, Fig. 13(a). Projection of the arrangement of Fig. 13 (a) onto a (001) plane is shown in Fig. 13(b). In calculating electron microscope image contrast due to strain, only those plates on (100) and (010) need be considered.

For the plate densities envisaged there are many particles within one extinction distance of the foil surface and the final image will consist only of wide, asymmetric black-white images. Calculation of the detailed image shape from each plate needs to take into account the elastic anisotropy of the matrix, but the nature of the final image can be seen in principle by superimposing the simple black-white strain contrast from each plate and in Fig. 13(c)-(d) the overlapping

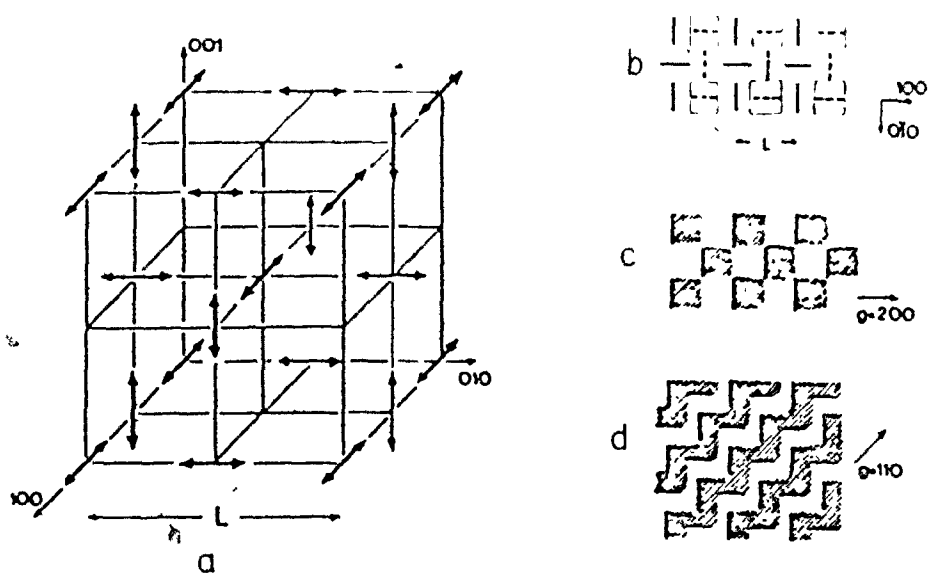


Fig. 13 (a) Disposition of plates in a b.c.c. lattice of edge length L . The arrows indicate the direction of the particular plate normal. (b) Projection of the arrangement of (a) onto a (001) plane. Plates depicted by dashed line lie at $L/2$ above and below the plane of the projection. (c) Schematic tweed contrast from overlapping black-white images, $\vec{g} = 200$, beam direction $[001]$. (d) Schematic tweed contrast $\vec{g} = 110$, beam direction $[001]$ (after (35)).

contrast for $\vec{g} = 200$, and $\vec{g} = 110$ is sketched schematically and corresponds to the tweed striations actually observed.

As already mentioned, the streaks in $\langle 110 \rangle$ (in Cu-Be alloy) are attributed to shear waves which are considered to arise owing to effect of the primary $\langle 100 \rangle$ tetragonal displacement acting in an elastically anisotropic matrix. However, Lou and Jack (77) have pointed out that it is not necessary to postulate an anisotropic matrix in order to explain the $\langle 110 \rangle$ streaks.

If the array of strain centres in Fig. 13(a) is projected onto a $\{001\}$ plane, the arrangement of Fig. 14(a) results, with distortions of the matrix lattice as shown.

McConnell (78) has pointed out, such distortions are equivalent to two orthogonal transverse waves with wave vectors $[110]$ and $[1\bar{1}0]$, and displacement vectors $[1\bar{1}0]$ and $[110]$, respectively. For a single transverse wave, Fig. 14(b), with wave vector k ($|k| = 1/\lambda$) and amplitude vector a , additional satellite diffraction spots will appear on either side of matrix diffraction spots in positions given by $(g_{hkl} \pm k)$ where \vec{g} is the reciprocal lattice vector of the matrix spot. The amplitude of the satellites are proportional (79) to $a \cdot (g \pm k)$, whence it can be seen that no intensity is observed around a particular matrix spot where the displacement vector is normal to the reciprocal lattice vector for that spot, i.e., where the transverse wave does not alter the spacing of

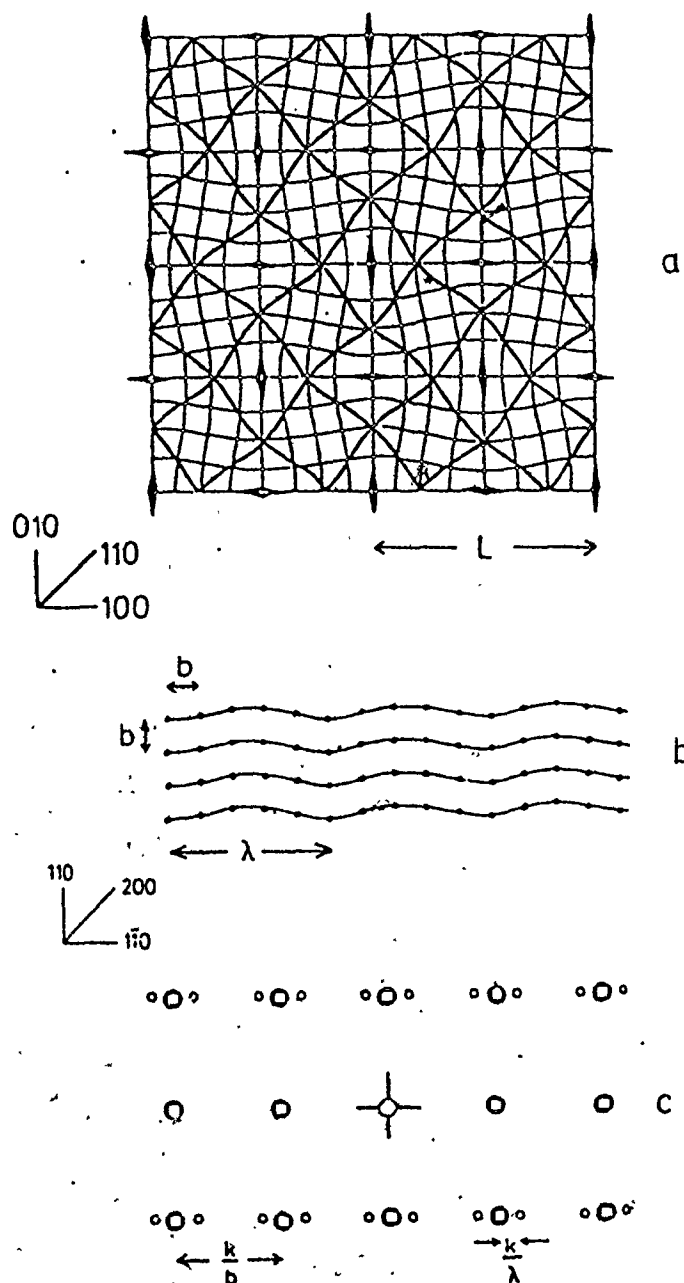


Fig. 14 (a) Schematic pattern of distortions due to projection of strain centres in Fig. 13 onto (001). Two orthogonal transverse waves with wave vectors parallel to $[1\bar{1}0]$ and $[110]$ are produced, with $\lambda = L/\sqrt{2}$. (b) Diffraction pattern associated with lattice disturbed by single transverse wave of wavelength λ (after (77)).

hypothetical diffraction pattern of Fig. 14(c) is obtained. Superimposing the effect of two orthogonal transverse waves gives a pattern characteristic of those observed in association with tweed contrast except that discrete satellites are never seen, always diffuse streaks without any apparent maxima. This would indicate imperfect periodicity, as might perhaps be expected.

1.5.e OPTICAL DIFFRACTION OF ELECTRON MICROGRAPHS

Just as in electron diffraction, the form of the optical diffraction pattern is directly related to the structural detail of the micrograph (80). If the micrograph is of an amorphous specimen area and shows no periodic or regular detail, then the optical diffraction pattern will contain only a diffuse "noise" spectrum radially distributed about the central diffraction spot. The "noise" spectrum may be altered by the presence of astigmatism, specimen drift or out-of-focus effects in the microscope image, and in this way provides information about the recorded micrograph; but it does not provide any information about the structure of the specimen except, of course, that it is amorphous.

If the specimen area is crystalline or the micrograph contains periodic detail then, in addition to the noise spectrum, discrete diffraction spots will be observed in the optical diffraction pattern, at distances and orientations from the central diffraction spot that can be analyzed to provide information about the periodic structure of the corres-

ponding specimen area, Fig. 15(a)-(d) and Fig. 16(a)-(d).

As in electron diffraction, the optical diffraction spots become sharper the more regular and extensive is the periodic array recorded in the micrograph.

It must be remembered in optical diffraction analysis that the diffraction object is the electron micrograph and not the specimen itself, and so even if the specimen itself is crystalline or periodic, unless these features are resolved in the micrograph, the periodic spacings cannot be observed and analyzed by optical diffraction methods.

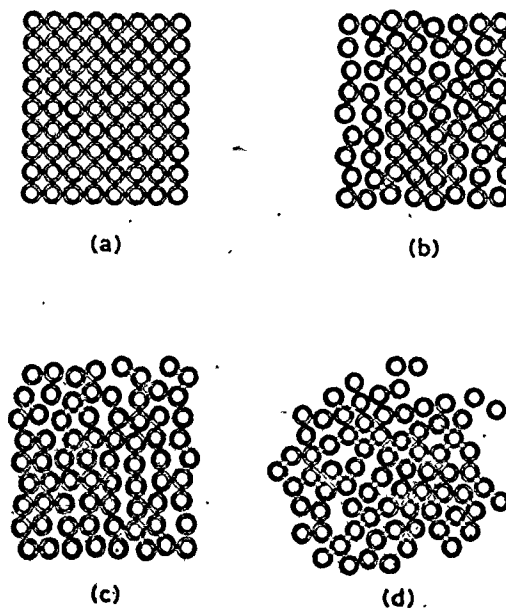
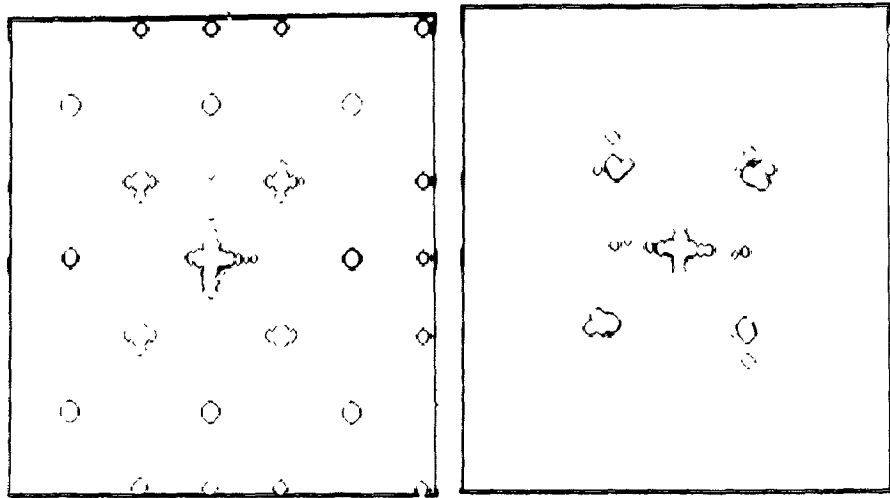
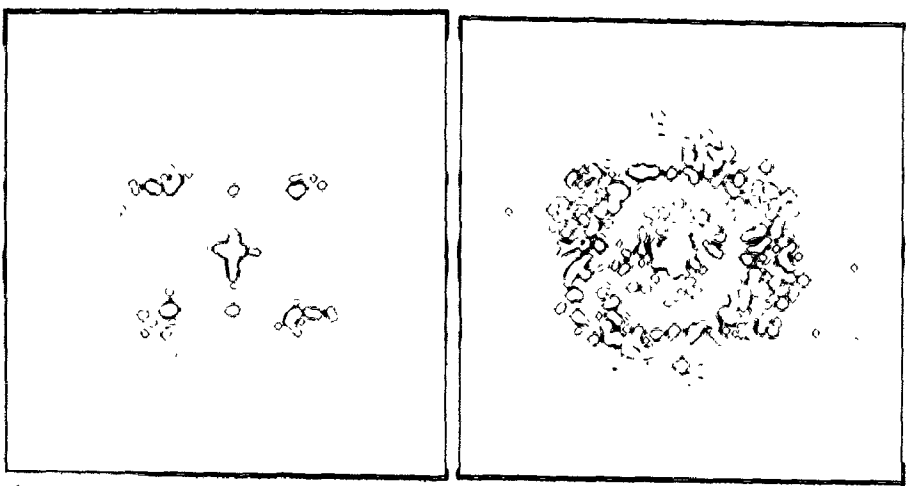


Fig. 15 Arrays of circular rings ranging from perfect square alignment (a) to complete disorder (d). Optical diffraction patterns made from negative copies of these arrays are shown in Fig. 16 (after (81)).



(a)

(b)



(c)

(d)

Fig. 16 Optical diffraction patterns made from negative copies of the arrays of rings in Fig. 15. Note that the diffraction pattern of the regular square array (a) gradually disappears and is replaced by an approximation to the diffraction pattern for a single ring (d). Note also that the first order diffraction spots in (a) fall within the limits of the rings in (d) (after (81)).

CHAPTER 2

EXPERIMENTAL PROCEDURES

2.a PREPARATION OF SINGLE CRYSTALS*

The material used in this work was supplied by Alcan International Ltd. in the form of hot rolled plate. The chemical analysis carried out on the material using spark analysis techniques gave in weight per cent:

3.62 Cu, 0.002 Fe, < 0.001 Mg, 0.002 Si, remainder Al.

The production of single crystal rods (1 cm diameter) was carried out by directional solidification using a modified Bridgeman technique.

The results of the chemical analysis showed that there were slightly different amounts of copper in the top and bottom. The results of 10 tops and bottoms show

TOPS : 2.96±0.10 wt % Cu

BOTTOMS: 3.08±0.15 wt % Cu

From the analysis of back reflection Laue X-ray photographs taken from different places on the top and bottom it was confirmed that the rods were indeed single crystals.

*The single crystals of Al-3% Cu alloy used in this work were very kindly supplied by J. D. Moan and the shortened description of single crystal preparation presented here is taken from his Ph.D. thesis (McMaster University, 1977).

2.b SPECIMEN PREPARATION

1 cm diameter crystals were spark-cut using a Servomet Spark Cutting Machine with an orientation close to (100). The spark-cut slices of about 0.3 mm thickness were carefully hand ground on both sides to about 0.1 mm, using 600 grade paper. Discs of 3 mm diameter were cut, wrapped in aluminum foil, and heat treated.

2.c PRECIPITATION HEAT TREATMENT

All samples were solution treated at 530°C for at least 24 hours, then water-quenched.

Immediately after the solution treatment samples were aged at various temperatures and times;

- At 160°C, i.e. below θ'' solvus line, up to 100 hours.
- At 240°C, i.e. above θ' solvus line up to 23 hours
(Some foils of the Al-3.6 % Cu polycrystal were aged up to 500 hours.)
- Double heat treatment: first step 240°C, 1 hour
second step 160°C, 23 hours
- Some of the foils were observed in the as-quenched state.

2.d THIN FOIL PREPARATION

Discs were electrochemically thinned by the double jet technique (a Streuers' "tenupol") in a mixture of 33% nitric acid, 67% methanol at -30°C, at 12 V.

Before thinning, discs were cleaned in the NaOH solution (20 gr NaOH+100 cm³ H₂O) at 70°C for very short time (~ 1 sec) to remove the stable oxide layer. After polishing the foils were kept about 5 minutes in the cleaning solution washed out in a methanol and dried.

2.e ELECTRON MICROSCOPY OPERATION

A Philips 300 electron microscope operating at 100 KV with a tiltable specimen holder was used in this study. The magnification was calibrated from a series of photographs of a carbon replica of a diffraction grating. The rotation was determined as a function of magnification selecting using these photographs and pairs of microscopy and diffraction photographs. Transmission electron micrographs were recorded along with selected area diffraction patterns, in order to permit determination of the foil orientation as well as of the diffraction conditions responsible for the contrast effects in the micrographs. Bright and dark fields using both matrix and precipitate reflections and weak beam techniques were employed in this study.

2.f OPTICAL DIFFRACTION

Some of the electron micrographs were examined in the optical diffractometer in order to study the periodic structure. The optical diffractometer used in this work is schematically shown in Fig. 17. The techniques employed are described in more detail by Horne and Markham (81)..

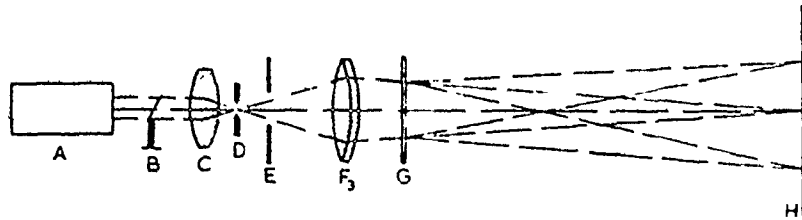


Fig. 17 Simple optical diffractometer. The diagram shows the arrangement of the components used to construct a simple optical diffractometer. A, laser; B, beam expanding lens; D, pinhole; E, adjustable diaphragm; F_3 , diffraction lens; G, electron micrograph; and H, viewing screen or camera (81).

CHAPTER 3

RESULTS AND DISCUSSION

3.a PROLOGUE

The aim of this work is the investigation of the role of the elastic interaction energy of the plate shaped precipitate, causing tetragonal distortion, on their spatial distribution, nucleation, growth and coarsening.

The theoretical and experimental results are presented in three separate sections. First, the interaction energy and stability parameters against coarsening for a simple and symmetrical three dimensional array of plate shaped precipitates are considered. The second section explores the contribution of the elastic interaction on the initiation and propagation of linear arrays of plate shaped precipitates and stabilization of such elastically locked arrays against growth and coarsening. The third part considers driving (chemical) and repulsive (interaction energy) forces acting on the ledge interfaces of the plate-shaped precipitates during their thickening.

3.1 ON THE STABILITY OF ARRAYS OF PRECIPITATES*

The purposes of this section are two: we will first give the results of a series of approximate numerical cal-

*The essential content of this section has been published by the author and Professors Purdy and Brown (82,83).

culations of the interaction energy and mechanical stability for a particularly simple and symmetric array of disc-shaped precipitates, assuming that the elastic properties of the matrix are isotropic. The array is of the form suggested by Eurin et al. (10). We will then give the results of a series of approximate numerical calculations of the stability parameters against coarsening of the above mentioned array, and we will explore the general conditions for the stability of an array against coarsening. This represents a refinement of an earlier suggestion based on the same concepts (9).

3.1.1 ELASTIC PROPERTIES OF THREE-DIMENSIONAL ARRAYS OF PLATE SHAPED PRECIPITATES

3.1.1.1 ELASTIC SELF ENERGY

This section deals with the strain fields of plate-like precipitates (to be used in a subsequent calculation) and in the total self-energy of such inclusions.

As already mentioned (see section 1.3) the strain field of G.P. zone may be approximated by that of a prismatic dislocation loop with Burgers vector proportional to the difference between the size of solute and solvent atoms. Kroupa (69) specialized a derivation due to Eshelby (4) for application to the displacement field of an infinitesimal dislocation loop.

The stress tensor $d\sigma_{ij}$ at a point r_i near an infinitesimal prismatic dislocation loop at the co-ordinate origin

is given by eq. (61'). If the "infinitesimal" approximation is a poor one, the strain field of large loop can often satisfactorily be approximated by the superposition of the strain fields of a regular planar array, or raft of such infinitesimal loops. This improved approximation will be used in subsequent pair and lattice energy calculations.

If a simple square plate-shaped precipitate has misfit parameters that permit it to be treated, in approximation, as a dislocation loop with Burger's vector of magnitude, $b = \epsilon d$, then the elastic self energy is,

$$E_{el} = \frac{\mu \epsilon^2 \ell d^2}{\pi(1-\nu)} \ln \frac{8\ell}{\epsilon d} \quad (67)$$

where ℓ is the length and d is the thickness of the precipitate (84). This model assumes that d/ℓ is very small and that almost all strain is located at the edge of precipitate; the core cut-off radius has been taken equal to ϵd .

3.1.1.2 THE INTERACTION ENERGY

This term is specific to the type of arrangement of precipitates actually formed, and it is therefore this term which, "a priori" presents the greatest computational difficulty.

One must first have some knowledge of the type of array formed or some method of selecting arrays which are energetically the most favourable. We have used two approximations; one being the "infinitesimal approximation" (section

1.4), and a second in which "large" precipitates are modelled as square rafts of such infinitesimal disturbances. The distinction between the results for "infinitesimal" and for "large" inclusions allows one to evaluate the adequacy of the simple infinitesimal approximation.

The total energy of a pair of dislocation loops is the self energy of each loop plus the interaction energy between the two. The interaction energy may be defined as the energy required to create one loop in the stress field of the other. For infinitesimal loops, it is given by eq. (64).

This expression has the virtue of simplicity. However, Brown et al. (9) and Khachaturyan and Shatalov (6) have shown that the elastic interaction between pairs of "large" precipitates can be quite different from those modelled as infinitesimal centres of disturbance.

For the two precipitate interactions, the following procedure was performed.

A plate, taken in approximation as a dislocation loop, was modelled as a square raft of one hundred small platelets. After computing the interaction energies among all of the platelets (using the infinitesimal approximation) the sum of all these energies was taken to give the total interaction energy between two precipitates. Taking $\rho = r/L$, and $f = v/\eta L^3$, the interaction energy between two such "large" precipitates can be written in more general form as:

$$E_{12} = \mu \eta V f \epsilon^2 \sum_{\rho=1}^n \frac{\Delta}{\rho^3} f(\theta) \quad (68)$$

where r is the separation of the precipitates centres, L is the nearest neighbour spacing, ΔV is the volume of the infinitesimal plate-like precipitates, $n = \Delta^{-1}$ is the number of infinitesimal precipitates in the raft, μ is the shear modulus, ϵ is the constrained elastic mismatch, f is the volume fraction of precipitate, and $f(\theta)$ is a function of the mutual position and the orientation of the precipitates in the space. The number η depends upon the type of array.

For a regular array of precipitates, the energy-separation relationships will be determined by a summation of all two-precipitate interactions i.e.

$$E_{1L} = \frac{1}{2} \sum_{i=1}^{N-1} \sum_{j=i+1}^N E_{ij} \quad (69)$$

where N is the total number of precipitates being considered, E_{ij} is the interaction energy between i -th and j -th precipitates as given by eq. (68).

3.1.1.3 THE ENERGETICS OF THE <1230> ARRAY

In this section, the energy-separation relationship for pairs of precipitates, and the corresponding results for a large number of precipitates arranged in a <1230> array (Fig. 18) are presented. The four digit notation for the geometry of the arrays is that of Eurin et al. (10). For the

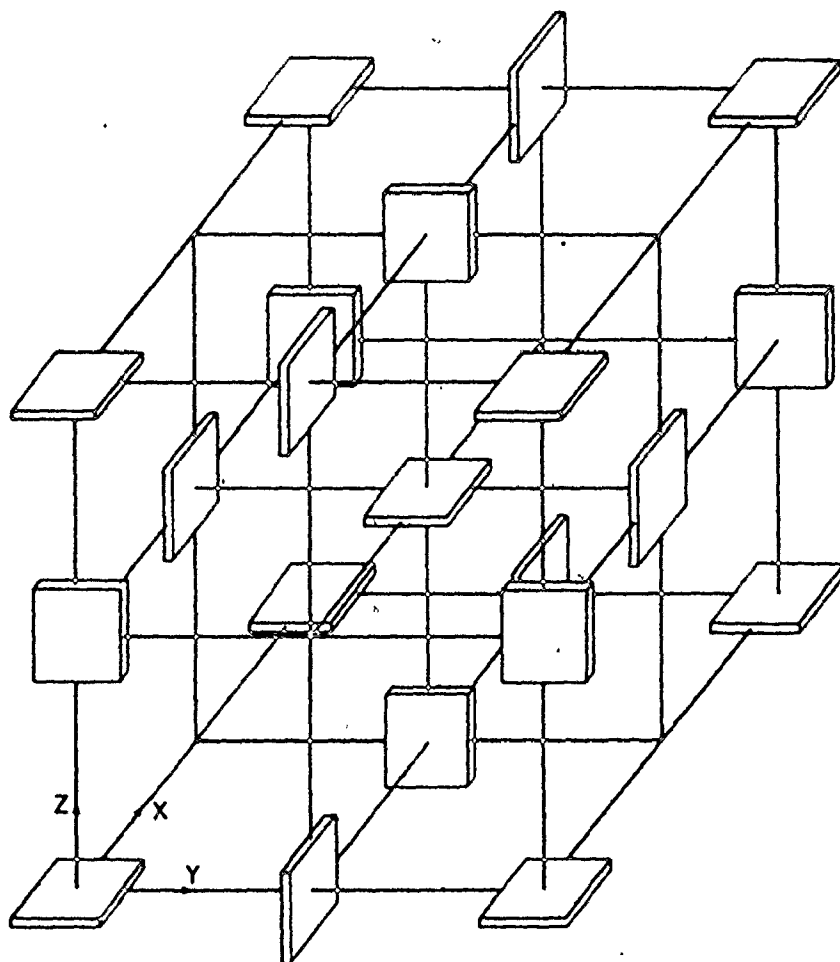


Fig. 18 The $\langle 1230 \rangle$ array.

$\langle 1230 \rangle$ array, the number in equation (67) is equal to $4/3$.

We have chosen the long edge-length of the "large" square plate precipitates as a convenient characteristic unit with which to measure the interparticle spacing. In comparing the results for these "large" precipitates with those for infinitesimal, or point precipitates, the interactions of the latter are computed by collapsing all of the elements of the square raft into a central point, and holding all other factors constant.

The interaction energies between two plates versus the distance between them, when they are mutually parallel (face-face and edge-edge configuration) and when they are mutually perpendicular (edge-edge and edge-face configuration) are shown in Figs. 19-22. This is compared with the interaction of infinitesimal precipitates (broken lines).

It is clear that the interaction energy of two "large" plates in the face-face configuration (Fig. 19) is much less positive (repulsive) than the corresponding interaction energy of two infinitesimal precipitates. This stems from the interaction of the elements far away from the centres of the precipitates. For the same reason the interaction energies of two "large" plates in both edge-edge configurations (Figs. 20 and 21) are much more negative (attractive) than the corresponding energies of two infinitesimal precipitates.

More significantly, the interaction of elements far from the centres of precipitates leads to the minimum in the interaction energy of two "large" precipitates when they are

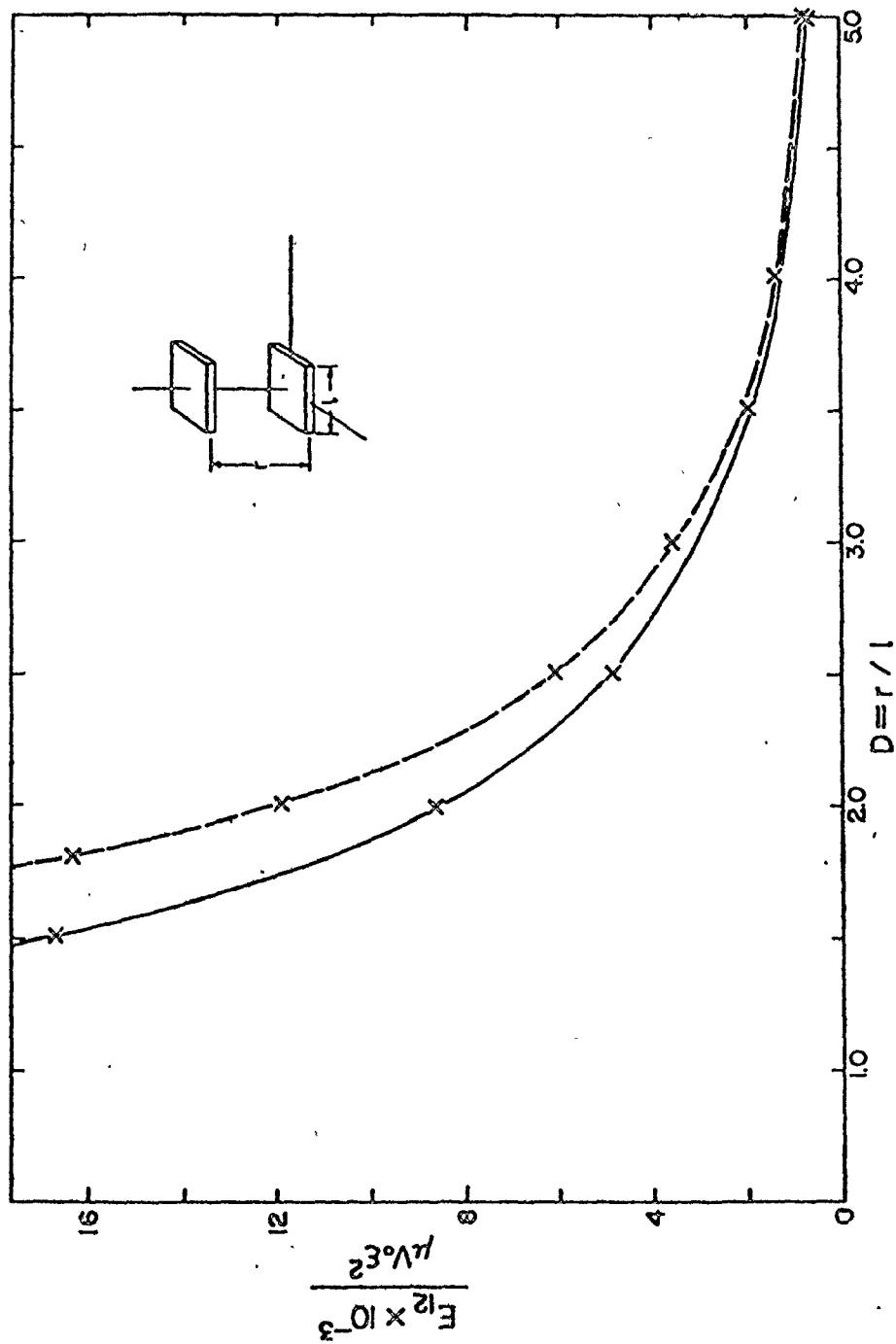


Fig. 19 Interaction energy of two square shaped particles when they are mutually parallel (face-face configuration) as a function of separation. The broken line indicates the interaction of infinitesimal precipitates of the same strength. D is the centre-to-centre distance; each unit represents the edge-length of the particles (D has the same meaning, r/l , in all other figures in which it appears).

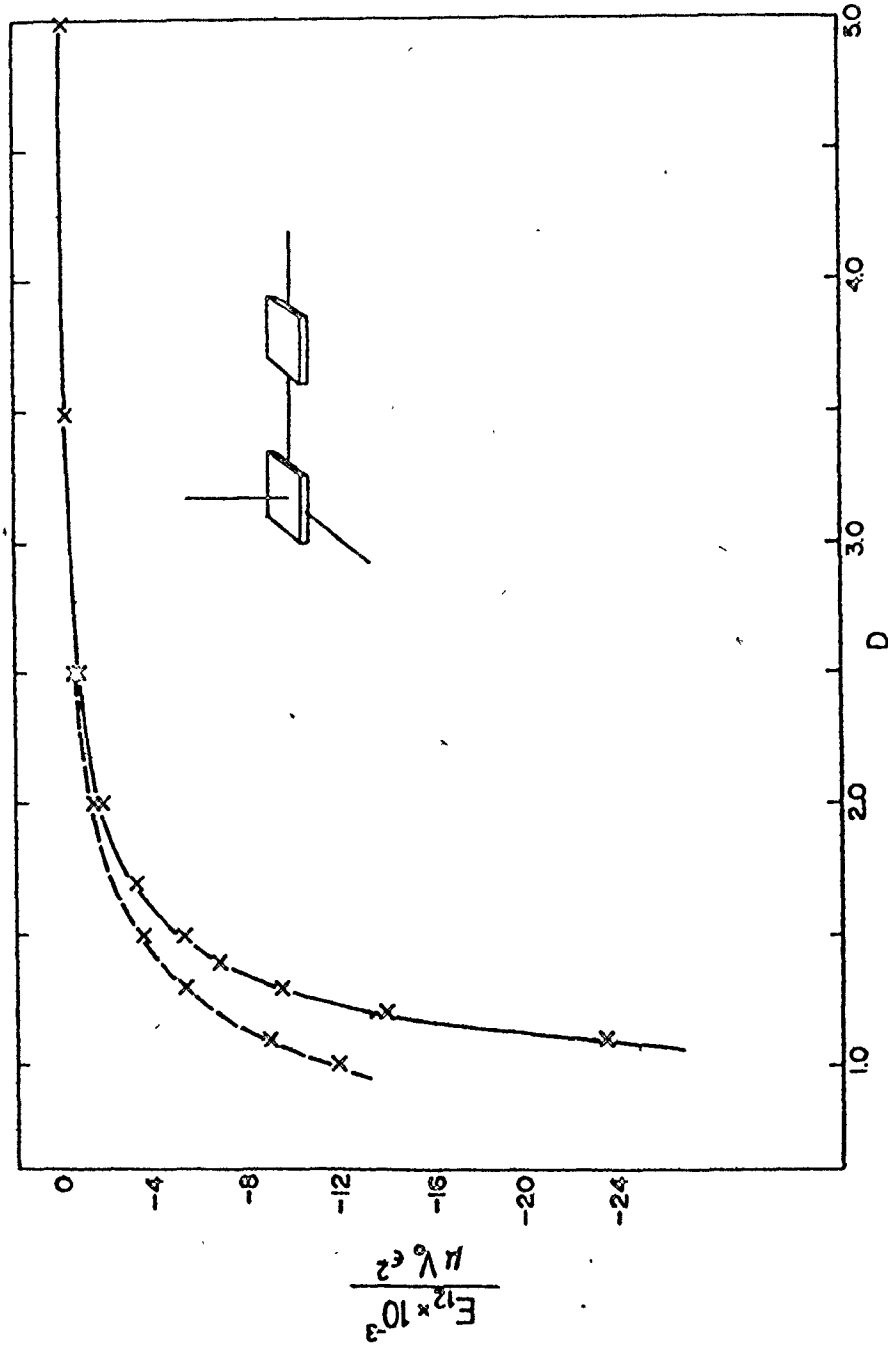


Fig. 20 Interaction energy of two square shaped particles when they are mutually parallel (edge-edge configuration) as a function of separation. The broken line indicates the interaction of infinitesimal precipitates of the same strength.

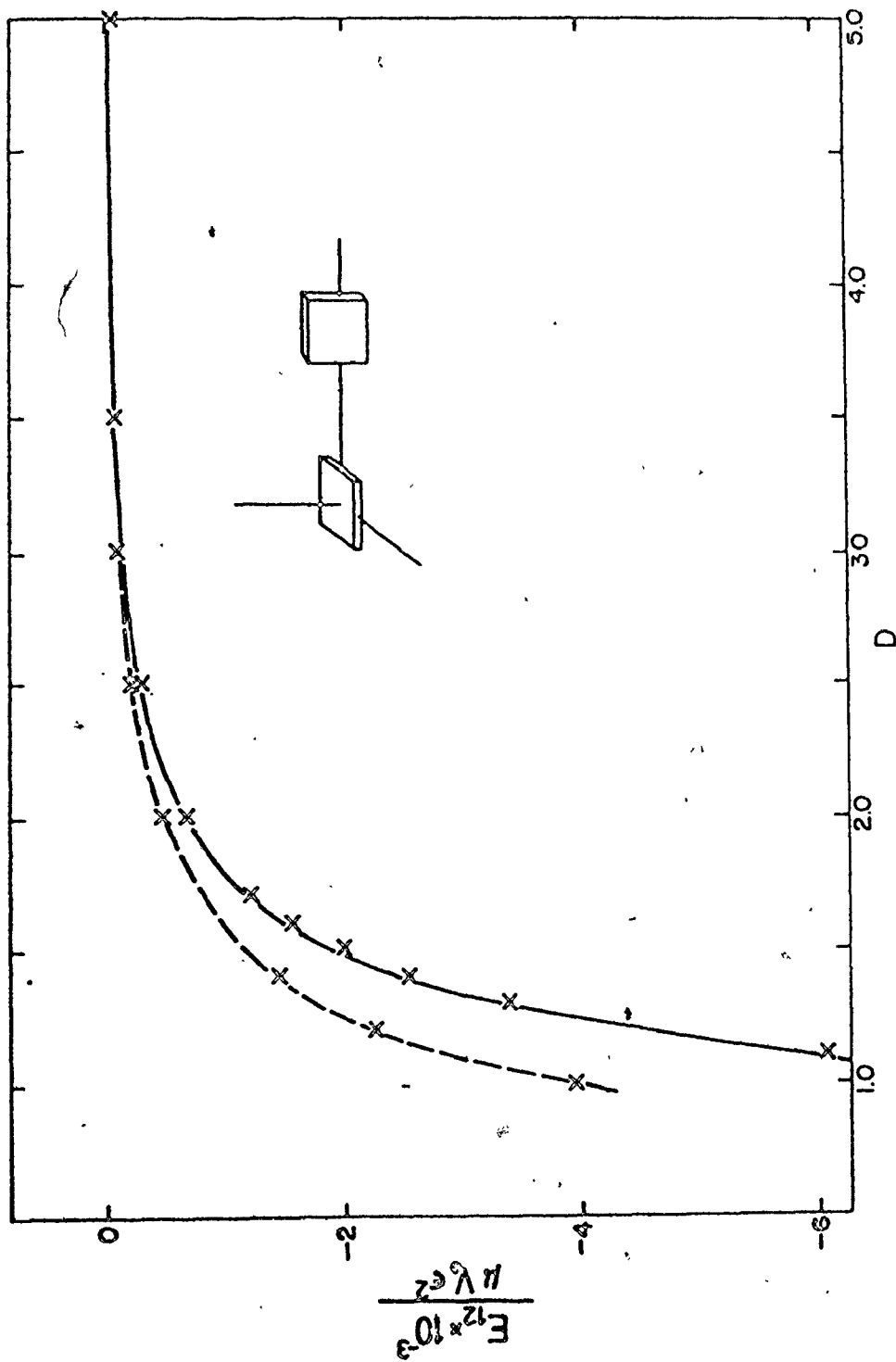


Fig. 21 Interaction energy of two square shaped particles when they are mutually perpendicular (edge-edge configurations) as a function of separation. The broken line indicates the interaction of infinitesimal precipitates of the same strength.

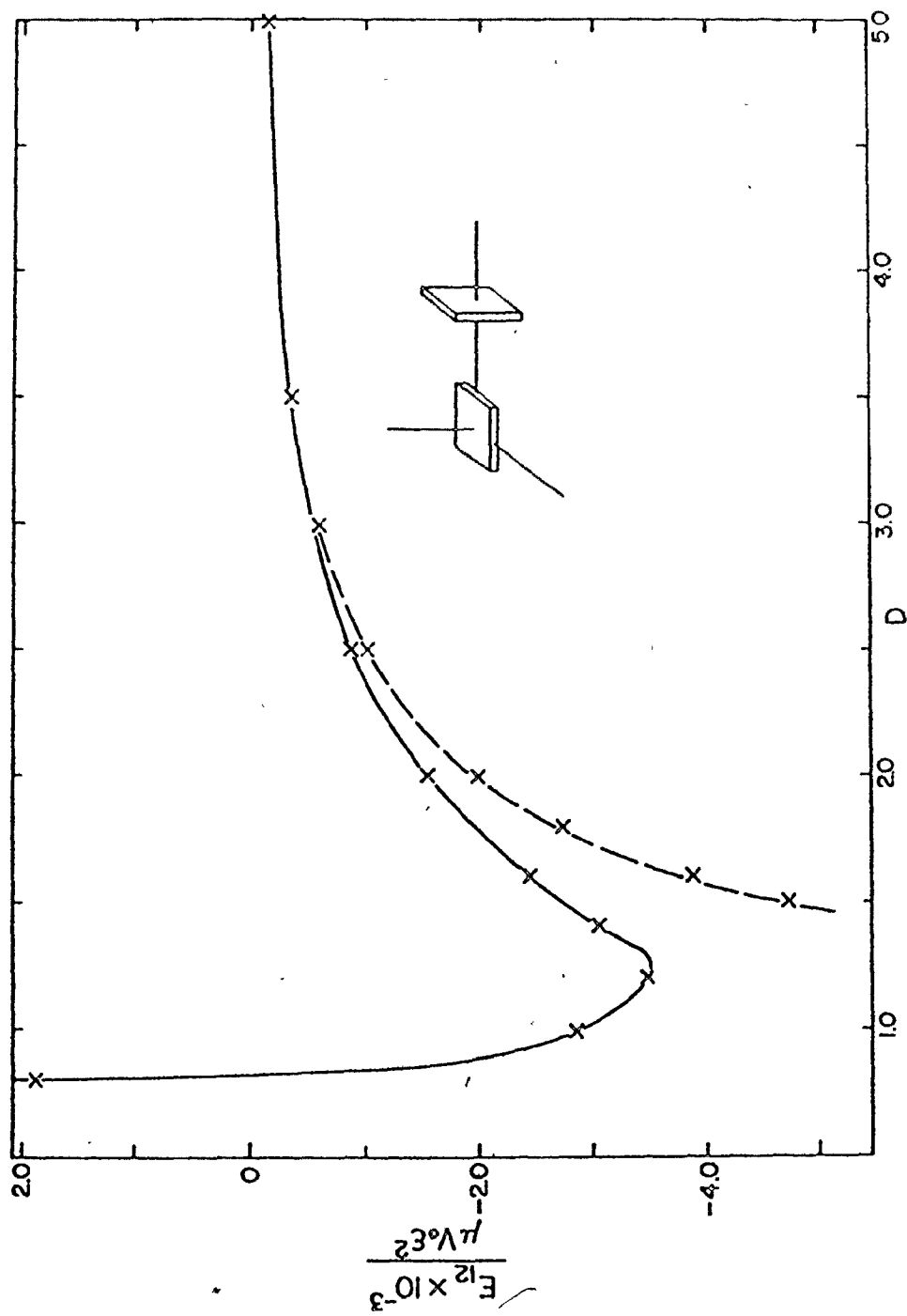


Fig. 22 Interaction energy of two square shaped particles when they are mutually perpendicular (edge-face configuration) as a function of separation. The broken line indicates the interaction of infinitesimal precipitates of the same strength.

mutually perpendicular, in the edge-face configuration; Fig. 22 (again this is in contrast to the result using the infinitesimal approximation).

The total elastic interaction energy (per central plate for the $\langle 1230 \rangle$ array in the "large" approximation) versus the distance between neighbouring plates is shown in Fig. 23. The calculation was performed using cut-off radii of 6.4, 7.5 and 10 units (i.e. no interactions beyond these radii were included in the calculation). Note that there is a minimum in these energy curves suggesting that short or long range order may occur for a near-neighbour spacing of about 1.2 units. This is determined e.g. by combinations of the potentials given in Figs. 19 and 22.

From an examination of Fig. 23 it is apparent that the energies are similar and that the energy minimum occurs at approximately the same separation for each curve: Table 1 shows the total number of precipitates enclosed by sphere of radius 6.4 to 10 units for near-neighbour separations of 0.8, 1.0, 1.2, 1.6 and 2.0 units. In view of these results a radius of 10 units is considered a reasonable point at which to begin using the infinitesimal, approximation in computing the interaction energy for a large perfect array. The total elastic energy per plate of the $\langle 1230 \rangle$ array was calculated on this basis. It is shown plotted against, the number of

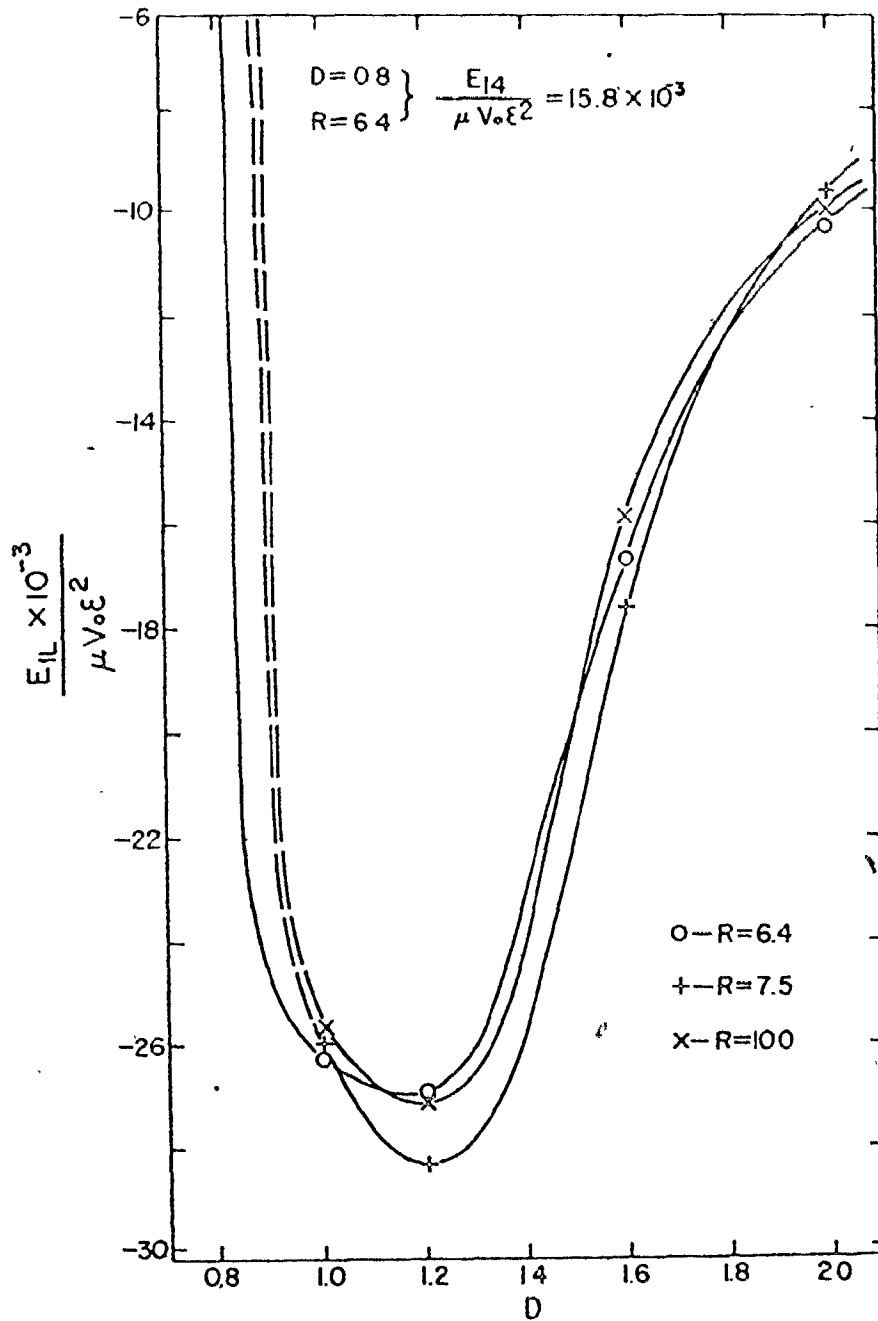


Fig. 23 The total elastic energy of the $\langle 1230 \rangle$ array per plate vs the distance between the plates enclosed by the sphere of radius of 6.4, 7.5 and 10.0 times the plate-length.

TABLE 1

| RADIUS TIMES THE PLATE EDGE-LENGTH | NUMBER OF PARTICLES | | | | |
|--|---|------|------|-----|-----|
| | DISTANCE (CENTRE TO CENTRE) TIMES THE PLATE EDGE-LENGTHS | | | | |
| | 0.8 | 1.0 | 1.2 | 1.6 | 2.0 |
| 6.4 | 1584 | 794 | 468 | 184 | 106 |
| 7.5 | | 1294 | 766 | 328 | 186 |
| 10.0 | | 3128 | 1848 | 950 | 388 |

precipitates (or the radius of the sphere which includes that number of precipitates) in Fig. 24.

Fig. 24 shows that the elastic energy per plate reaches a plateau and that, on further addition of precipitates to the system, the energy changes are negligible. The greatest contribution to the elastic energy of the array comes from the nearest neighbours, as expected from the general form of the potential: ($\sigma_{ij} \approx 1/r^3$).

Fig. 25 represents the interaction of infinitesimal plates in a $\langle 1230 \rangle$ array. As expected from the two-precipitate interactions, Figs. 19-22, this array shows completely different characteristics, in particular, there is no energy minimum for small separations.

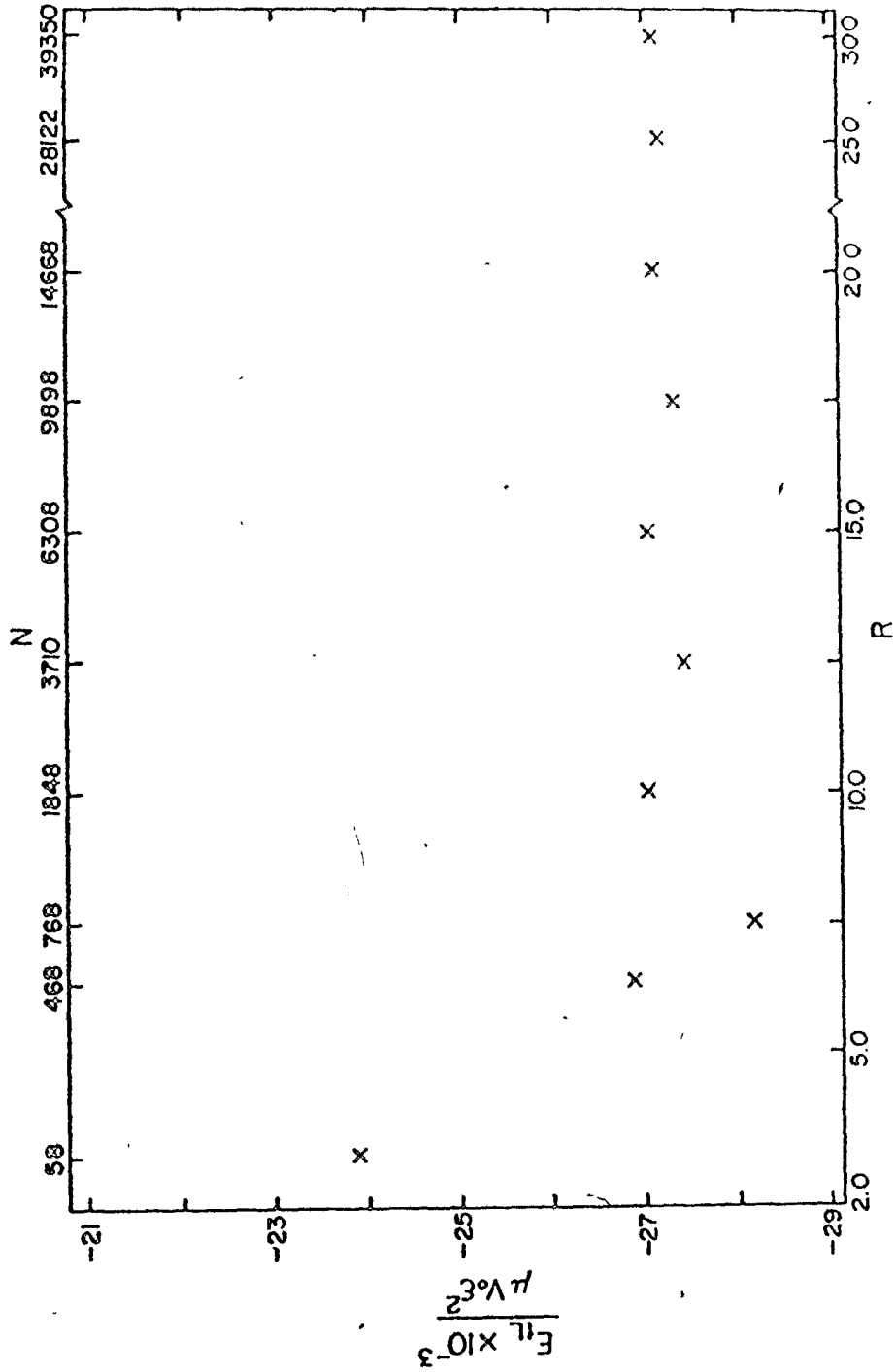


Fig. 24 The total elastic energy per plate of the $\langle 1230 \rangle$ array vs the number of precipitates, N (or R , the radius of the sphere which includes that number of precipitates). The distance between the particles is 1.2 times the plate-length.

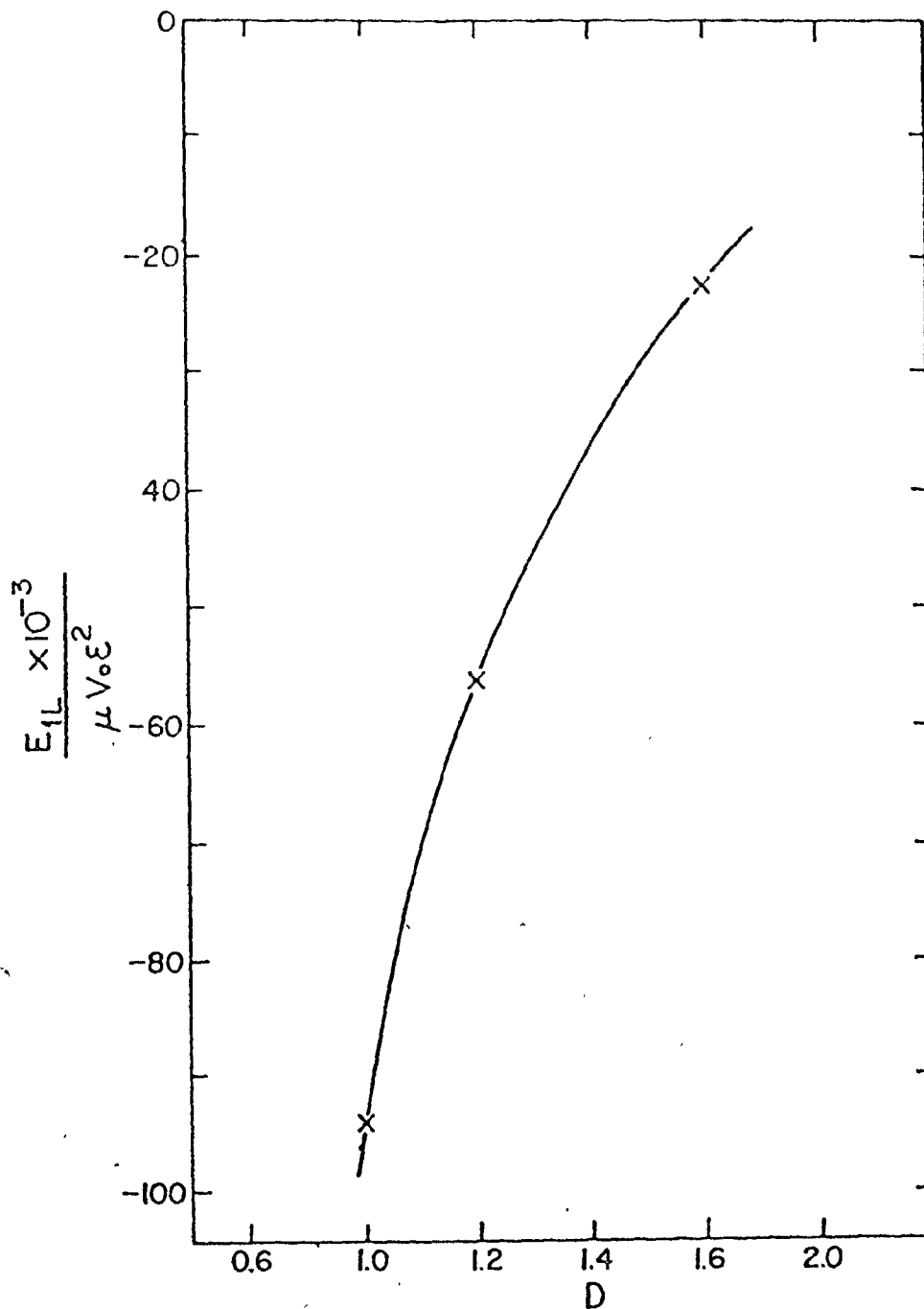


Fig. 25 The total elastic energy per plate of the $\langle 1230 \rangle$ array vs the distance between the plates (infinitesimal approximation). The energy was calculated between the central plate and the plates enclosed by the sphere of radius of 10.0 plate edge-lengths.

3.1.1.4 NUMERICAL TEST OF THE MECHANICAL STABILITY OF THE $\langle 1230 \rangle$ ARRAY

In order to be sure that a periodic distribution of inclusions is stable, it is necessary to study the changes of the interaction energy of precipitates with respect to displacement from the ideal lattice sites, (as might be accomplished by surface diffusion within one precipitate) and with respect to volume exchange (as might be accomplished by volume diffusion between precipitates). Here, we will consider only mechanical stability (the second kind of displacement will be considered in the section 3.1.2.1).

The interaction energy calculations were made for the $\langle 1230 \rangle$ array (in the infinitesimal approximation) but with the central plate's position altered a small amount, i.e. subjected to displacement along the x, y and z axes and the total elastic interaction energy calculated after each displacement. The results for infinitesimal precipitates are shown in Figs. 26-28. From these, it was found that the interaction energy increases with displacement along the x and z axes but decreases with displacement along the y axis.

When these calculations were carried out in the large precipitate approximation however, the array was found to be stable against displacements in all three directions, Fig. 29. Thus, the $\langle 1230 \rangle$ array is mechanically stable.

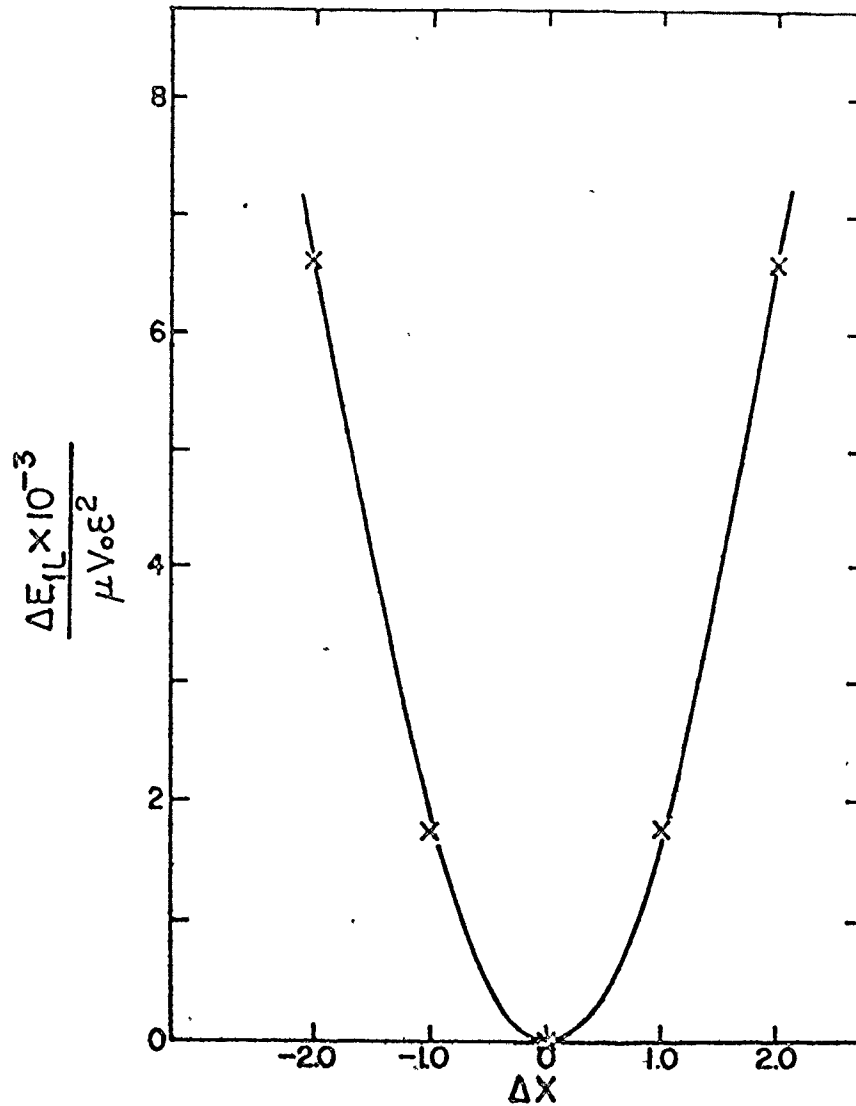


Fig. 26 The elastic energy change per plate of the $\langle 1230 \rangle$ array in the infinitesimal approximation as a function of the displacement of the central plate along the x-direction (each division is 1/10 plate edge-length). The radius of the sphere is 10.0 times the plate edge-length and the distance between the particles (centre-centre) is 1.2 plate edge-lengths.

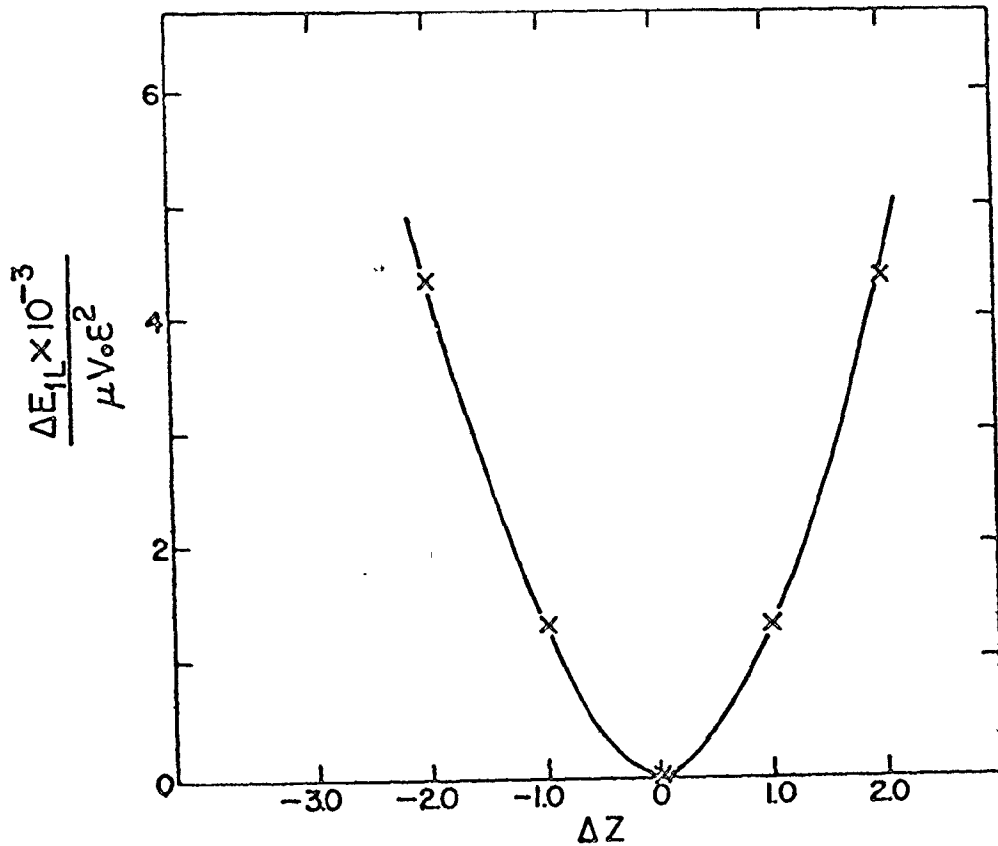


Fig. 27 The elastic energy change per plate of the $\langle 1230 \rangle$ array in the infinitesimal approximation as a function of the displacement of the central plate along the z -direction (each division is $1/10$ plate edge-length). The radius of the sphere is 10.0 times the plate edge-length and the distance between the particles (centre-centre) is 1.2 plate edge-lengths.

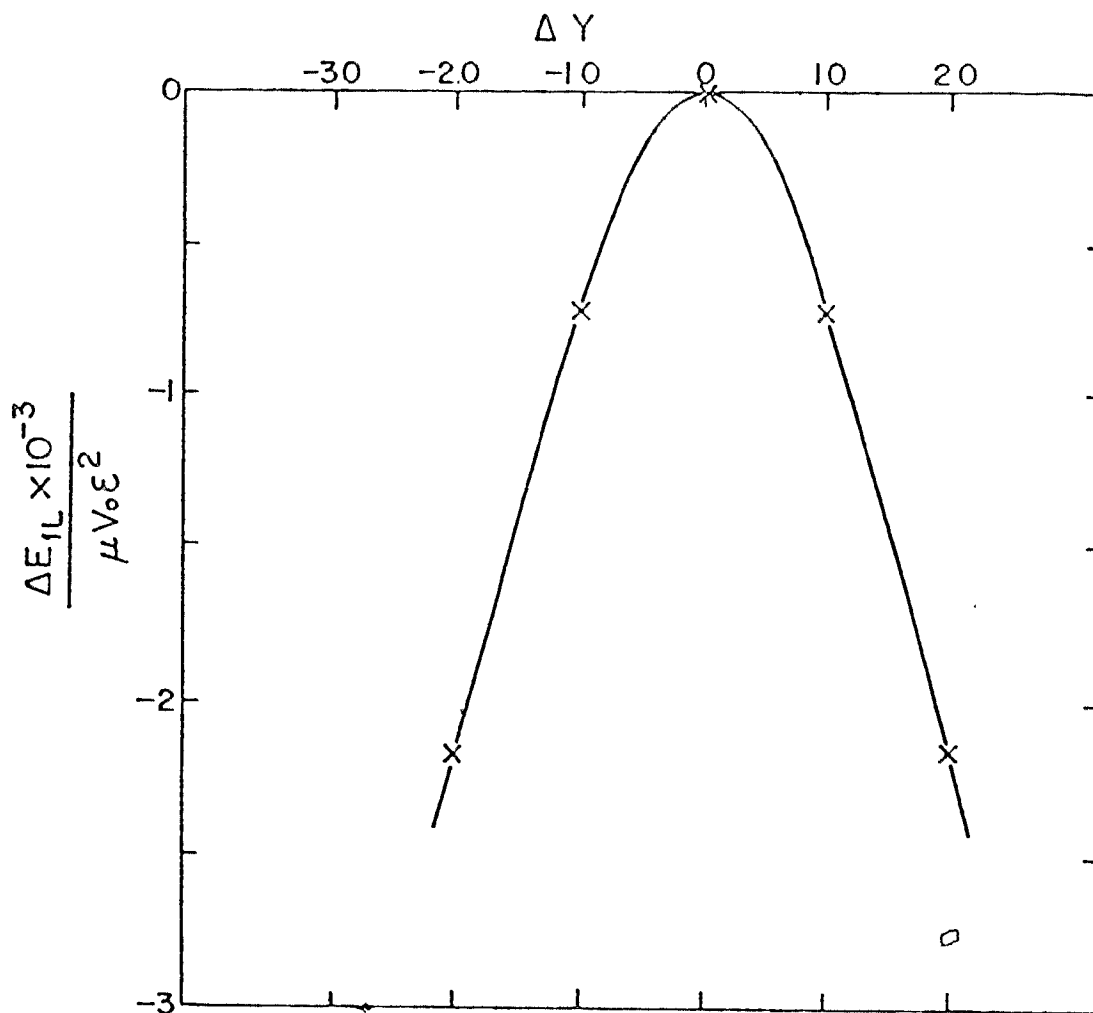


Fig. 28 The elastic energy change per plate of the $\langle 1230 \rangle$ array in the infinitesimal approximation as a function of the displacement of the central plate along the y-direction (each division is 1/10 plate edge-length). The radius of the sphere is 10.0 times the plate edge-length and the distance is 10.0 times the plate edge-length and the distance between the particles (centre-centre) is 1.2 plate edge-lengths.

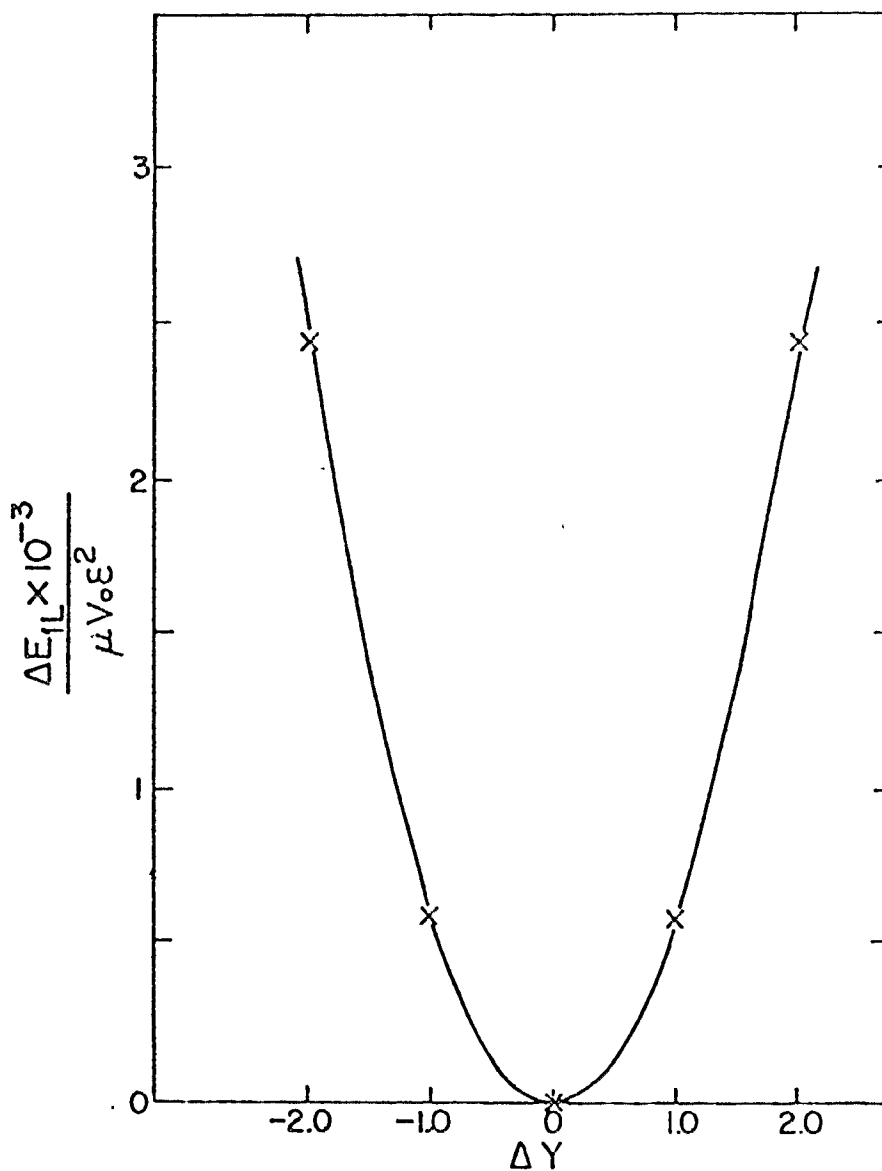


Fig. 29 The elastic energy change per plate of the $\langle 1230 \rangle$ array in the 'large precipitate' approximation as a function of the displacement of the central plate along the y-direction (each division is 1/10 plate edge-length). The radius of the sphere is 7.5 times the plate-length and the distance between the particles (centre-centre) is 1.2 plate edge-lengths.

3.1.1.5 EXPERIMENTAL RESULTS

In this section, some experimental results concerning the elastic interaction of plate-like precipitates and possible ordering of the precipitates will be reported. The Al-Cu system was chosen for two reasons; first, θ'' and θ' produce tetragonal distortion which is requisite for strong elastic interaction, and secondly the aluminum matrix in this system is nearly isotropic as was assumed in the interaction energy calculations.

Observations were made on specimens aged at 160°C, i.e. below the θ'' solvus for up to ~ 100 hours. Fig. 30 shows the microstructure of the specimens aged 6 hours at 160°C. This represents early stages of development, and its main characteristic is the "tweed" micro structure. Particles are not clearly seen, only the overall strain field. Fig. 31 represents the microstructure of specimens aged 24 hours at 160°C. The micrograph is taken under such conditions that only one of the $\{100\}$ plates are visible. The particles are now revealed (a few hundred angstroms long), together with the strain fields around them. The micrographs and corresponding diffraction pattern shown in Fig. 32(a)-(b) represents the microstructure of specimens aged 96 hours at 160°C. The main characteristic of this micrograph is the very high strain field with the wave-like tendency, which could be regarded as a very coarse "tweed" structure. These coarse waves are the result of the complex elastic interactions among the indivi-

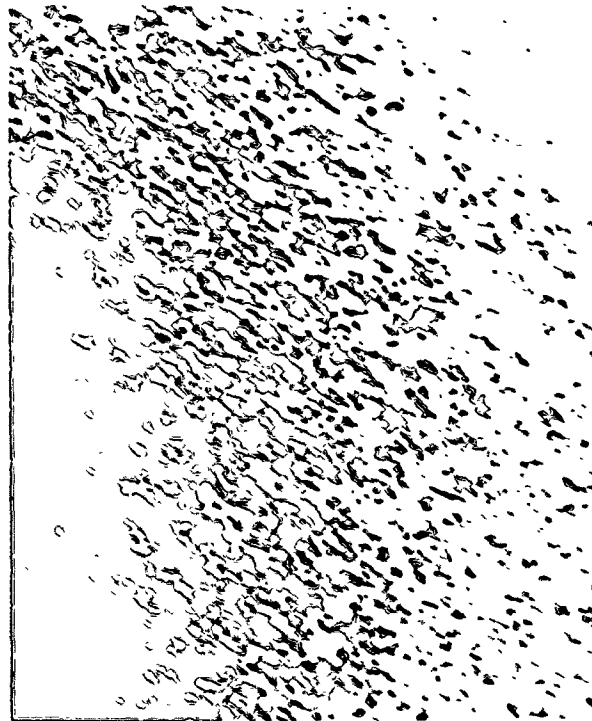
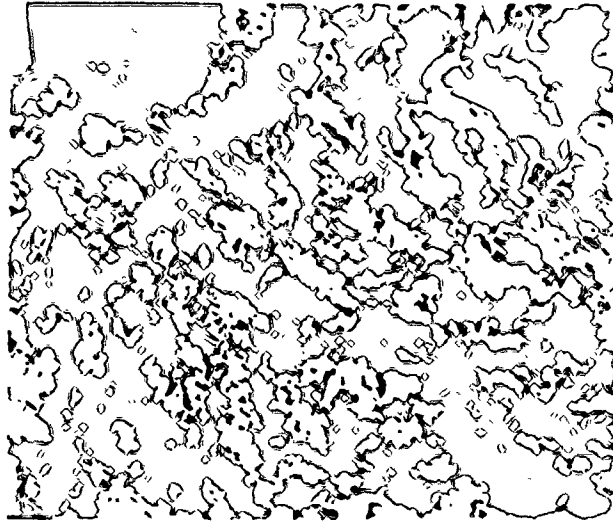


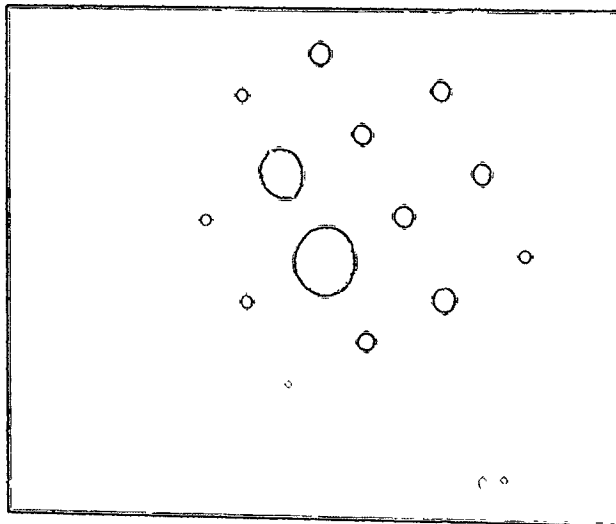
Fig. 30 Al-3% Cu crystal with (001) orientation, solution-treated and aged 6 hours at 160°C. Bright-field conditions show tweed contrast. θ particles are not clearly seen (94500 \times).



Fig. 31. Bright field micrograph of Al-3% Cu crystal with (001) orientation, solution-treated and aged 24 hours at 160°C, showing strain fields of the individual θ'' particles. The particles are now revealed as about 400 Å in diameter (94500×).



a



b

Fig. 32. Al-3% Cu crystal with (001) orientation, solution-treated and aged 95 hours at 160°C. a) Bright field micrograph shows coarse tweed-like contrast (27500 \times); b) Corresponding selected-area electron diffraction pattern.

dual precipitates.

In order to get some evidence concerning long-range ordering, optical diffraction patterns of the series of micrographs of the type shown in Fig. 32 were recorded. Diffraction patterns were taken with the laser beam expanded to ~ 1 cm diameter, which allowed a large number of precipitates to be analyzed. The real micrographs were compared with models having different degrees of ordering. The main characteristic of these results, as shown in Fig. 33(a)-(b) is that there is some degree of ordering, but that the arrays are highly imperfect. Some of this apparent disorder could be attributed to imperfect imaging of the particles; many of them were completely obscured by the strain fields of neighbouring precipitates.

Some of these micrographs were photographically enlarged, Fig. 34(a)-(b) in order to study directly the precipitate environs. The main feature is that the particles have relative orientations of two types. One is the edge-face orientation which is expected from the interaction potential shown in Fig. 22, and the second one is the "parallel-step" configuration (see Fig. 59(c)).

Thus for this system, there is little evidence for long-range ordering which would lead to stable three-dimensional arrays. However, these observations clearly show that the energetically favourable edge-edge face configuration is very common, suggesting that a degree of short-range order exists.

100

70

Fig. 33 Optical diffraction patterns corresponding:
a) to the model lattices of different
degrees of ordering and b) to the series of
micrographs of the types shown in Fig. 32.

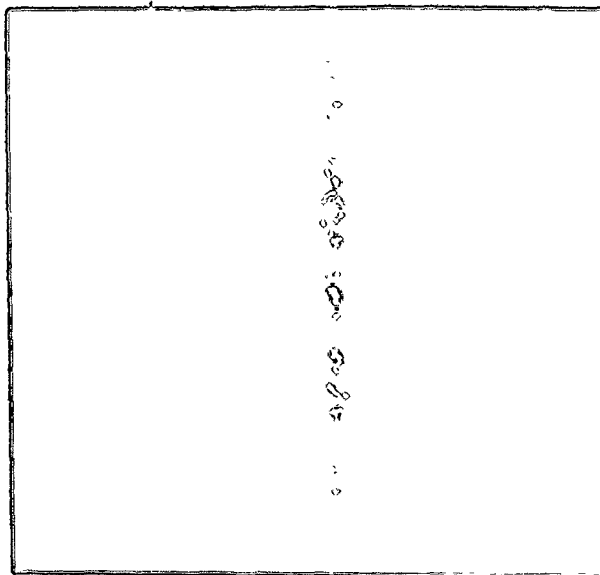
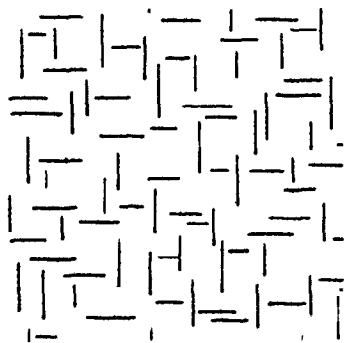
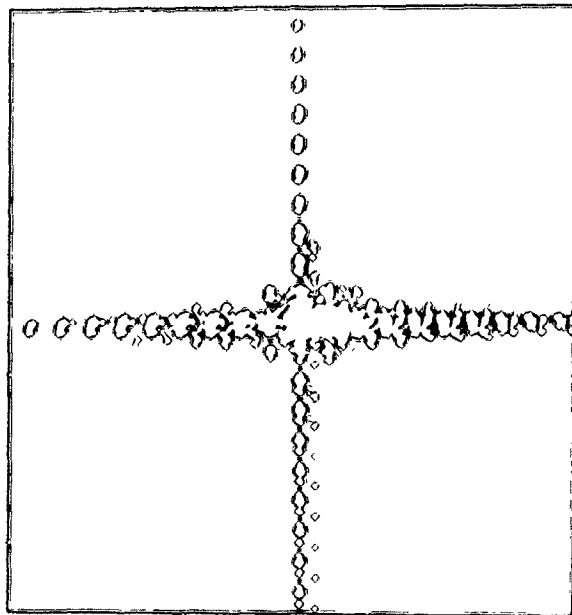
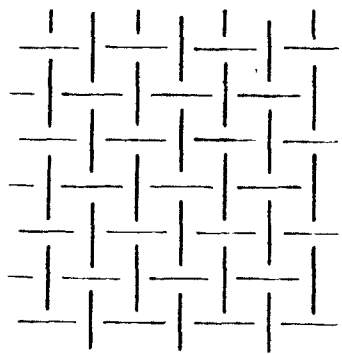


Fig. 33 (a)

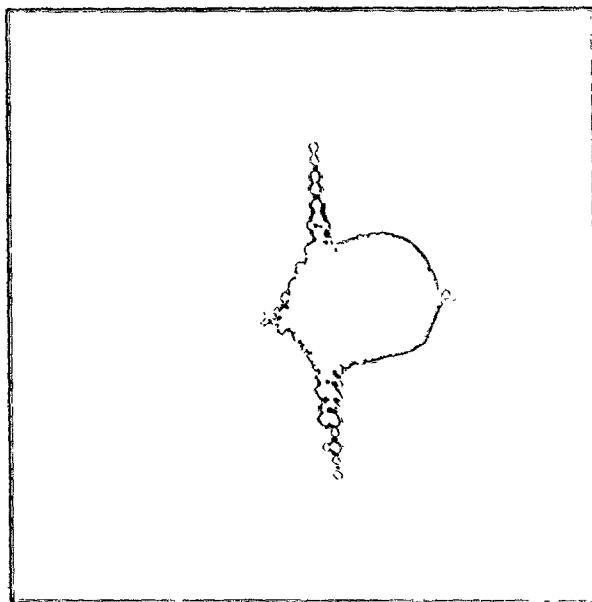
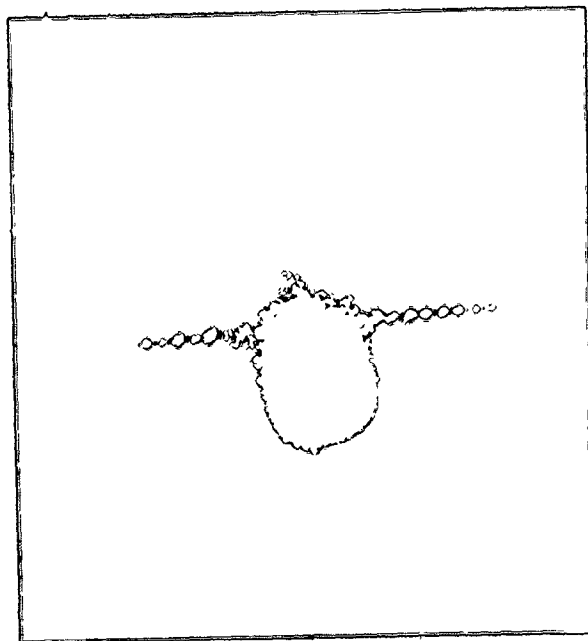


Fig. 33 (b)

Fig. 34 Bright field micrographs of Al-3% Cu crystal with (001) orientation, solution-treated and aged 95 hours at 160°C. Both micrographs show that the energetically favoured edge-face and "parallel step" orientations are well represented, clearly showing evidence of short-range ordering.
(a) 55000×; (b) 33000×.

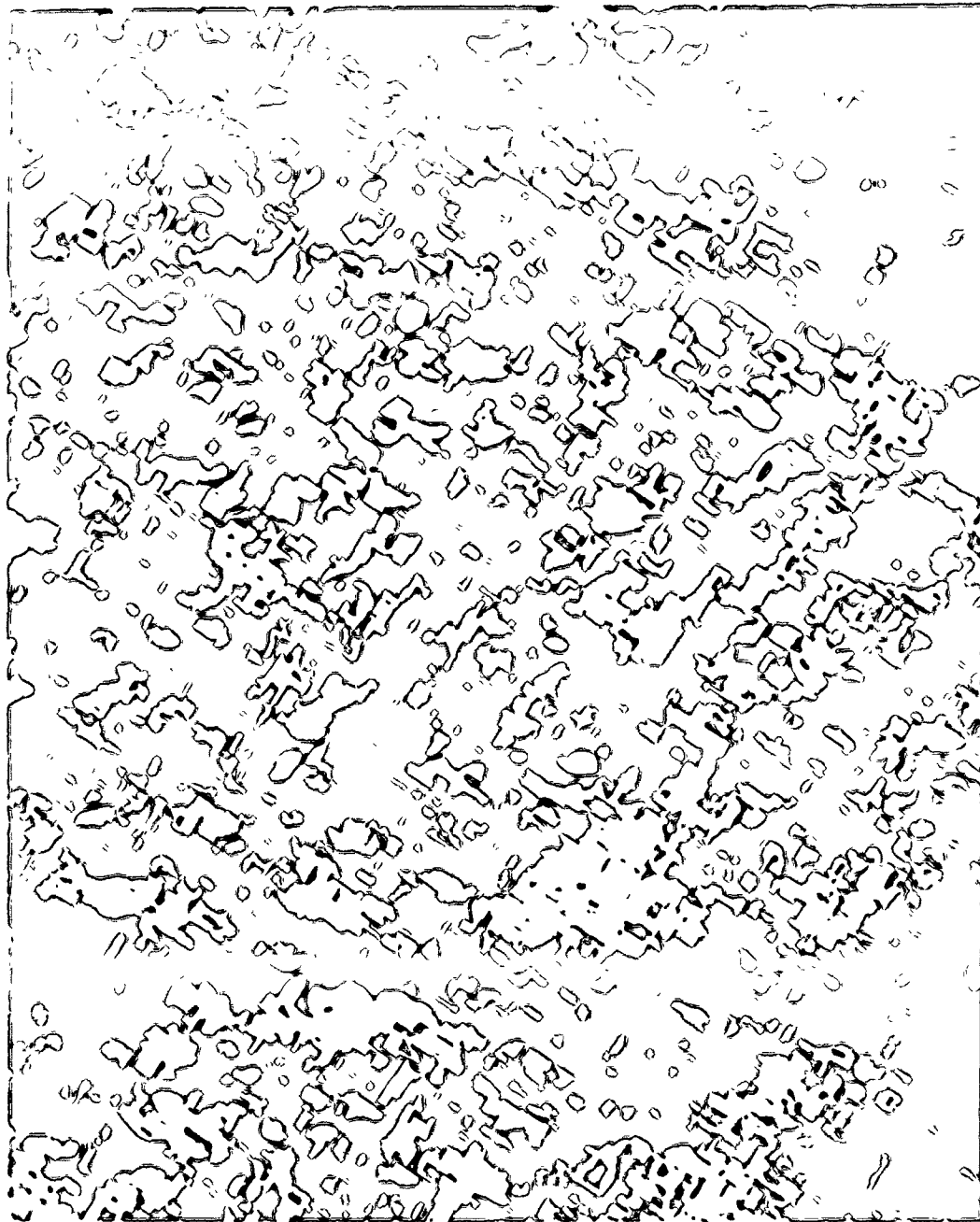


Fig. 34 (a)



Fig. 34 (b)

In the next section (section 3.2) we will show that the "parallel step" configuration for small inclination angles (see Fig. 60) is also very attractive and one of the dominant factors in θ' nucleation.

3.1.1.6 DISCUSSION

The elastic interaction among large precipitates causing tetragonal distortions is qualitatively and quantitatively distinguishable from that for infinitesimal precipitates. It is clear, as shown in Figs. 19-22 that the "infinitesimal" approximation is not adequate of an array in the separation range of greatest interest. The distinction is also clear from the energy-separation plots for pairs of precipitates. Quite naturally, the array characteristics reflect those of the dominant near-neighbour interaction; if a minimum appears in the pair-interaction/separation relation, we might expect that an array will form which emphasizes that near-neighbour configuration. The extent to which the energy/separation characteristics of the array match those of the dominant near-neighbour pair is of interest. From a comparison of Figs. 22 and 23, we see that the minimum occurs at nearly the same separation in both cases, suggesting that the main characteristics of the full array, are dictated by those of the pair.

It was shown that the $\langle 1230 \rangle$ array is mechanically stable since any displacement of the central precipitate in

either $x(y)$ or z direction leads the system to a higher energy state. The opposite result was obtained in the infinitesimal approximation. The reason for this lies in the energy-separation curve which in the "infinitesimal" approximation does not possess a minimum.

The present experimental results are not conclusive but suggest that long-range ordering, if it exists in this system, is highly imperfect. It should be noted that Boyd and Nicholson (85,86) did not find kinetic evidence for θ stabilization. In the following sections we will show that the requisite for stability against coarsening is formation of regular three-dimensional or linear arrays elastically stabilized.

However, short-range ordering which emphasizes the attractive pair-interactions (the edge-face and the inclined face-face configuration) is very evident. Indeed, it is possible in Fig. 34(a)-(b) to find small clusters (a few particles) ordered in the way predicted by the interaction energy calculations. The optical diffraction also indicates some measure of periodicity. The wave-like strain field is evident through all micrographs and it is clear that it is a result of strain field interactions from the closely spaced particles. The origin of those wave-like strain fields may therefore be interpreted in the way described by Jack (35) (see section 1.5.d).

It should be mentioned that the analysis of the perio-

dicity is a difficult problem because it requires very thin foils with uniform thickness and proper orientation. Any larger thickness leads to an effect related to overlapping of the images from particles at different heights which seriously complicates the image. The same is true for foil (section) orientation relative to the symmetry planes of the array. As already mentioned, the diffraction object is the electron micrograph and not the specimen itself, and so even if the specimen itself is periodic, unless these features are not resolved in the micrograph, the periodicity can not be observed and analyzed by optical diffraction methods. Nevertheless in this particular case, where the θ phase has rather small elastic mismatch, it is hard to expect long-range ordering to a larger extent, in the nucleation and early growth stage, under the very high chemical driving force.

A higher degree of ordering might be expected for systems with higher elastic mismatches and higher anisotropy as is observed in many systems which produce tweed structure.

It is interesting to note that R. Cahn (87) has discussed the present work and its connection with the genesis of a void lattice. In some metals, voids (formed after a metal crystal is irradiated with neutrons or other more massive particles) arrange themselves in an orderly three-dimensional array - a void lattice. The voids are originally formed in a random pattern, and a void lattice is formed only later when a much higher radiation dose has been absorbed and

individual voids have grown to a sufficient size. Liou et al. (88) pointed out that the formation of void lattice is analogous to the alignment of precipitate plates on different planes to form a preferred, stable array. In the case of precipitate array, each precipitate plate creates an anisotropic field; whereas in the case of voids, it is only the anisotropy of the medium which allows a void lattice to form at all.

Finally it should be mentioned that J. Cahn (89) pointed out that the symmetry of the $\langle 1230 \rangle$ array is that of V_3Si . To see this clearly, the origin of the array shown in Fig. 21 should be taken at $\frac{1}{2}, \frac{1}{2}, 0$.

3.1.2 ELASTIC STABILIZATION OF THREE-DIMENSIONAL ARRAYS AGAINST OSTWALD RIPENING

3.1.2.a INTRODUCTION

There are several reported cases (90,91) where a very fine dispersion of a coherent ordered precipitate resists coarsening. This behaviour is shown for example in alloys of iron containing 5 to 9 atomic percent aluminum in which the ordered Fe_3Al phase has precipitated. Warlimont and Thomas (91) showed that the particle radius was less than 100 \AA and there was a precipitate density of 10^{17} cm^{-3} for an alloy with 15 atomic percent aluminum whose microstructure did not change detectably even after long annealing time.

Boyd and Nicholson (85,86) have measured coarsening rates and particle-size distribution, in Al-Cu alloys, using

the Wagner-Lifshitz-Slyozov theory (92,93) modified for the case of disc-shaped particles. They have found that the coarsening behaviour of θ'' agrees quantitatively and qualitatively with the theory, but coarsening behaviour of θ' is anomalous.

Ham et al (94) reported on the solidification, ageing behaviour and creep properties of the intermetallic compound $\text{Ni}_3(\text{Al}, \text{Ti})$, strengthened by a bimodal distribution of γ precipitates. They have found, when these alloys are solidified rapidly under planar interface conditions to give a uniformly supersaturated parent phase, and then aged, that no correlation of γ platelet length with ageing time exists for the resulting unimodal dispersion of platelets. They have presumed that the platelets give rise to tetragonal distortion and that the array is stabilized by elastic interaction.

3.1.2.1 CONDITIONS FOR STABILITY AGAINST OSTWALD RIPENING

To investigate the stability of a regular array against Ostwald ripening the variation of the elastic energy of a perfect array with small volume exchanges between neighbouring precipitates will be considered. To facilitate the rather detailed calculations of this section, it is assumed that apart from simple rotations all precipitates have the same environment.

The total energy of one precipitate can be expressed in a general form as:

$$E_1 = E_s + E_{1L} \quad (70)$$

where

$$E_s = E_{\text{self}} + E_{\text{surface}} \quad (71)$$

where E_{self} and E_{surface} are the strain and the surface energy of a disc-shaped precipitate, E_{1L} is the elastic interaction energy between the precipitate (1) and the whole lattice. E_s in eq. (70) is given for the equilibrium shape, as a consequence of the competition between the elastic and surface energies.

It is instructive to consider the interaction between precipitate (1) and any other precipitate in the array; if we label that precipitate (2), eq. (70) may be written in a slightly different form as:

$$E_1 = E_s + (E_{1L} - E_{12}) + E_{12} \quad (72)$$

Similarly, for the other precipitate (2);

$$E_2 = E_s + (E_{2L} - E_{12}) + E_{12} ; \quad E_{1L} = E_{2L} \quad (73)$$

where E_{12} is the interaction energy of the pair. We will next take δV_1 from precipitate (1) and δV_2 from precipitate (2); if $\delta V_1 = -\delta V_2$, matter will be exchanged between precipitate (1) and (2).

Expanding $E_1(V_1)$ about $V_1 = V_0$ one gets:

$$\begin{aligned}
\delta E_1 = & \left(\frac{\partial E_s}{\partial V} \right)_{V_0} \delta V_1 + \frac{1}{2} \left(\frac{\partial^2 E_s}{\partial V^2} \right)_{V_0} \delta V_1^2 + \dots \\
& + \left[\frac{\partial (E_{1L} - E_{12})}{\partial V} \right]_{V_0} \delta V_1 + \frac{1}{2} \left[\frac{\partial^2 (E_{1L} - E_{12})}{\partial V^2} \right]_{V_0} \delta V_1^2 + \dots \\
& + \left(\frac{\partial E_{12}}{\partial V} \right)_{V_0} \delta V_1 + \frac{1}{2} \left(\frac{\partial^2 E_{12}}{\partial V^2} \right)_{V_0} \delta V_1^2 + \dots \quad (74)
\end{aligned}$$

and a similar expression for δE_2 , at $V_2 = V_0'$.

The first condition for equilibrium is:

$$\frac{\partial (E_1 + E_2)}{\partial V} = 0 \quad (75)$$

It must be remembered that the exchange of volume between any two precipitates gives a general test of stability against coarsening; so we may have

$$\delta V_1 = -\delta V_2 = \delta V \quad .$$

Thus, for arrays in which $E_{1L} = E_{2L}$, i.e. arrays for which precipitates have equivalent environments,

$$\begin{aligned}
& \left\{ \left[\frac{\partial E_s}{\partial V} \right]_{V_0} - \left[\frac{\partial E_s}{\partial V} \right]_{V_0'} \right\} \delta V + \\
& + \left\{ \left[\frac{\partial (E_{1L} - E_{12})}{\partial V} \right]_{V_0} - \left[\frac{\partial (E_{1L} - E_{12})}{\partial V} \right]_{V_0'} \right\} \delta V + \\
& + \left\{ \left[\frac{\partial E_{12}}{\partial V} \right]_{V_0} - \left[\frac{\partial E_{12}}{\partial V} \right]_{V_0'} \right\} \delta V = 0 \quad (76)
\end{aligned}$$

This is only true at $V_0 = V_0'$; all precipitates must therefore have equal size for equilibrium.

The second condition for a stable equilibrium is:

$$\frac{\partial^2 (E_1 + E_2)}{\partial V^2} > 0 \quad (77)$$

or

$$\frac{\partial^2 E_s}{\partial V^2} + \frac{\partial^2 (E_{1L} - E_{12})}{\partial V^2} + \frac{\partial^2 E_{12}}{\partial V^2} > 0 \quad (78)$$

We will now take $V_1 = V_2 = V_0$, so that the condition for stability becomes

$$\left(\frac{\partial^2 E_s}{\partial V^2} + \frac{\partial^2 E_{1L}}{\partial V^2} \right)_{V_0} > 0 \quad (79)$$

It should be emphasized that this condition for stability includes volume exchange between any two precipitates in the array. Thus equation (79) is a stability condition based on the rational addition of an infinitesimal volume to one of the precipitates, although the fulfillment of equation (79) guarantees the stability of the array against the exchange of an infinitesimal volume between any two precipitates of the array.

In equation (79), the elastic self energy, E_{self} , which is a part of E_s , is a constant for a given volume fraction in the linear elastic approximation and does not depend on the relative positions of the precipitates. The surface energy, which is also a part of E_s , will always promote coarsening, so stability can be achieved only by elastic interac-

tions for which $\partial^2 E_{1L} / \partial V^2$ is large and positive.

3.1.1.2 ALGEBRAIC CONDITIONS FOR STABILITY

In order to establish the conditions of stable equilibrium in terms of the interfacial energy, elastic mismatch, volume fraction and spatial configuration, it is necessary to calculate or estimate the following quantities:

- elastic self energy
- interfacial energy
- equilibrium shape
- elastic interaction energy .

Elastic self energy and elastic interaction energy are already discussed in the first part of this section (see sections 3.1.1.2 through 3.1.1.5). We will here consider interfacial energy, equilibrium shape and stability of the $\langle 1230 \rangle$ array against coarsening, in turn.

3.1.2.2.a THE INTERFACIAL ENERGY

For a simple square plate-like precipitate the surface energy can then be written as:

$$E_{\text{surf.}} = 2\ell^2\gamma_{\ell} + 4\ell d\gamma_e \quad (80)$$

where ℓ is the side-length and d is the thickness of the precipitate, γ_{ℓ} is the surface energy of the habit plane interface, and γ_e is the edge surface energy.

3.1.2.2.b THE EQUILIBRIUM SHAPE

Accepting the dislocation loop model, and putting the expressions for E_{el} (eq. (67)) and E_{surf} (eq. (80)) in eq. (71) it becomes

$$E_s = \frac{1}{4} \frac{\mu \epsilon^2 V}{2(1-\nu)} S \ln\left(\frac{8}{\epsilon_S}\right) + 2\gamma_\ell V^{2/3} S^{-2/3} + 4\gamma_e V^{2/3} S^{1/3} \quad (81)$$

where $S = d/\ell$ is the aspect ratio and $V = \ell^2 d$, is the volume of the particle.

The elastic energy tends to "roll" the precipitates into thin plates. However, the effect of the surface energy is to prevent this elongation of the second-phase particles. The equilibrium shape can thus be obtained by minimizing E_s , eq. (81), at constant volume, or $\ell^2 d = \text{const.}$

Thus, we find

$$S = \frac{\gamma_\ell}{\gamma_e} - \beta \quad (82)$$

where

$$\beta = \frac{\mu V^{1/3}}{\gamma_e} \frac{3\epsilon^2 S^{5/3}}{32(1-\nu)} \ln\left(\frac{8}{\epsilon_S}\right) \quad (83)$$

is the correction term due to the elastic energy. The effect of the elastic energy is to reduce S , i.e. to act like a decreased γ_e .

For cases when the surface energy is large and the misfit small, $\gamma_e \beta / \gamma_\ell$ is a small number and can be neglected; one then obtains for the minimum E_s

$$E_s = 6V^{2/3}\gamma_{\text{eff}} \quad ; \quad \gamma_{\text{eff}} \approx (\gamma_i \cdot \gamma_e)^{1/3} \quad (84)$$

According to equation (79), the quantity of importance is the second derivative of E_{1L} with respect to volume. It is convenient to define the dimensionless number K which is a function only of volume fraction (f) and array-type (P).

$$K(f,P) = \frac{V_o}{\mu\epsilon^2} \left(\frac{d^2 E_{1L}}{dV^2} \right)_{V_o} \quad (85)$$

Here, V_o refers to the precipitate size corresponding to a given volume fraction and spacing. From equation (84) one gets

$$\frac{\partial^2 E_s}{\partial V^2} = -\frac{4}{3} \gamma_{\text{eff}} V_o^{-4/3} \quad (86)$$

With the help of equations (79), (85) and (86), it is now possible to give an improved condition for the stability of an array against coarsening

$$\frac{3}{4} \frac{\mu\epsilon^2 K(f,P) V_o^{1/3}}{\gamma_{\text{eff}}} > 1 \quad (87)$$

From these considerations it is clear that stability will be promoted by:

- low interfacial energy,
- large elastically-accommodated misfit,
- large or optimal value of $K(f,P)$.

3.1.2.3 NUMERICAL TEST OF THE STABILITY OF THE <1230> ARRAY AGAINST COARSENING

In section 3.1.1.5 it was shown that the <1230> is mechanically stable, i.e. with respect to displacement from the ideal lattice sites. Here, we are interested in the stability of a periodic distribution of inclusions with respect to volume exchange, as might be accomplished by volume diffusion, between precipitates.

The situation with regard to stability with respect to volume exchange is somewhat more complex. Consider first the interaction between a single pair of precipitates, E_{12} . Since $E_{12} \propto V_1 V_2$, E_{12} is stationary when $V_1 = V_2$, other conditions being equal. This means that the particles tend to have the same dimensions if E_{12} is negative. If the elastic interaction is repulsive E_{12} is positive, then the elastic interaction will tend to promote the diffusional growth of one precipitate at the expense of the other. The energy change for small volume exchanges between members of an isolated pair of precipitates for different distances between them, in the face-face and edge-face configuration is shown in Figs. 35 and 36. (The perturbations were carried out at fixed aspect ratios.)

Fig. 35 shows that all volume exchanges decrease the elastic interaction energy. This might be expected from Fig. 19, which shows that E_{12} in the face-face configuration is always positive. However, Fig. 36 shows that volume ex-

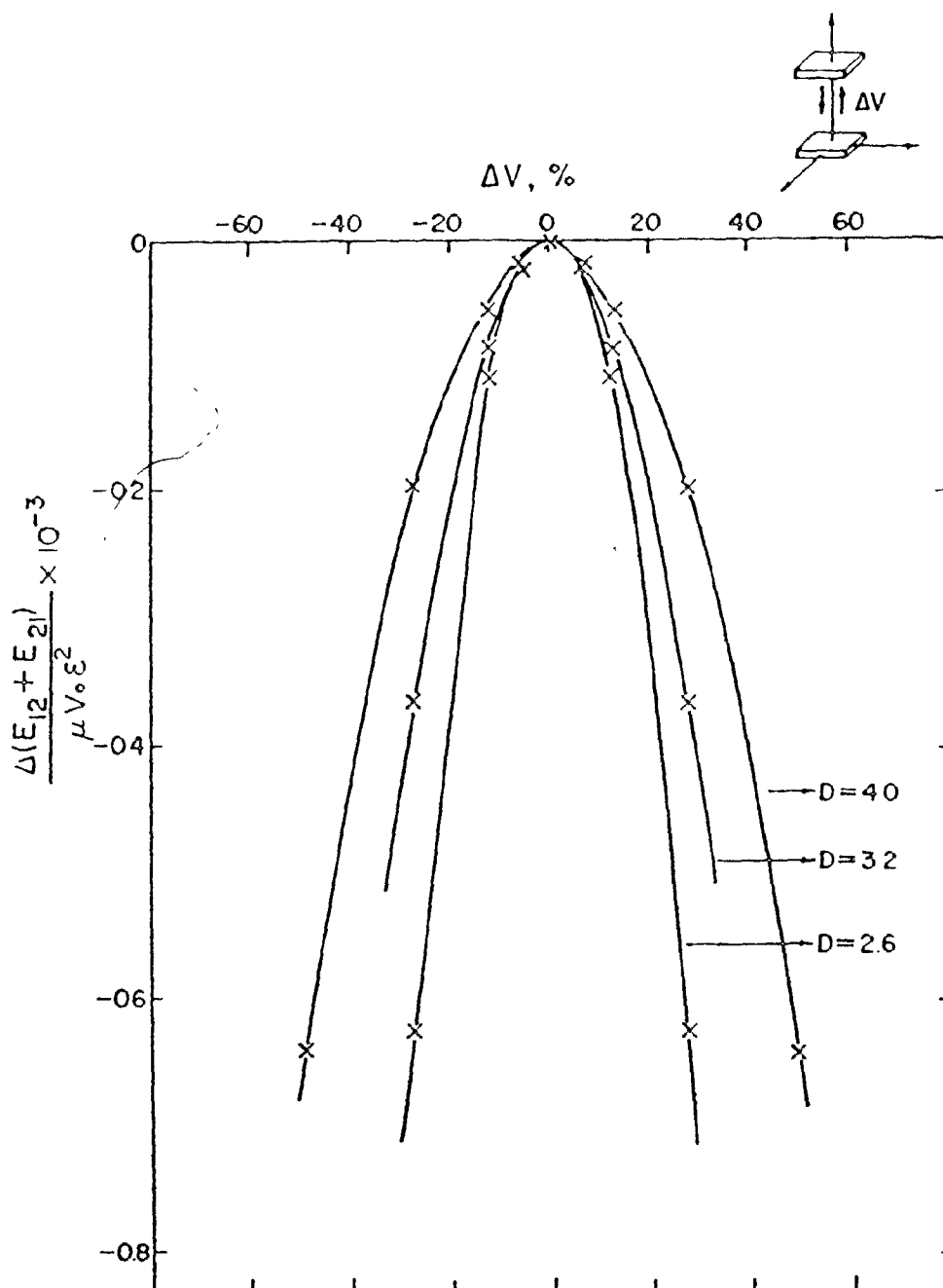


Fig. 35^c The change of elastic energy due to volume exchange between a pair of 'large' precipitates in the face-face configuration. The distance between the precipitates is 2.6, 3.2 and 4.0 times the plate edge-length.

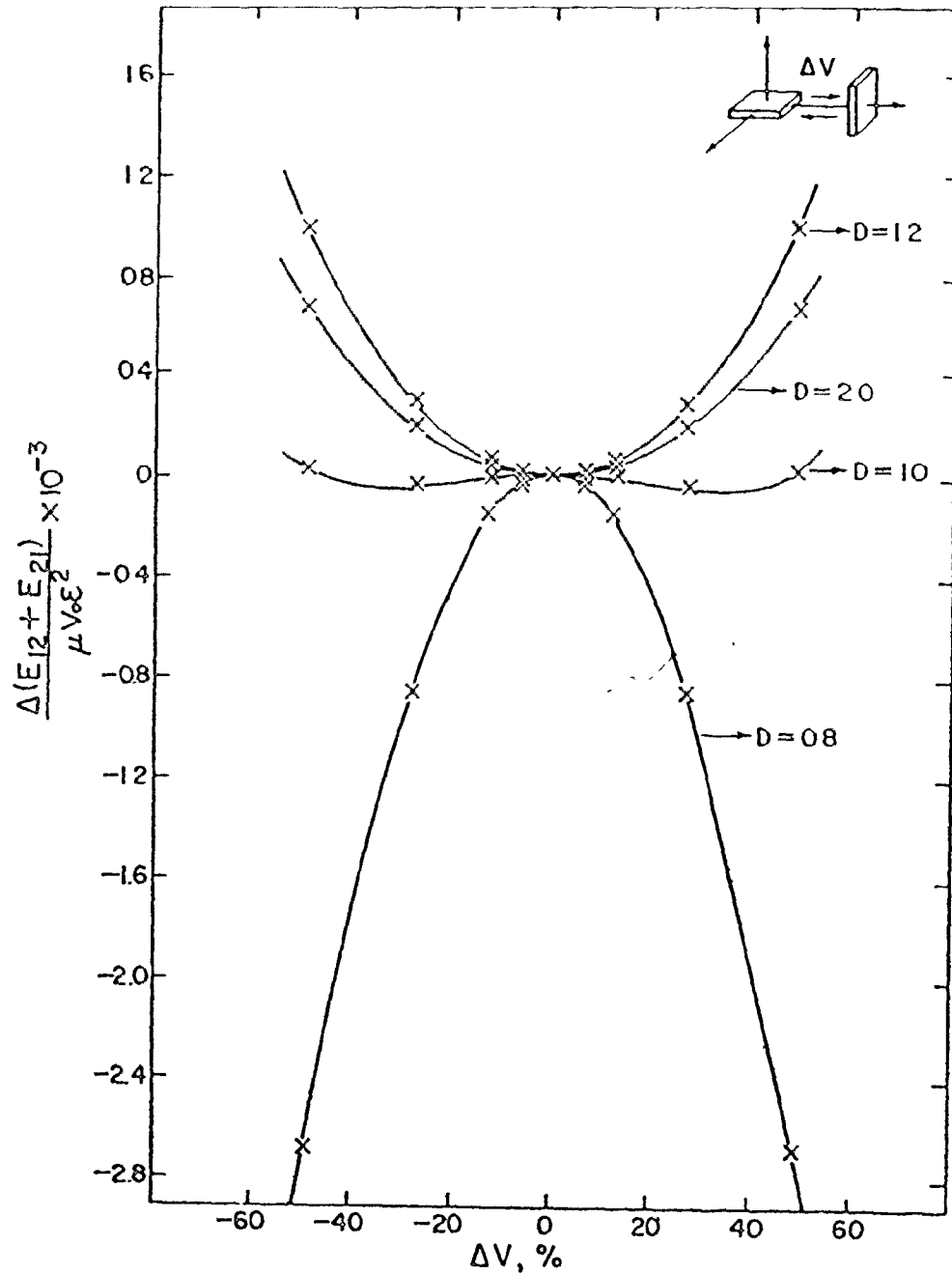


Fig. 36 The change of elastic energy due to volume exchanges between a pair of 'large' precipitates in the edge-face configuration. The distance between the particles is 0.8, 1.0, 1.2 and 2.0 times the plate edge-length.

changes decrease the elastic interaction energy for small separations, but increases it for larger separations. Again this is consistent with Fig. 22, where E_{12} for the edge-face pair changes sign with increasing separation.

Thus, the elastic interaction energy appears as a factor which stabilizes equal dimensions of the particles in a pair only if this interaction is attractive. This point has also been made by Khachatryan and Shatalov (6).

From the above considerations it might then be concluded that the $\langle 1230 \rangle$ lattice is stable with respect to volume transfer in the "attractive" direction but not in the "repulsive" direction; this conclusion, however, would be reached without considering the possible stabilizing influence of the lattice against volume transport in the latter direction. In order to investigate the stability of the unstable pair in the strain field of the lattice, the following calculations were done:

The total interaction energies per plate for equal size precipitates surrounded by an interaction sphere of radius of 7.5 units spaced at different distances were calculated; and the energies of the perfect lattice ($\Delta V = 0$) were calculated and compared with those of the perturbed ones with the same number and volume of precipitates.

The results of these calculations are shown in Fig. 37. For interparticle spacing of 0.8 units or less, it is apparent that volume transfer in the "repulsive" direction leads to

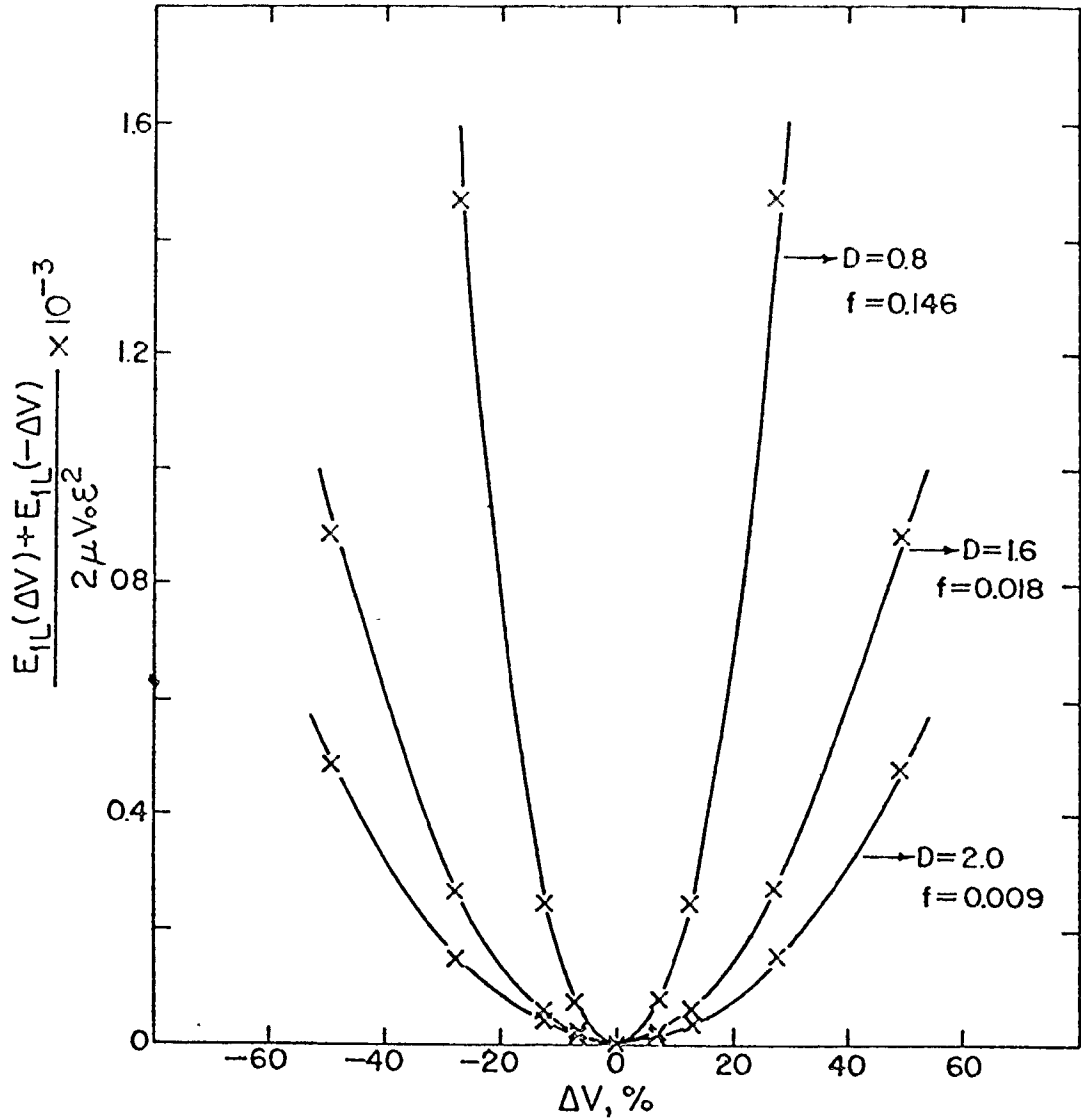


Fig. 37

The elastic energy change per plate of the $\langle 1230 \rangle$ array due to volume exchanges between a pair of 'large' precipitates in the edge-face configuration. The distance between the first neighbours is 0.8, 1.6 and 2.0 plate edge-lengths. The radius of the sphere is 6.4 times the plate edge-length. The ordinate represents the even part of the variation of E_{1L} with V_1 and so clearly shows the positive curvature and the array stability.

an increase in the total energy of the lattice, in spite of the strong positive interaction energy of closely spaced pairs of precipitates in the edge-face configuration. On the basis of this result it is concluded that the lattice has a stabilizing effect with respect to this type of volume exchange.

Finally the behaviour of $K(f,p)$ was investigated, using essentially the methods of the previous section. The resulting curve, which is specific to the $\langle 1230 \rangle$ array, is shown in Fig. 38. It is particularly interesting to note that K increases continuously (indicating increased stability of the array of equal sized precipitates) as the interparticle spacing is diminished, and that the behaviour of K with separation does not reflect the minimum in the interaction energy-separation curve (Fig. 23).

3.1.2.4 NUMERICAL TEST OF THE STABILITY OF ARRAYS OF PRECIPITATES AGAINST CO-ORDINATED DIFFUSION

In a discussion of the published form of the preceding numerical results, Aubauer (95) claimed that co-ordinated volume exchange between several precipitates in the array may not lead to metastability. He made two points: (i) although consideration of energy changes caused by exchange of infinitesimal volume between any two precipitates in the array demonstrates that the array is in some sense metastable, the array may not be metastable against co-ordinated diffusion;

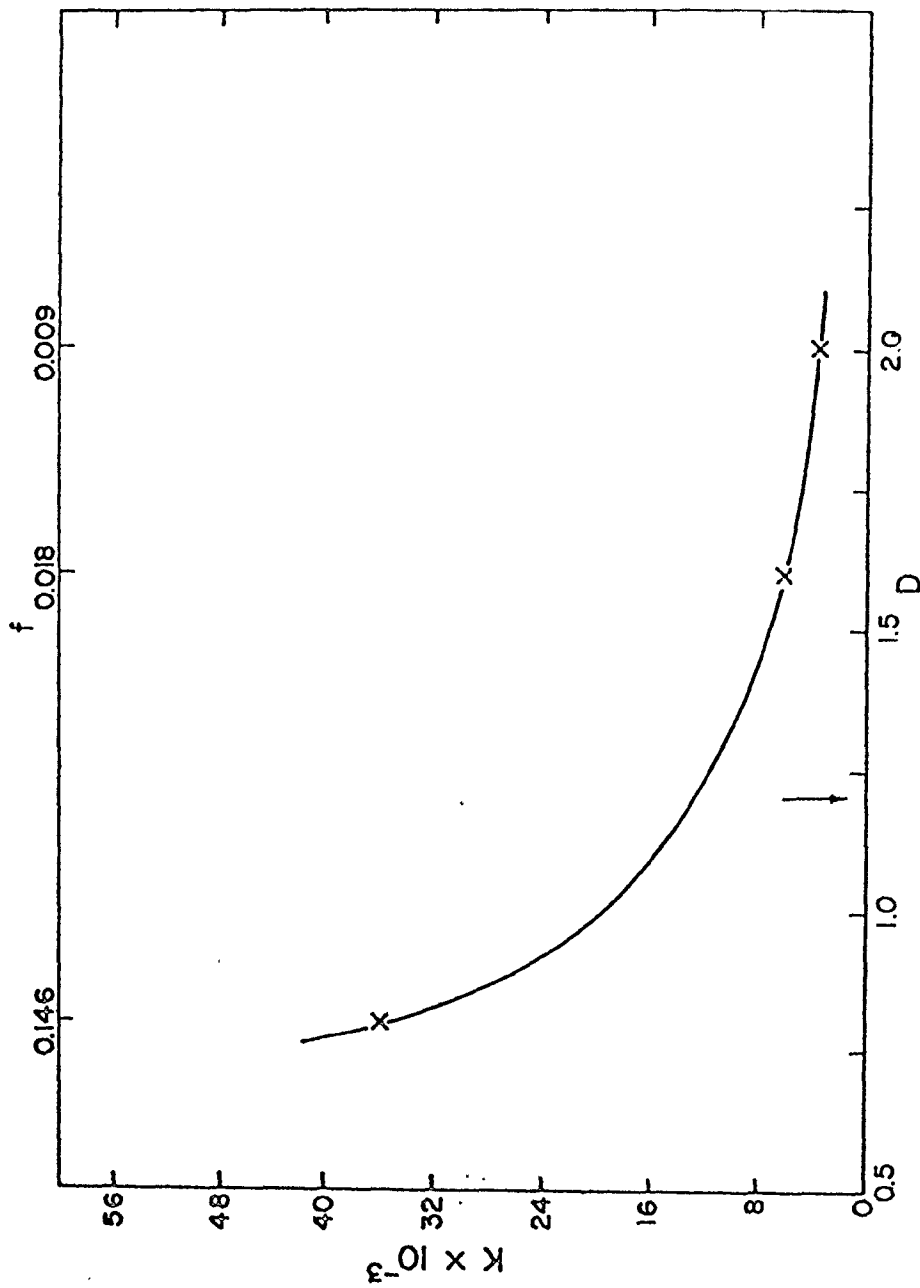


Fig. 38 The variation of $K(f, p)$ function vs the volume fraction f (or D , the distance between the precipitates). The arrow indicates the D value at which the interaction energy is a minimum; see Fig. 23. The aspect ratio l/d is kept constant at a value of 10.

in particular, Aubauer claimed that simultaneous exchange between several precipitates as indicated in his Fig. 1 (see the scheme in Fig. 40) results in a continuous lowering of the energy so there is no metastability; and (ii) Aubauer pointed out (correctly) that the existence of metastability is no guarantee of the existence of a kinetic process which leads to the formation of a regular array of precipitates.

Regarding the first point, a co-ordinated diffusion process which obviously leads to a continuous lowering of the energy is the simultaneous growth of all precipitates together with an increase in their separation to keep the volume fraction constant, a process which produces a reduction in interfacial energy with no change in elastic energy. This process of course involves an infinite number of precipitates in an infinite medium. However, Aubauer claimed that co-ordinated processes involving a finite number of precipitates also exist. The mathematics underlying this claim is incomplete because the interaction energy between a precipitate and the rest of the array involves second-order terms in ΔV not considered by Aubauer. In particular, the argument produced by Aubauer would suggest that exchange between precipitates C3 and B4 alone would continuously lower the energy; i.e. for these two, the interaction energy is positive and both the interface and the elastic energy are reduced by such an exchange. However, the calculations of

the previous section show that the presence of the array stabilizes these two precipitates; second-order terms enter the calculation which are not present in the equations of Aubauer. Still, as Aubauer suggested, the array may be unstable to co-ordinated exchanges of volume between more than two precipitates. This point was tested by using the computer program to investigate exchange between infinite lines of nearest-neighbour precipitates in the [010] direction. Some results of these calculations are shown in Fig. 39. The full line represents the change of elastic interaction energy due to co-ordinated volume exchange between nearest neighbour precipitates in the [010] direction; corresponding to the $\langle 1230 \rangle$ array. The broken line represents the volume exchange between the pair labelled as (2) and (5) in Fig. 39. The cut-off radius was 7.5 times the plate edge-length, which includes about 1000 particles, around the pairs subjected to the simultaneous volume exchange. Fig. 37 clearly shows that the array is stable against this perturbation.

The specific exchange proposed by Aubauer, which involves third nearest neighbours was also tested, and the array again found to be stable, Fig. 40.

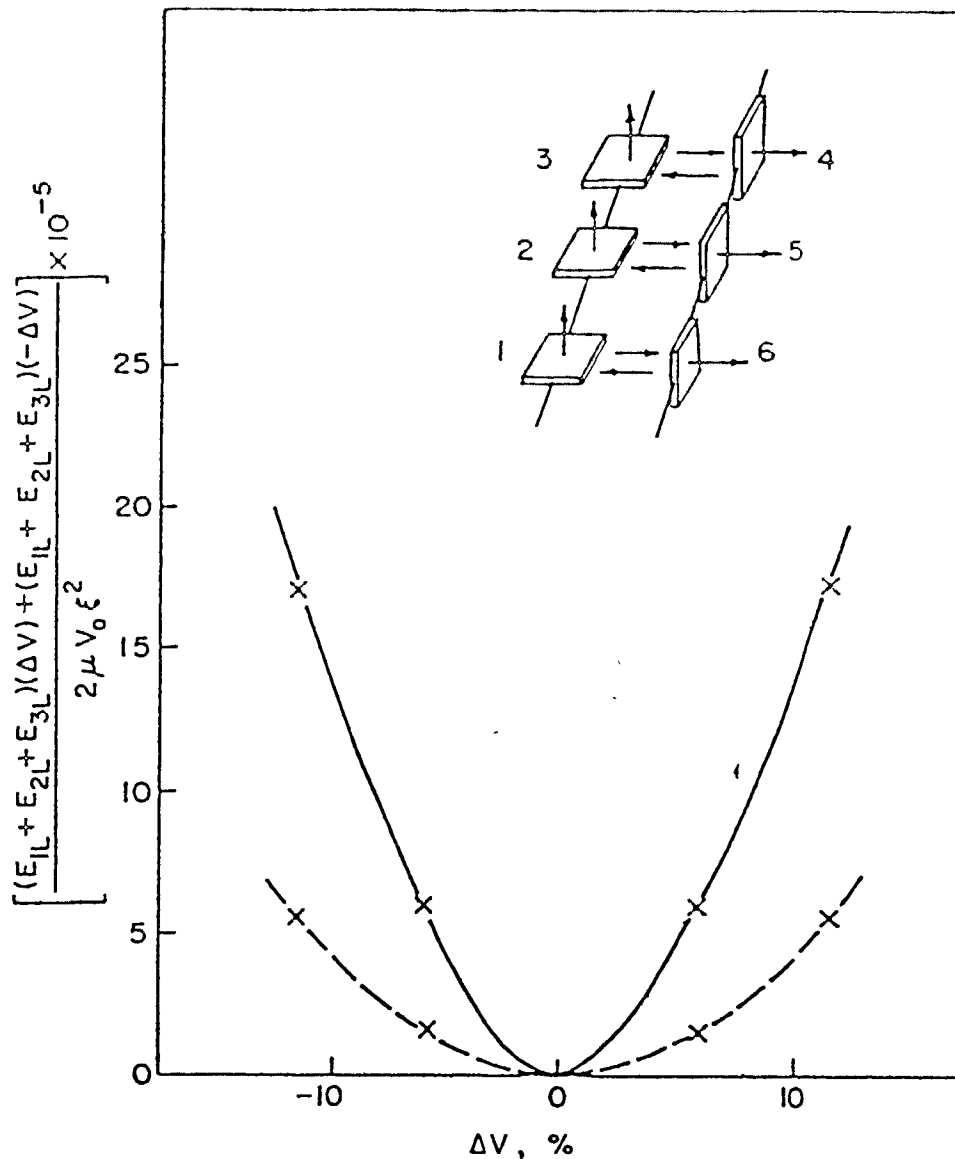


Fig. 39 The elastic energy change of the $\langle 1230 \rangle$ array due to co-ordinated volume exchanges among the nearest neighbours in the $[010]$ direction (full line). The broken line represents the volume exchange between the single pair labelled (2) and (5). The distance between the first neighbours is 1.5 plate edge-lengths, and the cut-off radius of the sphere is 7.5 times the plate edge-length. The ordinate represents the even part of the variation of E with V and so clearly shows the positive curvature out of the stability of the array.

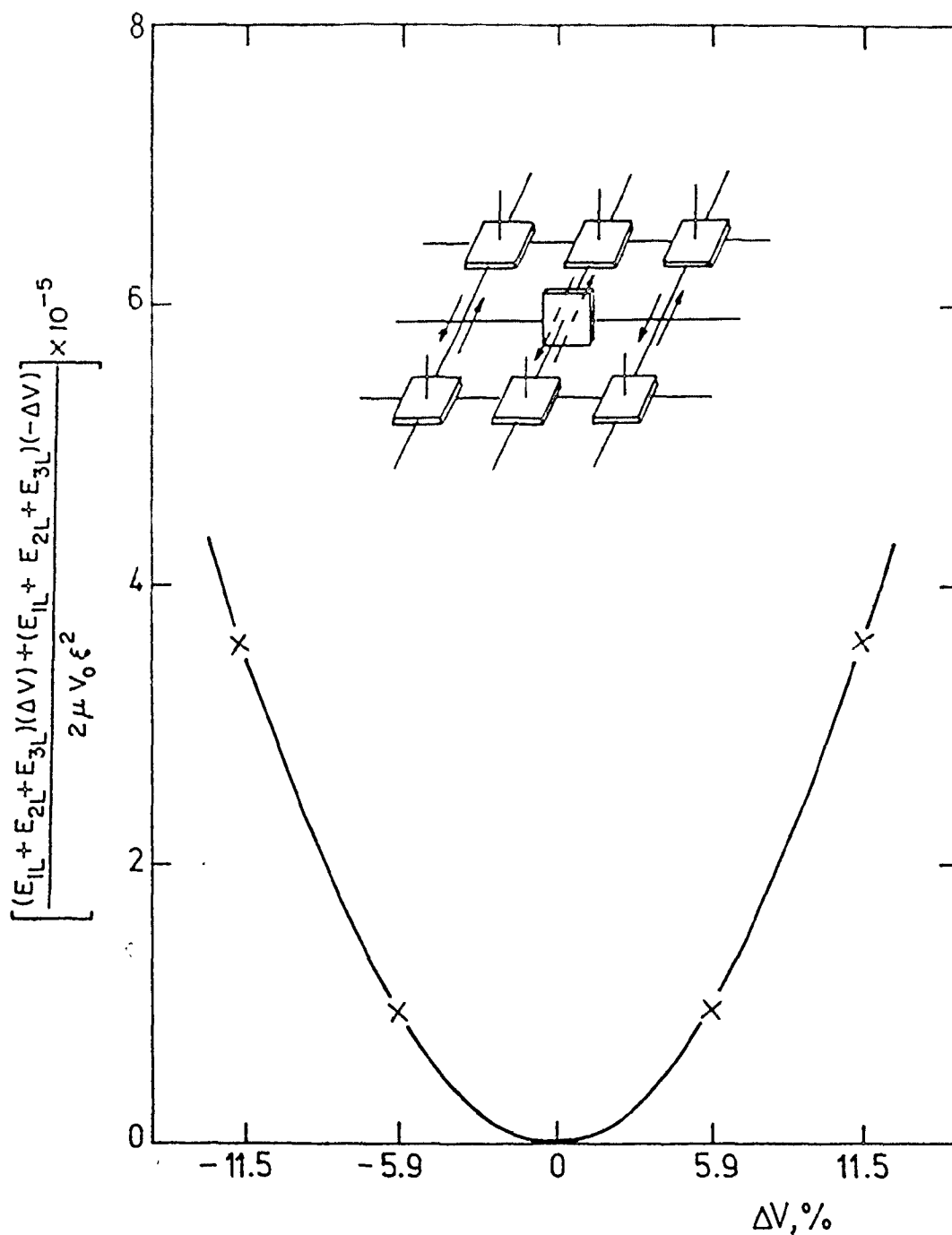


Fig. 40 The elastic energy change of the $\langle 1230 \rangle$ array due to co-ordinated volume exchanges among the third nearest neighbours in the $[100]$ direction. The distance between the first neighbours is 1.5 plate edge-lengths, and the cut-off-radius of the sphere is 7.5 times the plate edge-length. The ordinate represents the even part of the variation of E with V and clearly shows the positive curvature and the stability of the array.

3.1.2.5 DISCUSSION

The question of the stability of an array of precipitates against coarsening has rather far-reaching implications, both for the understanding of microstructure and as a possible basis for the design of alloys. We will begin by discussing those general factors that determine whether a particular system is likely to show array-forming tendencies, and whether such arrays are likely to be stable against coarsening.

The kinetics of initial coarsening of precipitates under conditions of strong elastic interaction will not be considered. It is assumed, rather, that the effects of elastic interaction during nucleation and initial coarsening of precipitate groups will lead to the selection of a particular type of array of equal-size inclusions, provided that the elastic strain field, volume fraction, and aspect ratio of the included phases is such that the interaction energy of the array is large and negative. (In the case of the $\langle 1230 \rangle$ array, as already discussed, this means an overall composition corresponding to a near-neighbour separation of about 1.2 precipitate diameters. Other arrays, which emphasize different kinds of near-neighbour interactions, may well be stable at different volume fractions.) It is expected that mechanical stability is also a prerequisite for the formation of an array.

Once an array has been selected, its stability with respect to coarsening must be considered in the light of the types of constraints presumed present when the system is perturbed. To illustrate this point, note that the total energy of an array of equal sized precipitates, as a function of precipitate size, for given volume fraction, shows no indication of metastability. Such a plot simply reflects the expected decrease of surface free energy and the constancy of all volume free energy terms, i.e. chemical and elastic energy with increasing particle size. It is only when one considers that no mechanism exists for continuously increasing the scale of the array that the need for a perturbation analysis becomes evident, and a form of metastability is found.

So far, the only known process which does not show metastability is the "infinite homogeneous coarsening process" referred to above. Such a process seems to be physically quite impossible; indeed any other co-ordinated diffusion involving large numbers of precipitates must be extremely slow. Such processes rely upon simultaneous fluctuations; let the probability per second of one fluctuation occurring be v - a small number. Then if N precipitates are involved in specified simultaneous fluctuations, the probability is v^N , which becomes vanishingly small for large N .

Similarly, it is found that stability against coarsening, as indexed by $K(f,P)$, may exist for an array whose total interaction energy is positive (e.g. the $\langle 1230 \rangle$ array at small interparticle spacing). If such an array could be

formed, for example by manipulation of the temperature and pressure during ageing, then the present analysis indicates that it would indeed be metastable against coarsening. As already discussed, the array characteristics reflect those of the dominant near-neighbour relation, we might expect that an array will form which emphasizes that near-neighbour configuration.

From a comparison of Figs. 22 and 23 we see that the minimum occurs at nearly the same separation in both cases, suggesting that the main characteristics of the full array are dictated by those of the pair. It is, however, in the assessment of stability against coarsening that the characteristics of the dominant pair and the full array are in sharp contrast. This is shown in Figs. 35 and 37, where the stabilizing effect of the array on a repulsive pair is evident. Similarly, a series of pair stability calculations (Fig. 36) implied that the array should become unstable with respect to volume transfer when the pair separation becomes small; this was later refuted when the effect of the full array on the perturbed pair was evaluated, (Fig. 38). It is therefore clear that the important properties of a particular type of array are accessible only through rather extensive calculations; we believe that the level of approximation used in the present calculations is adequate for the broad understanding of the behaviour of these arrays.

For the $\langle 1230 \rangle$ array, taking an aspect ratio $l/d = 10$,

Fig. 38 shows that the quantity KD^3 is approximately constant and equal to 2×10^{-2} . Then the stability condition of equation (87) becomes

$$\frac{\mu \epsilon^2 \ell f}{\gamma_{\text{eff}}} \times 0.12 \leq 1 . \quad (88)$$

This is to be compared with the crude estimate given by Brown et al. (9); the more accurate estimate given here differs only in the numerical factor; it is 0.12 rather than 0.2 in the earlier estimate. Many examples, including "tweed" structures in Cu-Be and θ' precipitates in Al-Cu have dispersions for which equation (88) is satisfied, or nearly satisfied, and it may be concluded that the array-forming tendencies of certain plate-line inclusions have a profound influence on the development and stability of microstructure. A recent study in steels (35,77) shows that the effects are not confined to non-ferrous alloys.

Finally, regarding the existence of a kinetic process which leads to the formation of a regular array of precipitates, there is of course no theoretical guarantee that kinetic routes exist which select a particular type of array. It is assumed that in competitive growth favourably placed neighbours prosper at the expense of unfavourably placed ones, and that this will lead to stable 'elastically-locked' arrays. This remains to be proven; however, the experimental evidence

strongly suggests that such arrays do form, particularly in interstitial alloys or alloys with very large misfit where "tweed" structures are a common observation. More experimental work on the kinetics of coarsening in these systems will be of great interest.

3.2 AUTOCATALYTIC NUCLEATION AND ELASTIC STABILIZATION OF LINEAR ARRAYS OF PLATE-SHAPED PRECIPITATES

3.2.a INTRODUCTION

Autocatalytic nucleation, the process whereby one precipitate of a daughter phase catalyses the formation of another, is a well documented phenomenon in martensite transformations; the concept has received less attention in diffusional transformation systems, although the work of Lorimer (96), and Aaronson (97) clearly deserves mention. Lorimer conjectured that the strain field of the θ' phase in Al-Cu alloys could cause the spreading of colonies by an autocatalytic process, in which successive new plates were nucleated in the stress and diffusion fields of existing ones. Aaronson found that proeutectoid ferrite sometimes forms on existing ferrite crystals in steel and termed the effect "sympathetic nucleation". Indeed, the phenomenon may be more widespread than is commonly supposed: it is possible for example that the "repeated subunit" morphology of Bainite colonies rests on the autocatalytic nucleation of the individual units.

In this section the evidence for the autocatalytic

process in Al-3.0 % Cu will be examined and the stability against growth of stacks of θ' precipitates assessed. The precipitate grows as thin plates on $\{001\}$ planes in the aluminum rich (α) matrix, so that $(001)_{\theta'}$ planes are parallel to $\{001\}$ planes. The equilibrium ratio is thought to be about 40 (98).

The misfit is such that the broad faces are completely coherent at lower ageing temperatures, and may contain widely-spaced misfit dislocations at higher ageing temperatures (98).

Aaronson and Laird (99) demonstrated that the strain fields of the θ' plates are not entirely relieved when the plates become incoherent. They showed that the diffraction contrast is similar to that of a prismatic dislocation loop, with Burgers vector parallel to the plate normal, $b = n(001)_{\theta'}$.

It is clear however that a high elastic misfit obtains at the nucleation stage so that θ' plate nucleates first on dislocations, and, probably, in the stress fields of existing plates. Headly and Hren (100) have recently shown that the nucleation of θ' often occurs (during the quench from the solution treatment temperature) on climbing dislocations.

Lorimer (96) had earlier proposed that subsequent nucleation and growth may occur in the autocatalytic fashion, such that the new θ' particle may be nucleated, essentially homogeneously, under the influence of the elastic stress-field of the θ' particles already present.

The fact that quite a small stress field can have a

large effect on θ' formation has been demonstrated by Nakada et al. (101) and Hosford and Agrawal (102). Recently, Stobbs and Purdy (103) observed that, in specimens aged above θ'' solvus line, the most striking feature, (for early stages of development) is the presence of inclined stacks of parallel θ' plates. They too suggested that after the heterogeneous nucleation of one platelet, many others could be formed in this first precipitate's environment, by successive nucleation and growth in their respective stress and diffusion fields.

In preceding sections it was proposed (82) (see sections 3.1 to 3.1.5) that elastically stabilized three-dimensional arrays can resist coarsening. Here the suggestion is put forward that autocatalytic nucleation may develop precipitate arrays of 1 and 2 dimensional character which may also be resistant to growth and/or coarsening.

This section is divided into two parts: one treats nucleation of stacks and their morphology and the second deals with the stabilization against growth of precipitates within the stacks.

3.2.1 NUCLEATION AND MORPHOLOGY OF STACKS

3.2.1.a RESULTS

Observations were made on specimens aged at 240°C, i.e. above θ' solvus line, so that θ' precipitates formed directly from supersaturated solid solution. Samples were aged for relatively short times so that the microstructure was in an early stage of development.

Figs. (41), 42(a)-(b) and 43(a)-(d) show characteristic microstructures of the specimens aged 1 and 3 h at 240°C. At this stage of the transformation, the microstructure consists mainly of inclined stacks of parallel θ' plates, as shown in Figs. (41) and 42(a)-(b) and of arrays containing more than one variant, Fig. 43(a)-(d).

The microstructure is however very inhomogeneous; it will be shown later that the regions between stacks are supersaturated.

Fig. 41 represents a part of one "array" of the total length more than 20 μm , which is composed of many small parallel stacks in which nearly all of the precipitates have the same habit. Fig. 42(a)-(b) also represent inclined stacks of parallel θ' plates, but here the stacks are longer and subtend a much smaller angle with $\{100\}$ habit plane (see also Fig. 44(c)).

In contrast, the precipitates in Fig. 43(a)-(d) are non-parallel, corresponding to two or three $\{100\}$ variants. The same is true of the stacks shown in Fig. 44(a)-(d) but here we have different proportions of the respective habit plane variants.

It is interesting to note that neighbouring precipitates are oriented such that the edge of one often confronts the face of the other (Figs 43 and 44). We will see later, that this configuration is very stable. The θ' precipitates shown in Figs. 41 and 42 are mainly in parallel orientation but in

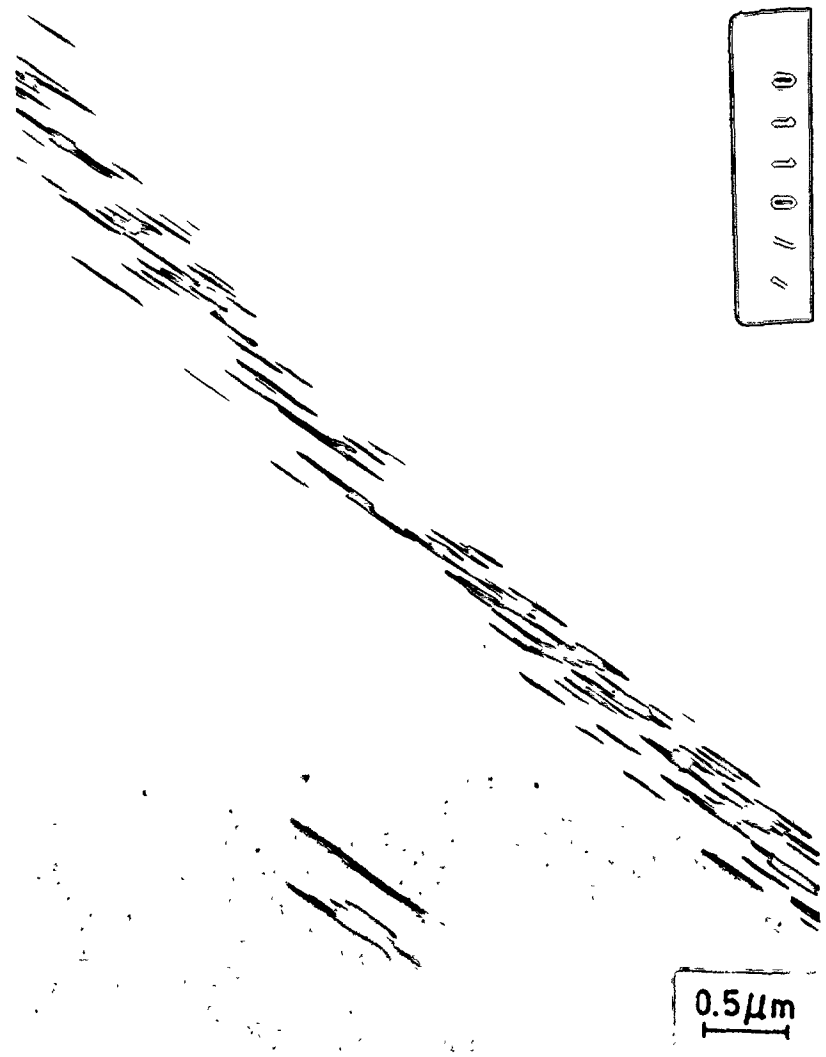


Fig. 41 Al-3% Cu crystal with (001) orientation, solution-treated and aged 1 hour at 240°C. Bright field conditions show inclined stacks of parallel θ' particles, containing only one {100} variant (24750 \times).

Fig. 42 Bright field micrographs of Al-3% Cu crystal with (001) orientation, solution-treated and aged 1 hour at 240°C, show inclined stacks of parallel θ' particles. The inclination angle with {100} habit plane is much smaller than that of Fig. 41. (a) 53250 \times ; (b) 33000 \times .

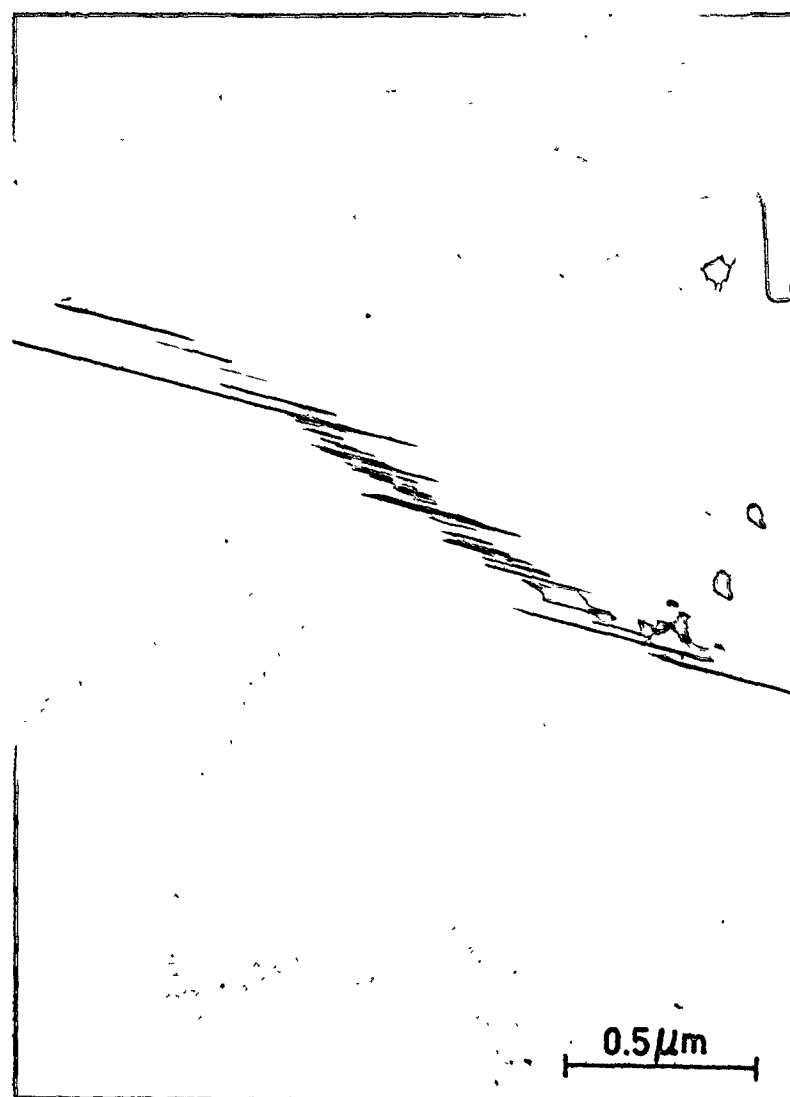


Fig. 42 (a)

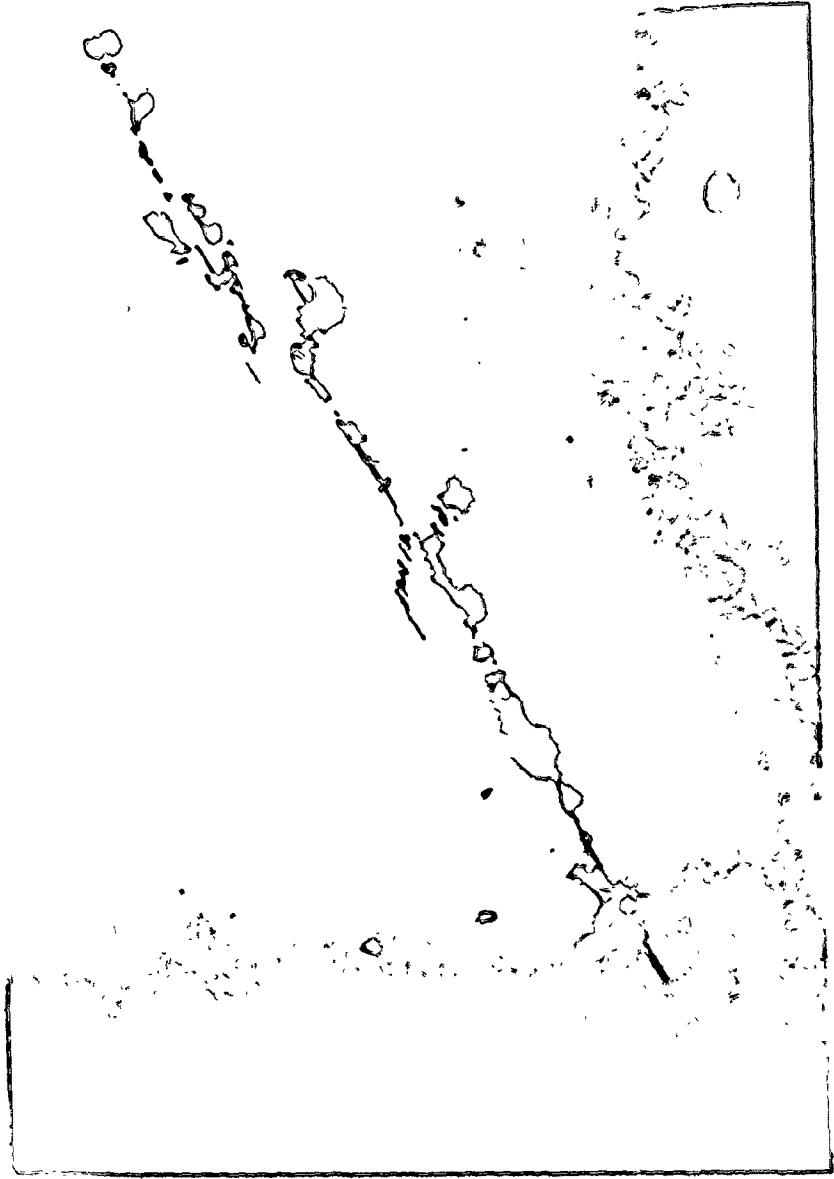


Fig. 42 (b)

Fig. 43 Al-3% Cu crystal with (001) orientation, solution-treated and aged 1-3 hours at 240°C. This series of micrographs shows non-parallel stacks containing more than one {001} variant. (a) and (b) contain two {100} variants and (c) and (d) contain three {100} variants. Note much smaller θ' particles between larger θ' plates, and also larger θ' particles on the ends of the stacks.
(a) aged 3 hours, 12450 \times , (b) aged 1 hour; 25000 \times ,
(c) aged 1 hour, 55000 \times , (d) aged 1 hour, 41250 \times .

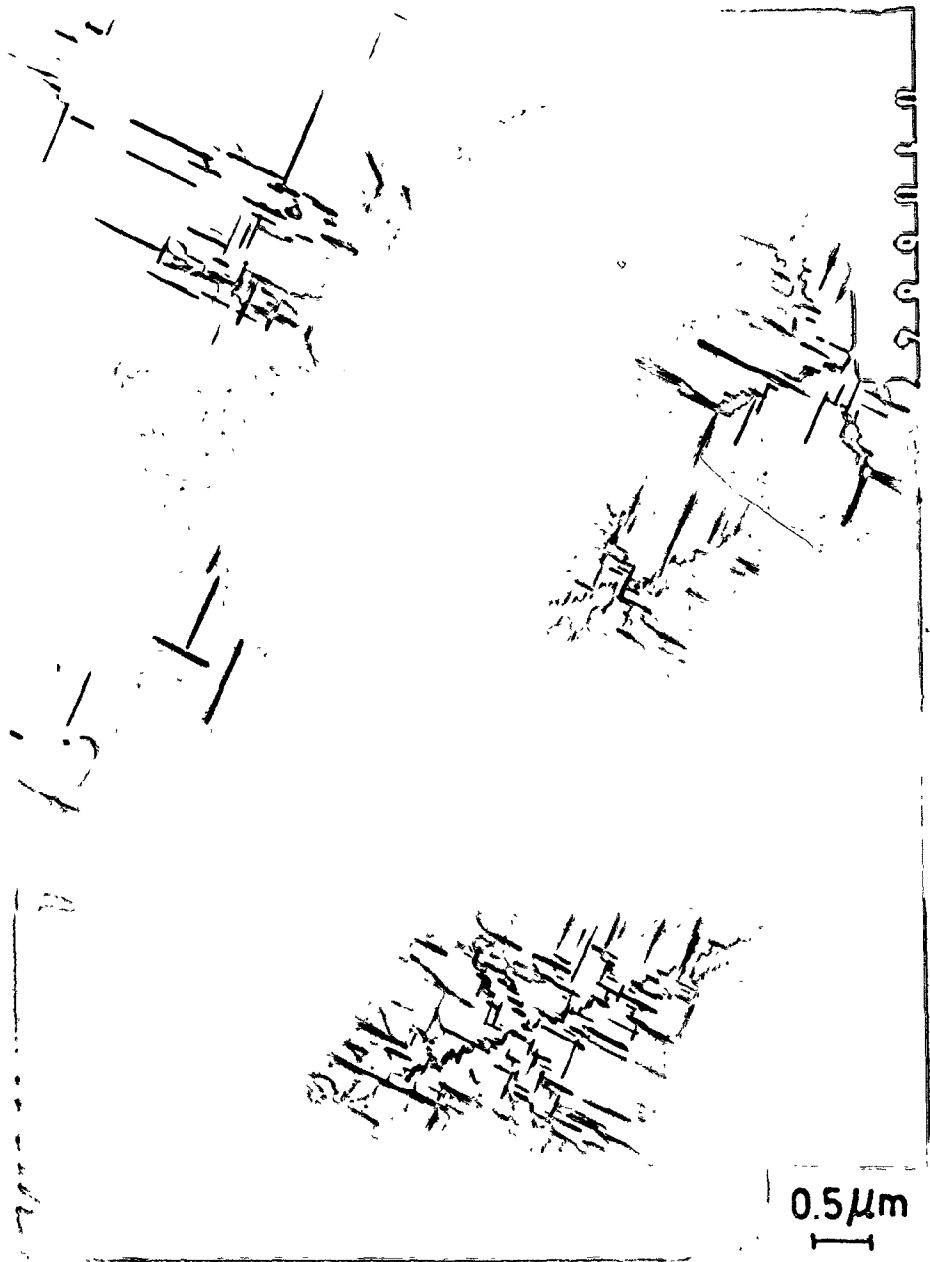


Fig. 43 (a)

11/19

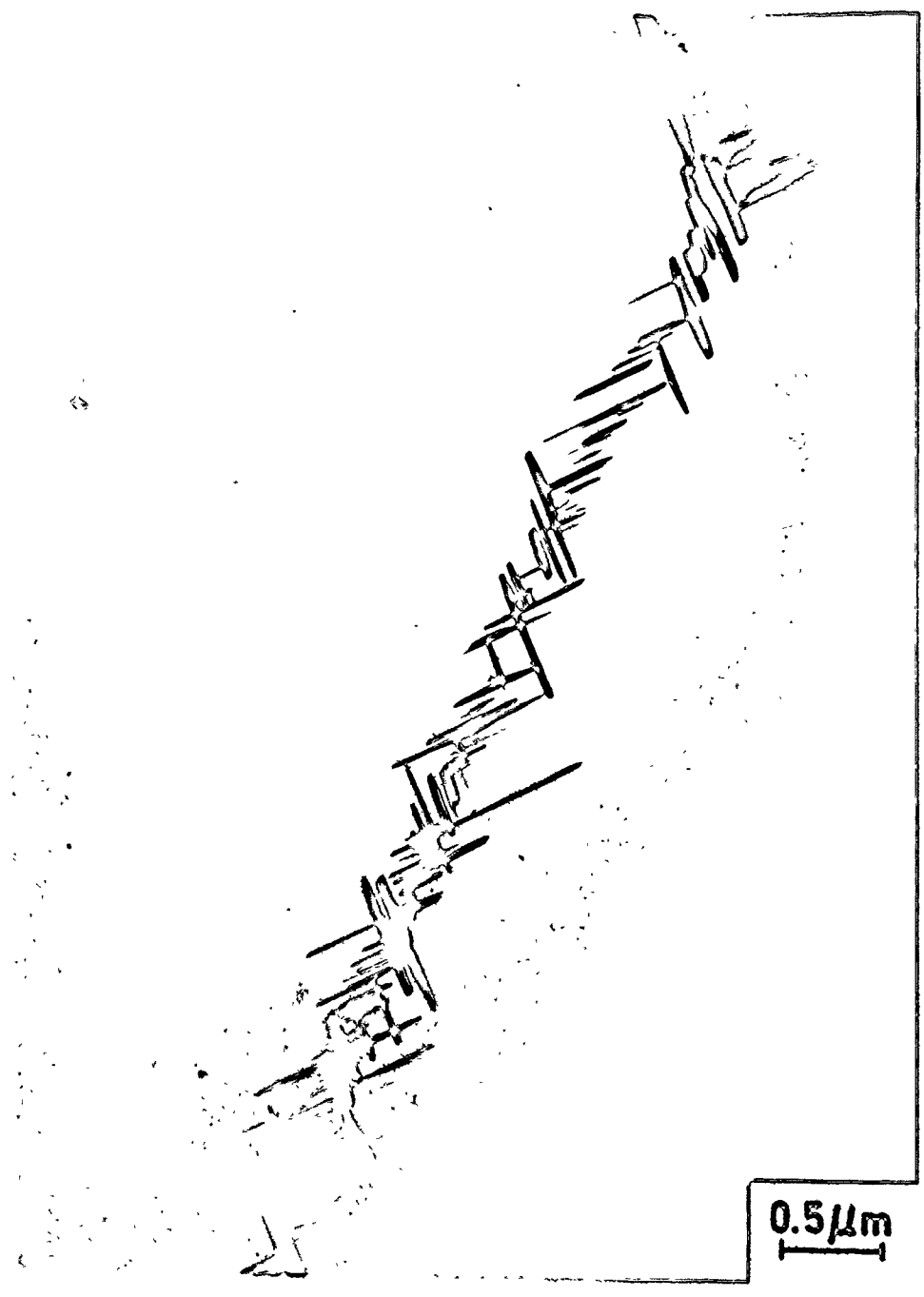


Fig. 43 (b)

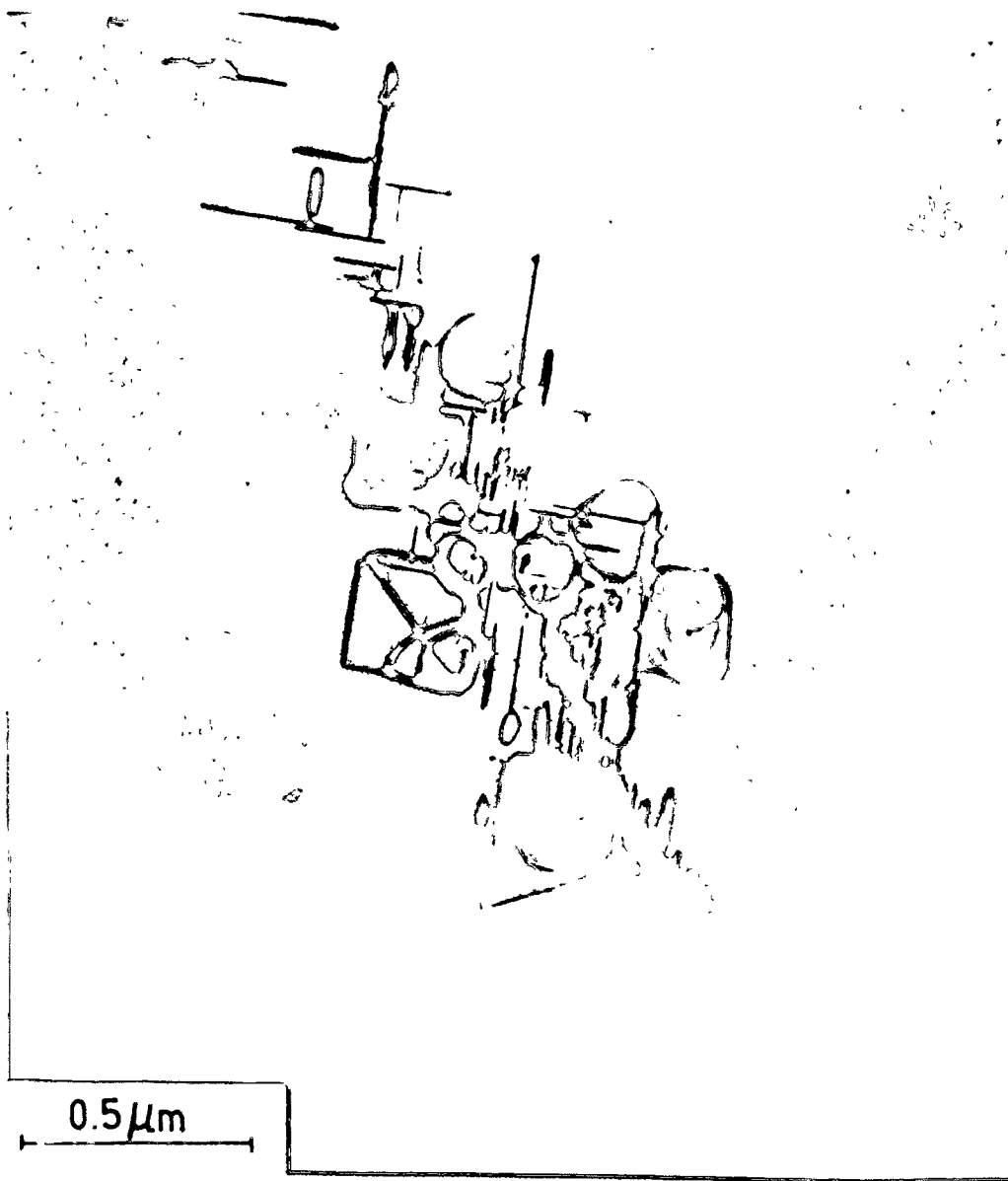


Fig. 43 (c)

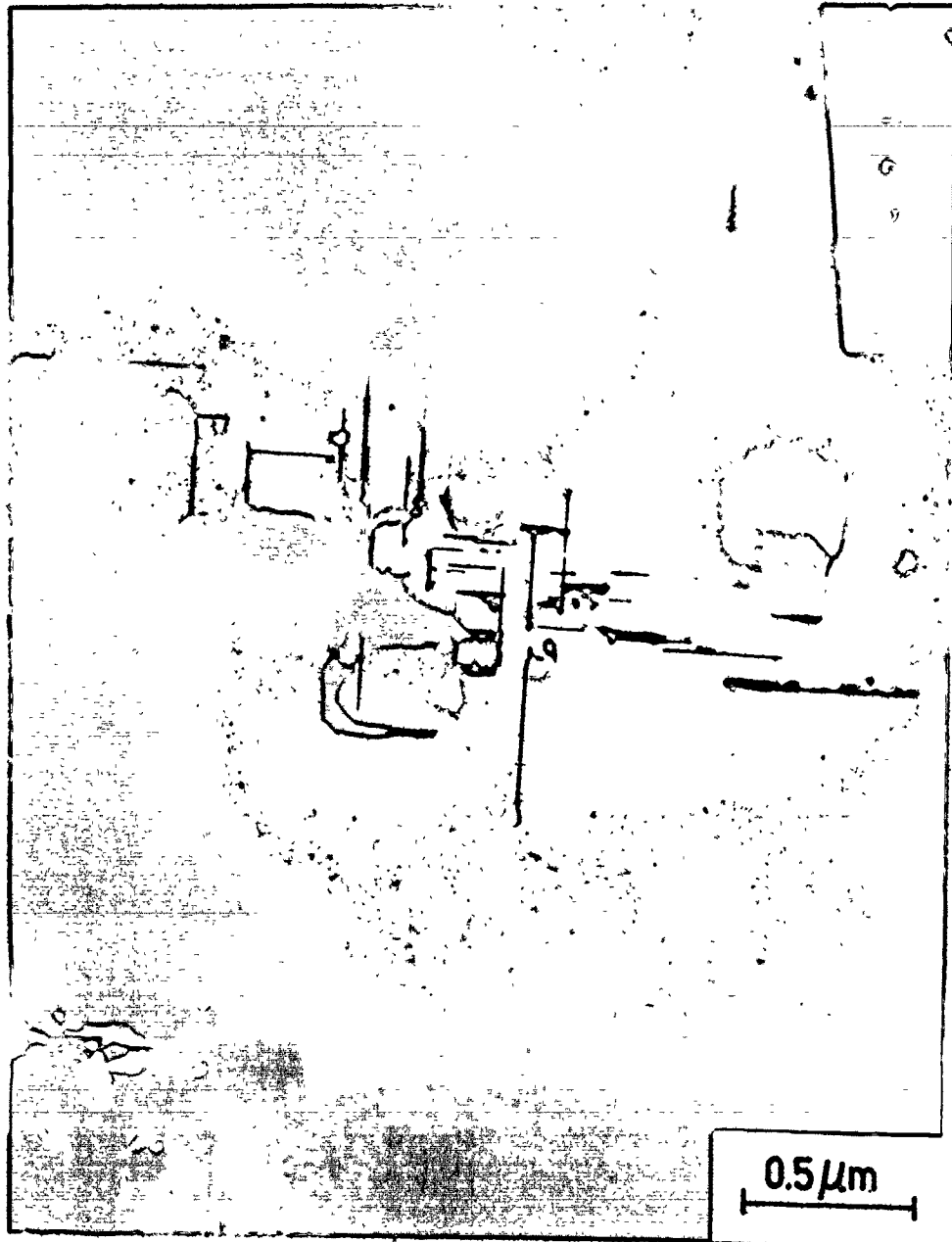


Fig. 43 (d)

Fig. 44 A series of micrographs similar to Fig. 43 but with different proportions of the respective habit plane variants. Note, again, smaller θ' precipitates between larger θ' particles. (a) aged 3 hours at 240°C; 41250 \times (b) aged 1 hour at 240°C; 14250 \times (c) aged 3 hours at 240°C; 65250 \times (d) aged 9 hours at 240°C; 41250 \times .

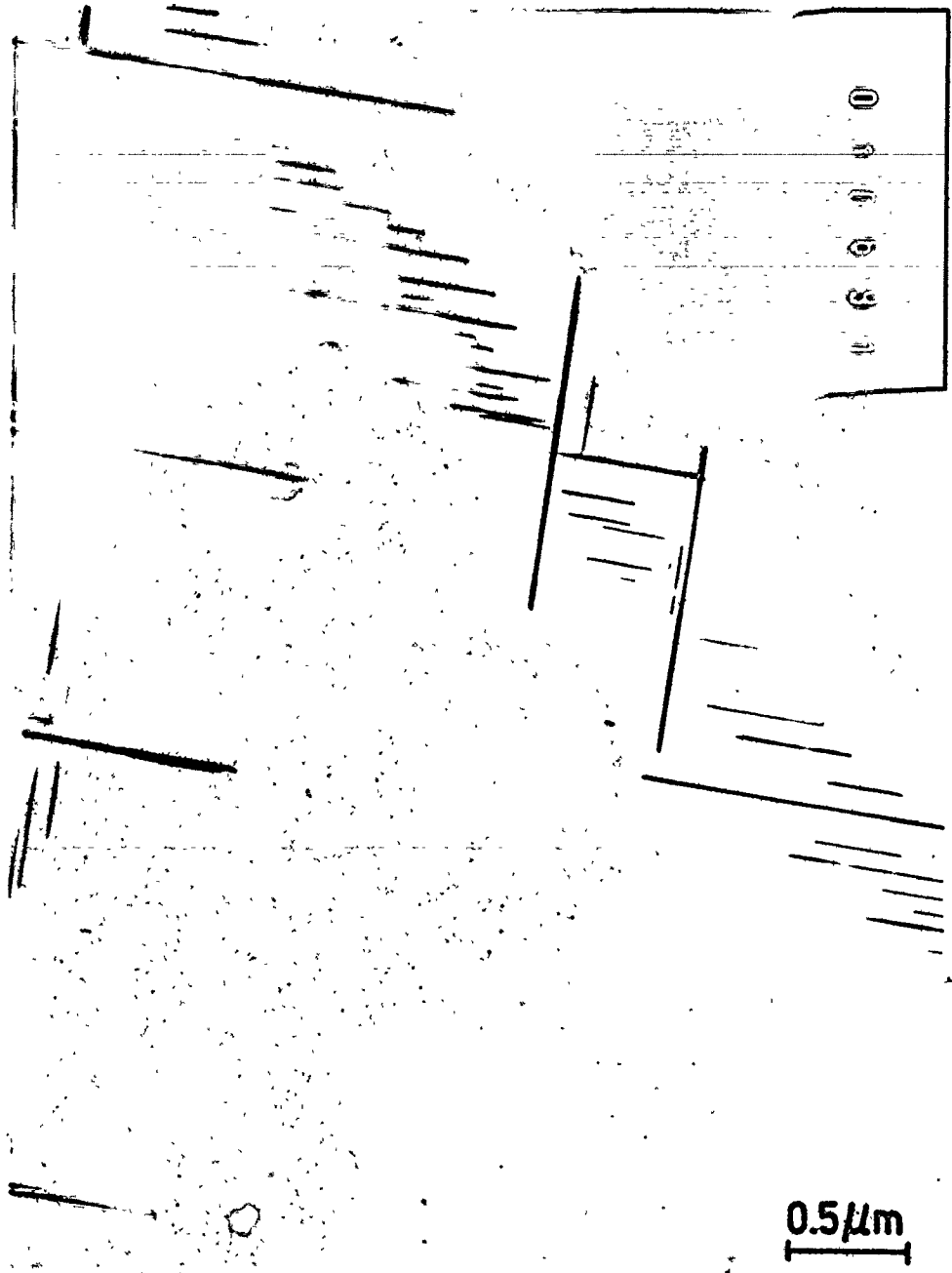


Fig. 44 (a)

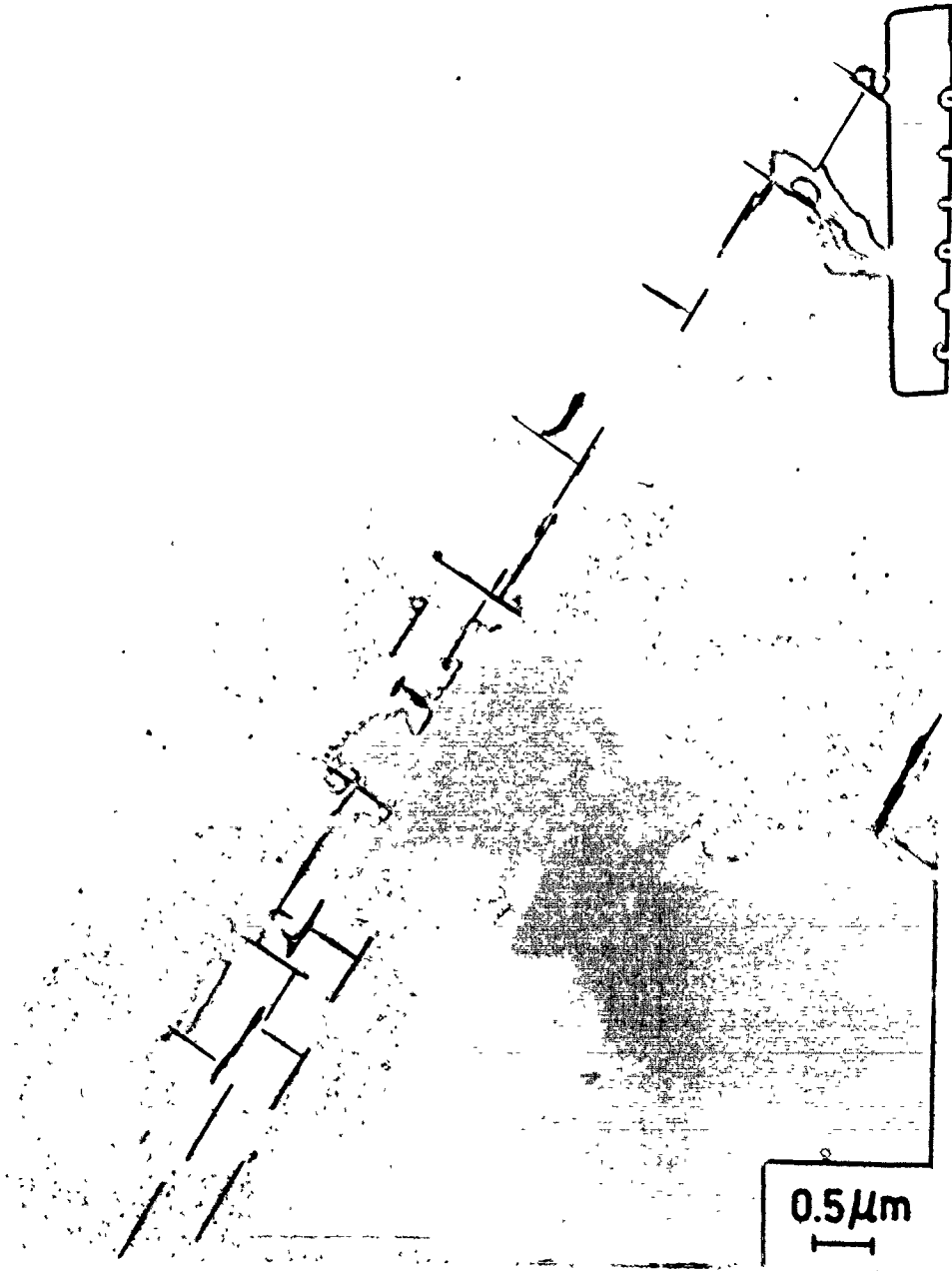


Fig. 44 (b)

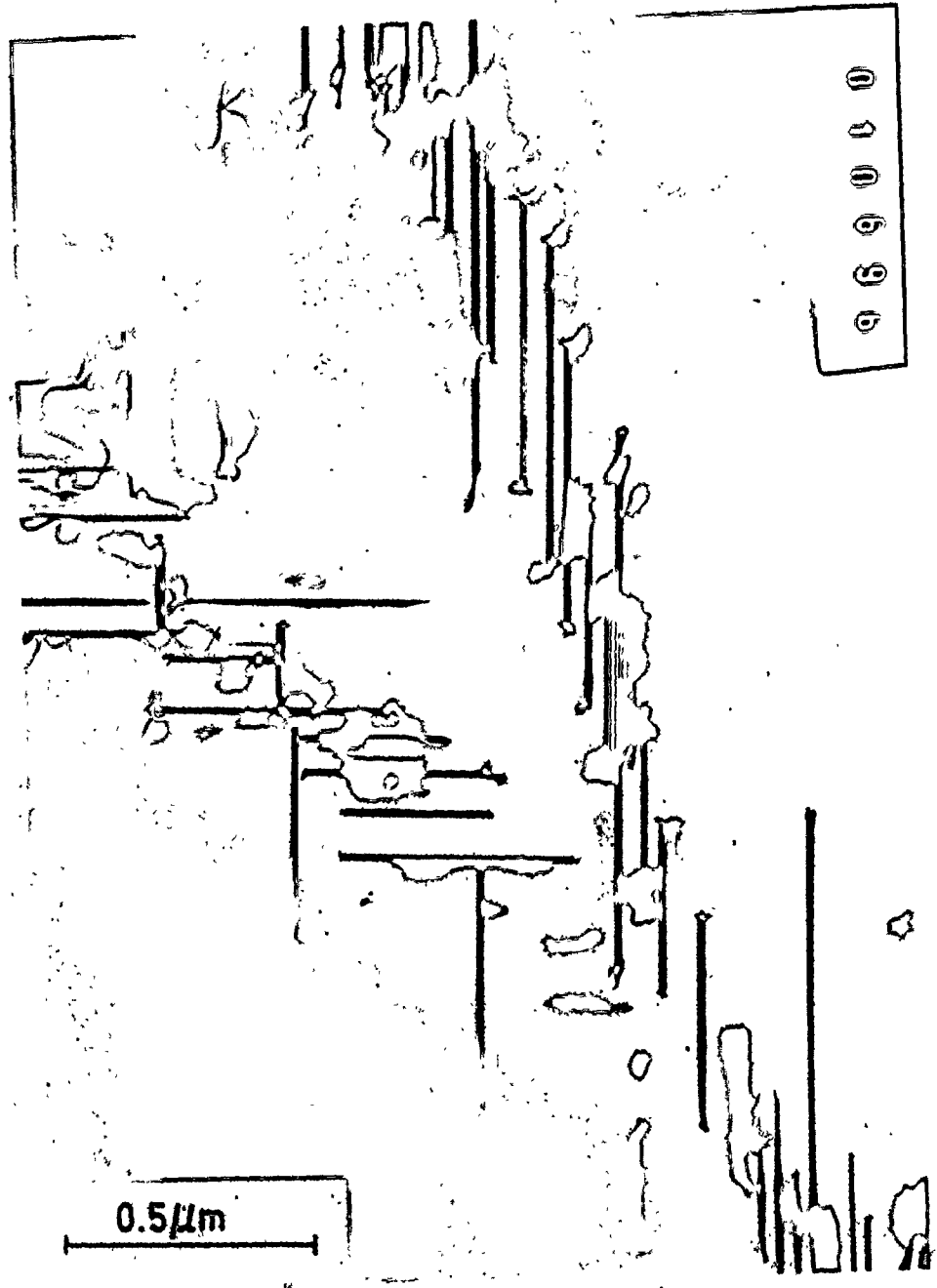


Fig. 44 (c)

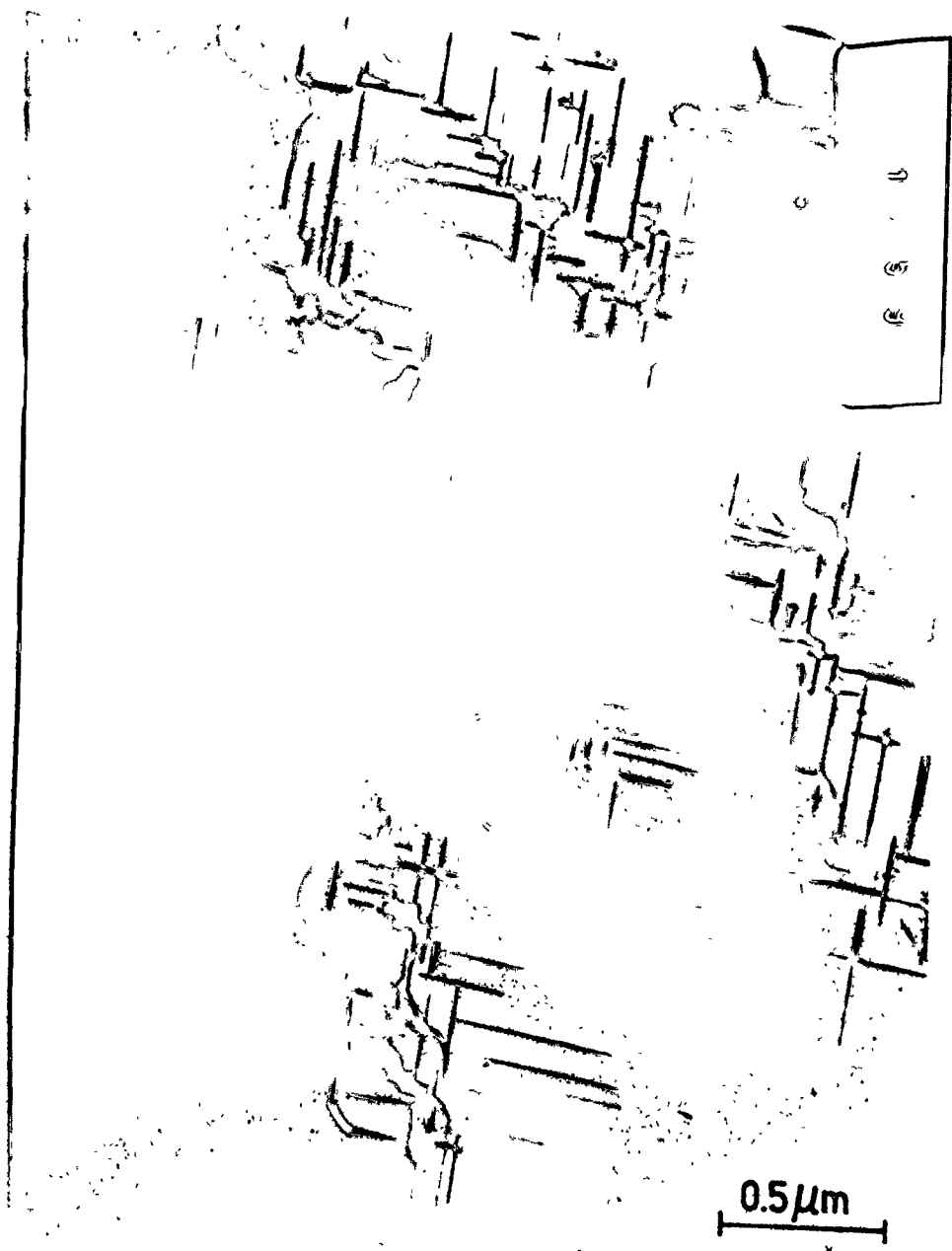


Fig. 44 (d)

such a way that they are displaced by a small amount with respect to each other. This configuration ("parallel-step") is also energetically favoured.

The overall morphology of the θ' precipitates in the early stage of their development is shown in Fig. 45(a)-(b). It is seen that the main feature of these microstructures is a large number of different stacks. However, all these stacks are in energetically favoured orientations as will be shown later. Some of the stacks were imaged in a dark field using both matrix and precipitate reflections, Fig. 46(a)-(d).

Finally, in order to find out whether these stacks are one or two-dimensional some of the observations were made on the foils close to the $\langle 111 \rangle$ section, Fig. 47. Results of these examinations have shown that most of the stacks were in fact linear arrays.

Occasionally a dislocation was seen to join some of the larger precipitates. However, it must be noted that the great majority of θ' precipitates examined, particularly the smaller ones between these larger plates, were not so connected.

These smaller θ' precipitates very often formed close to the larger plates. This effect is particularly pronounced in Figs. 43 and 44(d).

Since we were aware that nucleation on moving or static dislocations occurs in this system a detailed search was made for evidence that these stacks were somehow generally associated with dislocations. The weight of evidence is that they are not. This result is in accord with the conclusions of

Fig. 45 Al-3% Cu crystal with (001) orientation, solution-treated and aged 1 hour at 240°C. Bright field micrographs show overall structure of θ' precipitates in their relatively early stage of development. Both micrographs contain different kinds of stacks, already described in Figs. 43 and 44. (a) high strain field around stacks is very visible. (b) only particles are imaged by tilting the foil from the Bragg condition (bright field weak beam condition). (a) 15000 \times (b) 25000 \times .

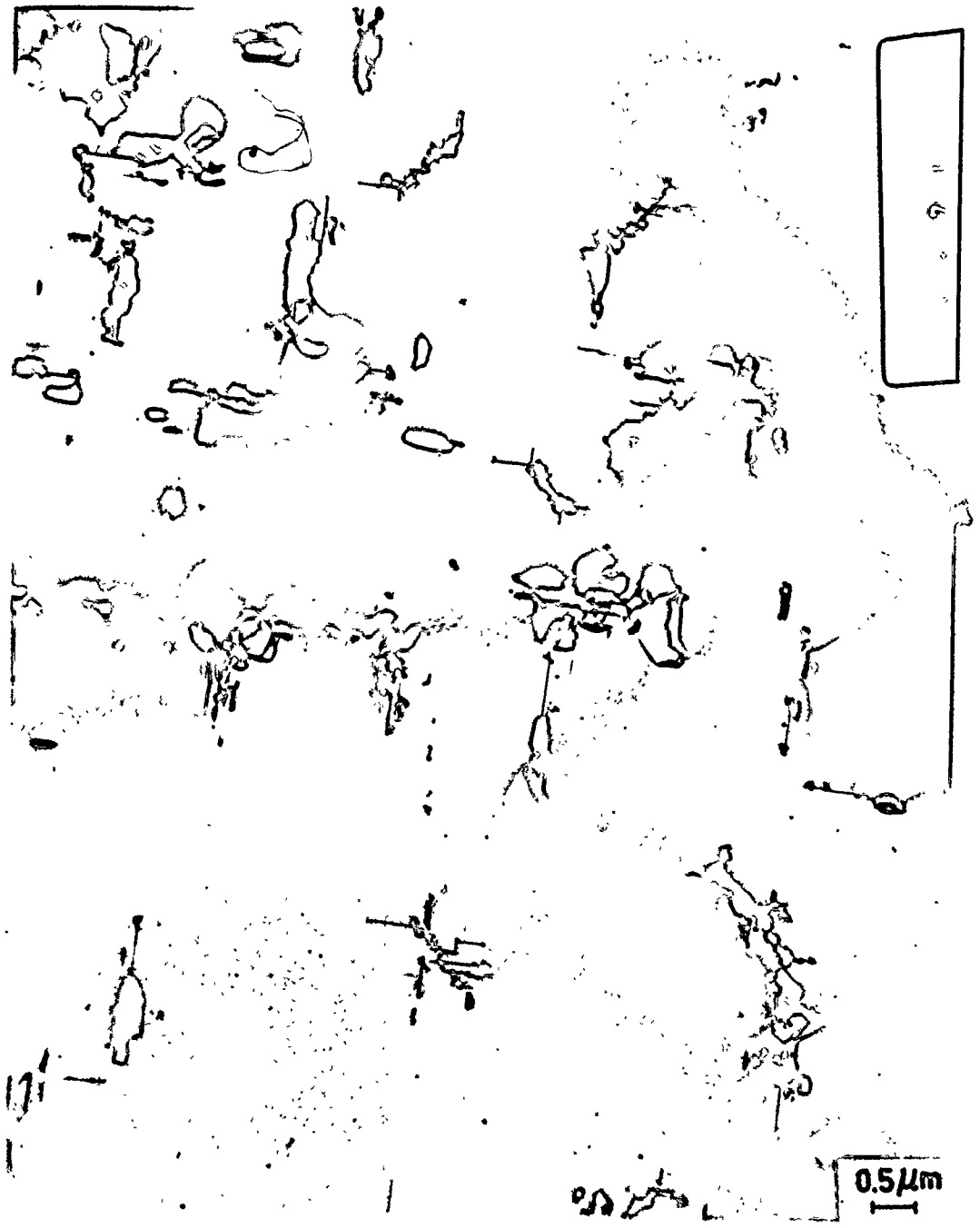


Fig. 45 (a)



Fig. 45 (b)

Fig. 46 Al-3% Cu crystal with (001) orientation solution-treated and aged 1 hour at 240°C. The series of micrographs show stacks in dark field. (a) and (b) stacks imaged in dark field using matrix reflections, show strain field around particles; Note also the stack in (a) imaged by differential absorption. (c) and (d) show stacks in dark field using precipitate reflections. (a) 42000x , (b) 14250x ; (c) 33000x (d) 14250x.

1143

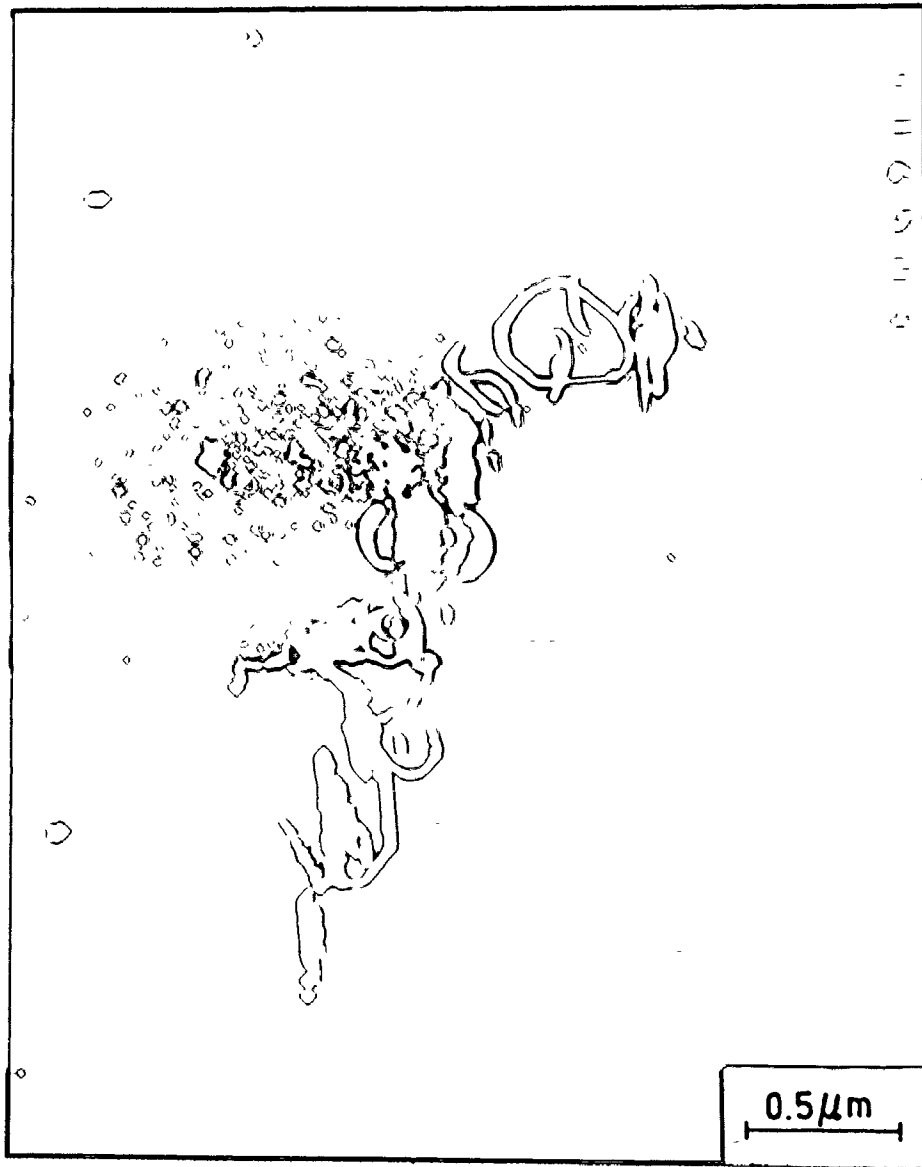


Fig. 46 (a)

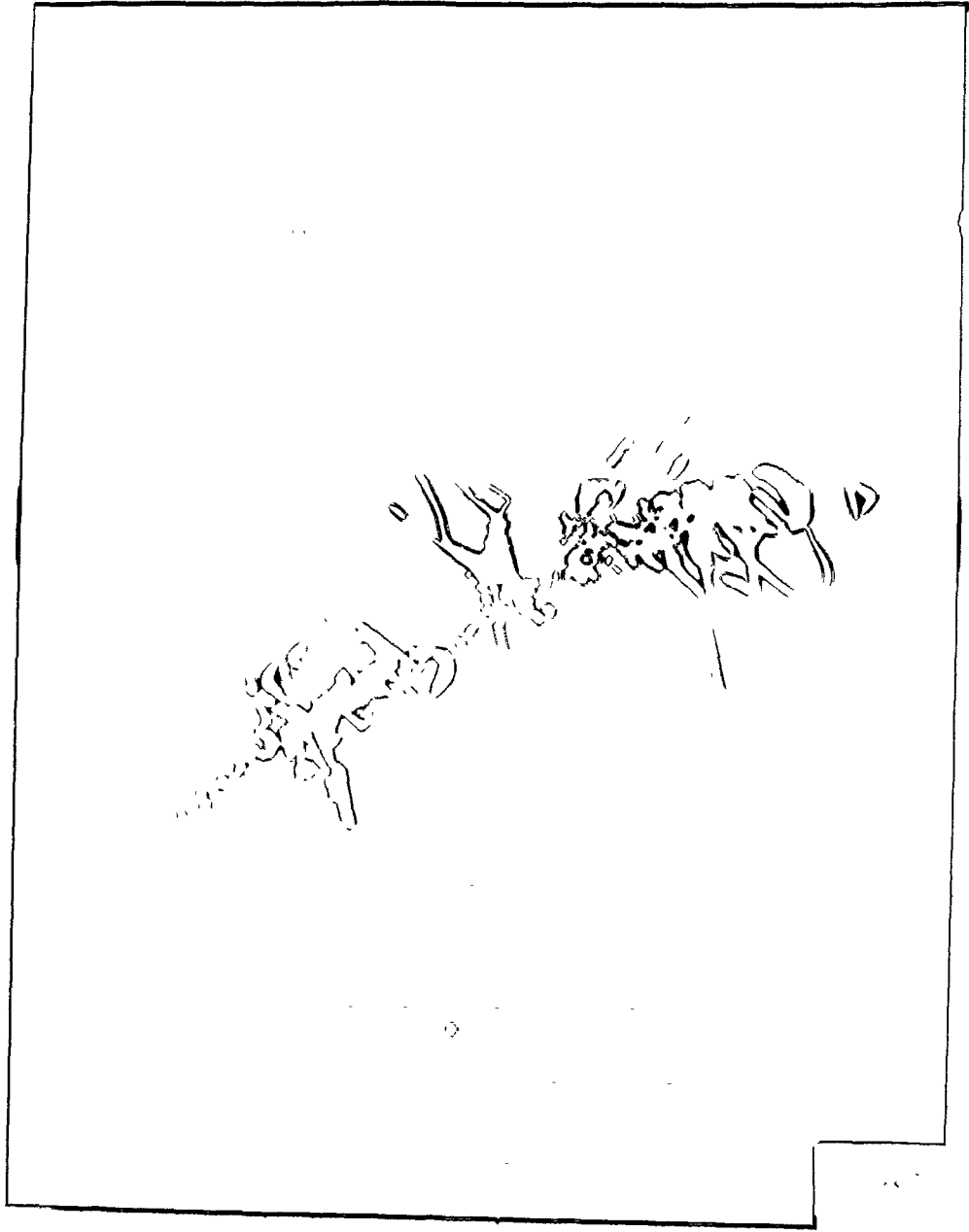


Fig. 46 (b)

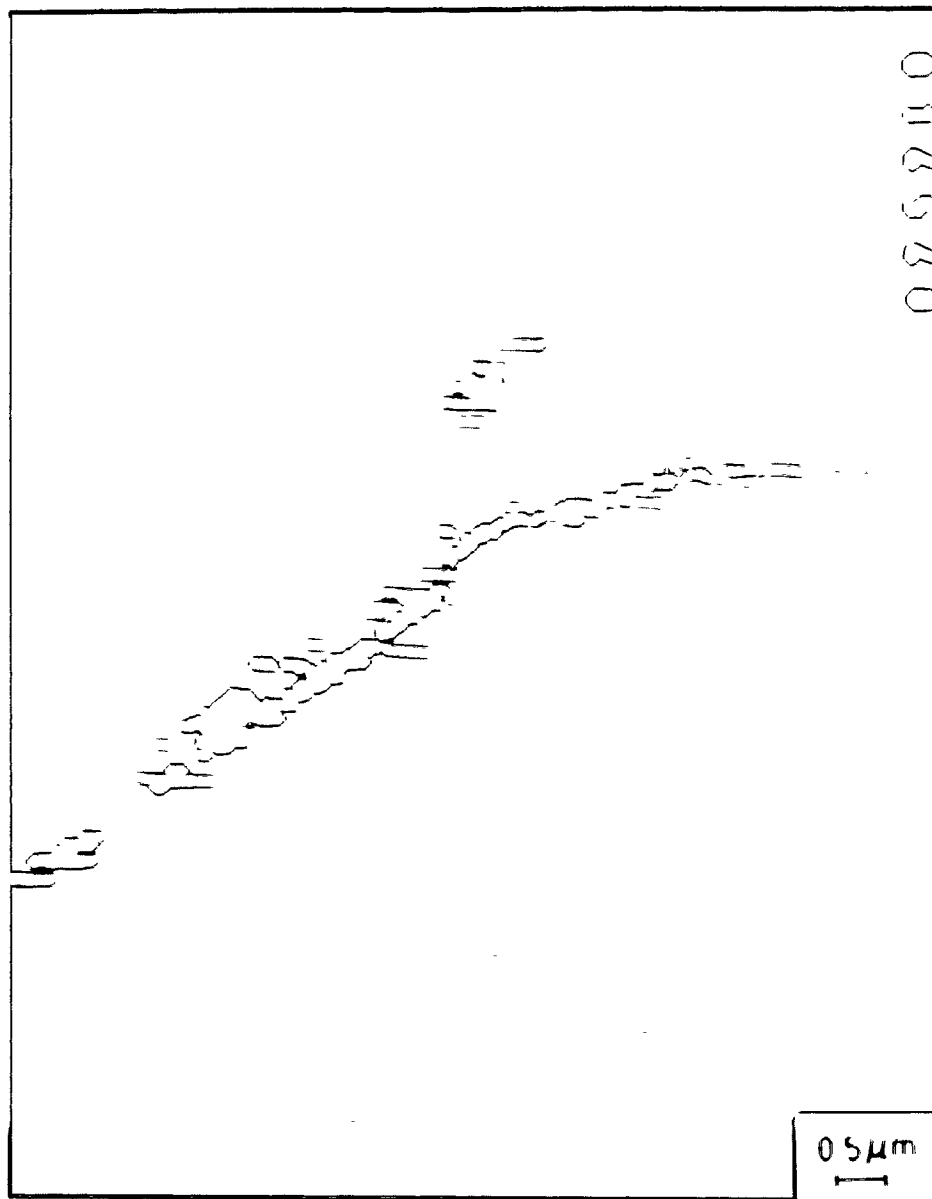


Fig. 46 (c)

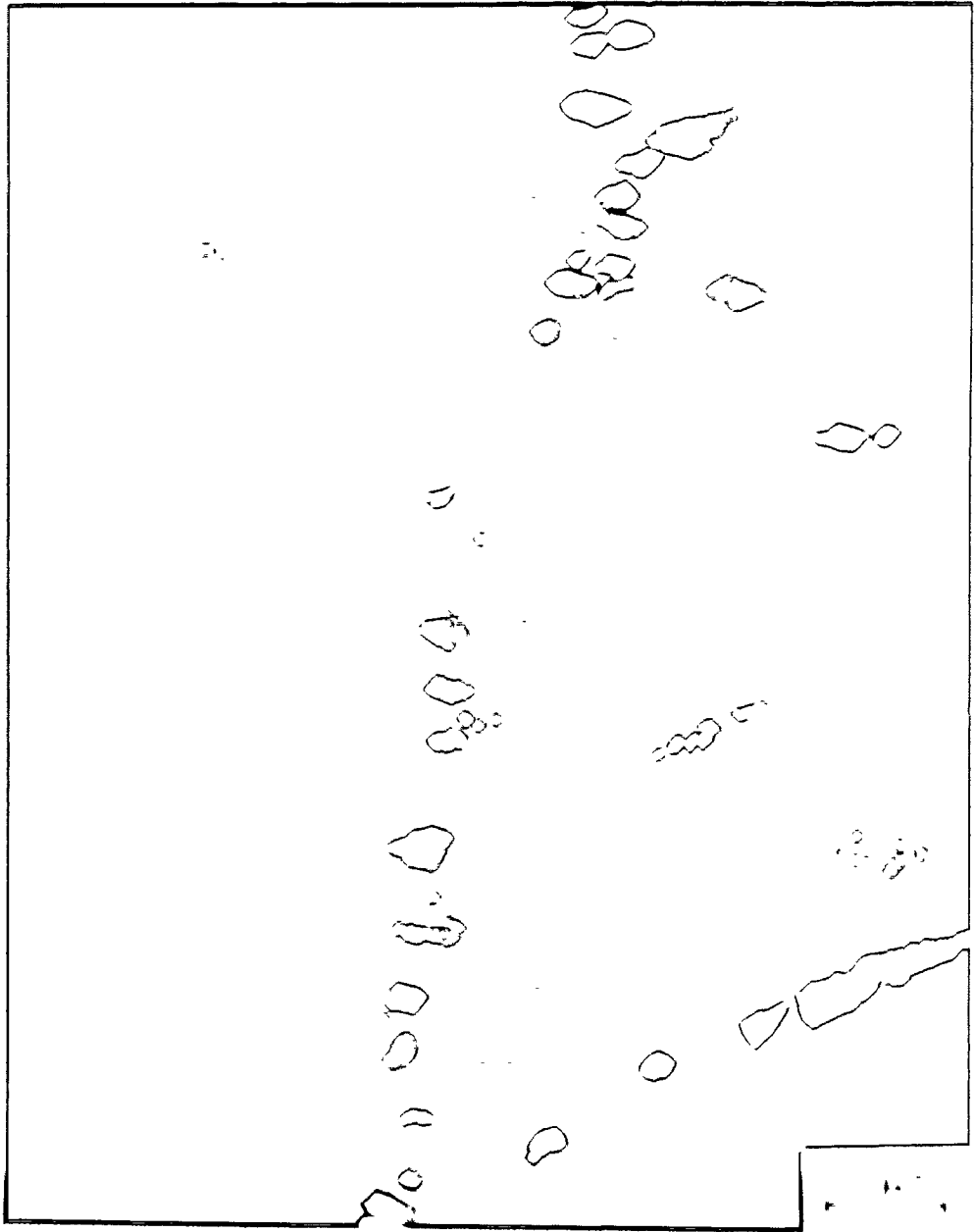


Fig. 46 (d)

142

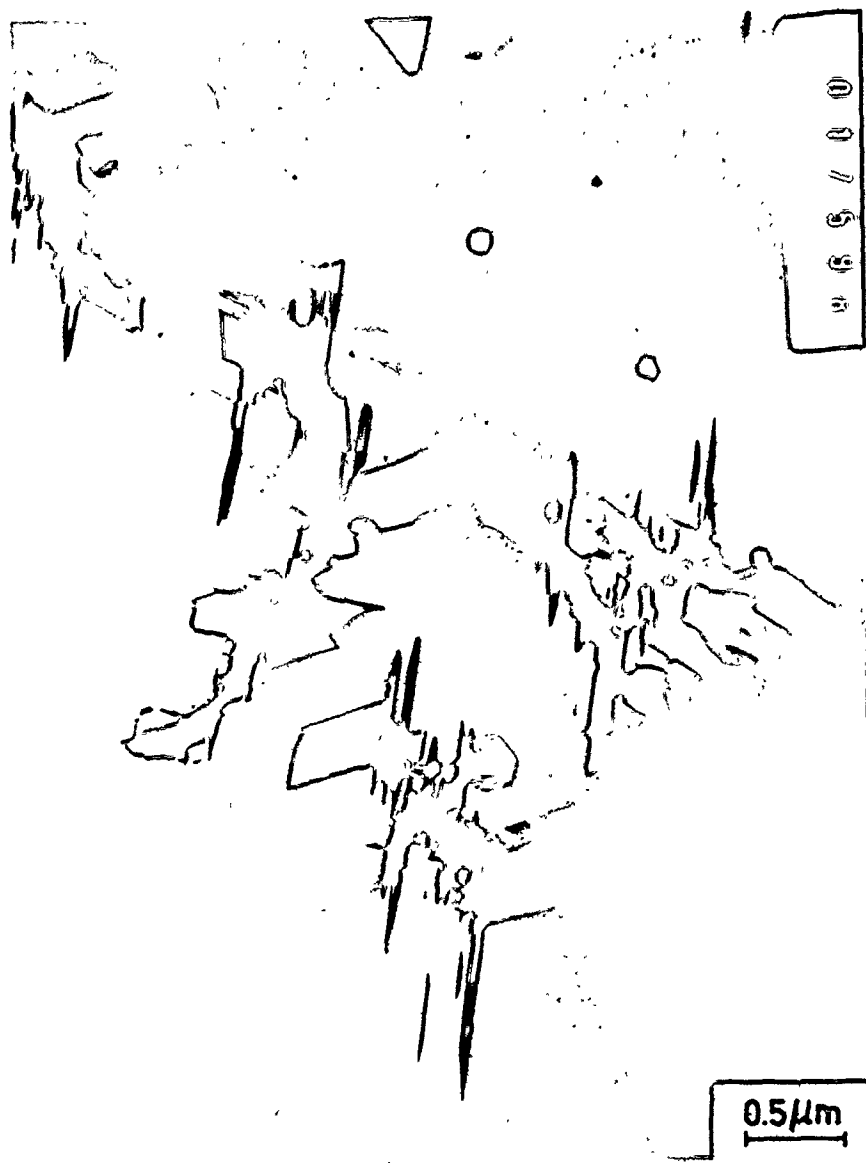


Fig. 47 Al-38 Cu crystal, solution-treated and aged 1 hour at 240°C. Bright field micrograph showing stacks in the foil of approximately (111) orientation. (28000x)

Stobbs and Purdy (103),

Some of the foils were observed in the as-quenched state. Results of these observations are shown in Fig. 48(a)-(b). The main feature of these microstructures is a very small fraction of defects. As can be seen there are small clusters which could not be resolved. These (and a few dislocations) may serve as a place for heterogeneous nucleation of the first θ' particle, from which new particles can start spreading in preferred orientations, directions and spacings. It should be noted that dislocation loops or helical dislocations were not observed in these samples.

A number of stacks were imaged in different operating reflections and these generally proved to be free of dislocations. (It is assumed here that an energetically favourable interaction would tend to keep the dislocation pinned to the stacks, so that they could be readily detected after specimen preparation). This suggests therefore, that upon the heterogeneous nucleation of at least one platelet, many others are formed, by successive nucleation and growth in their respective stress and diffusion fields. This type of array was observed and interpreted in much the same way by Lorimer (96) and by Stobbs and Purdy (103).

One set of the specimens was plastically deformed during cutting. The characteristic structure of these specimens is shown in Fig. 49. The microstructure is quite different from the stacks described in Figs. 41 through 47, and is very

Fig. 48 Solution-treated and water-quenched Al-3% Cu crystal with (001) orientation. (a) dark field micrograph shows punching of dislocation loops from an inclusion (14250 \times). (b) Bright field micrograph shows the matrix with only a few defects; small defects could not be resolved (53250 \times).

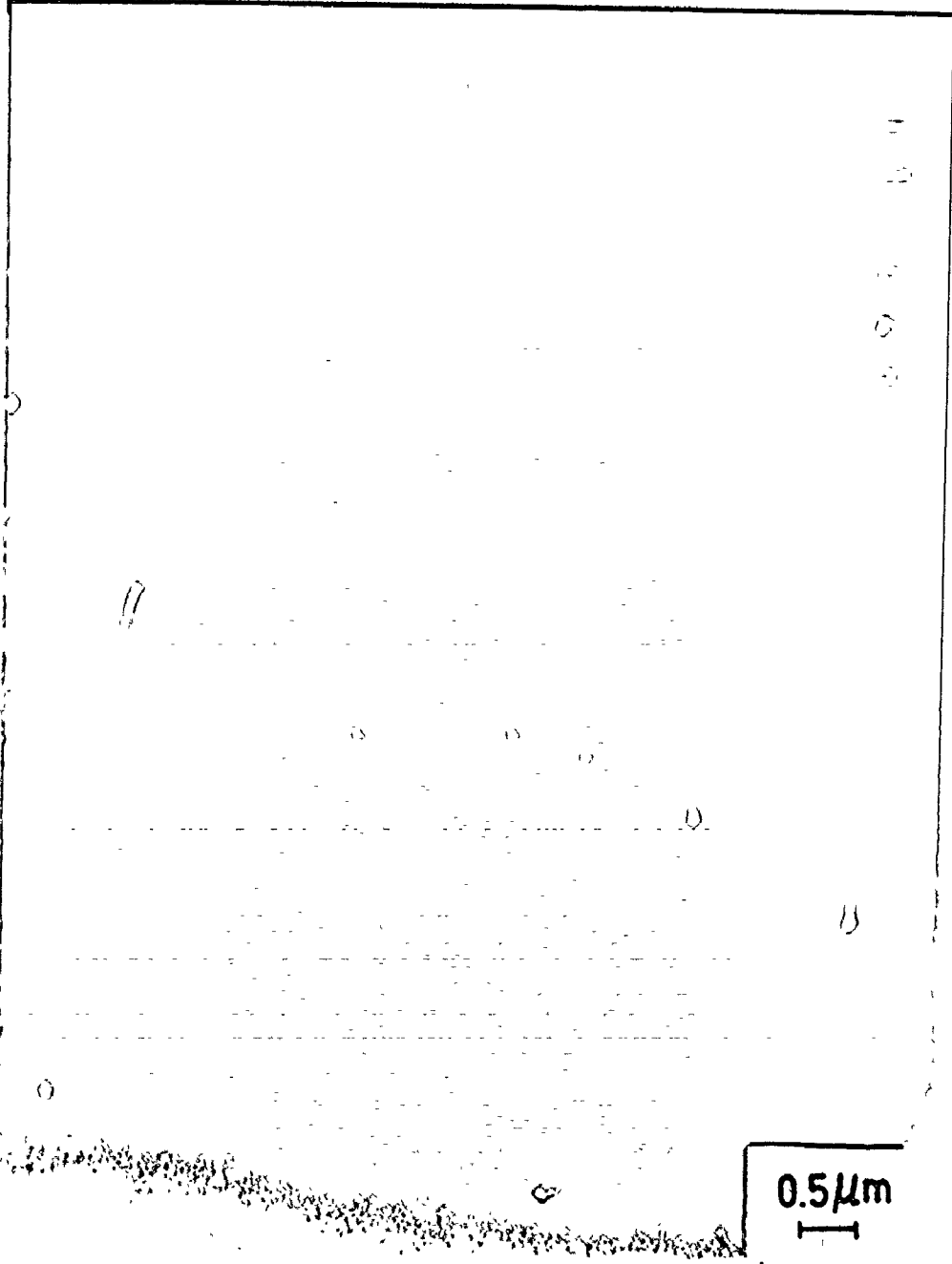


Fig. 48 (a)

1150



Fig. 48 (b)

115d

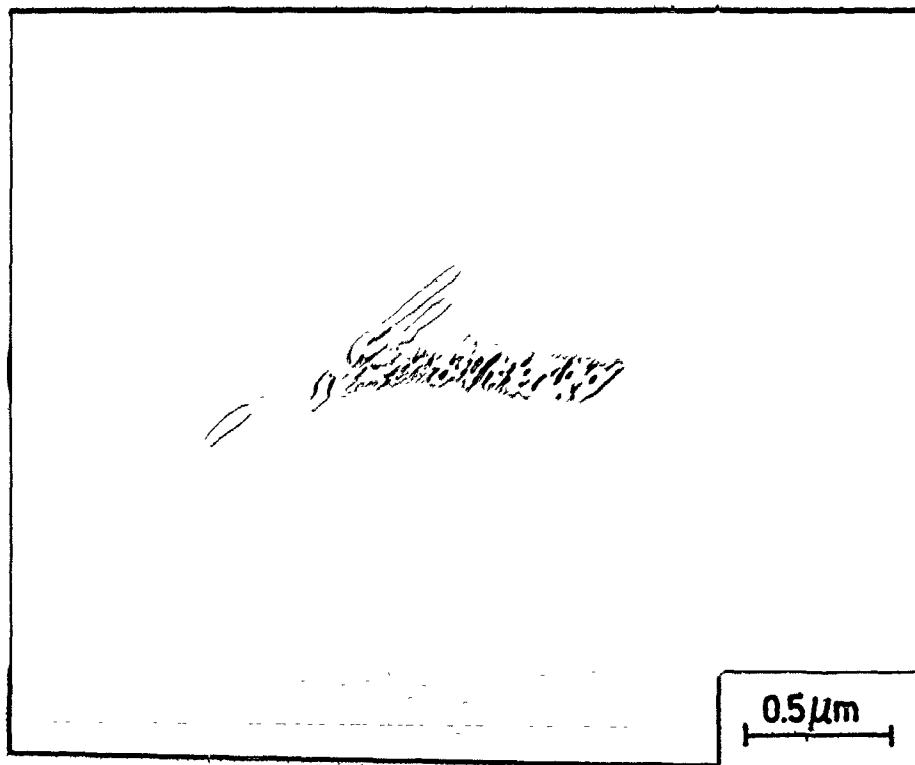


Fig. 49 Al-3% Cu crystal with (001) orientation, plastically deformed during cutting, solution treated and aged 1 hour at 240°C. Dark field micrograph shows repeated nucleation on moving dislocation; note the leading dislocation (42500x).

similar to the colonies of θ' precipitates thought to be formed by repeated precipitation on climbing dislocations, as described by Headley and Hren (100). The leading dislocation is clearly visible.

Some observations were made on specimens aged 15 min at 240°C. These are shown in Fig. 50(a)-(f).

Fig. 50 represents possible spreading of the θ' precipitates from the cluster on the top. The very small θ' particle at (A) has presumably formed at the edge of the last large particle.

Besides the common morphology Fig. 50(b) and (c) show small "clusters" of only a few particles. Similar effects are shown in Fig. 50(e)-(f), where the small θ' particles are very close to the larger θ' plates.

In some foils aged 1 h at 240°C clusters of a few particles in the energetically favoured, edge-face orientation are observed, Fig. 51(a)-(b).

To check on the solute distribution in the matrix, double heat treatments were carried out. The first step was the same as above, i.e. specimens were aged 1 h at 240°C in order to obtain stacks, and subsequently aged 23 h at 160°C (below the θ'' solvus line).

Results of observations of these double-aged specimens are shown in Fig. 52(a)-(b). Here the solute fields around the original θ' particles are well defined by θ'' precipitates.

Fig. 50 Al-3% Cu crystal with (001) orientation, solution-treated and aged 15 minutes at 240°C. This series of bright field micrographs shows small clusters of only a few particles, all in energetically favourable orientations. Note possible spreading of θ' precipitates from the cluster on the top (a) and small particles very close to the large ones (c) and (d). Two particles, large and small, in very favourable orientation (face-face and edge-face) are seen in (e) and (f). Also note in (c) and (d) how the strain field can obscure visibility of small particles.
(a) 27500 \times , (b) 43500 \times , (c) 27500 \times , (d) 27500 \times ,
(e) 79500 \times , (f) 94500 \times .

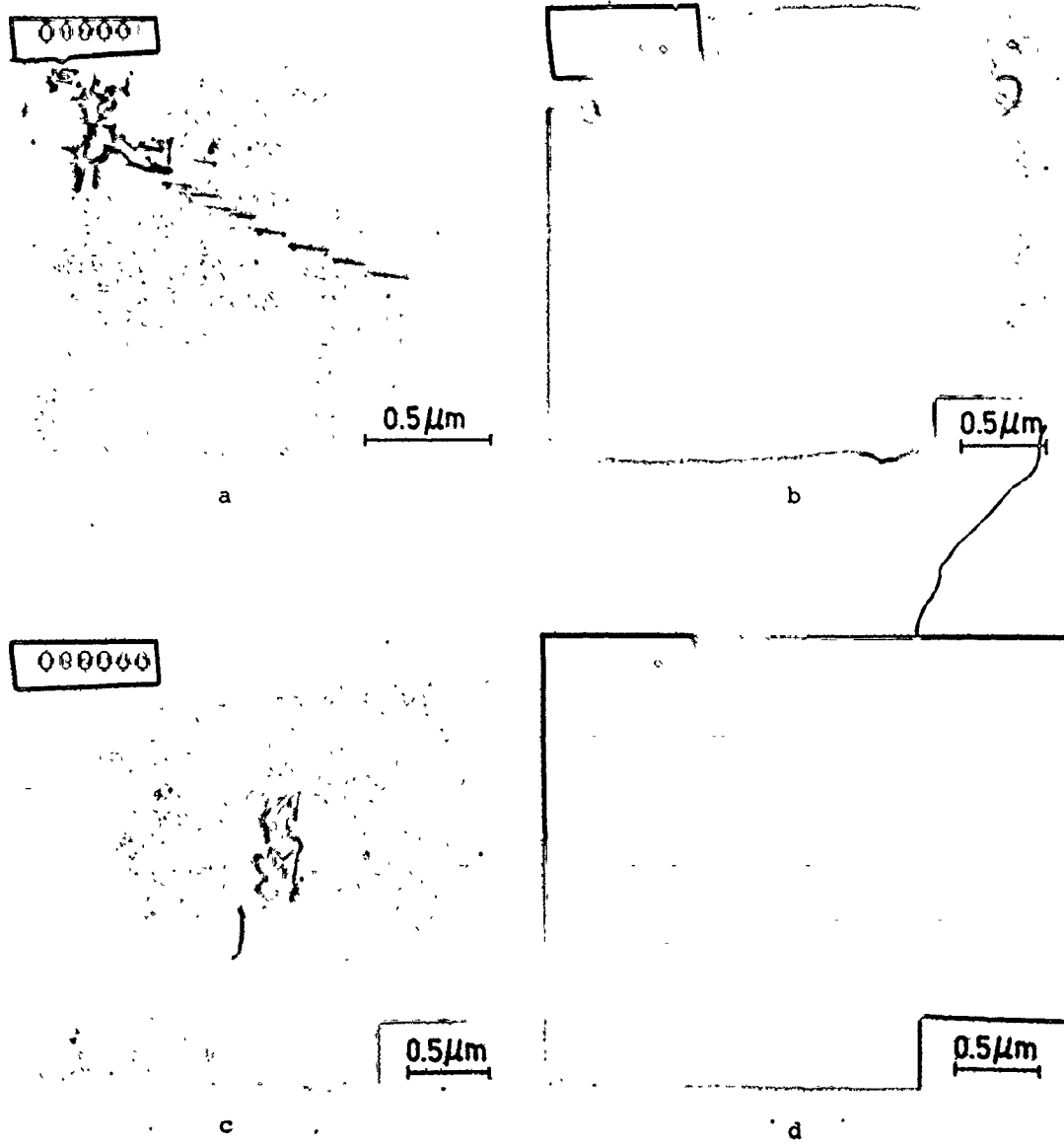
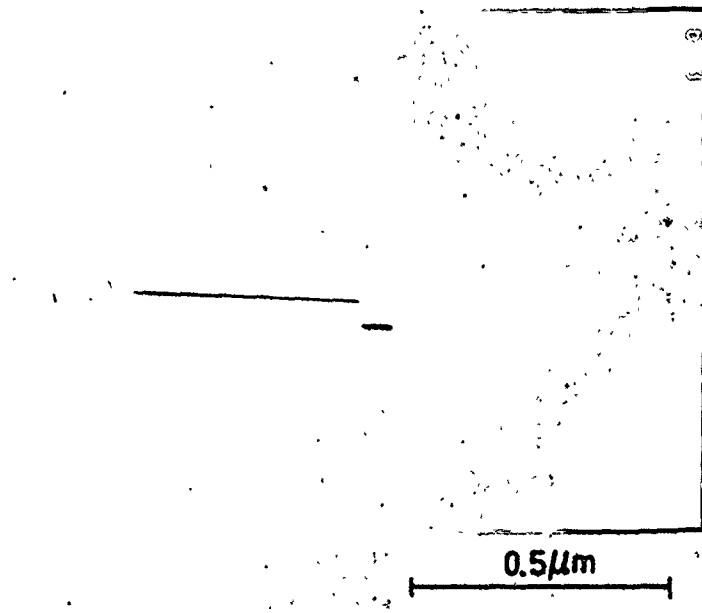
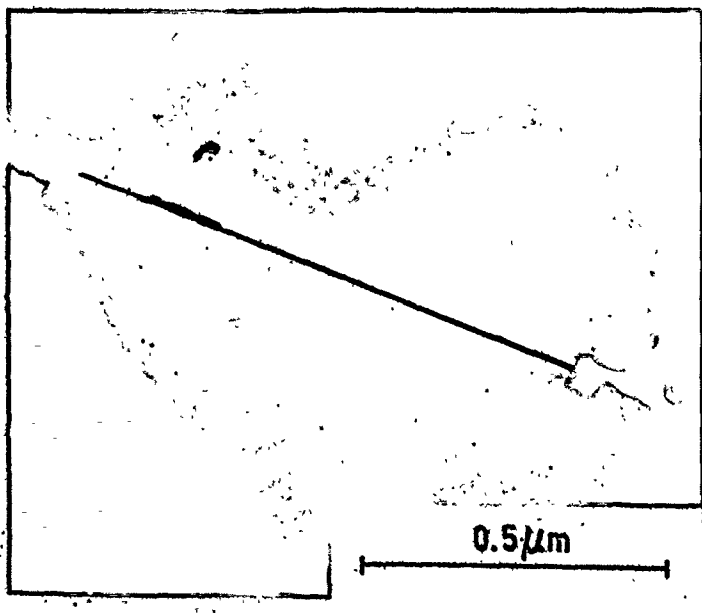


Fig. 50

116 C



e



f

Fig. 50

Fig. 51 Bright field micrographs of Al-2% Cu crystal with (001) orientation, solution-treated and aged 1 hour at 240°C, show clusters of a few particles in the energetically favoured, edge-face orientation. Note how diffusion and strain interaction fields have influenced the particle shape.
(a) 16000x, (b) 16000x.

116e

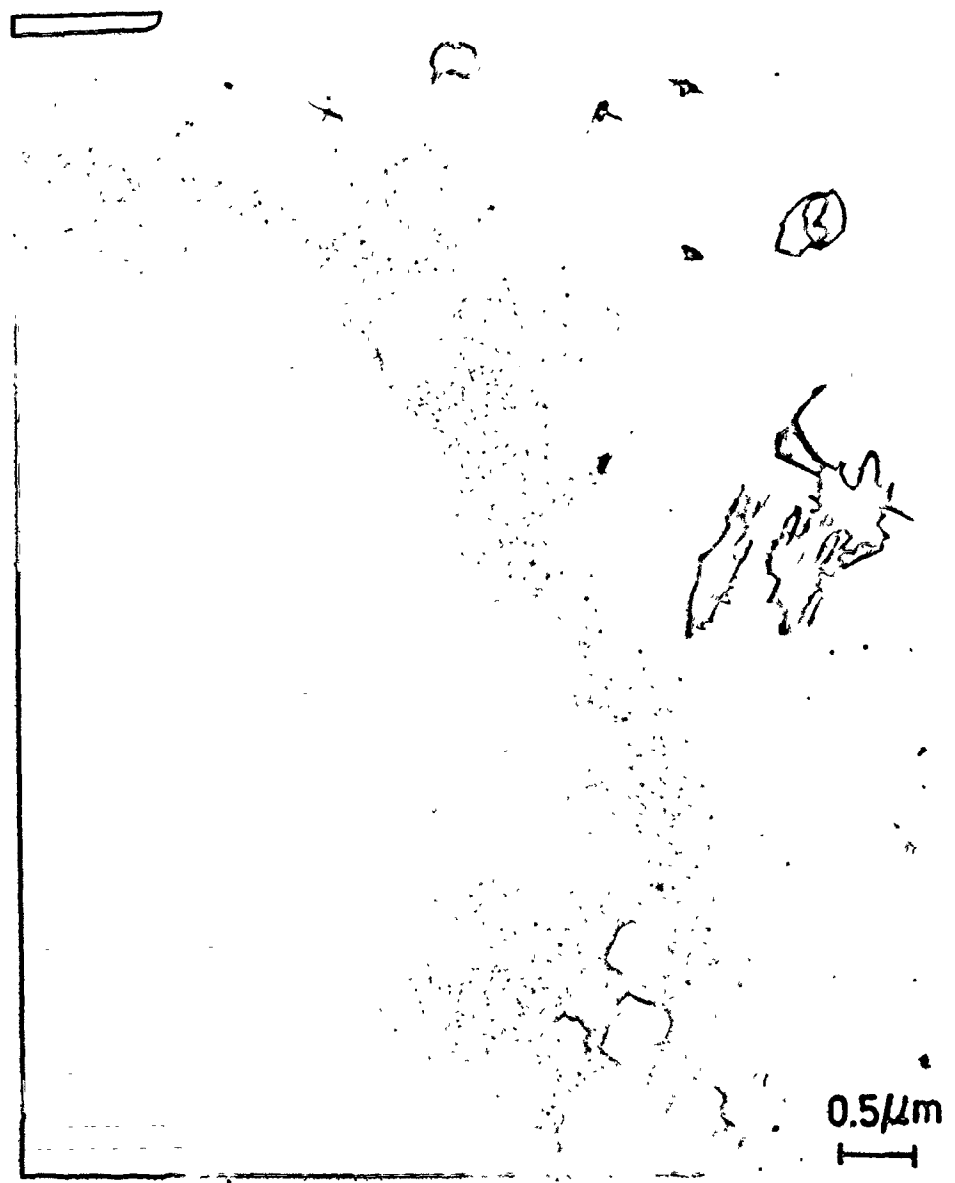


Fig. 51 (a)

116f

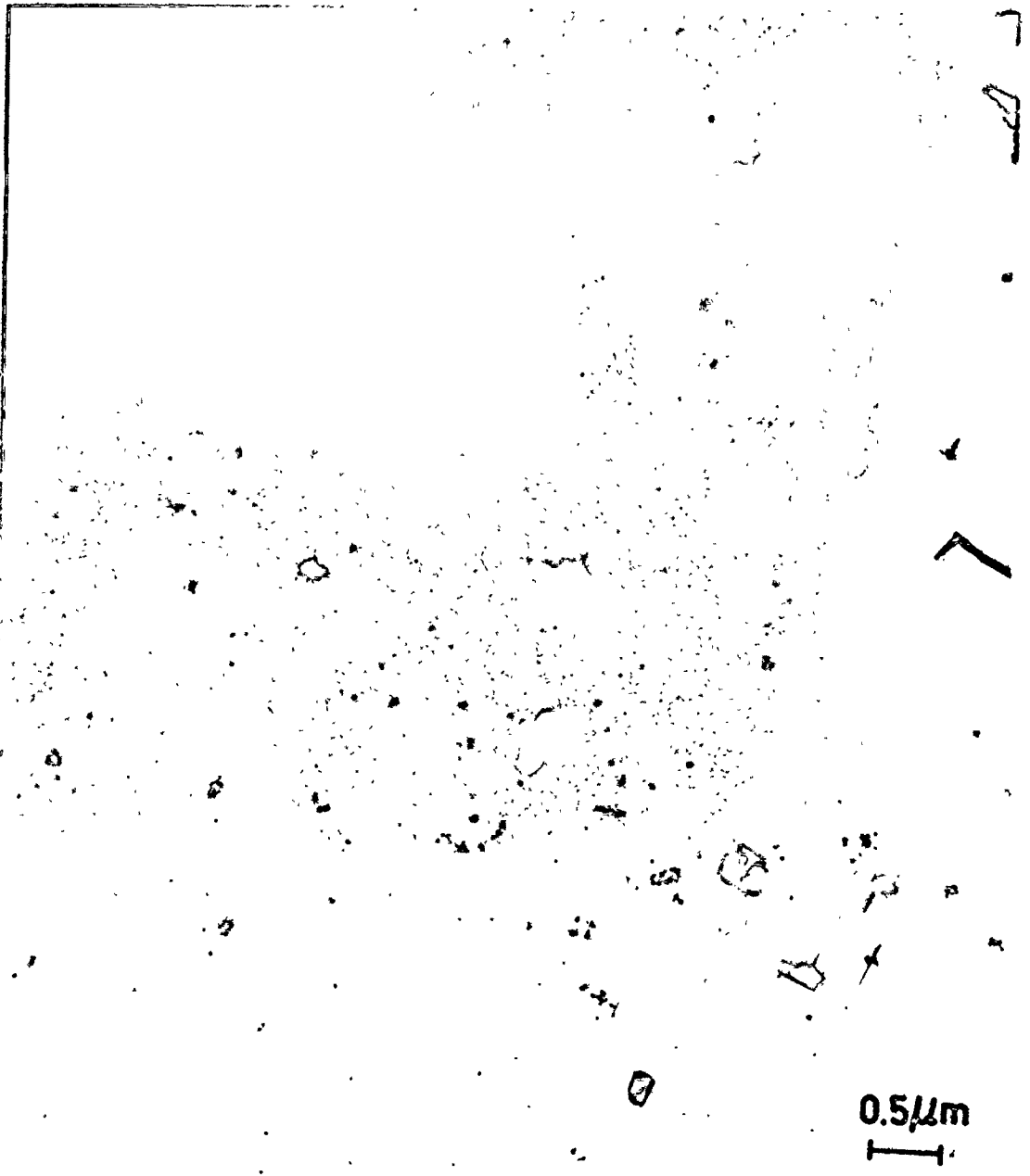


Fig. 51 (b)

Fig. 52 Al-3% Cu crystal with (001) orientation, solution-treated and double-aged (1 hour at 240°C and 23 hours at 160°C) to show the solute fields around the original θ' particles by well defined θ'' precipitates.
(a) 53250 \times , (b) 31500 \times .



Fig. 52 (a)

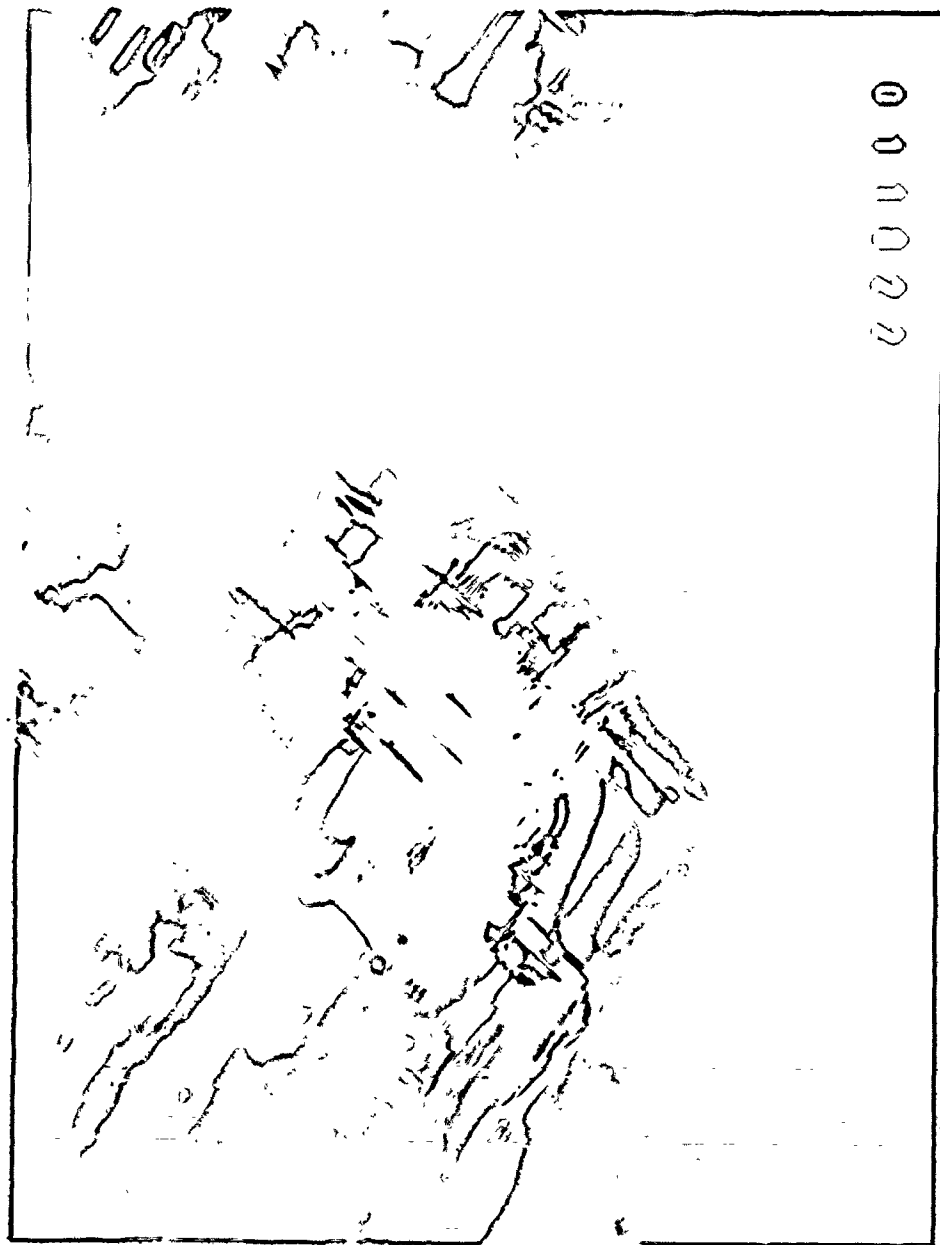


Fig. 52 (b)

To summarize the observations of the general micro-structure; it has been demonstrated that stack formation is a feature of initial nucleation and growth.

Stacks appear to result from the competition between growth of existing plates and nucleation of new θ' precipitates in the stress and diffusion fields of these neighbours. The stack morphology is not generally related to dislocations.

Finally, it should be mentioned that a series of "in situ" ageing experiments were conducted in the electron microscope, with the objective of seeing the nucleation of the new particles in the vicinity of stacks in the way described above. These experiments failed because of very easy nucleation of the equilibrium θ phase on the free surfaces, and the very fast loss of coherency of the existing precipitates, Fig. 53.

3.2.1.b NUCLEATION OF θ'

In solid-solid transformations the total energy change accompanying the formation of a new phase, may be expressed as

$$\Delta G = -A\Delta G_v + B\gamma + C\varepsilon + E_{int} \quad (89)$$

where A , B and C are shape constants, ΔG_v is a volume free energy term, and γ is a surface energy. The third term of eq. (89) represents the strain field of the nucleus, and the fourth term, E_{int} takes into account the elastic interaction energy between the strain field of the nucleus and any other elastic strain field in the system.

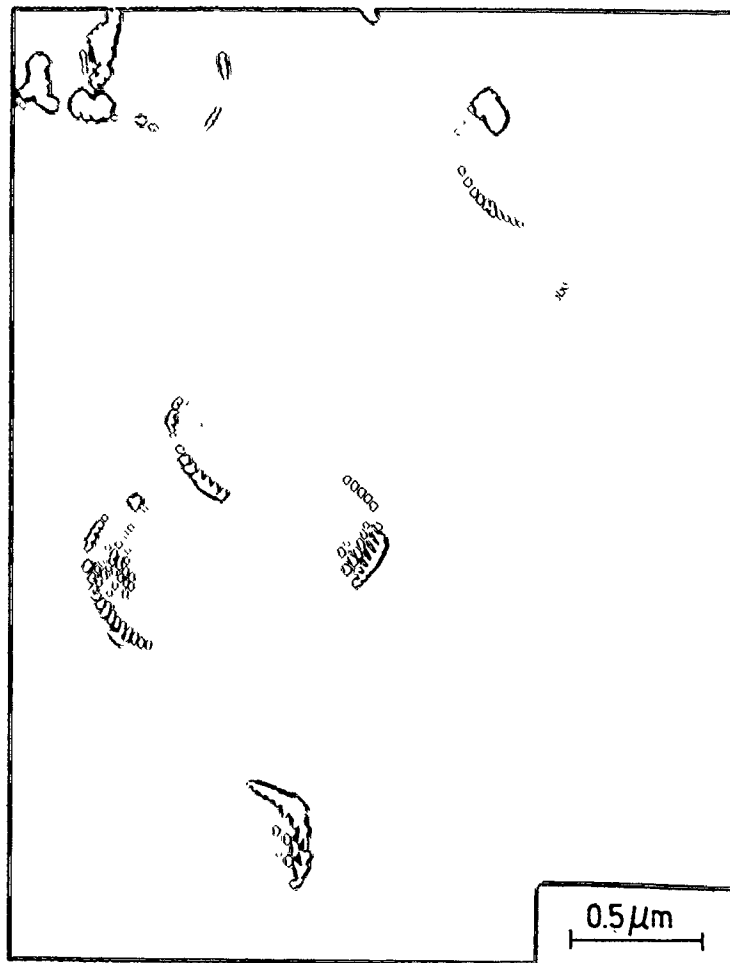


Fig. 53 Al-3% Cu crystal with (001) orientation, solution-treated, aged 15 minutes at 240°C followed by in situ hot stage ageing at 240-300°C. Matrix dark-field micrograph shows a dislocation network on the semicoherent θ' particles (42000 \times).

The nucleation process in this system does not admit a simple description in terms of classical nucleation theory. This is essentially because the concept of monomer addition to a critical-size cluster whose properties are similar to the fully developed precipitate is inappropriate to the semi-coherent misfitting disc (103). Here we will concern ourselves only with the relative effects of elastic interaction on nucleation.

It is assumed that the interaction term will dictate the favourable site for nucleation.

In order to determine the effect of elastic interaction on nucleation we have calculated the elastic interactions between precipitates of different size, orientation and separation as described in section 3.1.2.d.

Similar calculations have also been performed to determine stack stability against growth.

3.2.1.c NUMERICAL ESTIMATIONS OF THE ELASTIC INTERACTION ENERGY

The pair interactions between "large" equal size plates versus the distance between them, when they are mutually parallel and co-axial (face-face configuration), and when they are mutually perpendicular (edge-face configuration) are shown in Figs. 54 and 55.

It is clear that the interaction energy depends on the separation and orientation of the particles. Fig. 54 shows that the face-face configuration is unfavourable because the interaction is repulsive for any separation distance.

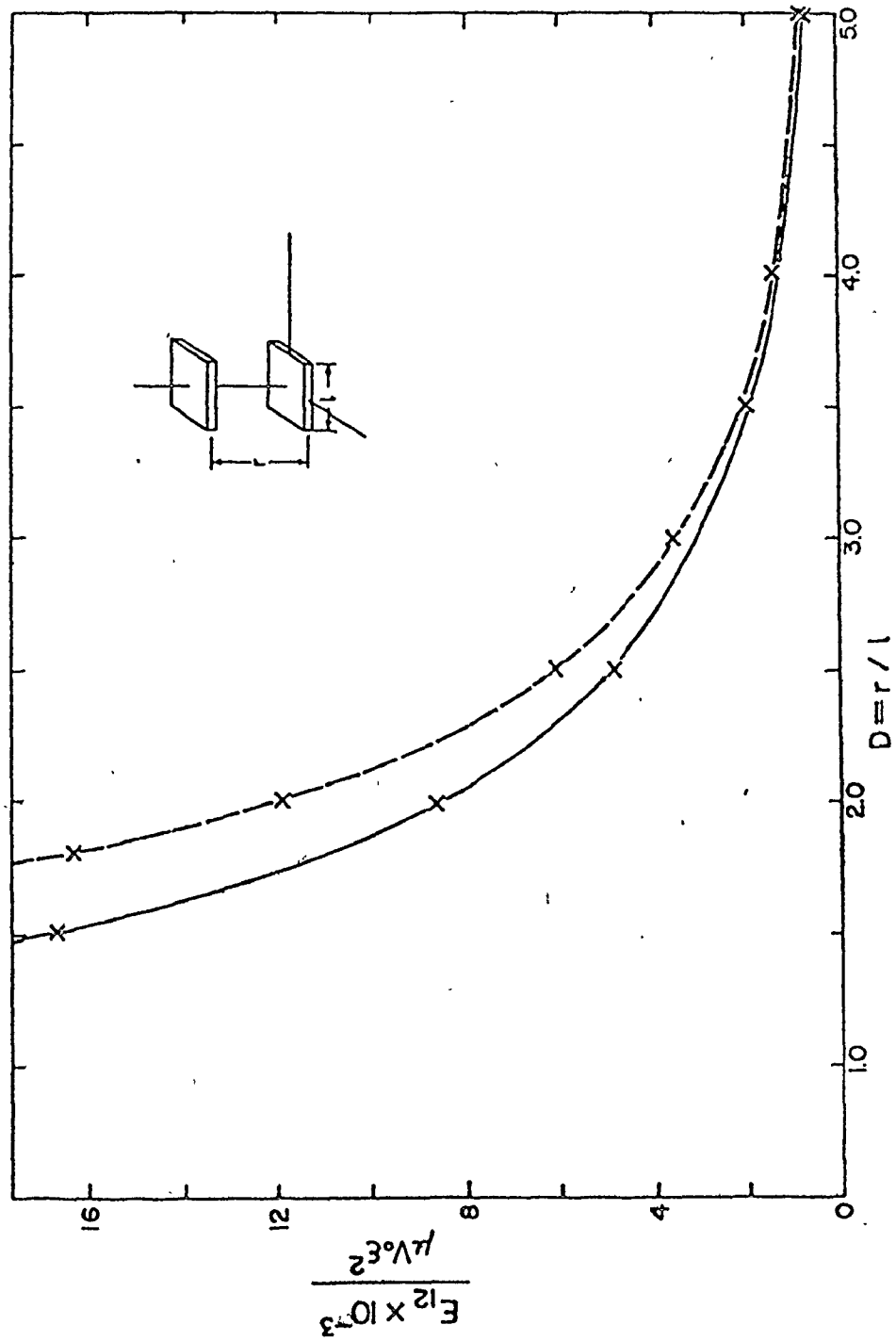


Fig. 54. Interaction energy of two square shaped particles when they are mutually parallel (face-face configuration) as a function of separation. The broken line indicates the interaction of infinitesimal precipitates of the same strength.

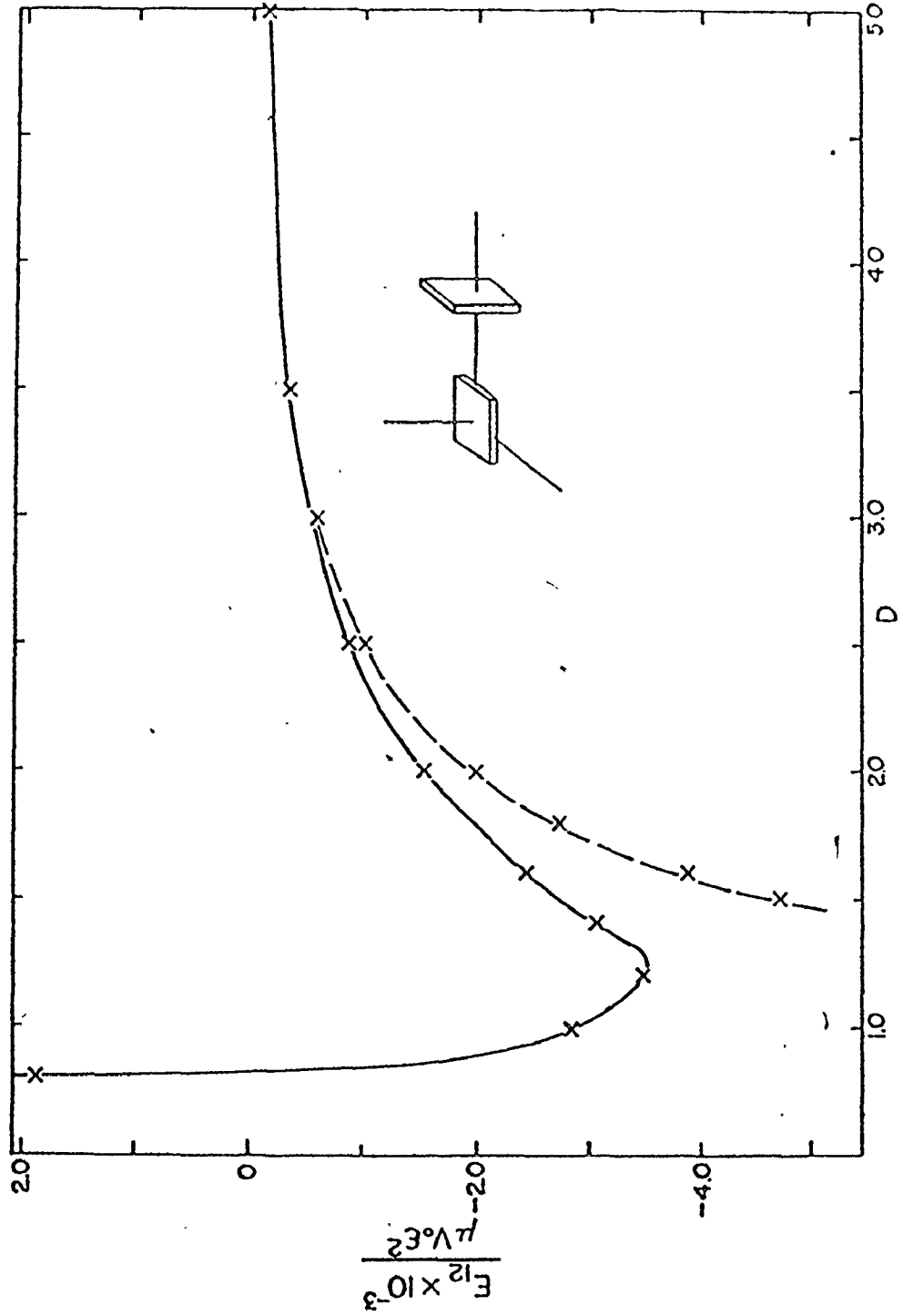


Fig. 55 Interaction energy of two square shaped particles when they are mutually perpendicular (edge-face configuration as a function of separation. The broken line indicates the interaction of infinitesimal precipitates of the same strength.

The edge-face configuration (Fig. 55) is attractive, and the minimum in the interaction energy curve at the 1.2 plate length distance suggests a likely place for the nucleation of the new particle in the stress field of the pre-existing particle. Results of calculations in which particles are moved from their minimum (Fig. 55) and maximum (Fig. 54) energy positions are shown in Figs. 56 and 57.

It is apparent (Fig. 56) that the configuration and separation corresponding to the minimum in the potential curve shown in Fig. 55 is very stable; any shift from the minimum energy position (keeping the centre-to-centre distance constant) results in a significant restoring force.

Fig. 57 indicates that translation (parallel to the plate plane) of one of a pair of particles initially in the high energy face-face configuration quickly brings it into a minimum energy position. (A similar result is obtained for the edge-face configuration, Fig. 58).

This effect is more pronounced when the separation between particles becomes smaller.

From the results shown in Figs. 54 through 57 it is of interest to speculate concerning possible linear configurations of precipitates, formed by chain autocatalysis and assuming that the driving force for homogeneous nucleation is of the proper magnitude that the elastic introduction becomes important.

Some hypothetical configurations are shown schematically

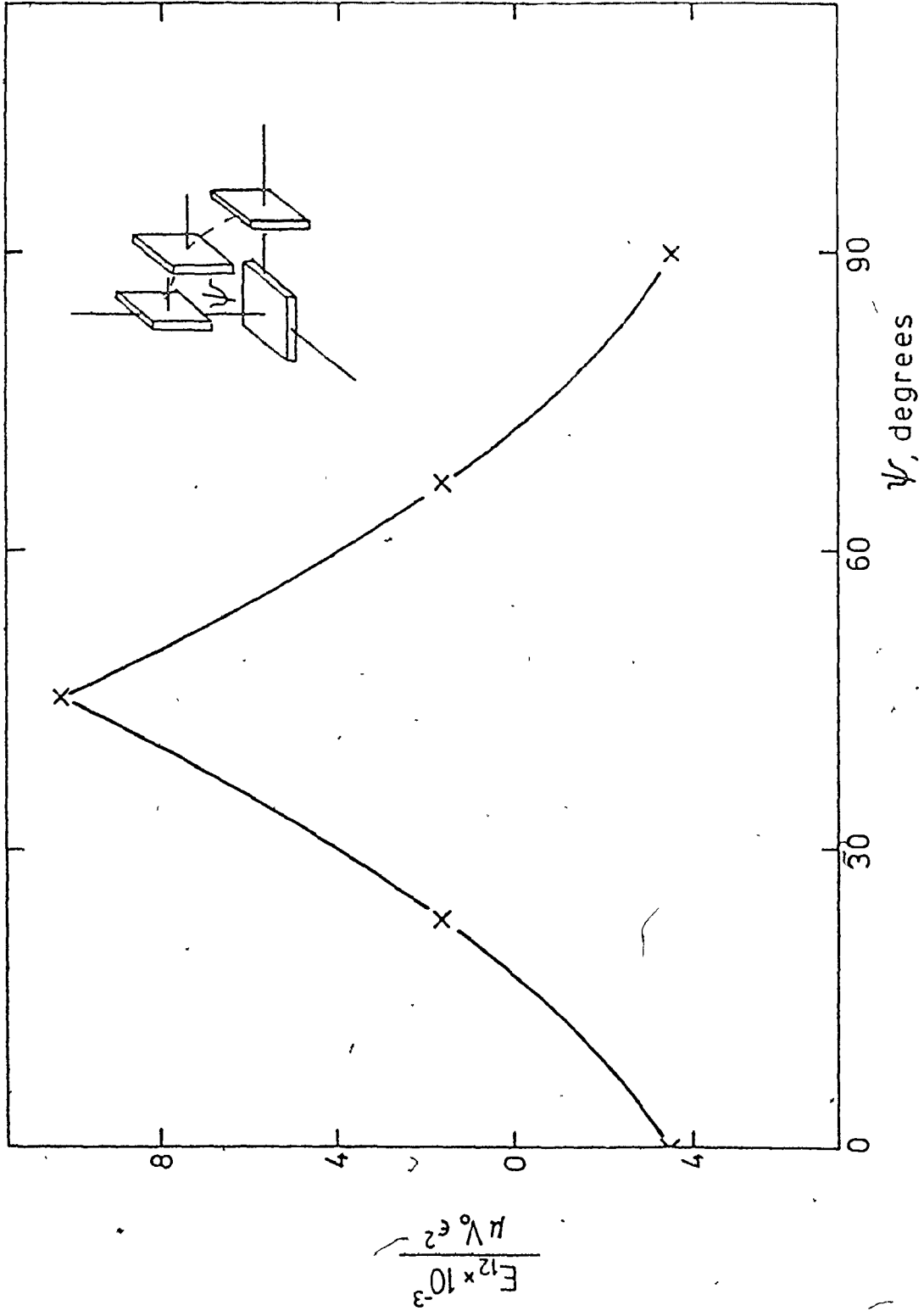


Fig. 56 Interaction energy of two equal size square-shaped particles, when they are mutually perpendicular (edge-face orientation) as a function of inclination angle ψ , keeping the centre-to-centre distance constant (1.2 times the plate length, which corresponds to the minimum in Fig. 55).

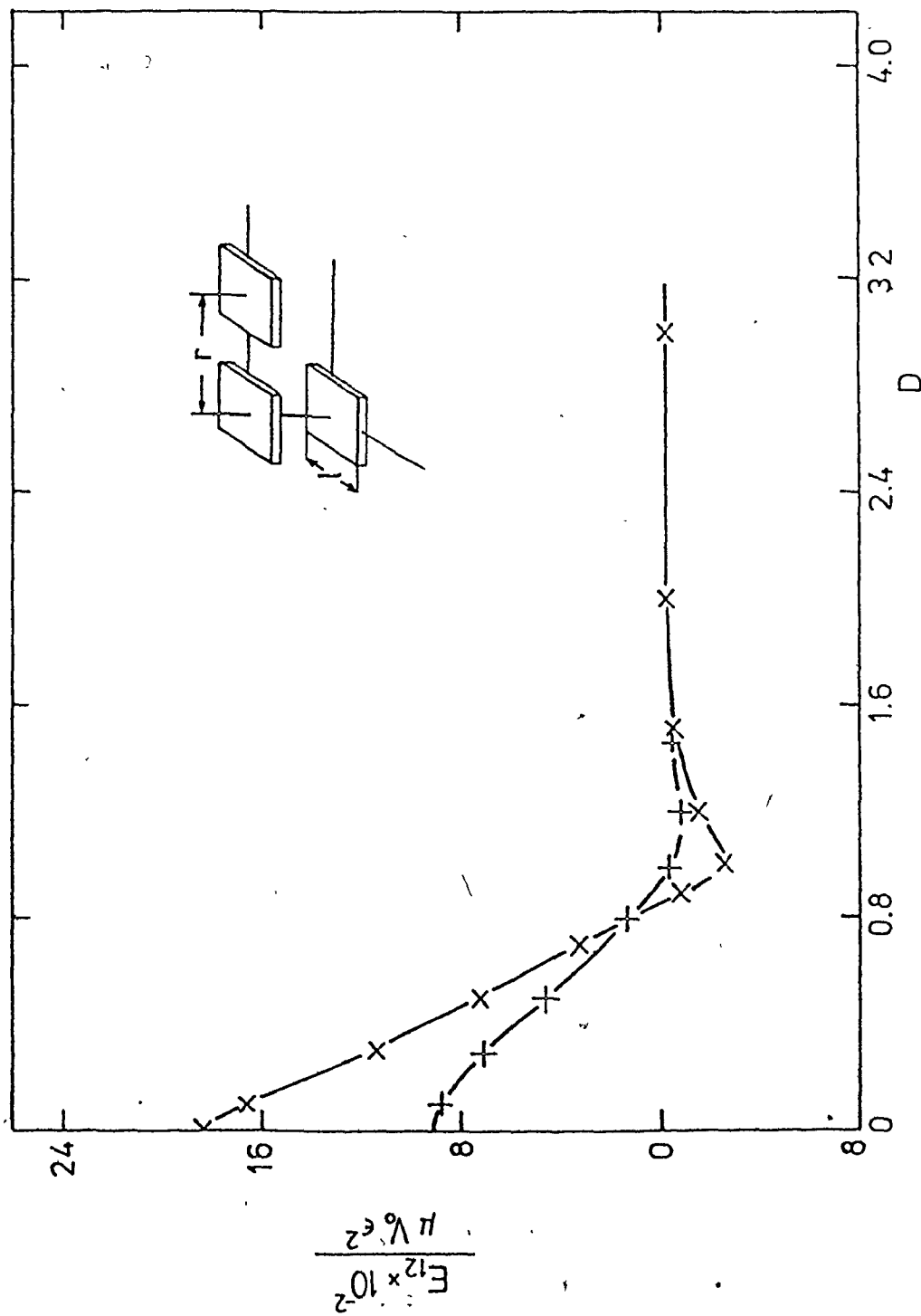


Fig. 57 Interaction energy of two equal size square-shaped particles, when they are mutually parallel (face-face configuration) as a function of trans-
 lation (parallel to the plate plane) of one particle. The effect of
 variation in the initial separation is also shown.

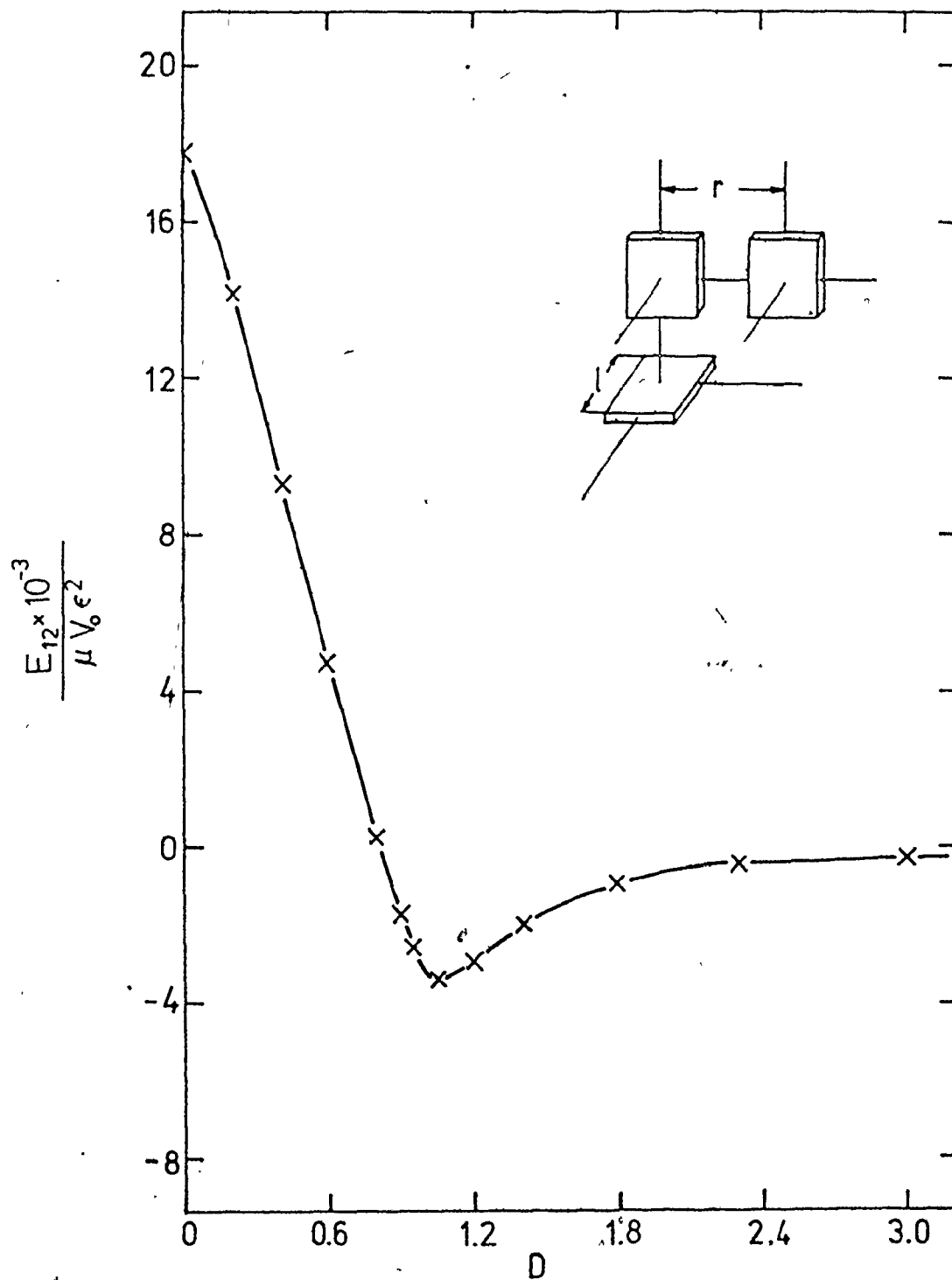


Fig. 58 Interaction energy of two equal size square-shaped particles when they are mutually perpendicular (edge-edge configuration) as a function of translation along the y-axis.

in Fig. 59(a)-(e). According to the potentials shown in Figs. 54 to 57 it is clear that the configuration shown in Fig. 59(a) is very unlikely (all interactions are repulsive) and that configuration in Fig. 59(b) is somewhat more stable. Near neighbour interaction between precipitates (1) and precipitates (2) are attractive, as well as interactions between second neighbour precipitates (1). These attractive interactions must be balanced against repulsive interactions between precipitates of orientation (2).

More stable configurations are depicted in Figs. 59(c) and (d). From the potentials shown in Figs. 10-12 it is again clear that both first and second neighbour interaction energy are negative.

To obtain a more quantitative insight into the energies of linear arrays of equal-size precipitates shown in Fig. 59(a)-(e), their interaction energies (per central plate) were computed.

Fig. 60 shows the potential of arrays of parallel precipitates as a function of their separation (centre-to-centre) and the inclination angle (ψ) between centres of precipitates. The hypothetical stack shown in Fig. 59(a) is represented by the angle $\psi = 90^\circ$; the stack (c) by the $\psi = 16^\circ$ and the array (e) by the $\psi = 0^\circ$.

According to the potentials shown in Fig. 60, it is clear that the potential depends strongly on separation of precipitates in the stacks, and on their inclination; it

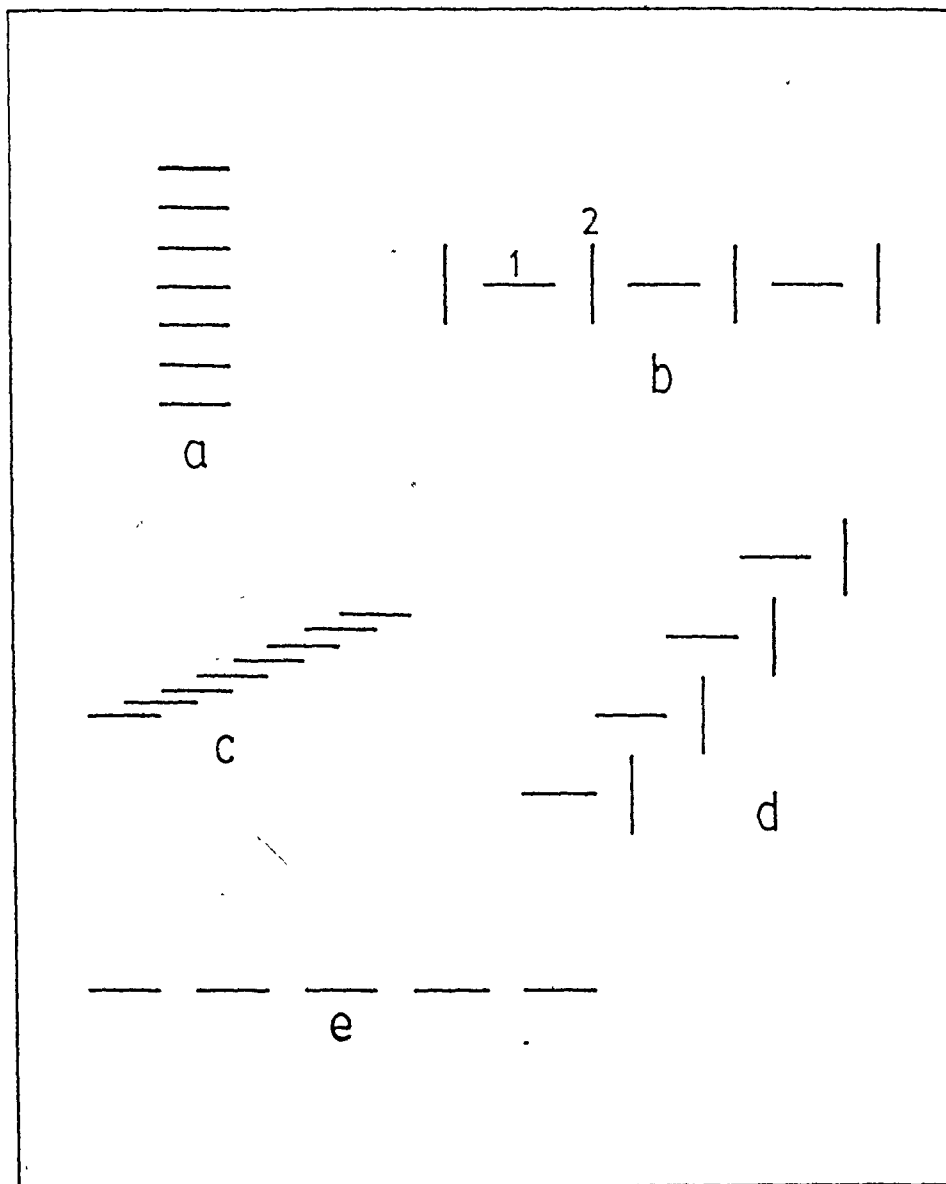


Fig. 59 Schematic representation of some linear arrays.

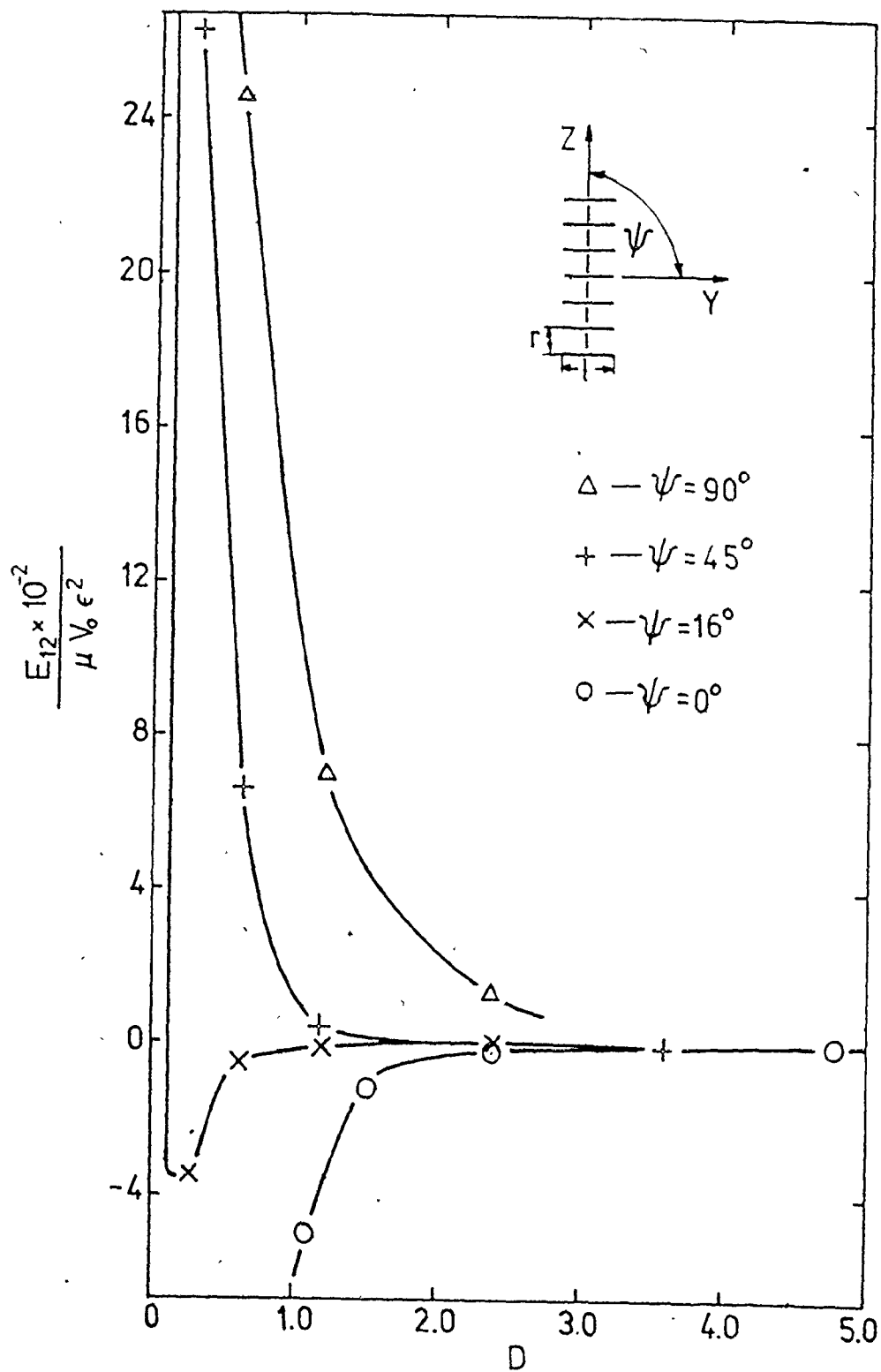


Fig. 60 The total elastic interaction energy of the linear array of equal size parallel particles (per central plate) as a function of the inclination angle and distance between the plates. The energy was calculated between the central plate and 9 particles the z .

goes from repulsive ($\psi = 90^\circ$) for any separation to attractive ($\psi = 0^\circ$), for any separation. The most important result was obtained for angles about 20° ; in these cases potentials possess a minimum for very small separations, indicating that the hypothetical array shown in Fig. 59(c) is energetically stable. In fact, this type of array was often observed. Note that the very attractive array ($\psi = 0^\circ$) has not been observed experimentally (nor has the configuration shown in Fig. 59(b)). This suggests that the nucleation event was somehow prevented. This point will be discussed later (see Figs. 67 and 68) when it will be shown that nucleation energetics will promote the development of arrays of the type shown in Fig. 59(c).

The interaction energy of the hypothetical linear array given in Fig. 59(d) is shown in Fig. 61. The potential possesses a minimum for a separation of about 1.5 plate lengths, and the inclination angle $\psi = 45^\circ$. Again, the interaction energy depends strongly on separation. This type of array was also found in the present observations.

A similar potential (per pair of precipitates) is shown in Fig. 62. This corresponds to the array of Fig. 59(b). Here, the minimum is less pronounced and appears at a larger separation.

So far this discussion has been concerned with interactions between equal-size particles. Experimentally, smaller θ' precipitates were often observed between large ones, (which again do not appear to be connected with dislocations). It

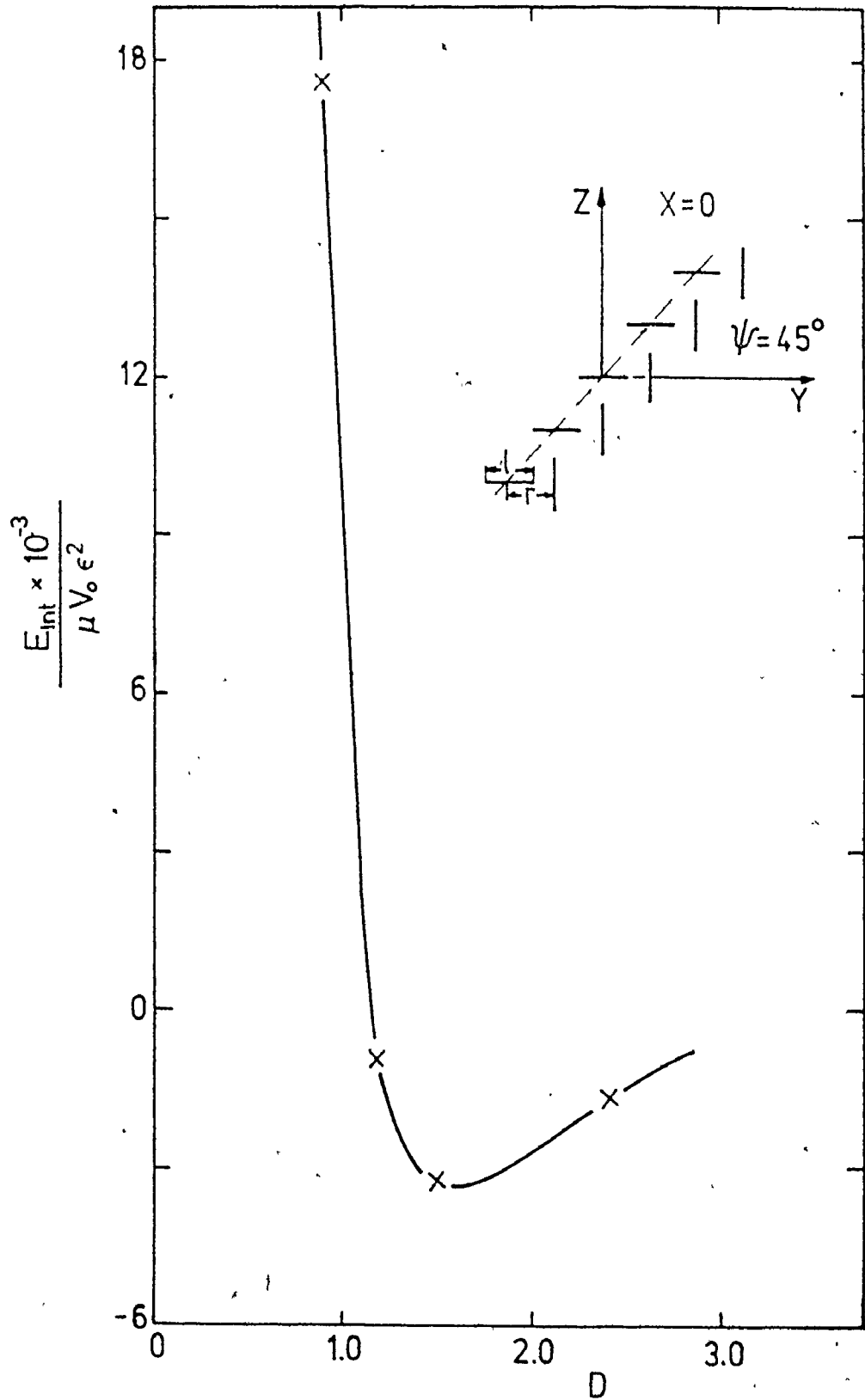


Fig. 61 The total elastic interaction energy of the linear array of equal size particles (per central plate) vs distance between the plates. The array is made up of parallel plates (the incination angle $\psi = 45^\circ$) and of perpendicular particles (edge-face configuration).

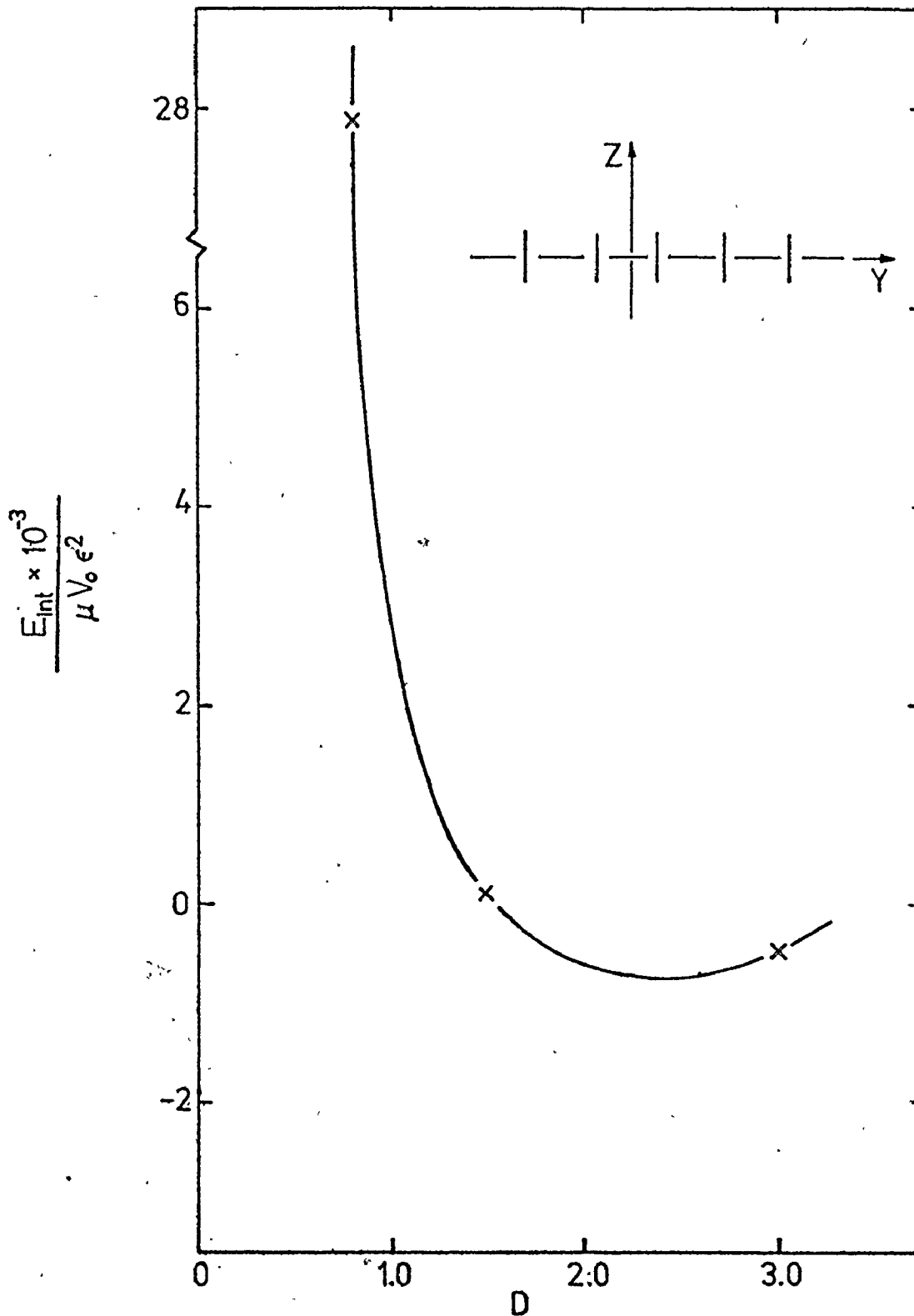


Fig. 62 The total elastic interaction energy of the linear array of equal size particles (per pair of central precipitates) vs the distance between the plates. The array is formed from parallel plates (with inclination angle $\psi = 0^\circ$) and from perpendicular plates (edge-face

has been suggested (103) that these smaller precipitates are formed in the stress field of those already present. For application to the nucleation event the elastic interaction between large and small particles was calculated using the methods discussed previously.

The interaction energy between large and small precipitates (the size ratio in all calculations was 1/10) versus separation is shown in Fig. 63 for the edge-face configuration. Comparing this result with the potential given in Fig. 55 it can be seen that the minimum in the curve is shifted towards the edge of the large particle. This configuration is very often observed experimentally. The stability of the configuration which corresponds to the minimum in the potential curve given in Fig. 63 can be further assessed from Fig. 64, where the small particle has been displaced in the z direction. Any displacement of the small particle along the z axis increases the energy sharply until, for a value of Δz about 0.6 times the length of the small particle, the interaction becomes repulsive.

Another interesting result is obtained for the face-face configuration. When the small particle is coaxial with the larger particle (Fig. 65) the interaction is repulsive, for any separation (see Fig. 54). Moving the small particle in the y direction causes the potential monotonically to increase until about 0.35 times the larger particle length. At that point it begins to increase sharply, reaching a maximum

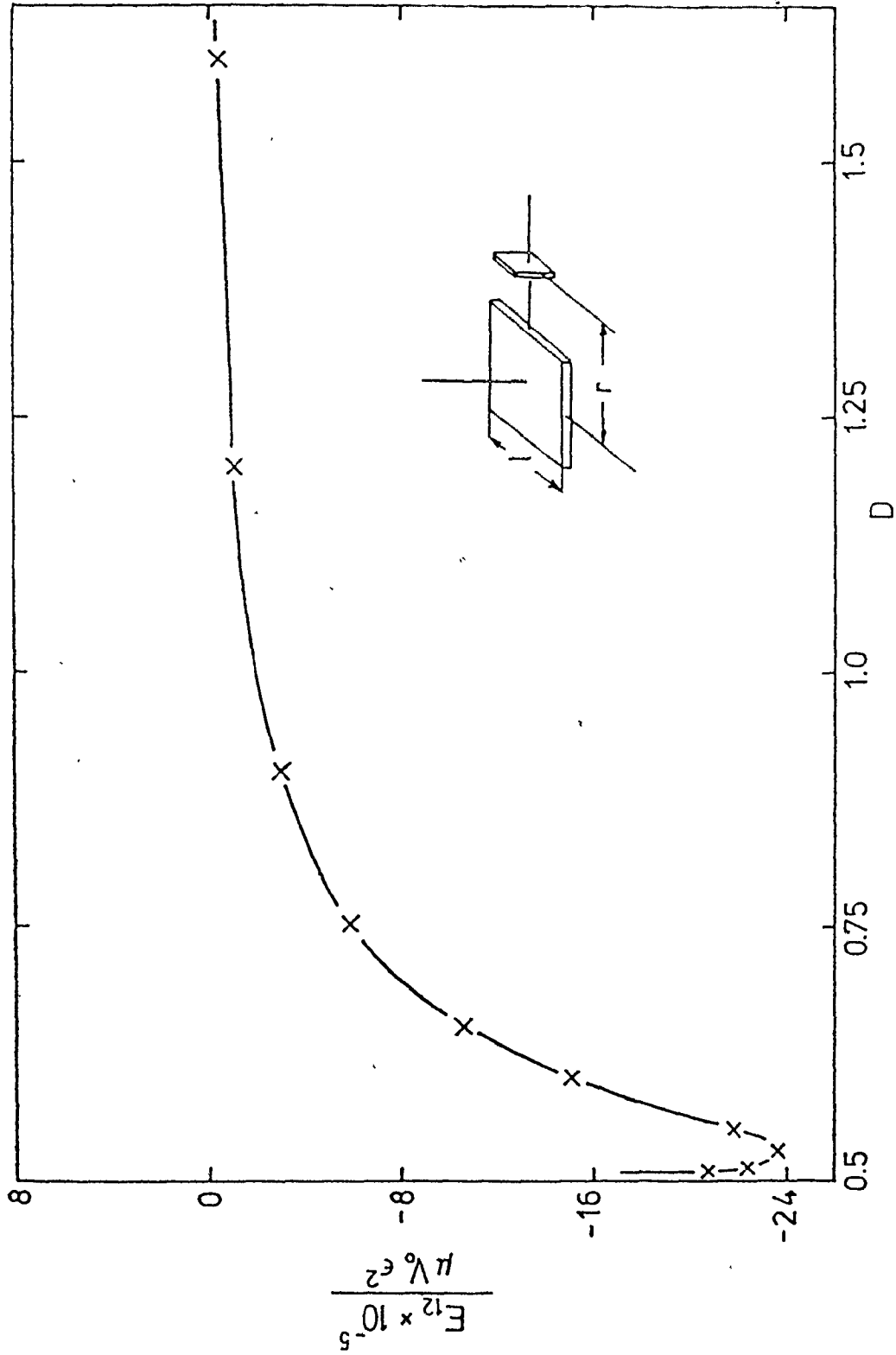


Fig. 63 Interaction energy between large and small particles when they are mutually perpendicular (edge-face configuration) as a function of separation. (The size ratio in this and all similar calculations was 1/10).

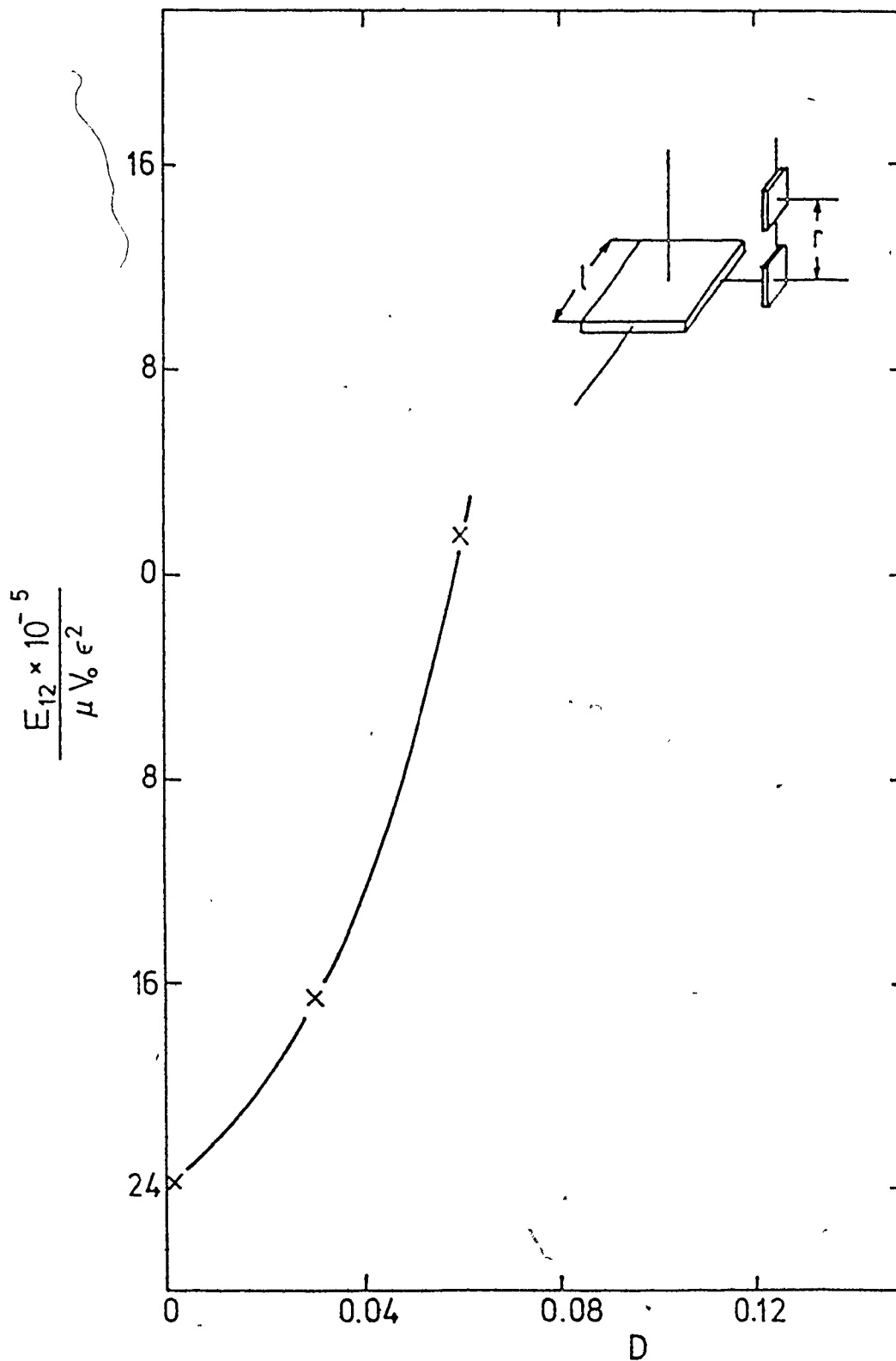


Fig. 64 The change of elastic interaction energy (for a pair initially at the minimum in the potential curve of Fig. 63) as a function of the displacement of the small particle along the z-axis.

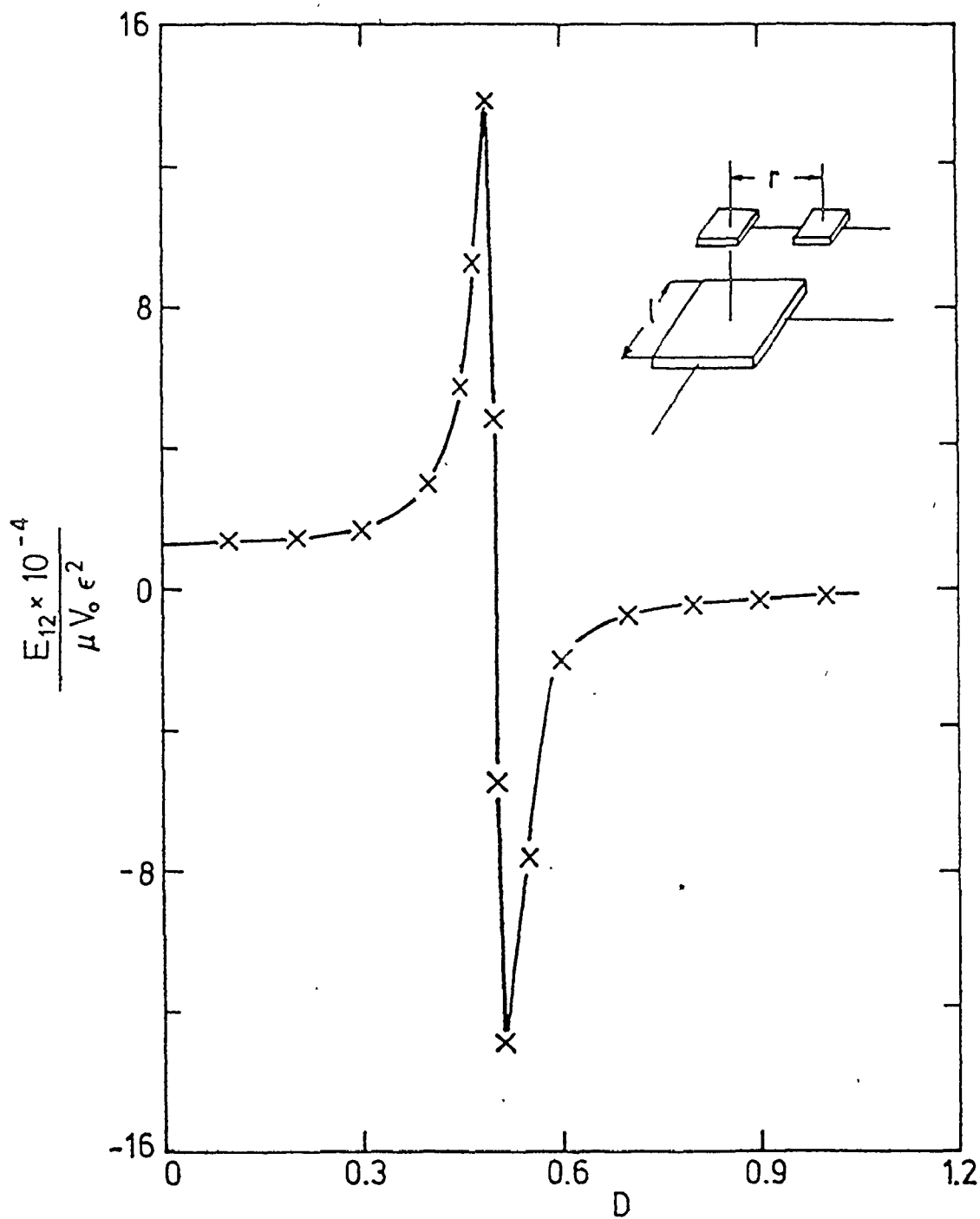


Fig. 65 The change of elastic interaction energy between large and small particles when they are mutually parallel (face-face configuration) as a function of the displacement of the small particle along the y-axis.

at the edge of the large particle. Further displacement causes a very sharp drop in the potential, bringing the particle into a stable position. (A similar interaction potential is obtained between an edge dislocation and a prismatic dislocation loop).

Returning now to the problem of strain induced nucleation, it is clear from the potential shown in Fig. 65 that the most likely place for the nucleation of the new particle is near the edge of an existing large one. Keeping this in mind, it is not difficult to imagine the autocatalytic formation of inclined stacks of parallel plates. A similar, but less pronounced effect is obtained for the edge-face configuration, Fig. 66.

As already mentioned, the hypothetical array shown in Fig. 59(e) of equal-size particles is attractive (see Fig. 60; $\psi = 0^\circ$), but was not observed experimentally. In order to determine the favourable nucleation site, interactions between large and small particles in the configuration which would lead to the array shown in Fig. 59 were evaluated. The potential is shown in Fig. 67 which clearly shows that it is attractive for any separation.

The stability of the configuration which corresponds to the minimum in the potential curve given in Fig. 67, was then tested by moving the small particle in the z-direction, (Fig. 68). Displacement of the small particle along the z-axis decreases the energy further, indicating that the array

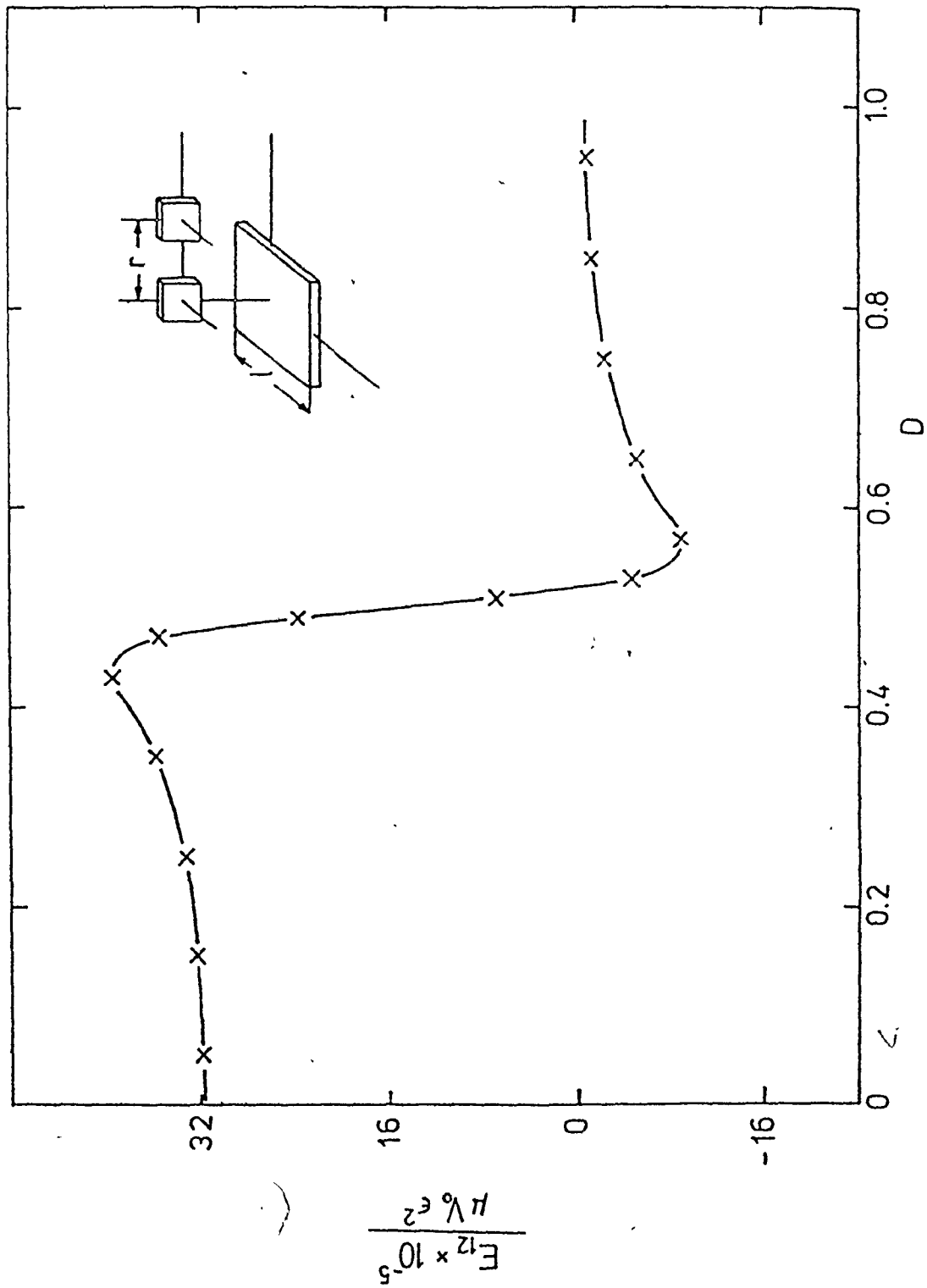


Fig. 66 Interaction energy between large and small particles when they are mutually perpendicular (edge-edge configuration) as a function of the displacement of the small particle along the y-axis.

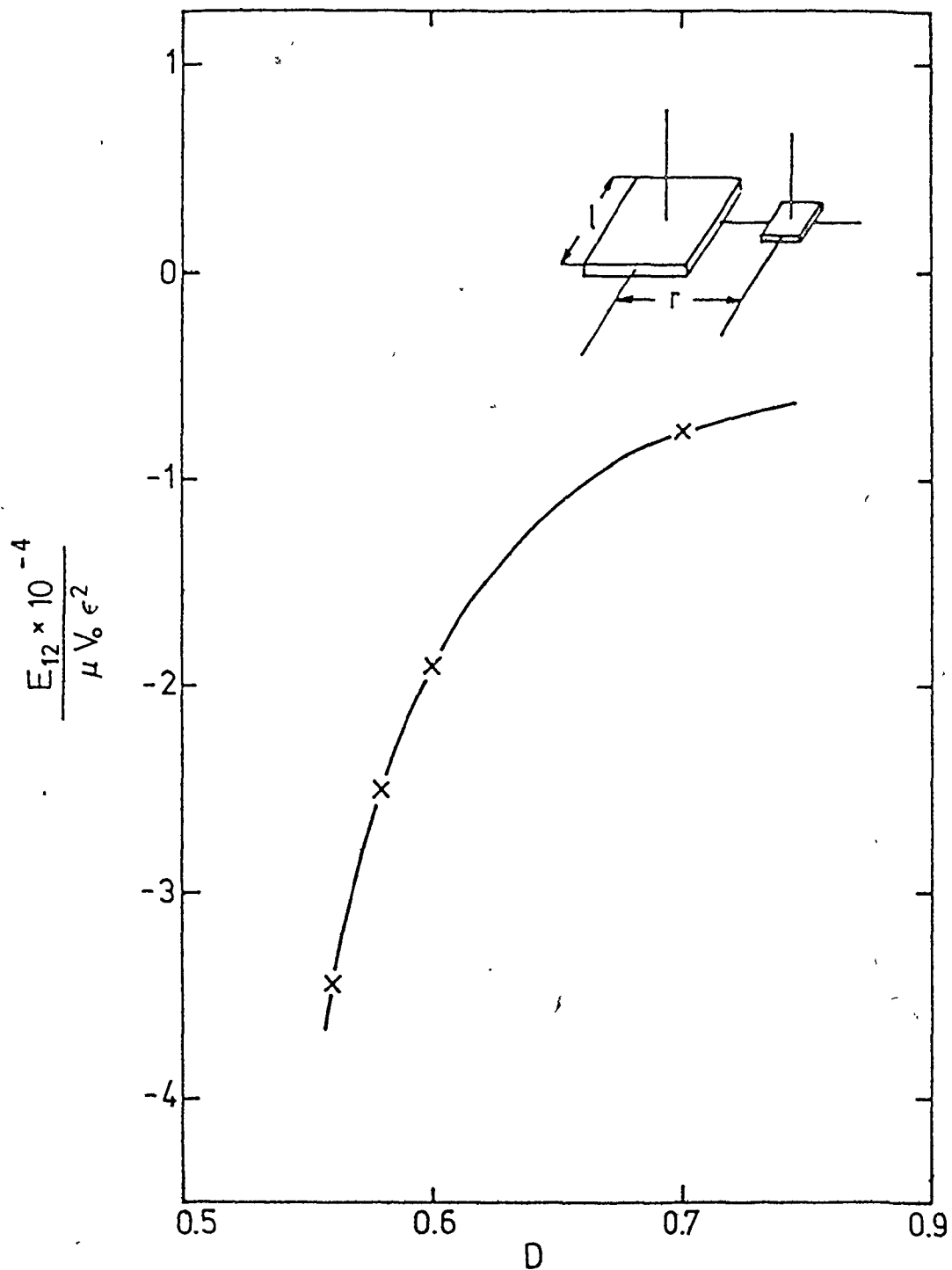


Fig. 67 Interaction energy between large and small particles when they are mutually parallel (face-face configuration; inclination angle $\psi = 0^\circ$) as a function of separation.

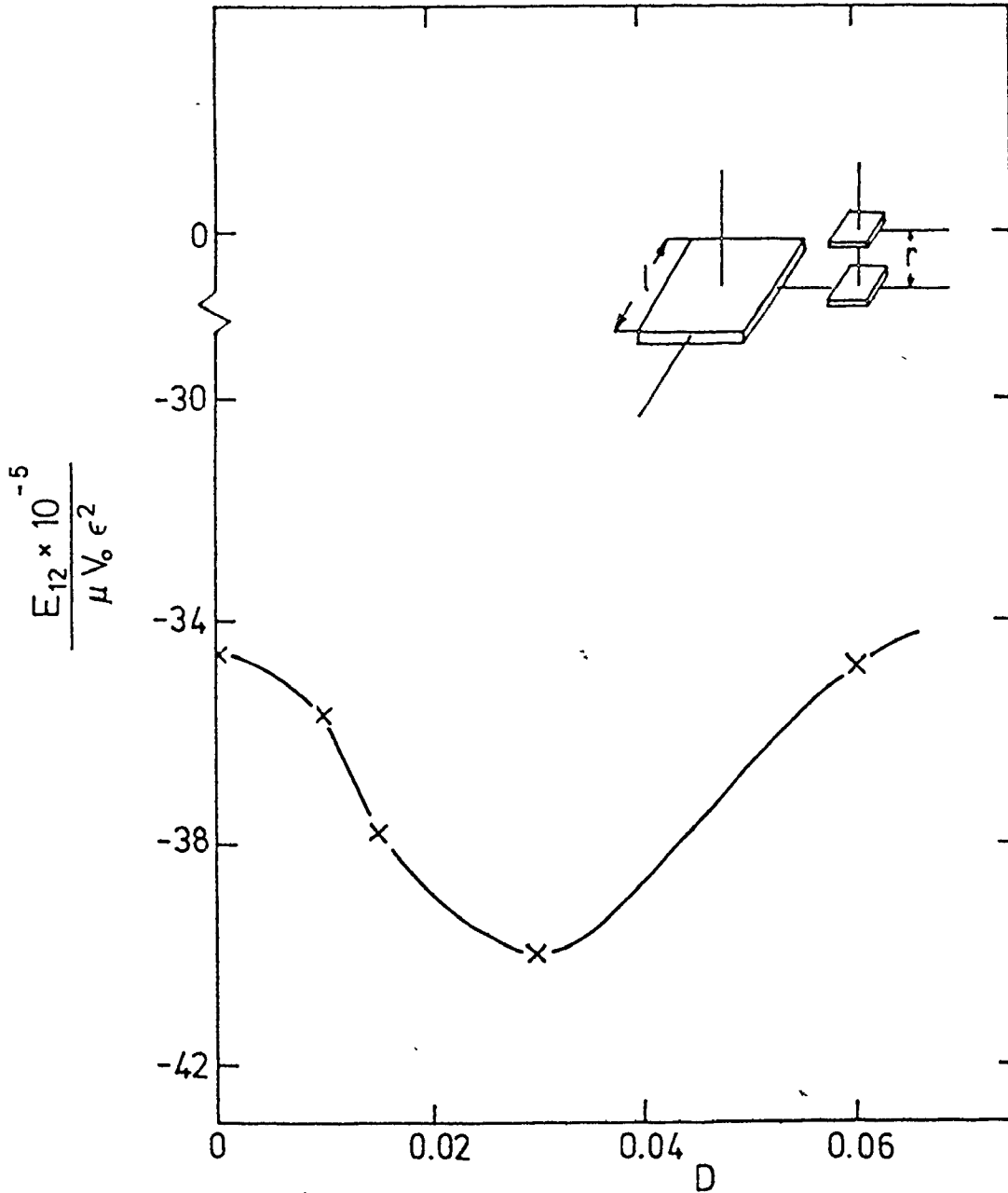


Fig. 68 The change of elastic interaction energy which corresponds to the minimum in the potential curve given in Fig. 67 as a function of displacement of the small particles along the z -axis.

of Fig. 59(e) will not be developed during nucleation. (A similar argument can be made for the array of 59(b)).

In all the above calculations a constant mismatch was assumed for all particles. Stobbs and Purdy (103) have recently shown that the misfit of semicoherent discs is not necessarily constant during particle thickening but is subject to periodic variation in magnitude and sign even before accommodation of the residual misfit of the thicker plates by the nucleation or capture of dislocations. Allowing the misfit to change sign and magnitude, it would be not difficult again to imagine a significant, but more complex, elastic interaction during nucleation. However, from Fig. 65, the favourable site for strain induced nucleation of small particles is roughly independent of the sign of the misfit.

3.2.2 THE STABILITY AGAINST GROWTH OF PARTICLES IN STACKS

3.2.2.a RESULTS

Observations were made on specimens aged at 240°C up to 23 h so that the θ' microstructure was well into the growth stage: Figs. 69 and 70 represent stacks at an early stage of development. These stacks have the same characteristics discussed earlier in section 3.2.1. Again, it should be recalled that the matrix around the stacks is supersaturated.

After holding the samples for 9 hours at 240°C, evidence for an impediment to growth (lengthening) was obtained, e.g. Fig. 71; the θ' particles in the stacks are much smal-

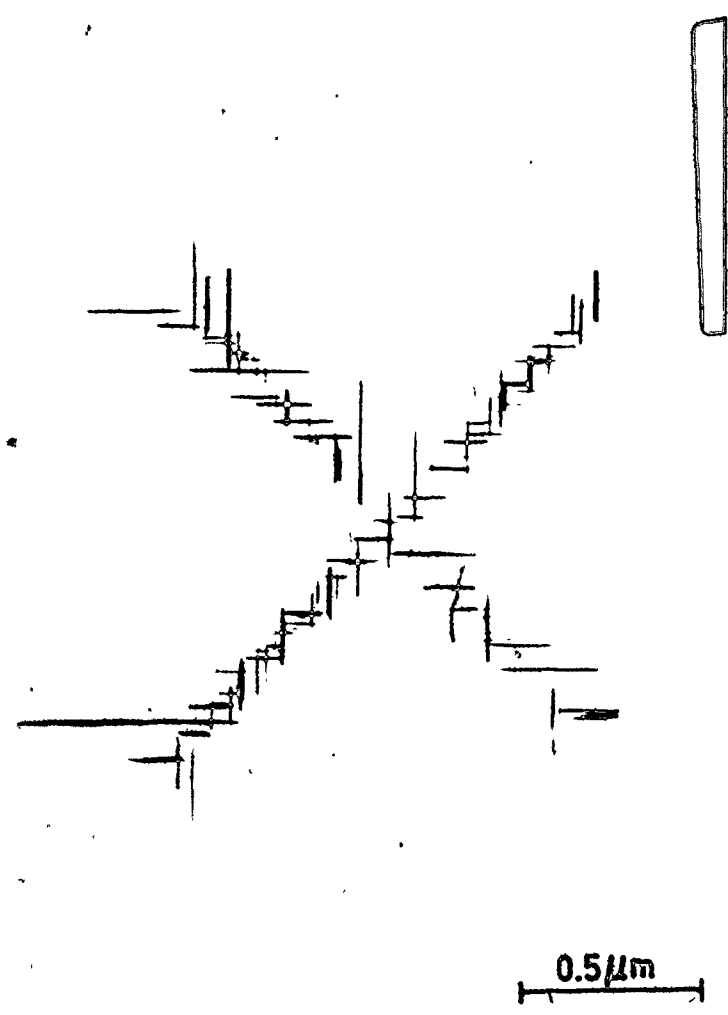


Fig. 69. Al-3% Cu crystal with (001) orientation, solution-treated and aged 1 hour at 240°C. Bright field micrograph shows stack development in relatively early stage. Note supersaturated matrix around the stack (53250x).

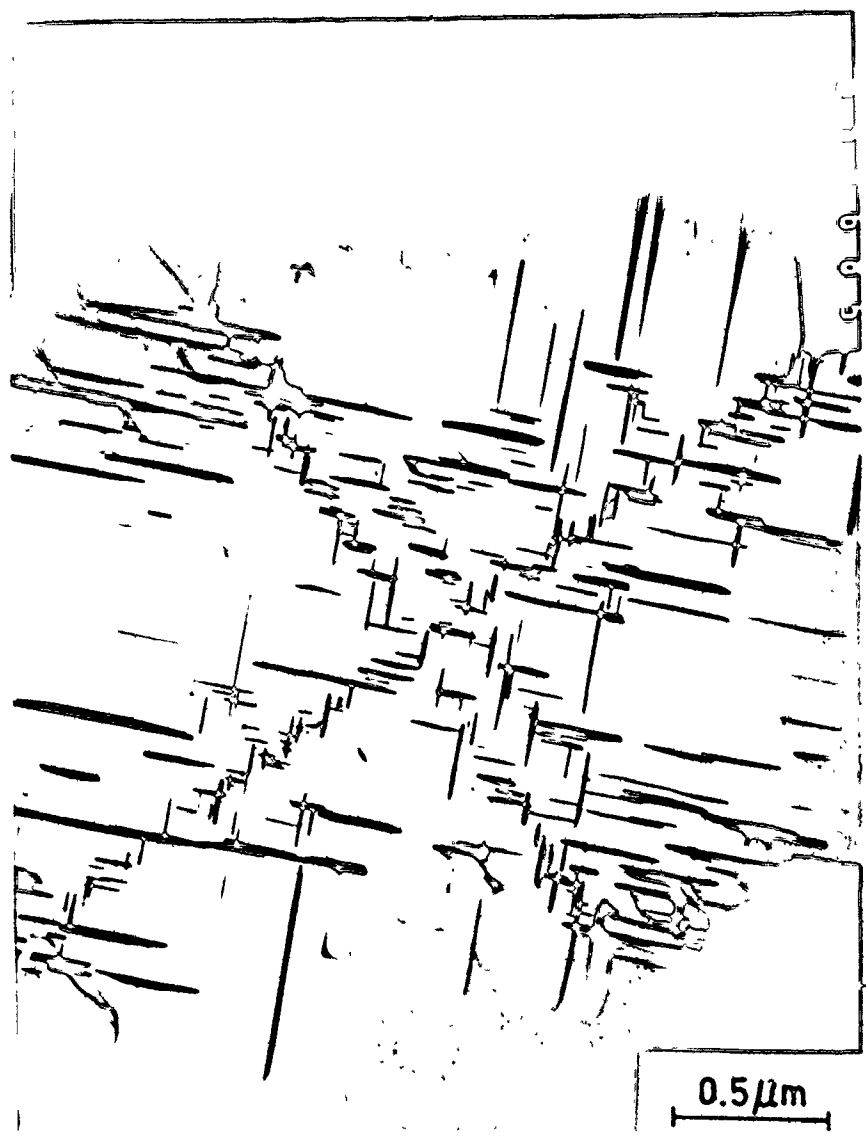


Fig. 70 Al-3% Cu crystal with (001) orientation, solution treated and aged 3 hours at 240°C. Bright field micrograph shows development of new θ' particles in the stack and around the stack (41250 \times).



Fig. 71 Al-3% Cu crystal with (001) orientation, solution-treated and aged 9 hours at 240°C. The θ' particles are much smaller than the θ' plates in the surrounding matrix. Particles on the ends of the stack are much longer than those within the stack (53250 \times).

ler than the particles in the surrounding matrix.

From the results given earlier above it is obvious that the stacks formed first; they must therefore be somehow stabilized against growth. It should also be noted that the θ' particles at the ends of the stack are much longer than those within the stack.

Similar results were obtained after 23 hours at 240°C, Fig. 72. Here, both stable configurations discussed in section 3.2.1 are present, and again it is seen that the θ' particles within the arrays do not appear to have grown. This again suggests that the stacks are elastically-locked and stabilized against growth in much the same way as proposed in section 3.1.4 for the three-dimensional case.

To summarize these observations of stack stability, it has been demonstrated that particles in the stacks may resist growth. In the first part we have shown that the stacks are very probably formed in an autocatalytic fashion. These arrays appear to be stable against growth even in the presence of high chemical driving force.

147a

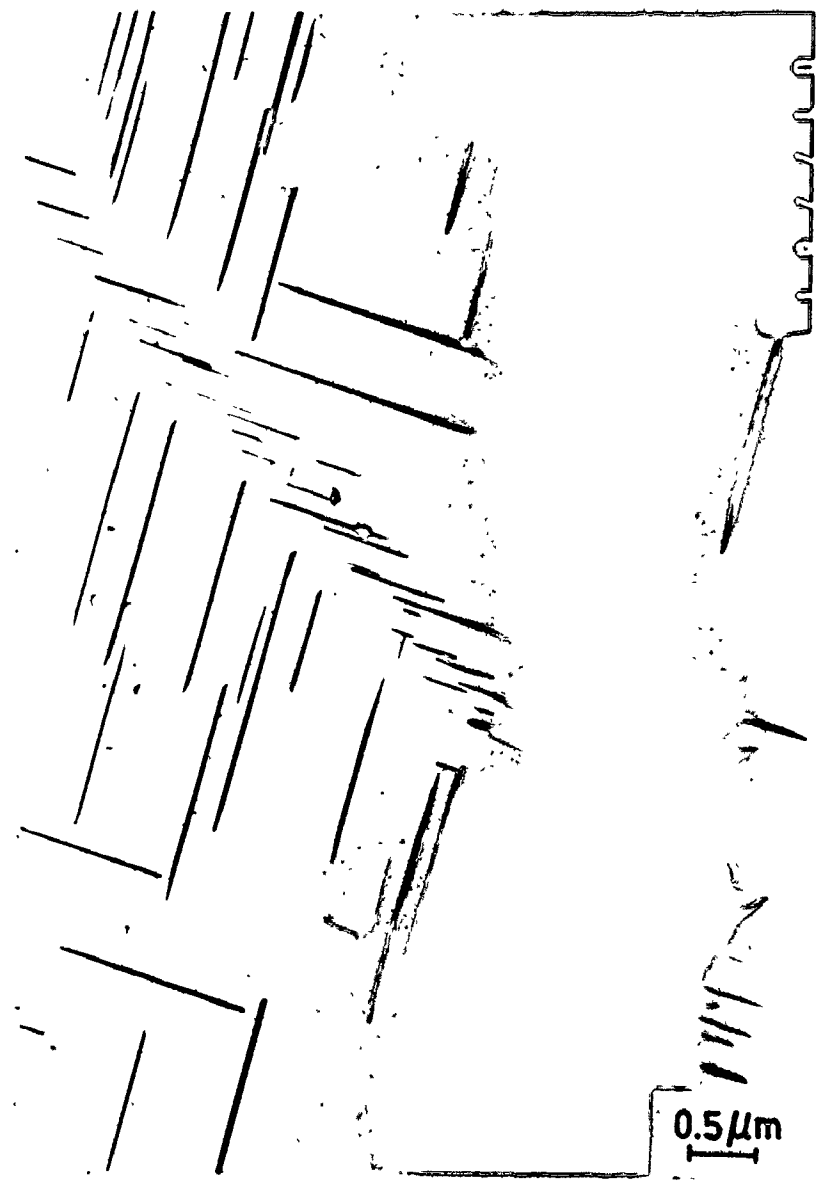


Fig. 72 Al-38 Cu crystal with (001) orientation, solution treated and aged 23 hours at 240°C. Bright field micrograph shows the stack possible elastically stabilized against growth. Note much longer θ' particles in the surrounding matrix (18750 \times).

3.2.2.b NUMERICAL ESTIMATIONS OF STABILITY

To show how the elastically-locked stacks may be stable against growth, the interaction energy was calculated for certain model arrays (Fig. 59(c)-(d)), for the case where a particle in the middle of the stack is allowed to grow (lengthen) into the matrix.

The results of these calculations are given in Figs. 73, 74 and 75, for several stable inclined arrays of parallel θ' plates.

The central particle was allowed to increase its length in one direction (Fig. 73) and in both directions (Fig. 74). The result in both cases is similar: The elastic interaction energy increases sharply as soon as the growing particle starts to overlap its first neighbours. This is consistent with the potential shown in Fig. 57. This result also shows clearly that stability is controlled in the main by interactions with first neighbours.

Fig. 75 represents stability calculations for the array of minimum energy (Fig. 60, $\psi = 16^\circ$). It shows that the elastic interaction energy increases much more sharply compared with the less stable arrays of Figs. 73 and 74.

The other kind of stable stack (Fig. 59(d)) shows similar behaviour (Fig. 76).

The observation that the last particles in the stacks are much longer than the particles within the stacks suggests that these larger particles were free to grow.

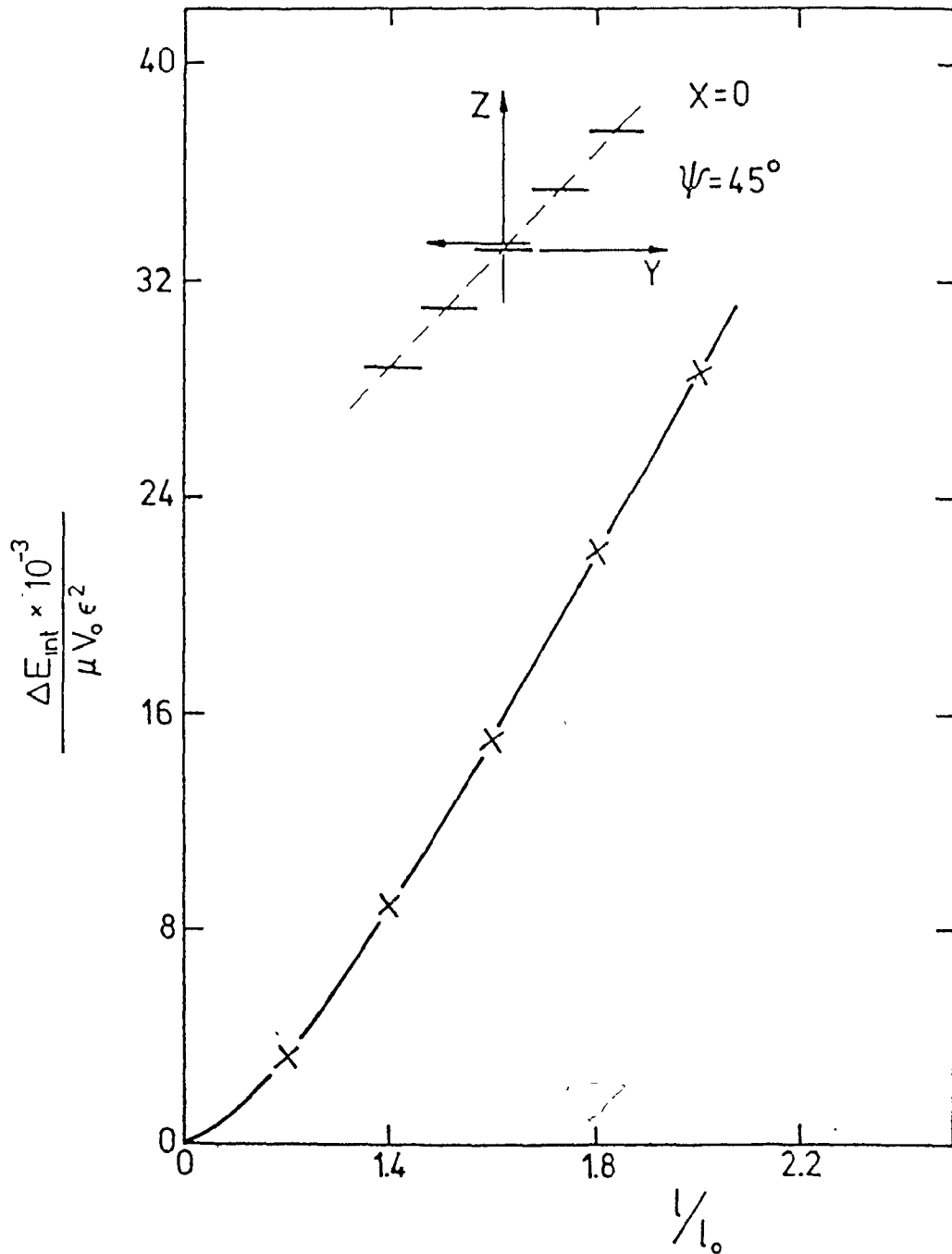


Fig. 73 The change of elastic interaction energy of the linear array of parallel plates (inclination angle $\psi = 45^\circ$, and vertical separation 1.2 times the plate length) due to lengthening of the central plate into the matrix. The rest of the particles in the array have equal dimensions. The central particle was allowed to increase to length in one direction as indicated by the arrow.

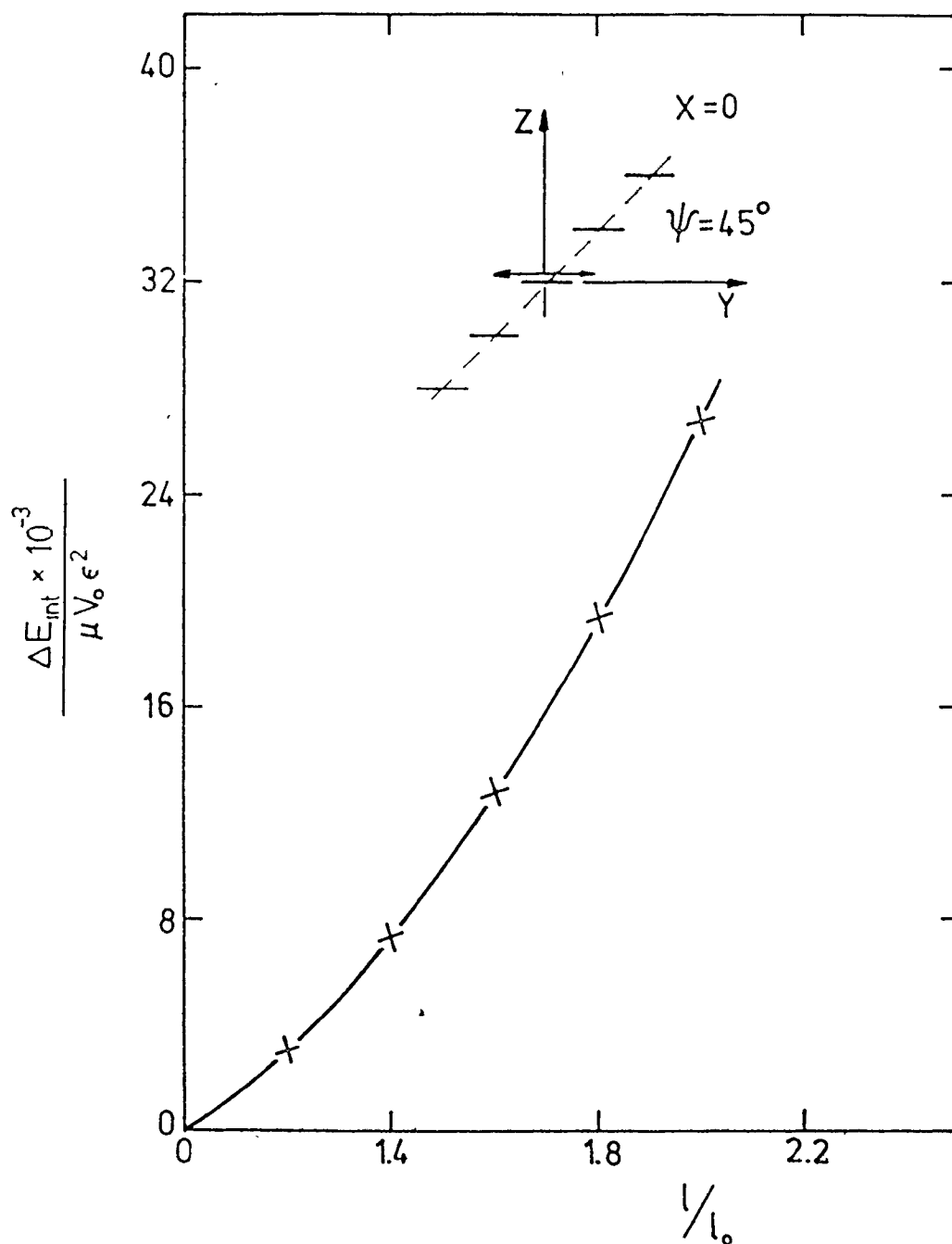


Fig. 74 The change of elastic interaction energy of the linear array of parallel particles (inclination angle, $\psi = 45^\circ$, the vertical separation is 1.2 times the plate length) due to lengthening of the central particle into matrix. The central particle was allowed to increase its length in two directions.

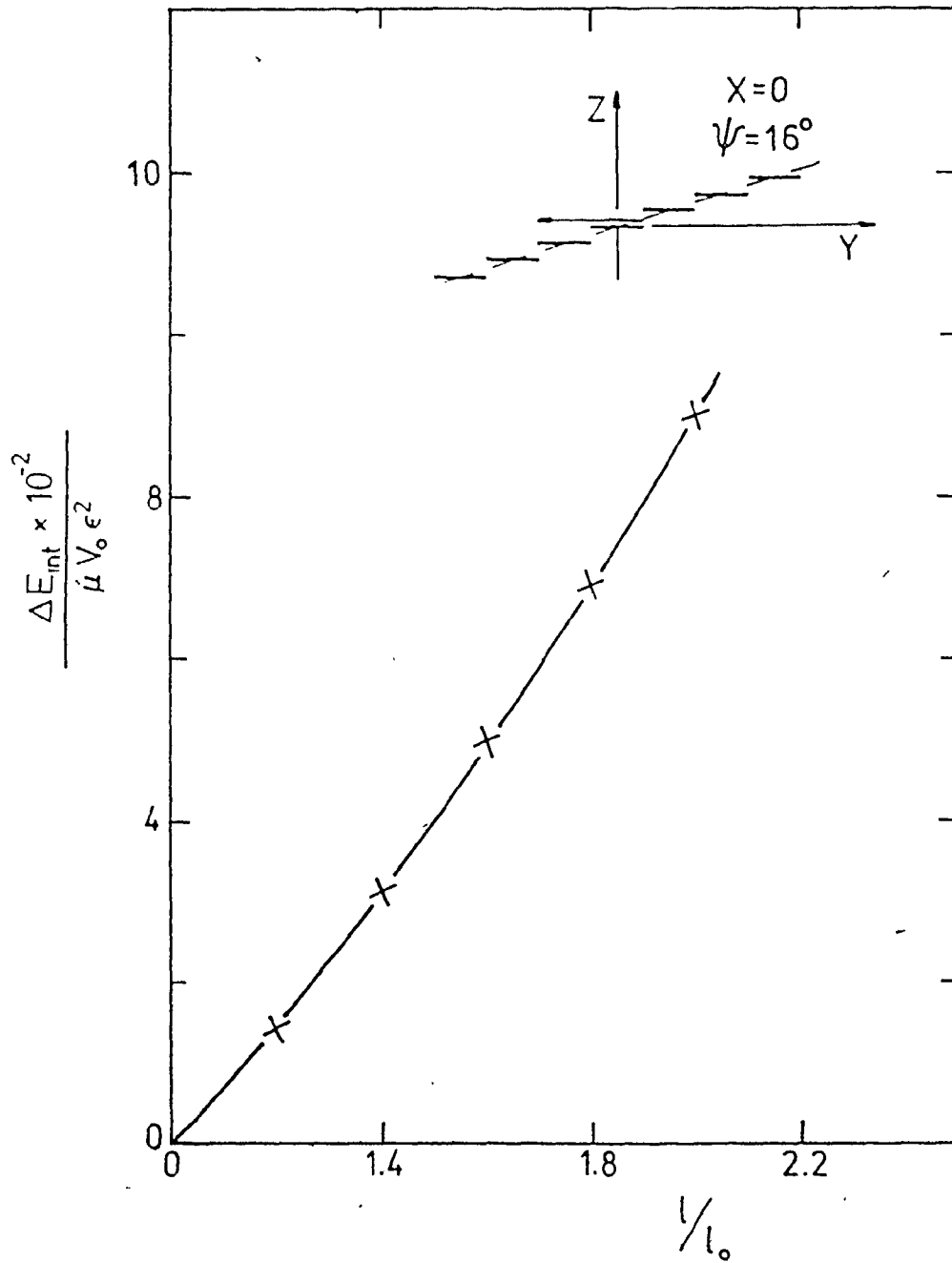


Fig. 75 The change of elastic interaction energy of the linear array of parallel particles (inclination angle $\psi = 16^\circ$, vertical separation 0.3 times the plate length) due to lengthening of the central plate. The central plate was allowed to increase its length in one direction only.

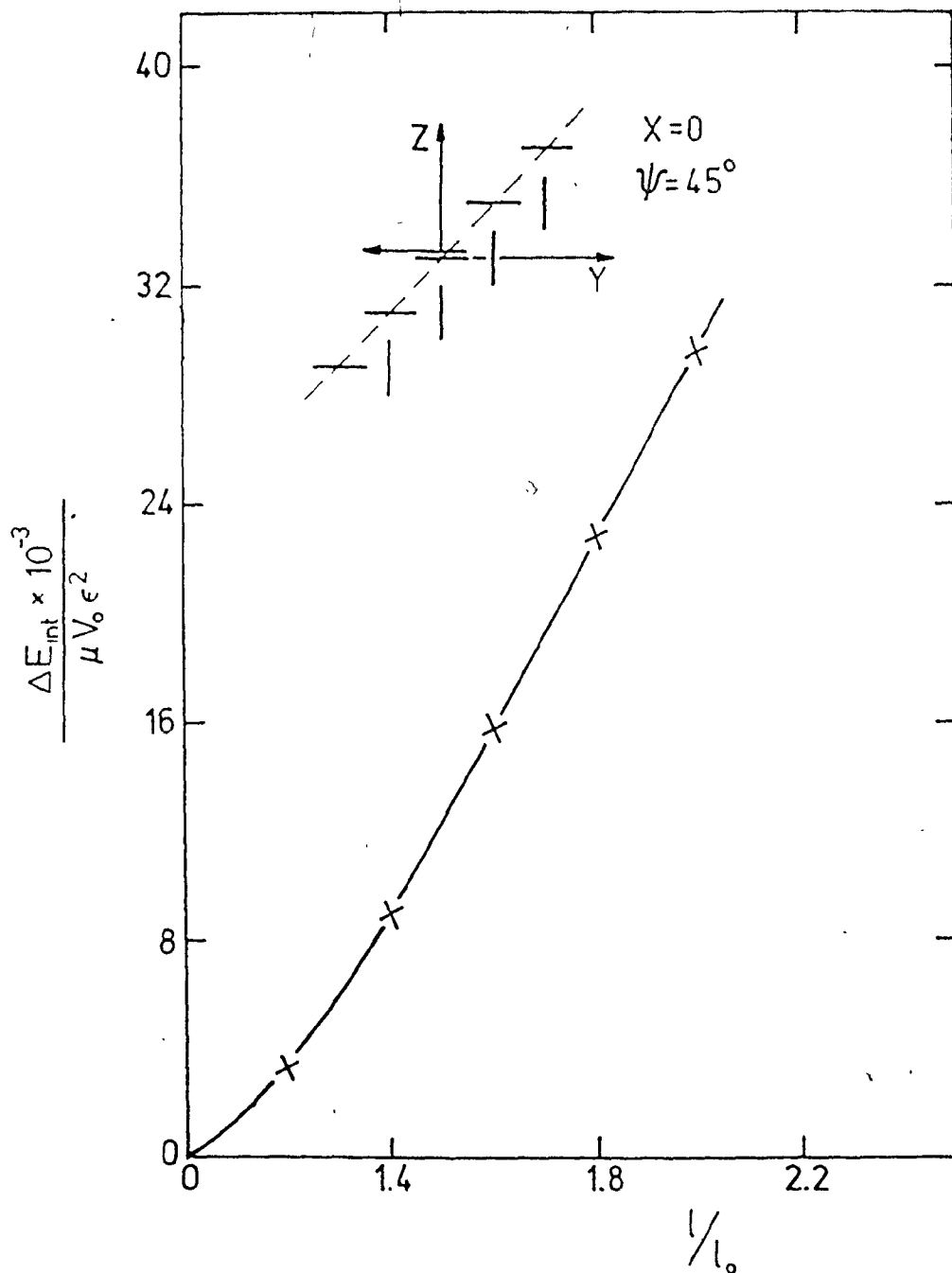


Fig. 76 The change of elastic interaction energy of the linear array due to lengthening of the central plate into the matrix. The central plate was allowed to increase its length in one direction. The array is formed from parallel plates (face-face configuration, $\psi = 45^\circ$, vertical separation 1.2 times the plate length) and perpendicular plates (edge-face configuration with the centre-to-centre distance 1.2 times the plate length).

To check this, the last particle in the model stack was allowed to grow; Fig. 77. This calculation shows that the potential decreases sharply with particle growth, suggesting that once the stack development stopped, the particles at the ends were not constrained and were therefore free to grow. It is thus demonstrated that the stacks are stable against growth.

These calculations are for growth into a supersaturated matrix. The possibility that the particles are prevented from growing by local solute depletion was not considered; clearly, however, this is a viable alternative explanation or an additional reason for the observed stability against growth; in many cases the plates could well have stopped because of overlap of solute fields from neighbouring precipitates.

The stability of the elastically stable stacks against coarsening has also been examined, by choosing the array of the equal size parallel precipitates with the lowest energy (Fig. 60; $\psi = 16^\circ$) and allowing volume exchange between the first neighbours in the centre of the stack.

The result of this calculation is given in Fig. 78 and clearly shows that the stack is also stable against coarsening.

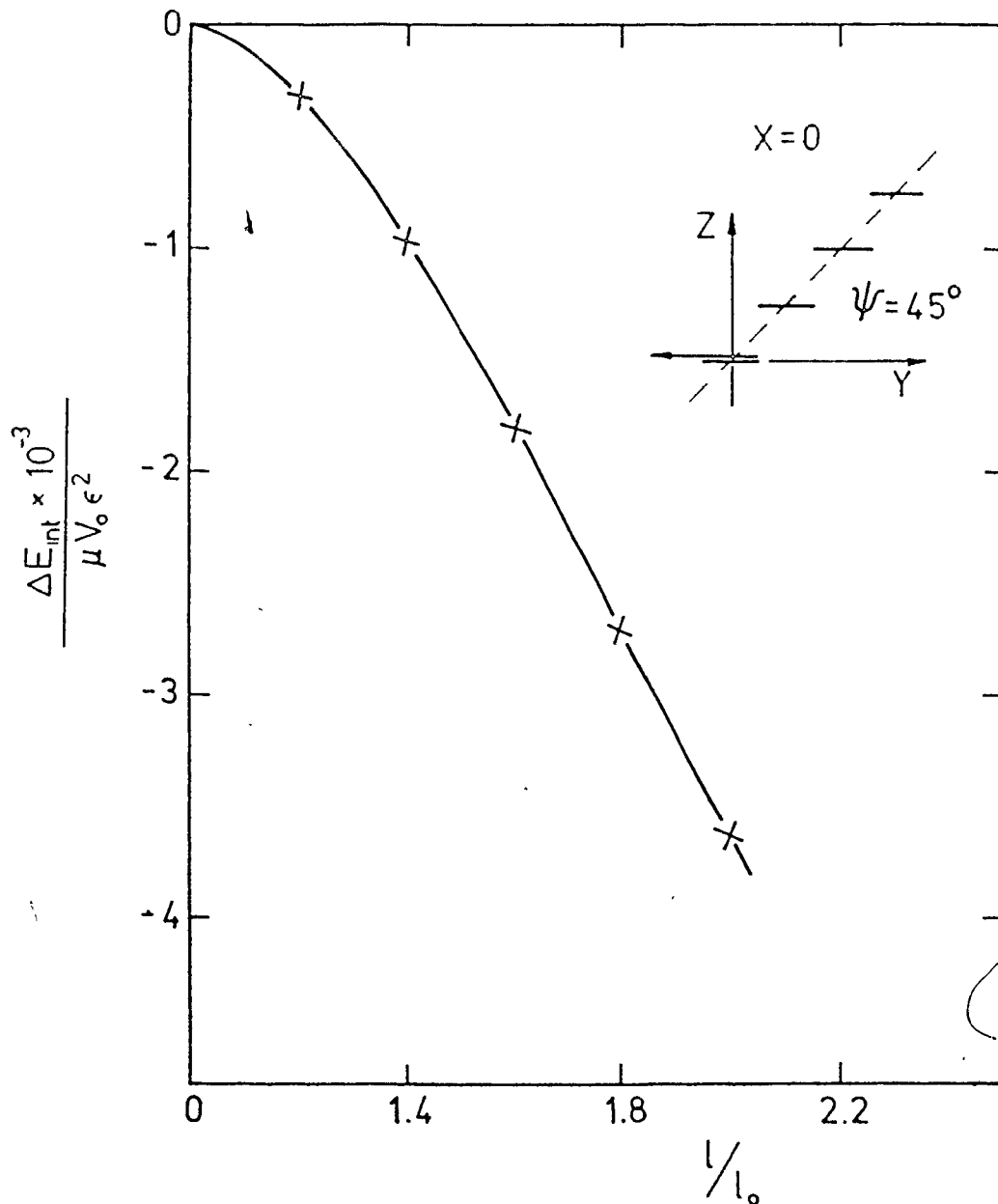


Fig. 77 The change of elastic interaction energy of the linear array of parallel particles (face-face configuration, $\psi = 45^\circ$, vertical separation 1.2 plate lengths) due to lengthening of the last particle in the array. The particle was allowed to grow in one direction.

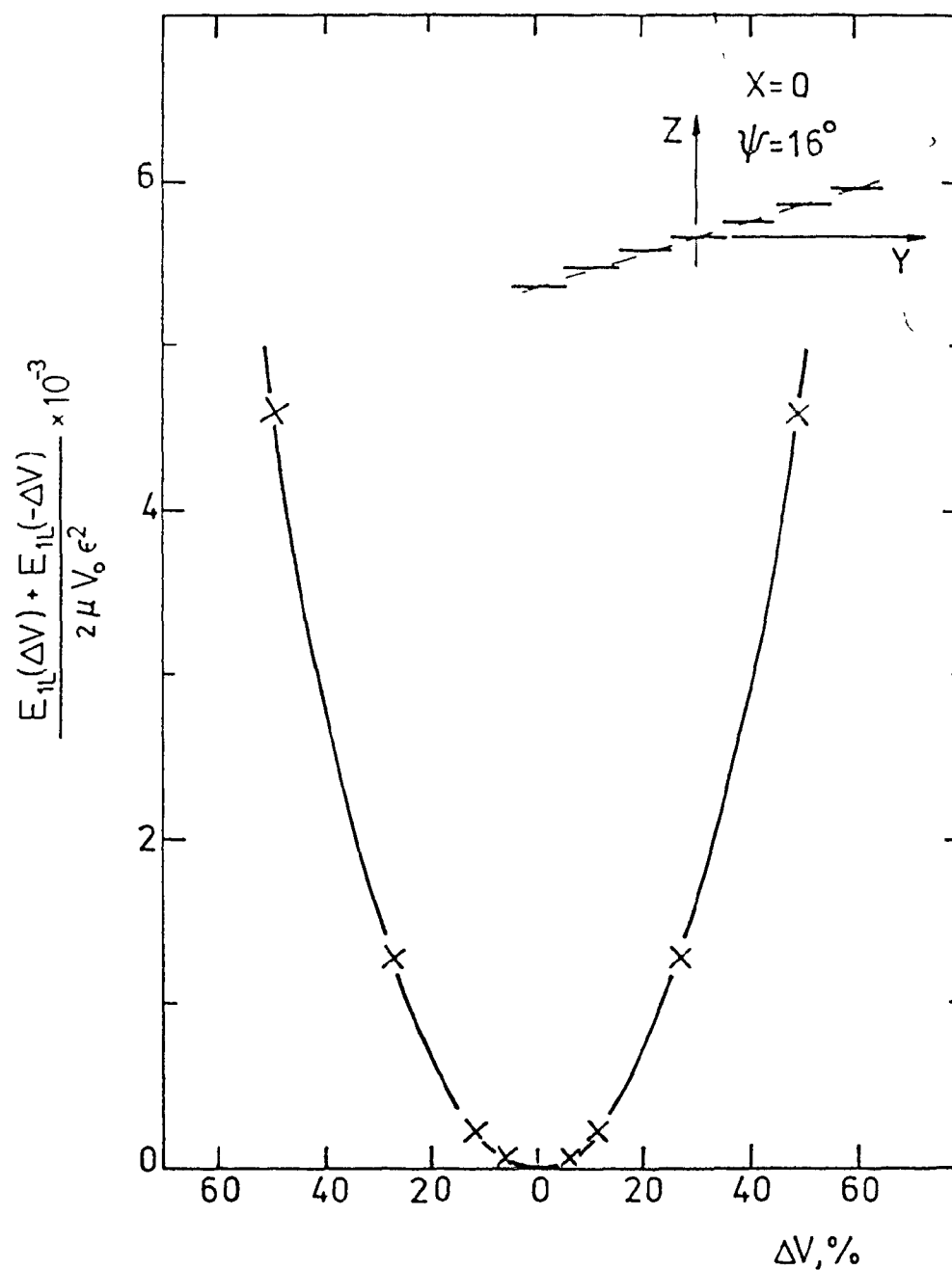


Fig. 78 The change of elastic interaction energy of the linear array of the parallel particles (face-face configuration, $\psi = 16^\circ$, vertical separation 0.3 times the plate length) due to volume exchanges between the central plate and its first neighbour.

3.2.3 DISCUSSION

These observations demonstrate that the formation of stacks of θ' precipitates is a prominent feature in the early stage of θ' microstructural development. Certainly, as already discussed, dislocations occasionally play a role in initiating or even in propagating linear chains. However, the weight of the present evidence is that θ' strain fields are effective in nucleating subsequent θ' particles and that it is this autocatalytic effect which is dominant in microstructural development under the conditions employed here.

Thus it is suggested that the first-formed precipitates were nucleated heterogeneously (perhaps on quenched-in defects) and that the nucleation of the subsequent precipitates generally occurred in the strain fields of their predecessors.

Nakada et al. (101) and Hosford and Agarwal (102) have demonstrated that even a very small applied stress during ageing has a large effect on the stability of certain precipitates. θ' is particularly susceptible to this influence.

The present observations and analysis indicate that the energetics of fully developed one-dimensional arrays is a good preliminary guide for their prediction. However, a more detailed analysis, involving relative sizes more typical of the nucleation stage, is required to distinguish the more probable arrays.

From these considerations of elastic interaction it is clear that the elastic-interaction energy depends strongly on the relative positions of the precipitates. Providing that the driving force for overall homogeneous nucleation is small, the role of elastic interactions must predominate in controlling the θ' morphology in its early stage.

Some preliminary evidence for the elastic stabilization of particles within stacks has also been obtained. The θ' particles in the stacks resist growth, and it is shown that this is consistent with the stability analyses. One can further distinguish between configurations which are stable against all modes of lengthening (eg: Fig. 69), and those which are unstable with respect to synchronous lengthening (eg. Fig. 72). Again, the present experimental evidence suggests that synchronous growth of parallel plates does not occur to any appreciable extent.

It is probable that plates within a linear chain will generally be stabilized with respect to coarsening. These preliminary investigations have failed to disclose any specific coarsening modes that lead to instability.

It is concluded that elastic interaction among precipitates plays a determining role in the formation and stabilization of one-dimensional arrays of precipitates; the evaluation of microstructure in this system is evidently heterogeneous and critically dependent on local interactions.

3.3 THE ELASTIC INTERACTION OF THE LEDGES ON PLATE-SHAPED PRECIPITATES

3.3.a INTRODUCTION

It has long been recognized that one of the principal mechanisms for interface motion during growth and dissolution processes involves the lateral movement of steps along an interface (104-114).

In particular cases where the precipitate and matrix crystal structures are related by a plane strain transformation, the structure of these ledges is simple and the precipitate can grow or shrink by the movement of glissile transformation dislocations (115). For more complex crystal structures, the ledges will probably not be glissile and may be several atom planes high.

Laird and Aaronson (116) observed ledge migration during the dissolution of θ' plates in an aluminum-copper alloy and deduced that the ledges were approximately 20 \AA high. Electron diffraction contrast from ledges at the interfaces of faceted θ' precipitates has been described by Weatherly and Sargent (72) (see section 1.5.b). A detailed study of the image enables the sense of the ledge to be determined; i.e. whether it is in fact a growth or dissolution ledge, and an approximate determination of the ledge height to be made. Recently, Stobbs and Purdy (103) reported that elastic misfit associated with θ' particles and ledges is not constant during

initial particle thickening but is subject to periodic variations in magnitude and sign. Weatherly (117) and Sankarn and Laird (118) have discussed the origin of steps on ". It seems that they are often nucleated "homogeneously" as pill-boxes during initial growth and form readily and heterogeneously at precipitate intersections, which become numerous during prolonged coarsening, as well as at the edges of precipitates which are dissolving.

As described in ref. (72) when a matrix reflection lying in the plane of the plate is excited in the transmission electron micrograph, a weak double image is observed with a line of no contrast running perpendicular to \vec{g} (see section 1.5.b; Fig. 12(d)). This contrast is typical of prismatic dislocation loops when $g \cdot b = 0$, and the contrast arises from the secondary displacements around the loops (71). The strain field of the precipitates is thus expected to be very similar to those of prismatic dislocation loops.

3.3.1 THERMAL NUCLEATION OF GROWTH LEDGES

Consider the nucleation of simple square plate-like ledge of length ℓ and thickness d at a planar precipitate-matrix interface, of the same shape. The energy change accompanying the formation of this ledge is,

$$\Delta G = \ell^2 d \Delta G_v + 4 \ell d \gamma_e + E_{\text{self}} + E_{\text{int}} \quad (90)$$

where ΔG_v is the driving force per unit volume for formation of

the new phase, γ_e is the edge surface energy. The third term, E_{self} , represents the strain field of the nucleus, and the last term, E_{int} takes into account the elastic interaction energy between the strain field of the nucleus and any other elastic strain field in the system. This term will dictate the elastically favourable site for nucleation.

In order to evaluate the magnitudes of forces acting on the steps, the chemical driving force and the elastic interaction force must be evaluated separately.

3.3.2 THE STRAIN FIELD OF PLATE-LIKE PRECIPITATES AND STEPS AT THE INTERPHASE INTERFACES

The strain field of a G.P. zone and a sessile ledge (if the length is much greater than the thickness) approximated by that of a prismatic dislocation loop of Burger's vector, $b = \epsilon d$, is discussed in detail in section 1.3 for an infinitesimal dislocation loop. For a large loop the strain field can often satisfactorily be approximated by the superposition of the strain fields of a regular planar array, or raft of such infinitesimal loops (82) (see sections 3.1.2.a. and 3.1.2.d.).

3.3.3 THE ELASTIC INTERACTION ENERGY

The elastic interaction energy between the ledges and the edge of the precipitate as well as among the ledges was calculated in the way described in section 3.1.2.d.

Assuming that the stress field around plate-like precipitates and ledges can be approximated as that of a prismatic dislocation loop, the elastic interaction of a ledge with the

plate (or that between ledges) reduces to that between two parallel and concentric prismatic loops.

3.3.4 NUMERICAL ESTIMATION OF THE ELASTIC INTERACTION ENERGY

In order to calculate the most favourable place for homogeneous nucleation of the ledges (from the point of view of elastic interaction) we have calculated this interaction between a plate-like precipitate and a small ledge (1/10 the size) for different positions of the ledge on the surface of the precipitate. The interaction obtained by moving the ledge from the centre of the plate to the edge of the precipitate in the x(y) direction are shown in Fig. 79*. When the ledge is located in the centre of the precipitate, the interaction energy is repulsive, as expected, for any ledge height. Displacing the small ledge from the centre of the precipitate, causes the potential to grow linearly until the ledge displacement is about 1/3 of the precipitate diameter at which point it begins to increase more sharply, reaching a maximum at the precipitate edge.

It is thus clear that the centre of the precipitate is the most favourable place for the homogeneous nucleation of the growth ledges. However, as in the evaporation of crystals, the edge of a precipitate should be the favoured site for dissolution. (There is no nucleation barrier to overcome.)

* A similar result was obtained by moving the ledge in the [110] direction.

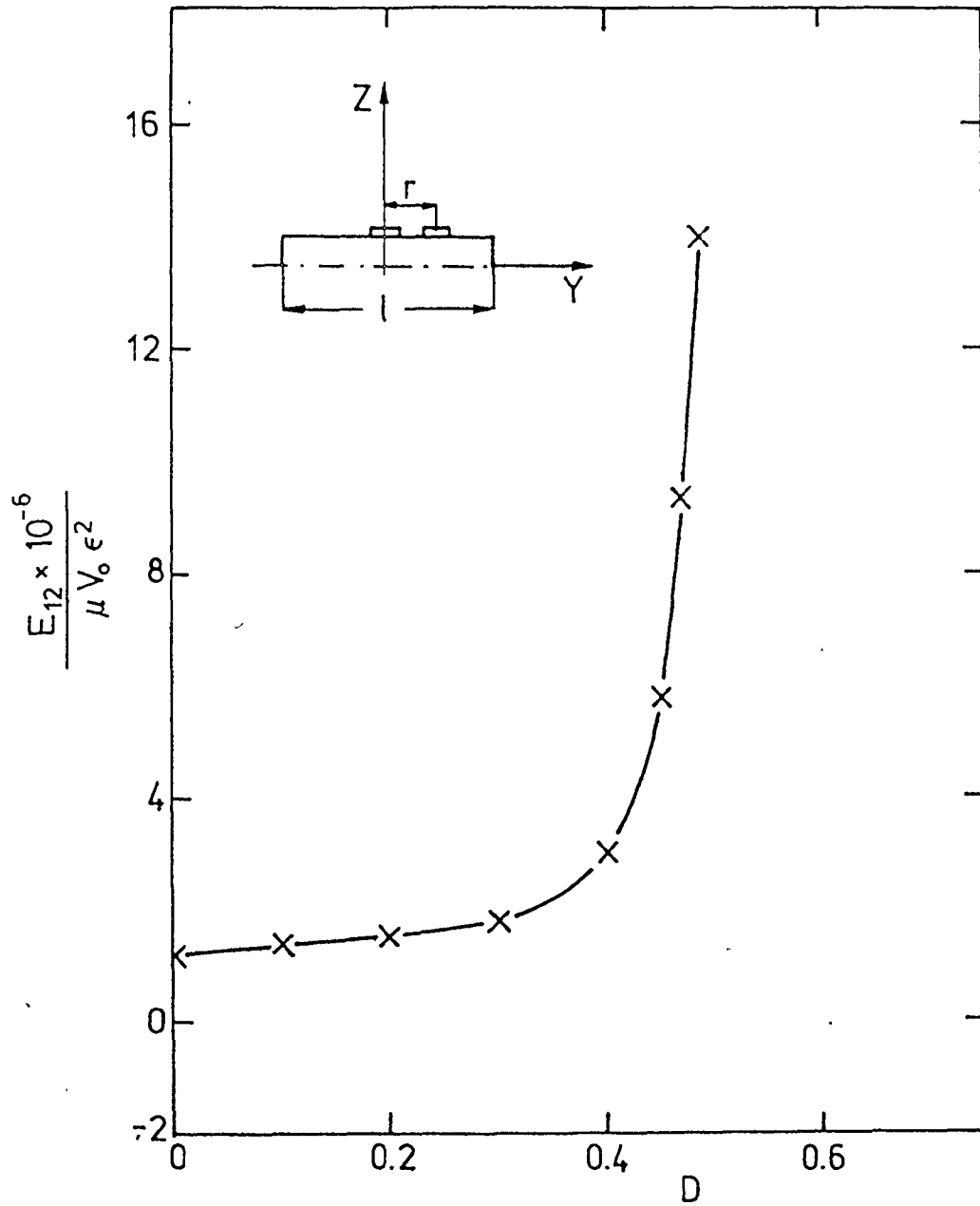


Fig. 79 Elastic interaction energy between large and small parallel plates as a function of the position of the small plate along the y-axis. The small plate lies on the large one.

Assuming that the ledge is "homogeneously" nucleated at the centre of the precipitate, we have calculated the interaction energy between the precipitate and the ledge, which is allowed to grow. Results of these calculations are plotted in Fig. 80, which demonstrates that the interaction energy becomes more and more repulsive as the size of the ledge is increased. This becomes most pronounced when the ledge size approaches the precipitate size. It is thus clear that the strain field associated with the edges of the precipitate exerts a repulsive force on the moving ledge interfaces. This repulsive force, F_{int} , has been evaluated from Fig. 80 as $\Delta E/\Delta l$. The interaction energy shown in Fig. 80 was calculated assuming the following parameters; $V_{ppt} = 1000 \times 1000 \times 20 \text{ \AA}$; $\epsilon = 0.005$ (103); $\mu = 3 \times 10^{11} \text{ dynes/cm}^2$ and the ledge of the same thickness and mismatch. As expected, the same result is obtained for interaction energies between the ledges with the same parameters.

Provided that the driving force is of the same order of magnitude, it is clear that this repulsive force can produce pile-ups of the ledges, in analogy with the dislocation case, as long as the total force is positive.

This total force is defined as the sum of the driving force, F_{chem} , and the repulsive force, F_{int} .

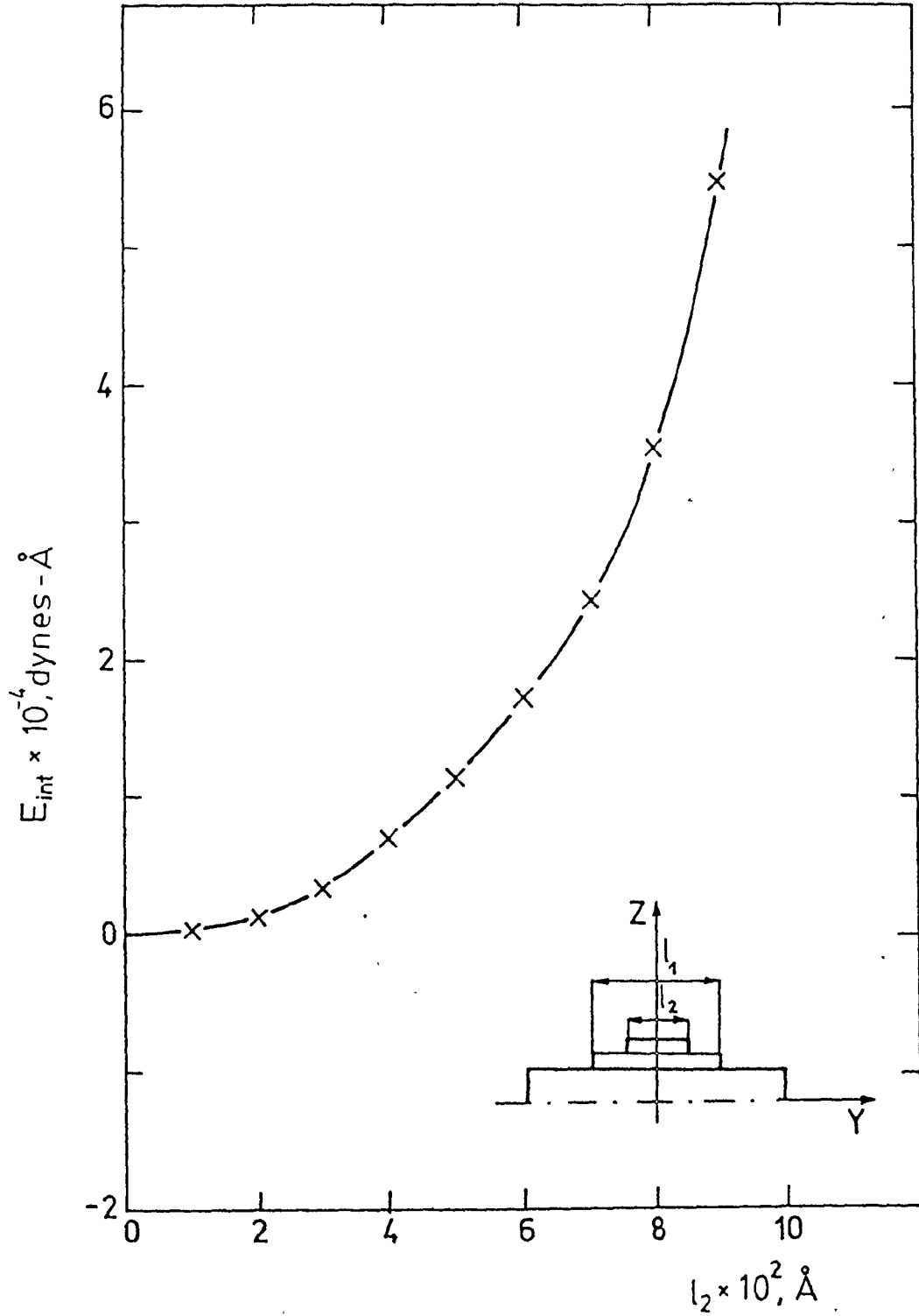


Fig. 80 Elastic interaction energy between two parallel and coaxial ledges as a function of size of the smaller ledge.

3.3.5 THE CHEMICAL DRIVING FORCE

To derive an expression for the driving force acting on the step, we should examine the free-energy change in the way described by Hillert (119).

By assuming ideal or dilute solution behaviour, Hillert obtained a simplified formula for the total driving force for the complete reaction:

$$\Delta G^{\text{total}} = \frac{RT}{V_m} \frac{(C_e - C_o)^2}{2C_o} \quad (91)$$

where C_e is the equilibrium interface composition, C_o is the composition of supersaturated matrix, V_m is the molar volume of the precipitate, and RT has its usual meaning.

The total free energy available in a transformation cannot, in general, be used to overcome the pressure difference at the curved surface but some free energy will be used to overcome friction and some free energy will be needed for diffusion.

Hence, of the total driving force, or potential for transformation, as indicated by ΔG (or the corresponding ΔC), some fraction is available to act directly at the interface. If we call this, ΔC_r , the remainder, ΔC_{diff} may be considered to be used in providing a concentration gradient for the diffusional supply of solute. The corresponding free energy change ΔG_{diff} is given by,

$$\Delta G^{\text{diff}} = \frac{RT}{V_m} \frac{(C_i - C_o)^2}{2C_o} \quad (92)$$

where C_1 is the actual interface concentration.

For the cases of the interface at rest and the slowly moving interface, chemical equilibrium is established locally, with corresponding concentration profiles in the matrix. The formation of concentration profiles in the matrix ahead of an advancing interface give rise to diffusion. The magnitude (height) of the concentration profiles should then be independent of the growth rate as long as there is a local equilibrium established at the interface. The free energy change in the case when the local equilibrium is established at the interface will give no force on the interface.

Consider now a disc-shaped precipitate of some radius r_1 , whose lengthening is controlled by volume diffusion, i.e. chemical equilibrium is established at the interface with a corresponding concentration profile in the matrix. The disc will grow with a certain rate V_1 , which depends on the disc's radius. The plane coherent faces of the disc are assumed immobile in the absence of a ledge. Assuming that there is no chemical interaction between the ledge and precipitate, the same diffusion field will exist in the front of a ledge. Consequently the ledge of the same shape, but smaller radius, r_2 , will grow faster with velocity V_2 , other conditions being equal.

Because of the existing strain fields and corresponding retarding forces the ledge will not grow with its independent velocity V_2 , but with constrained velocity V_1 . This constrained

velocity will give rise to a departure from local equilibrium at the moving interface. The difference between the new interface concentration, C_i , and concentration, C_e , dictated by the local equilibrium, will result in a chemical force acting on the interface.

To evaluate the constrained concentration, C_1 , at the ledge interface, we have to find the relationship between the velocity and the disc radius, under the condition that the sink is localized at the disc perimeter, i.e. thickening is not allowed. Ham (120) has pointed out that, to the extent that a steady state is established in the diffusion of atoms to a sink region, the diffusion equation may be approximated by Laplace's equation. Thus the profile, and hence the flux of atoms to the precipitate, is obtained from whatever solution of Laplace's equation, satisfies the appropriate boundary conditions. An alternative statement of this observation, borrowed from electrostatics, is that the effective radius of any geometry of localized sink is equal to the electrostatic capacity of a conducting body having the same dimensions as the sink. The effective sink radius (the precipitation flux) may therefore be found from tables of capacitances. Consider a disc-shaped precipitate, whose thickness, d , does not change with time. Only the radius is modified by absorption and, since the active sink is then localized at the perimeter, we may represent the sink geometry by a torus of approximate radius

$d/2$ and of principal radius r_0 , equal to the disc radius.

The capacity of such a torus is approximately (121).

$$C = \frac{\pi}{2} \frac{(4r_0^2 - d^2)^{\frac{1}{2}}}{\ln(16r_0/d)} \quad (93)$$

The description of precipitation from a dilute assembly to a central sink, assuming that the boundary conditions $C=0$ holds at the sink surface and $C(\infty) = C_0$, is therefore contained in the equations

$$\frac{\partial C}{\partial t} = - \frac{3\pi(4r_0^2 - d^2)^{\frac{1}{2}} D C_0}{2R^3 \ln(16r_0/d)} \quad (94)$$

and

$$2\pi r_0 d \frac{dr_0}{dt} = - \frac{4 R^3 \Omega}{3} \cdot \frac{\partial C}{\partial t} \quad (95)$$

where Ω is the atomic volume and R is the distance from the sink where $\left. \frac{\partial C}{\partial r} \right|_R = 0$.

With the above condition that $V_1 = V_2$, we are now able to find the relationship between concentrations and disc radii,

$$C_0^{r_2} = \frac{r_2}{r_1} \cdot \frac{d_2}{d_1} \cdot \frac{\ln(16r_2/d_2)}{\ln(16r_1/d_1)} \cdot \frac{(4r_1^2 - d_1^2)^{\frac{1}{2}}}{(4r_2^2 - d_2^2)^{\frac{1}{2}}} \cdot C_0^{r_1} \quad (96)$$

$C_0^{r_1}$ is dictated by the θ " precipitates homogeneously nucleated in the matrix, and according to the phase diagram (58) is taken as 0.010 at 160°C.

The difference between $C_0^{r_1}$ and $C_0^{r_2}$ gives the constrained concentration $C_i^{r_2}$ at the ledge interface. These $C_i^{r_2}$ concentrations were used in the eq. (92) to calculate the driving force

acting on the moving ledge interface. Results of calculations of the actual (constrained) concentration at the ledge, show that the chemical force is much higher than the elastic retarding force, unless the thickness of the ledge is half that of the initial precipitate.

However, ledges of the same thickness have the same capacity, and under that condition it is possible to get proper concentrations, $C_0^{r_2}$ (and corresponding concentrations, $C_1^{r_2}$, at the ledge interface of radius, r_2) for significant ledge interactions.

It should be mentioned that capillarity was not taken into account in these calculations; its effect is thought to be minimal, as discussed next.

The equilibrium shape of a disc-like precipitate is dictated by surface anisotropy (neglecting strain energy) and can be obtained by the Wulff construction (122), which requires that the radius of the perpendicular distances from the centre of a crystal to its various facets be equal to the ratios of their interfacial energies.

A homogeneously formed disc-like particle has energy cusp facet at the habit plane, Fig. 81. This gives a much larger radius of curvature, r , of the disc edges than that given by $r=d$ (where d is the thickness of the plate), as used by Aaronson and Laird for calculation of diffusional lengthening of θ' (123). Accordingly, we expect that the capillarity effect is rather small and have neglected it in our calculations of equilibrium concentration at the ledge

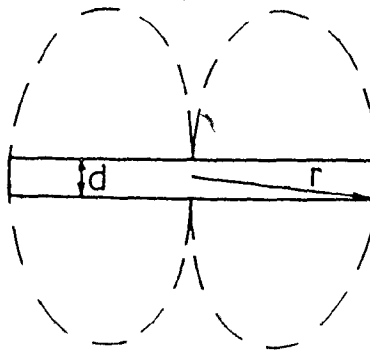


Fig. 81 The Gibbs-Wulff construction of the θ' precipitate ledge interfaces, given by eq. (96).

As already mentioned, Stobbs and Purdy (103) noted that the nucleation process in this system can not be described by the concept of monomer addition to critical size clusters whose properties are similar to the fully developed precipitate. Admitting that the thickening of the θ' particle takes place by nucleation of the ledges whose thickness is an integral number of half θ' unit cells, Stobbs and Purdy (103) have shown that the misfit of the θ' particle is subject to periodic variation in magnitude and in sign. The estimated misfits, and the corresponding elastic self energies (see appendix I), obtained by matching integral number of half θ' unit cells and matrix unit cells are shown in Table 2 (the estimated misfits are also shown in Fig. 82). The chemical free energy (see appendix II), available for nucleation is given in the same table.

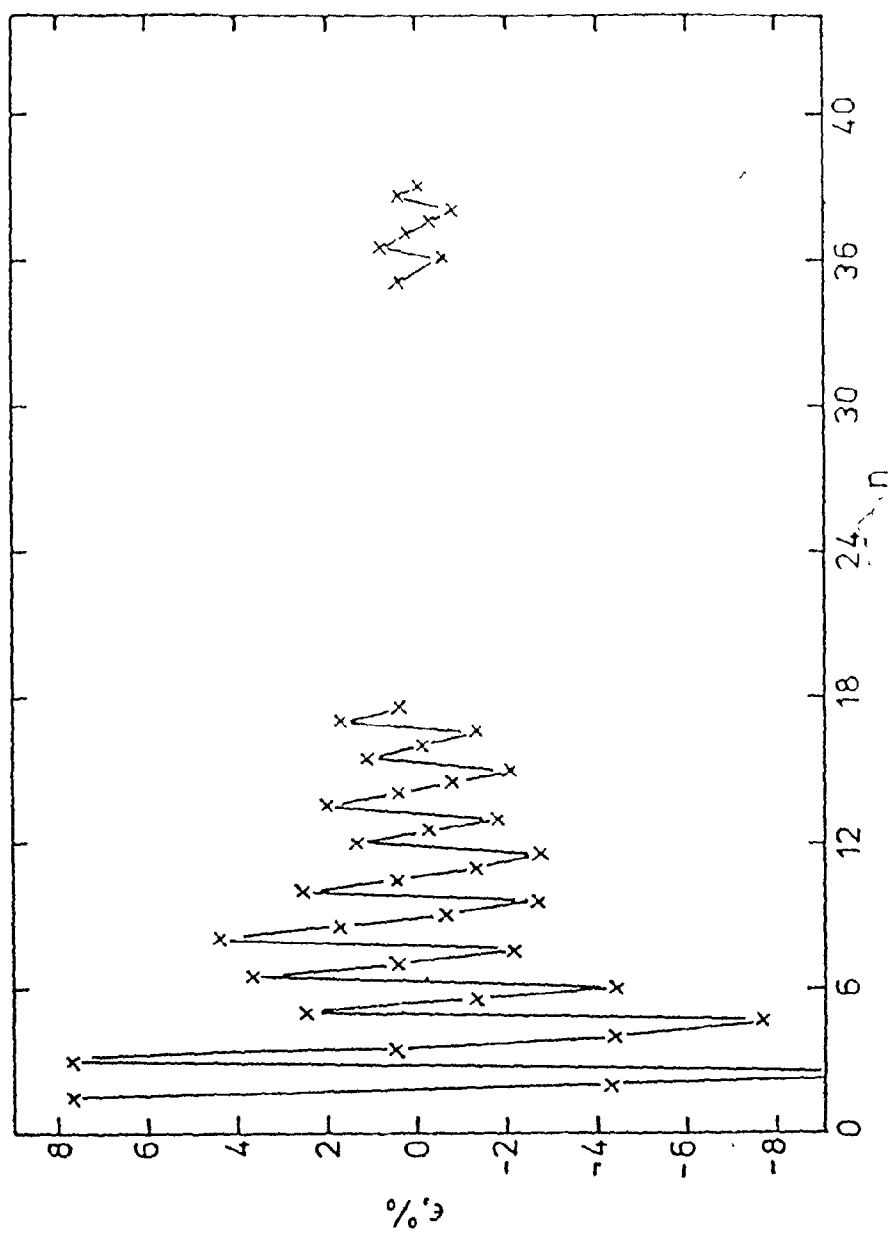


Fig. 82 Variation of the elastic misfit obtained by matching integral number of half θ' unit cells and matrix unit cells.

Table 2

| Chemical Free Energy ϵ_3 ergs/cm ³ | Number of θ' Unit Cells | Ledge Height h_1 | Number of α Unit Cells | Height of Matching Matrix h_2 | Mismatch $\epsilon = \frac{h_1 - h_2}{h_2} \times 100, \%$ | Elastic Self Energy, ergs/cm ³ |
|--|--------------------------------|--------------------|-------------------------------|---------------------------------|--|---|
| $\approx 3.0 \cdot 10^9$ | 1.5 | 8.7 | 2 | 8.08 | + 7.67 | 3.35×10^9 |
| | 2.0 | 11.6 | 3 | 12.12 | - 4.29 | 1.05×10^9 |
| | 2.5 | 14.5 | 4 | 16.16 | -10.27 | |
| | 3.0 | 17.4 | 4 | 16.16 | + 7.67 | |
| | 3.5 | 20.3 | 5 | 20.20 | + 0.49 | 1.43×10^7 |

The free energy (in arbitrary units) versus the size of the nucleus expressed in terms of number of the θ' unit cell (n) is schematically presented in Fig. 83.

The curves are not continuous because thicknesses different from integral values of n are not allowed.

From table 2, it can be seen that the ledges of 8.7 and 11.6 Å height have very large elastic self energies, which are comparable with the chemical driving force. This suggests that the nucleation of these ledges has small probability unless a complementary lattice strain exists to help them. However, the ledge of 20.3 Å height has negligible strain energy compared to the chemical free energy. This size was observed by Weatherly and Sargent (72) and by Laird and Aaronson (116) in coarsening studies. Taking the equilibrium aspect ratio as 1/20 it is seen that a nucleus of this thickness would have length 400 Å. Such a large nucleus is considered unlikely. The details of the

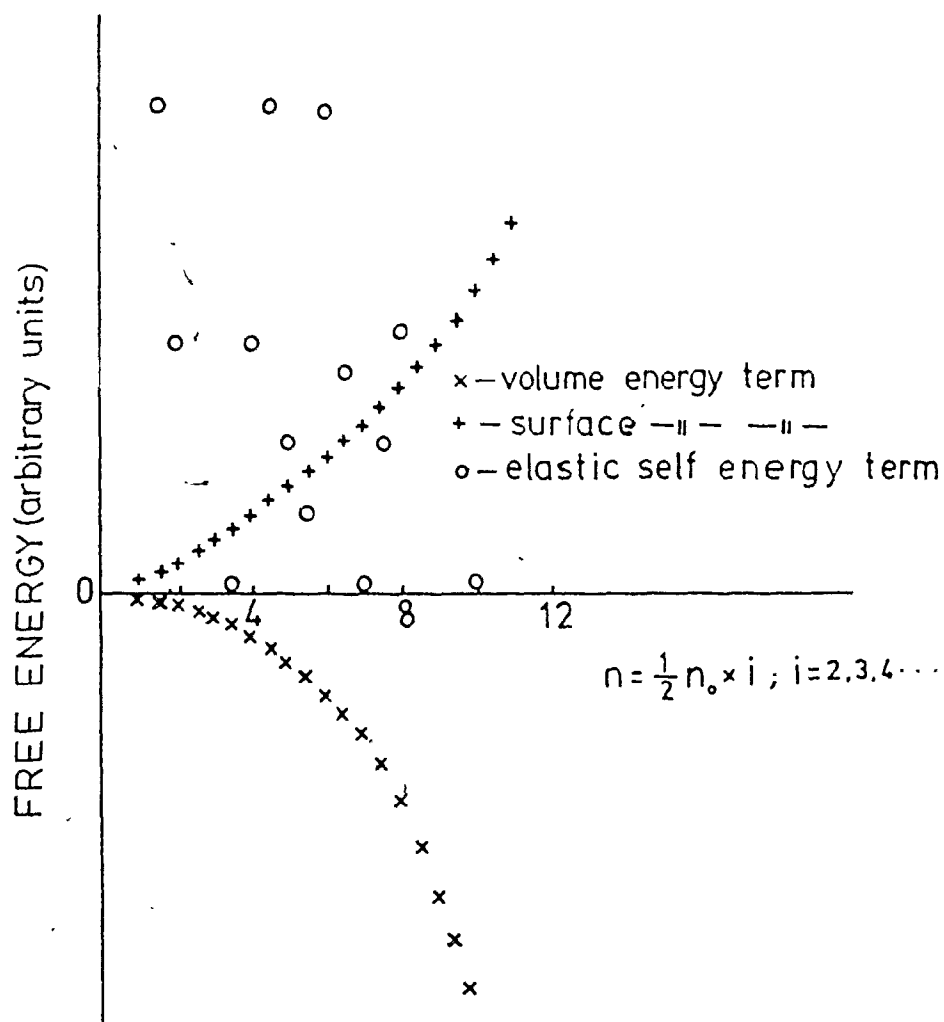


Fig. 83 The free energy change as a function of the nucleus size expressed in terms of integral number of half θ' unit cells.

transition to the low energy state are thus not clear at present. One possibility is the formation of a nucleus via elastic interaction of G.P. zones, allowing at the same time a chemical ordering which results in the θ' nucleus. Seitz and Defontaine (57) have recently shown that a minimum in the elastic energy four atomic planes from an existing G.P. zone enhance the formation of another G.P. zone. This may lead to formation of the θ' precipitate.

Using high resolution electron microscopy, Phillips (52) has observed two or more parallel G.P. zones separated by one to three atomic spacings.

If we have two ledges, of equal thickness and of the same sign which are repulsive (Fig. 79), the first ledge will exert retarding force on the growing second ledge forcing it to grow with the constrained velocity, v_2 .

This constrained velocity, as already mentioned, will give rise to the departure from the local equilibrium at the moving interface. Results of these calculations are shown in Table 3 for given conditions: $C_o^{r_1} = 0.010$, $r_1 = 1000 \text{ \AA}$, $d_1 = 40 \text{ \AA}$, $d_2 = 40 \text{ \AA}$, $T = 413^\circ\text{K}$ and $v_m = 10 \text{ cm}^3/\text{gr-mole}$, where r_1 is the radius of the first ledge and d_1 is the thickness of the torus, whose thickness is twice of the ledge thickness (r_1 and d_1 were kept constant); r_2 and d_2 are the radius and corresponding thickness of the second ledge.

Table 3

| $r_2, \text{\AA}$ | $\frac{r_2}{C_i}, \%$ | $F_{\text{chem}} \times 10^{-6}$ dynes |
|-------------------|-----------------------|--|
| 100 | 0.003717 | - 8.716 |
| 200 | 0.002651 | -13.245 |
| 300 | 0.001993 | -15.505 |
| 400 | 0.001520 | -16.183 |
| 500 | 0.001152 | -15.628 |
| 600 | 0.000849 | -14.053 |
| 700 | 0.000593 | -11.607 |
| 800 | 0.000371 | - 8.397 |
| 900 | 0.000175 | - 4.506 |

The results of the total force ($F_{\text{chem}} + F_{\text{int}}$) acting on the ledge interfaces versus the ledge size are shown in Fig. 84. Fig. 84 shows that the total force in the beginning dictated by the driving force, is more and more negative. This is in agreement with Fig. 80, where the slope of the interaction potential curve is very small up to 0.3 times the precipitate length, and with the fact that the driving force is also much larger for smaller radii (Table 3). With further ledge growth the curve reaches its maximum negative value, when the repulsive force comes into play, causing the attainment of an equilibrium position ($F_{\text{total}} = 0$) at the ledge length of about 0.9 times the precipitate length.

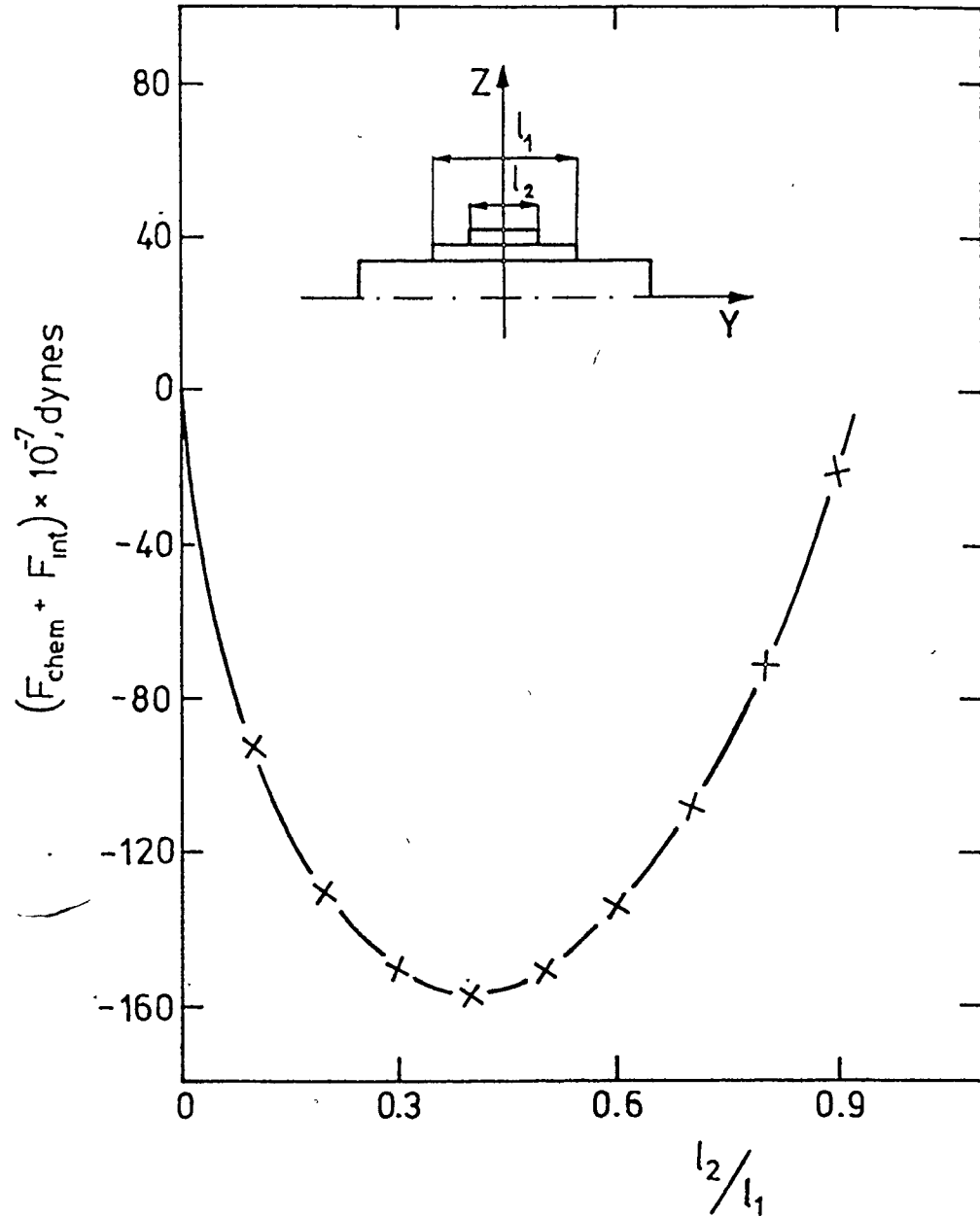


Fig. 84 The total force acting on the interface of the growing ledge as a function of the ledge size.

3.3.6 EXPERIMENTAL OBSERVATIONS

Observations were made on specimens aged above and below θ'' solvus line. Fig. 85(a)-(c) shows microstructures characteristic of specimens aged 5 hours at 240°C; i.e. above the θ'' solvus line, so that θ' precipitates formed directly from supersaturated solid solution.

At this stage of the transformation, the microstructure consists of a number of different ledge morphologies, mainly heterogeneous nucleated in the ways described by Weatherly (117) and Sankarn and Laird (118). The main characteristic of these microstructures is a very complicated ledge morphology which precludes the direct study of ledge interaction. Complications come from at least two sources; the very high driving force accompanying growth and heterogeneous nucleation of the ledges at points of precipitate impingement. Although these microstructures are complex, it is often possible to discern cases where ledges on the upper and lower surfaces of the precipitate (distinguished by contrast reversal (72); see section 1.5.6) appear to interact (see the arrowed region in Figs. 85(a) and (b)).

Fig. 86 shows microstructure of the specimen aged 1 hour at 240°C. The main characteristic of this microstructure is a high density of the equally spaced ledges. This suggests that the nucleation and growth of these ledges was completely controlled by the very high chemical driving force.

Fig. 85 Al-3% Cu crystal with (001) orientation, solution-treated and aged 5 hours at 240°C. This series of dark field micrographs show very complex ledges morphology of the particles. At arrowed regions in (a) and (b) it appears that the ledges on upper and lower surface interact. Heterogeneous nucleation of the ledges at points of precipitate impingement is evident in (c). (a) 87000x ; (b) 62500x ; (c) 42000x.

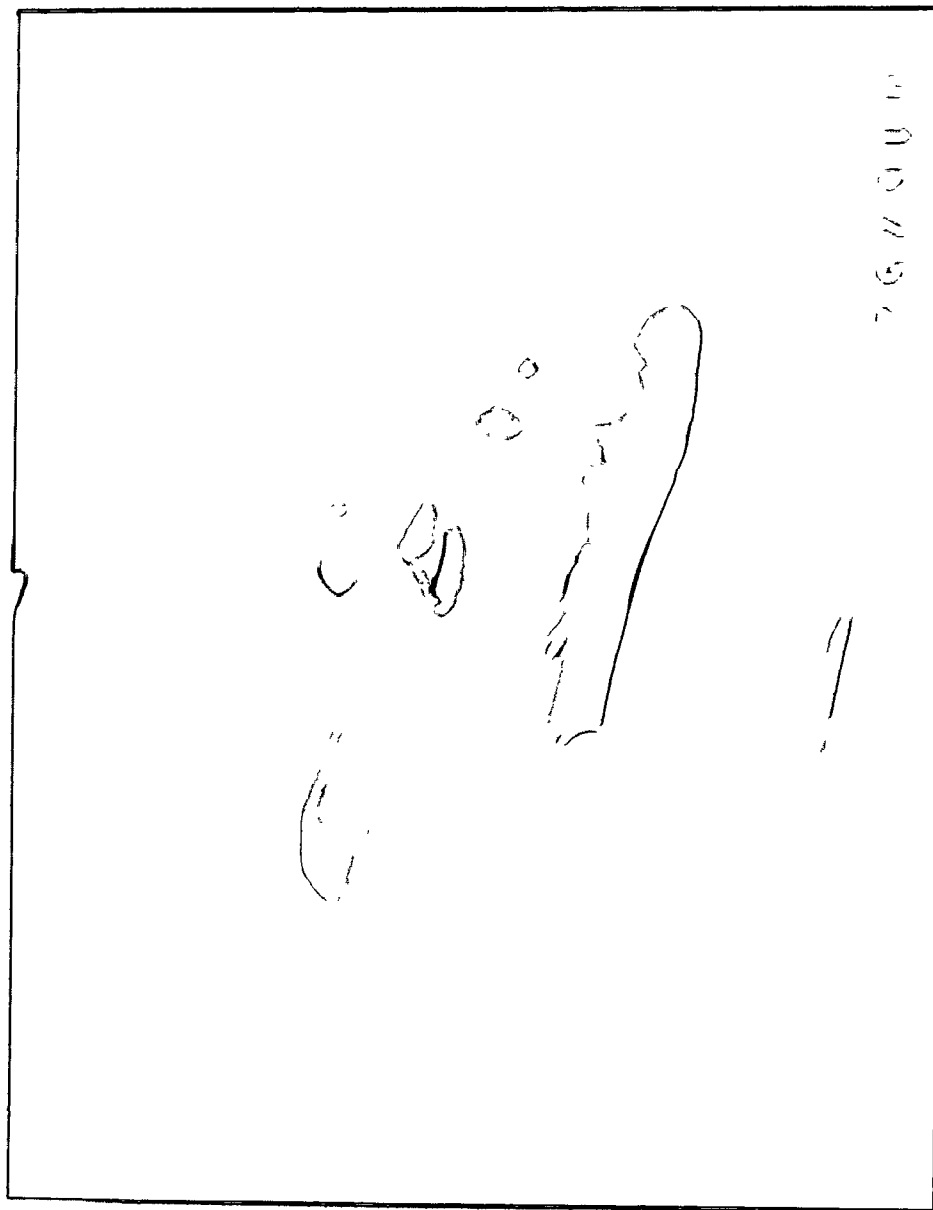


Fig. 85 (a)

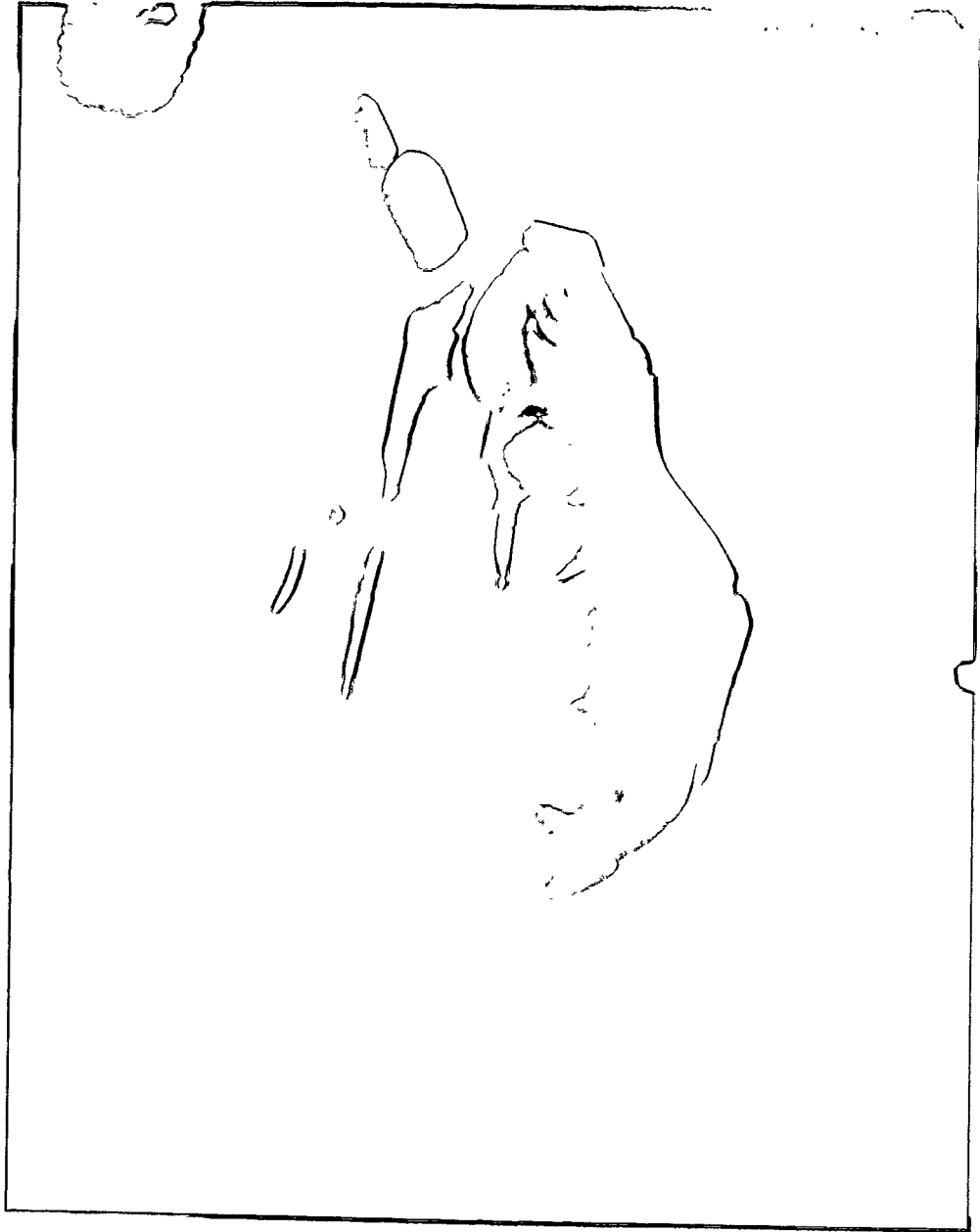


Fig. 85 (b)

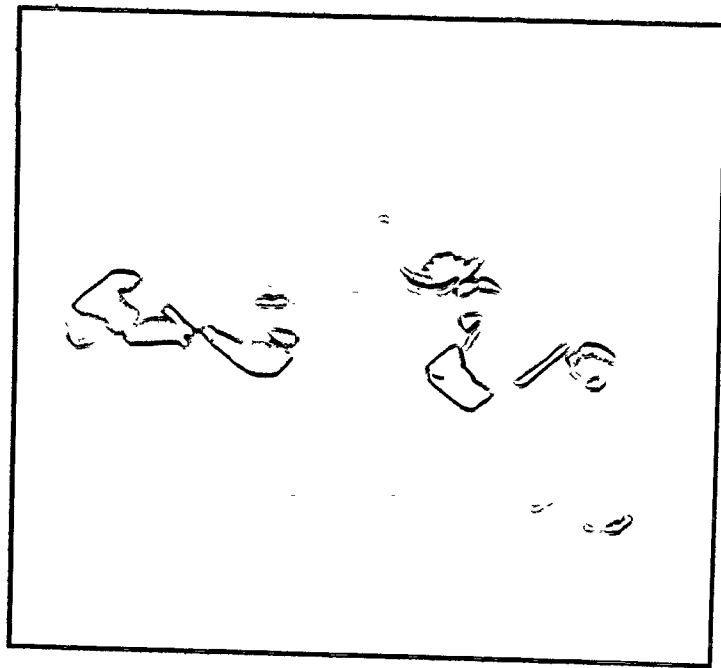
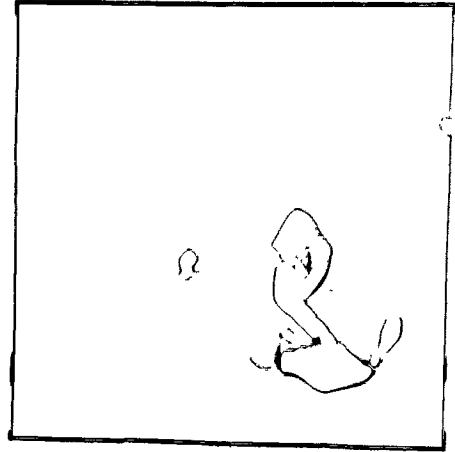
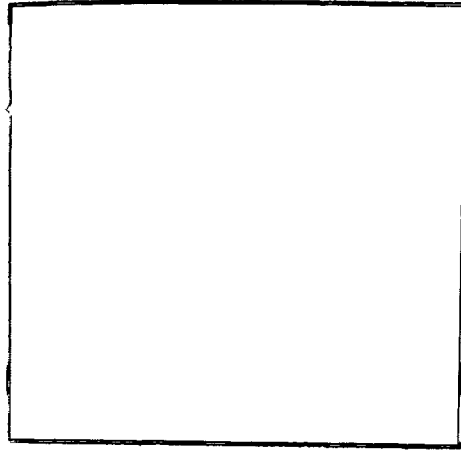


Fig. 85 (c)

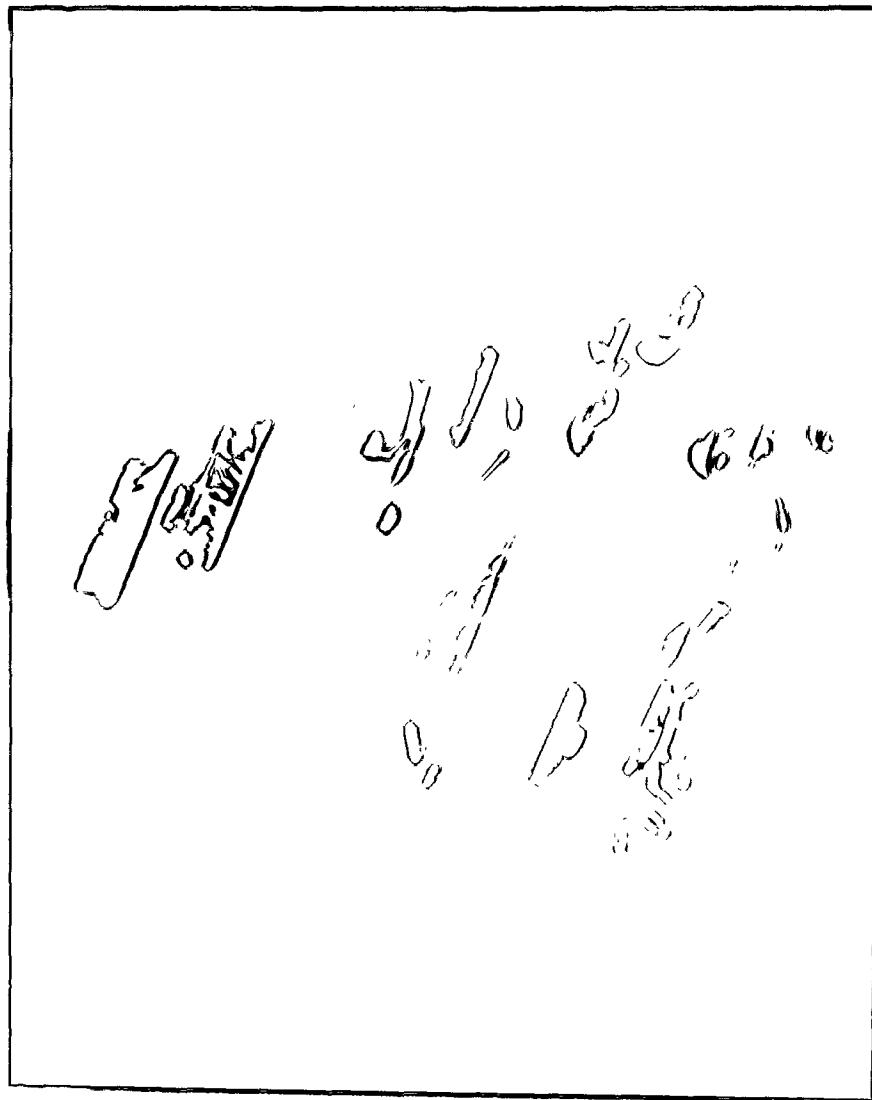


Fig. 86 Al-3% crystal with (111) orientation, solution-treated and aged 1 hour at 240°C. Dark field condition shows high density of equally spaced growth ledges (71000 \times).

Figs. 87 (a)-(b) are microstructure of specimens aged 92 hours at 160°C; i.e. below the θ'' solvus line, so that the driving force for θ' growth is considerably reduced, because of the presence of homogeneously dispersed θ'' precipitates. The main feature of these microstructures is the faceted nature of the ledges at θ' which show approximately the same symmetry as the peripheral interfaces of the θ' plates.

At coherent or semicoherent interfaces significant variations of ledge velocity with orientation may occur, due either to anisotropic diffusion rates or to variations in kink density. A series of ledge ("homogeneously" nucleated) spreading from the centre of the plate was frequently observed, suggesting that the centre is indeed a favourable place for nucleation of growth ledges.

Some of the experiments were done in the microscope, but because of the easy nucleation of θ on the free surfaces, these experiments failed. Fig. 88 shows high density of dissolution ledges which move synchronously, and which were easily nucleated on the plate edges.

Finally, some of the foils were aged 30 minutes at 390°C, Fig. 89. The main characteristic of these microstructures is the heterogeneous nucleation of the equilibrium θ phase on the θ' interfaces. Dissolution ledges are clearly seen on the θ' interfaces (they are clearly distinguished from the interface dislocations on the semicoherent θ' interfaces shown in Fig. 53).

153

Fig. 87 Al-3% Cu crystal with (001) orientation, solution-treated and aged 92 hours at 160°C. This series of dark field (weak beam) micrographs shows very regular shapes of θ' particles and ledges. Ledges are nucleated as pill-boxes in the middle of the plates. In many cases it seems that the edges clearly lead the ledges.
(a) 55000x; (b) 42000x.

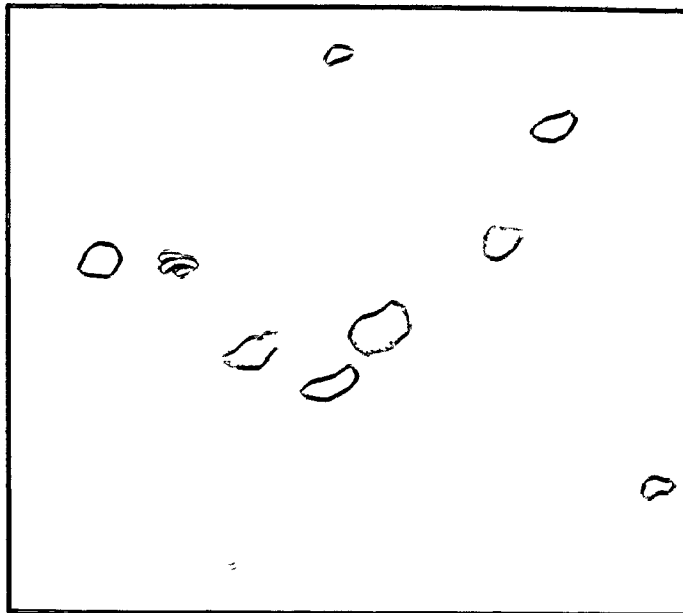
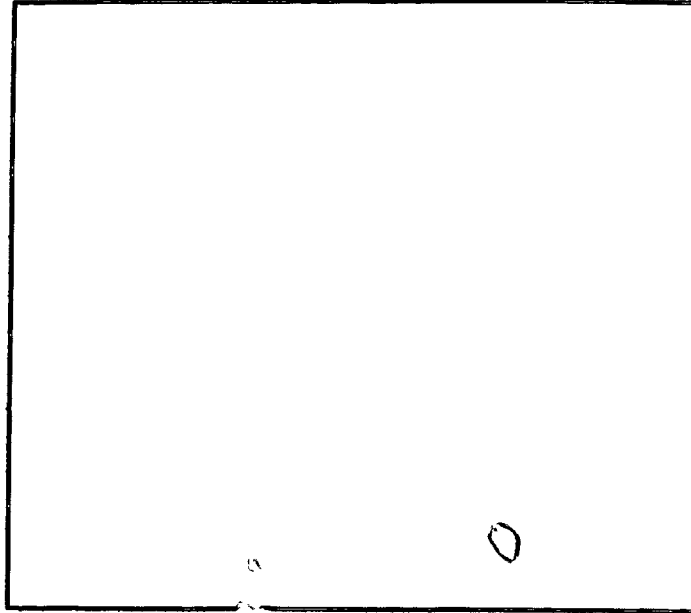


Fig. 87 (a)

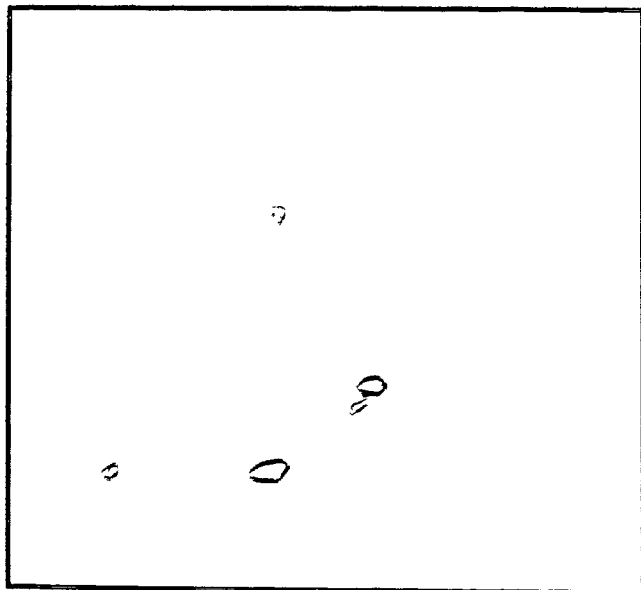
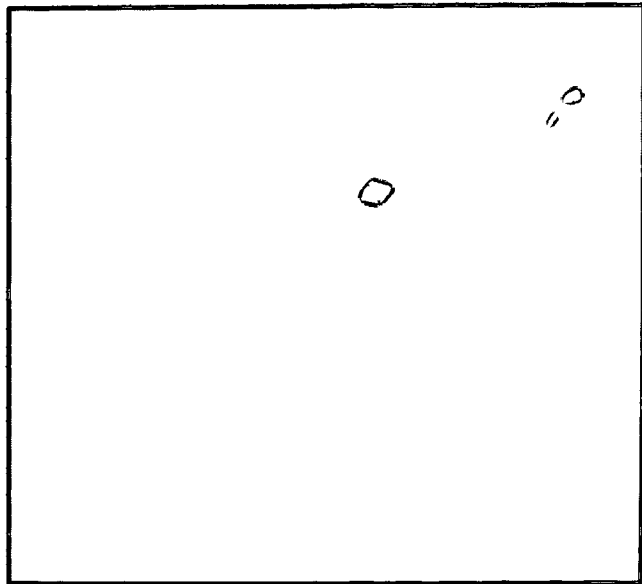


Fig. 87 (b)



Fig. 88 Al-3% Cu crystal with (001) orientation, solution-treated and in situ aged at 240-300°C. Bright field micrograph shows high density of equally spaced dissolution ledges (11250×).



Fig. 89 Al-3% Cu crystal with (001) orientation, solution-treated and aged 30 minutes at 390°C. Heterogeneous nucleation of the equilibrium θ phase on the θ' interfaces. Dissolution ledges on the θ' interfaces are clearly seen (11250 \times).

3.3.7 DISCUSSION

From the present consideration of elastic interaction energy it is demonstrated that strain energy exerts retarding force on the interface of the moving ledge. This retarding force may have, under certain conditions, strong effect on the ledges morphology.

In the case that the two ledges have equal thickness, the elastic interaction energy may cause departure from the local equilibrium at the moving interface, and generate driving force. Thus when the driving and retarding forces are compatible the ledge growth may be stabilized by the elastic interaction energy.

As already mentioned the elastic interaction energy may dictate the elastically favourable site for nucleation. This term becomes important when there is no possibility of heterogeneous nucleation, and the new ledge must be formed as a pill-box on an otherwise perfect interface.

Experimental results show that the ledges morphology is determined in a complex way by competition between nucleation and growth. Two types of experiments were conducted in order to see the effect of elastic interaction energy, one type of experiment was done under lower chemical driving forces and the other under higher chemical driving forces.

When the driving force for θ' growth is considerably reduced, because of the presence of homogeneously dispersed θ'' precipitates, the θ' particles have nearly ideal shapes. The

shape of the ledges is also very regular with approximately the same symmetry as the peripheral interfaces of the θ' plates.

For these low driving forces where the θ' particles are isolated, nucleation of the ledges may be controlled by the elastic interaction energy. It is demonstrated that under these conditions pill box nucleation is very common. New ledges are very often (if not always) in the middle of the plate, as would be expected from the interaction energy for nucleation of the growth ledges. In this case nucleation will occur when the plate is large enough that the repulsive interaction energy is diminished (see Fig. 79). (This is in contrast to the case of dissolution ledges which are nucleated at the plate edges).

The calculations of the total force suggest that if the initial plate thickness is 20 \AA and the ledge thickness is also 20 \AA , there will be no significant interaction between them and the edge will run away; this situation seems to be observed, e.g. Figure 87. However, a more quantitative study is required.

Fig. 87 (a)-(b) shows pronounced edge facetting, suggesting that particle and ledge growth was not completely controlled by volume diffusion. However, it is probable that the assumption that lengthening is controlled by volume is valid as a first approximation.

Finally, it should be pointed out that in the case of low chemical driving forces, the elastic interaction is comparable with these forces; there is therefore an opportunity for a complete and quantitative experimental study of ledge interactions.

SUMMARY

1. It was shown that the elastic interaction energy of the plate shaped precipitates, each causing tetragonal distortion, depends strongly on mutual orientation and separation, and that it can be minimized by the distribution of the precipitates in a regular three-dimensional array. The elastic interaction among large precipitates is qualitatively and quantitatively distinguishable from that for infinitesimal precipitates. This difference stems from the interaction of elements far from the centres of precipitates. This "peripheral" interaction causes a minimum in the interaction energy when two precipitates are mutually perpendicular, while in the parallel configuration it leads to a considerable decrease of the interaction energy (otherwise positive). The appearance of the minimum on the potential for large precipitate leads to the mechanical stability of the $\langle 1230 \rangle$ array. Opposite results were obtained in the "infinitesimal" approximation. The optimum separation of square-shaped precipitate is seen to occur at separation (centre to centre) of about 1.2 times the edge length.

Experimental results obtained in the θ " range show strong evidence of short-range ordering which emphasizes the edge-face configuration and face-face configuration with very low inclination angles and small separation distances. Both configurations are attractive. The wave-like strain field is

evident through all microstructures which is a result of complex strain field interactions from the closely spaced particles. Experimental results concerning long-range ordering in this system are not conclusive, even though along some lines in the microstructures, it is possible to see a tendency to long-range ordering with a preponderance of the edge-face orientation.

2. The investigation of the stability against volume perturbation of a single pair of precipitates show that the edge-face configuration is stable while the face-face configuration is an unstable one. The reason for this lies in the fact that the edge-face configuration is attractive, while the face-face configuration is repulsive. Thus, the elastic interaction energy appears as a factor which stabilizes equal dimensions of the particles in a pair only if this interaction is attractive. The investigations of the variation of the total elastic energy of the $\langle 1230 \rangle$ array caused by volume exchange between the unstable pair shows that the lattice has a stabilizing effect. The array therefore possesses a minimum in the elastic interaction energy when all precipitates have the same dimensions. The investigation of the stability of the $\langle 1230 \rangle$ array against co-ordinated diffusion between nearest neighbour precipitates shows that the array is stable against such perturbation. A similar result is obtained for volume exchange which involves third nearest neighbours.

General and algebraic conditions for stability against coarsening were developed which showed that stability will be promoted by: low interfacial energy, large elastically-accommodated misfit and large or optimal value of $K(f,p)$ (the second derivative of the elastic interaction energy with respect to volume fraction, f , and array - type, p).

3. Experimental observations show that the formation of stacks of θ' precipitates is a prominent feature in the early stage of θ' microstructure development. Elastic energy calculations for some hypothetical stacks show that the stack's morphology depends strongly on elastic interactions; their development can be explained in terms of minimization of the elastic interaction energy during nucleation. Only stacks with attractive interaction energy were observed experimentally. These stacks are based on the edge-face configuration and the face-face configuration with low inclination angles, ($\sim 20^\circ$) and small separations, both attractive.

The weight of the present evidence is that θ' strain fields are effective in nucleating subsequent θ' particles and that it is this autocatalytic effect which is dominant in microstructural development under the conditions employed here.

Some evidence for elastic stabilization of particles within stacks was also obtained.

4. Experimental results concerning ledge interaction give some evidence of the elastic interaction among ledges on the θ' precipitates. Development of the ledges morphology on the θ'

precipitates is complicated by high chemical driving force and due to precipitate impingement. Although these microstructures are complex it is often possible to discern cases where ledges on the upper and lower surface of the precipitates appear to interact. Development of the ledge morphology at low driving forces is more regular. Very frequently, a series of ledges ("homogeneously" nucleated) were observed spreading from the centre of the plate. The developed structures of the ledges are probably controlled by the elastic interaction energy either through nucleation or during growth.

In the absence of the heterogeneous nucleation, new ledges are nucleated "homogeneously" as pill boxes and the elastic energy calculations show that the nucleation event can be influenced by the elastic interactions.

Considerations of the chemical driving force and the retarding force (interaction energy) acting on the ledge interface suggest that under some conditions the ledge separation during growth may be stabilized by the elastic interaction energy.

APPENDIX I

THE ELASTIC SELF ENERGY

Eshelby (4) has obtained a general solution for the elastic state of an ellipsoidal inclusion and the matrix, when the inclusion within an isotropic elastic solid undergoes a change of shape and size, which would be homogeneous, but for the constraint imposed by the matrix. Because of the presence of the matrix, internal stresses exist both inside and outside the inclusion. Following Eshelby, the total strain energy in the matrix and inclusion is given by:

$$E_{el} = \frac{1}{2} \int_{\text{total volume}} \sigma_{ij} \epsilon_{ij} dv = - \frac{1}{2} \int_{V_I} \sigma_{ij}^I \epsilon_{ij}^T dv \quad (I1)$$

where σ_{ij}^I is the stress in the inclusion, and V_I is the volume of the inclusion, and the summation of repeated indices is implied.

ϵ_{ij}^T is the "stress-free strain" which the inclusion would undergo in the absence of the matrix.

The main problem is to find the "constrained strain", ϵ_{ij}^C , in the inclusion when it transforms while it is embedded in the matrix and also the strain set up in the matrix. Since ϵ_{ij}^C is uniform within the inclusion, eq. (I1) becomes:

$$E_{el} = \frac{1}{2} V \sigma_{ij}^I \epsilon_{ij}^T ; V = \frac{4}{3} \pi a b c . \quad (I2)$$

The stress in the inclusion is given by:

$$\sigma_{ij}^I = \sigma_{ij}^C - \sigma_{ij}^T \quad (I3)$$

where, σ_{ij}^C is the stress derived by Hooke's law from the strain ϵ_{ij}^C in the inclusion.

$$\sigma_{ij}^C = \lambda \epsilon^C \delta_{ij} + 2\mu \epsilon_{ij}^C \quad (I4)$$

and σ_{ij}^T is the stress derived from the stress-free strain ϵ_{ij}^T by Hooke's law:

$$\sigma_{ij}^T = \lambda \epsilon^T \delta_{ij} + 2\mu \epsilon_{ij}^T \quad (I5)$$

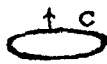
Substituting expressions for σ_{ij}^C and σ_{ij}^T from eqs. (I3) and (I4) into eq. (I2), we obtain:

$$\sigma_{ij}^I = \lambda (\epsilon^C - \epsilon^T) \delta_{ij} + 2\mu (\epsilon_{ij}^C - \epsilon_{ij}^T) \quad (I6)$$

The relation between the constrained and stress-free strains in the inclusion is given by:

$$\epsilon_{ij}^C = S_{ijkl} \epsilon_{kl}^T \quad (I7)$$

Eshelby described the general solution for S_{ijkl} in terms of the elliptical integrals, from which the strain energy can be obtained. All the components S_{ijkl} referred to the inclusion coordinates for ribbons, fibres, plates and spheres are tabulated by Brown and Clarke (124).

In the case of a disc-shaped precipitate most of the strain is taken in the "c" direction, (, and the ϵ^T and ϵ_{ij}^C are given by:

$$\epsilon^T = \begin{vmatrix} 0 & 0 & 0 \\ 0 & 0 & 0 \\ 0 & 0 & \epsilon \end{vmatrix} \quad (18)$$

and

$$\epsilon_{ij}^C = S_{ijkl} \epsilon_{kl} = S_{ij33} \epsilon = \begin{vmatrix} \frac{\nu}{1-\nu} & 0 & 0 \\ 0 & 0 & 0 \\ 0 & 0 & 0 \end{vmatrix} \epsilon .$$

Substituting expressions for strains, eq. (18) in eq. (16) and eq. (16) in eq. (12), the elastic energy becomes:

$$\begin{aligned} E_{el} &= \frac{1}{2} V \sigma_{33}^I \epsilon = \frac{1}{2} V \left[\frac{\lambda}{3} \left(\frac{\nu}{1-\nu} - 1 \right) \epsilon - 2\mu \epsilon \right] \epsilon \\ &= \frac{1}{2} \left(\frac{6-4\nu}{3(1-\nu)} \right) \mu V \epsilon^2 \end{aligned} \quad (19)$$

with $\nu = 0.3$

$$\mu = 5 \times 10^{11} \text{ dynes/cm}^2$$

$$\frac{E_{el}}{V} = 1.14 \times 5 \times 10^{11} \epsilon^2, \text{ ergs/cm}^3 .$$

APPENDIX II

THE CHEMICAL FREE ENERGY FOR NUCLEATION

The available free energy change, when unit volume of precipitate (β) of composition C^β is formed from a very large amount of matrix material (α) of composition C^α so that the composition of the latter is not sensibly changed is given by (125),

$$\Delta G_{\text{chem}} = - \frac{RT}{V^\beta} \left[C^\beta \ln \frac{a_B(C^\beta)}{a_B(C^\alpha)} + (1-C^\beta) \ln \frac{a_A(C^\alpha)}{a_A(C^\beta)} \right] \quad (\text{II1})$$

where $a_B(C^\beta)$ is the activity of component B in β of composition C^β and similarly for the other activities.

Direct measurement of activities in the metastable phase (via vapor pressure, electromotive force, etc.) is seldom practical and some method of extrapolation is needed. The simplest of these is the dilute solution model in which the activity is directly proportional to the composition (126). This model is usually adequate when a phase contains only a few percent of the second component. Then for β of composition C_e^β ,

$$\Delta G_{\text{chem}} = - \frac{RT}{V^\beta} \left[C_e^\beta \ln \frac{C^\alpha}{C_e^\alpha} + (1-C_e^\beta) \ln \frac{(1-C^\alpha)}{(1-C_e^\alpha)} \right] \quad (\text{II2})$$

with $C^\alpha, C_e^\alpha \ll 1$.

$$\Delta G_{\text{chem}} = - \frac{RT}{V} C_e^\beta \ln \frac{C^\alpha}{C_e^\alpha} \quad (\text{II3})$$

where C_e^β and C_e^α are the equilibrium concentration of solute in the β and α phase (with respect to stress free large particle) and C^α is the solute concentration in the supersaturated matrix. V^β is the molar volume of the nucleus and RT has its usual meaning.

in our case: $C^\alpha \approx 1$ wt% (denoted by the θ'' solvus line at $\sim 160^\circ\text{C}$, see Fig. 8)

$$C_e^\alpha \approx 0.2 \text{ wt \% (assumed)}$$

$$C_e^\beta \approx 53 \text{ wt \%}, \text{ (assumed CuAl}_2\text{)}$$

$$T = 433^\circ\text{K} (160^\circ\text{C})$$

$$V^{\theta'} = 10 \text{ cm}^3/\text{gr-mole}.$$

this gives,

$$\begin{aligned} \Delta G_{\text{chem}} &= \frac{8.314 \times 10^7 \times 433}{10} \cdot 0.53 \ln \frac{0.01}{0.002} \\ &\approx 3.0 \times 10^9 \text{ erg/cm}^3 \end{aligned}$$

References

1. F.R.N. Nabarro, Proc. R. Soc.(A) 175, 519 (1940); Proc. Phys. Soc. 52, 90 (1940).
2. E. Kroner, Acta Metall. 2, 302 (1954).
3. A.G. Khachaturyan and V.N. Hairapetyan, Phys. Status Solidi (B) 57, 801 (1973).
4. J.D. Eshelby, Proc. Roy. Soc.(A) 241, 376 (1957).
5. J.D. Eshelby, Appendix to Article by A.J. Ardell and R.B. Nicholson, Acta Metall. 14, 1295 (1966).
6. A.G. Khachaturyan and G.A. Shatalow, Sov. Phys. Solid State 11, 118 (1969).
7. A.G. Khachaturyan, Phys. Status Solidi 35, 119 (1969).
8. A.G. Khachaturyan and V.M. Airapetyan, Phys. Status Solidi(A) 26, 61 (1974).
9. L.M. Brown, R.H. Cook, R.K. Ham and G.R. Purdy, Scripta Metall. 7, 815 (1973).
10. Ph. Eurin, J.M. Penisson and A. Bourret, Acta Metall. 21, 559 (1973).
11. A.G. Khachaturyan, Sov. Phys. Solid State 8, 2163 (1967).
12. H. Yamauchi and D. DeFontaine, Acta Metall. 27, 763 (1979).
13. P.F. Papkovitch, C.R. Acad. Sci. (France), 195, 513 (1932).
14. H. Neuber, Z. Angew. Math. U. Mech. 14, 4 (1934).

15. A.E.H. Love, *Treatise on the Mathematical Theory of Elasticity*, MacMillan, New York (1927).
16. A.I. Lur'e, *Three-Dimensional Problems of the Theory of Elasticity*, John Wiley & Sons, Inc. (1964).
17. R. Dewit, *Sol. State Phys.* 10, 249 (1960).
18. M. Shibata and K. Ono, *Acta Metall.* 23, 587 (1975).
19. I.S. Sokolnikoff, *Mathematical Theory of Elasticity*, 2nd ed. McGraw-Hill, New York (1956).
20. E. Biederman and E. Kneller, *Z. Metall.* 47, 290 (1956).
21. M. Hillert, M. Cohen and B.L. Averbach, *Acta Metall.* 9, 536 (1961).
22. A.H. Geisler, *Trans. ASM* 43, 70 (1951).
23. M. Greaves, *Acta Cryst.* 4, 301 (1951).
24. J. Manenc, *Acta Cryst.* 10, 259 (1959).
25. J. Manenc, *Acta Metall.* 7, 124 (1959).
26. A.J. Ardell and R.B. Nicholson (Appendix J.D. Eshelby), *Acta Metall.* 14, 1295 (1966).
27. E. Hornbogen and M. Roth, *Z. Metallk.* 58, 1533 (1966).
28. T.J. Tiedema, J. Bouman and W.G. Burgers, *Acta Metall.* 5, 310 (1957).
29. R. Davies and R.H. Richman, *Trans. AIME* 236, 1551 (1966).
30. L.E. Tanner, *Phil. Mag.* 14, 111 (1966).
31. A.V. Gaurilova and Yu. D. Tyapkin, *Sov. Phys. Crystallogr.* 9, 166 (1964).

32. L.E. Tanner, *Phys. Status Solidi* 30, 685 (1968).
33. R.J. Rioja, Ph.D. Thesis; Carnegie-Mellon University, Dept. of Metallurgy & Materials Science (1979).
34. J.M. Penisson, A. Bourret and Ph. Eurin, *Acta Metall.* 19, 1195 (1971).
35. D.H. Jack, *Acta Metall.* 24, 137 (1976).
36. A.M. Hunt and D.W. Pashley, *J. Austral. Inst. Metals* 8, 61 (1963).
37. M. Hirabayashi and S. Weissmann, *Acta Metall.* 10, 25 (1962).
38. H. Lipson, D. Shoenberg and G.V. Stupart, *J. Inst. Met.* 67, 333 (1941).
39. J. Van Landuyt, *Phys. Status Solidi* 61, 957 (1964).
40. R. Smith and J.S. Bowles, *Acta Metall.* 8, 405 (1960).
41. J. Van Landuyt and C.M. Wayman, *Acta Metall.* 16, 803 (1968).
42. M.M. Crum (quoted by F.R.N. Nabarro, *Proc. Phys. Soc.* 52, 90 (1940)).
43. F. Bitter, *Physical Review* 37, 1527 (1931).
44. J.W. Cahn, *Acta Metall.* 9, 795 (1961).
45. J.E. Hilliard, *Ind. Eng. Chem.* 58, 19 (1966).
46. J.W. Cahn, *Acta Metall.* 10, 907 (1962).
47. J.W. Cahn, in "The Mechanism of Phase Transformations in Crystalline Solids", Institute of Metals, London, p. 1 (1969).
48. S. Chen, J.W. Morris, Jr. and A.G. Khachaturyan, to be published (quoted in Ref. 33).

49. H.K. Hardy and T.J. Heal, Prog. Met. Phys. 5, 143 (1954).
50. A. Kelly and R.B. Nicholson, Prog. Mat. Sci. 10, 193 (1963).
51. V.A. Philips, Acta Metall. 23, 751 (1975).
52. V.A. Philips, Acta Metall. 21, 219 (1973).
53. A. Guinier, Ann. Physique 12, 161 (1939).
54. G.D. Preston, Phil. Mag. 26, 855 (1938).
55. V. Gerold, Z. Metallk. 45, 593 (1954).
56. J.M. Silcock, T.J. Heal and J.K. Hardy, J. Inst. Metals 82, 239 (1954).
57. E. Seitz and D. DeFontane, Acta Metall. 26, 1671 (1978).
58. K.C. Russell and H.I. Aaronson, J. Matl. Sci. 10, 1991 (1975).
59. A. Guinier, Solid St. Phys. 9, 293 (1959).
60. V. Gerold, Z. Metallk. 45, 593, 599 (1954).
61. V. Gerold, Acta Cryst. 11, 236 (1958).
62. K. Toman, Acta Cryst. 8, 587 (1955); 10, 187 (1957); 13, 60 (1960).
63. K. Doi, Acta Cryst. 13, 45 (1960).
64. D.R. James and G.L. Liedl, Acta Cryst. 18, 678 (1965).
65. F.R.N. Nabarro, Proc. Phys. Soc. 59, 256 (1947).
66. H. Franz and E. Kroner, Z. Metallk. 46, 639 (1955).
67. B. Bullough and R.C. Newman, Phil. Mag. 5, 921 (1960).
68. F. Kroupa, Czech. J. Phys. B(10), 284 (1960).
69. F. Kroupa, Phil. Mag. 7, 783 (1962).

70. P.J. Phillingham, H.J. Leamy and L.E. Tanner, *Electron Microscopy and Structure of Materials*, p. 163, University of Cal. Press, CA (1972).
71. P.B. Hirsch, A. Howie, R.B. Nicholson, D.W. Pashley and M.J. Whelan, *Electron Microscopy of Thin Crystals*, Butterworths, London (1967).
72. G.C. Weatherly and C.M. Sargent, *Phil. Mag.* 22, 1049 (1970).
73. H. Gleiter, *Acta Metall.* 17, 565 (1969).
74. L.E. Tanner, P.C. Clapp and R.S. Toth, *Matter. Res. Bull.* 3, 855 (1968).
75. V.A. Phillips and L.E. Tanner, *Acta Met.* 21, 441 (1973).
76. A.V. Gavrilova, Yu. D. Tyapkin and M.P. Usikov, *Sov. Phys. Dokl.* 12, 970 (1968).
77. L.K. Lou and D.H. Jack, *Met. Sci. J.* 11, 46, (1977).
78. J.D.C. McConnell, *Mineral Mag.* 38, 1 (1971).
79. R.W. James, 'Optical Principles of the Diffraction of X-Rays', London (Bell) (1950).
80. B.E.P. Beeston, in "Practical Methods in Electron Microscopy", vol. 1, ed. A.M. Glauert, North-Holland Publishing Company, Amsterdam (1972).
81. R.W. Horne and R. Markham, in "Practical Methods in Electron Microscopy", vol. 1, ed. A.M. Glauert, North-Holland Publishing Company, Amsterdam (1972).

82. V. Perovic, G.R. Purdy and L.M. Brown, Acta Metall. 27, 1075 (1979).
83. V. Perovic, G.R. Purdy and L.M. Brown, Scripta Metall. 14, 81 (1980).
84. D.J. Bacon and A.G. Crocker, Phil. Mag. 12, 195 (1965).
85. J.D. Boyd and R.B. Nicholson, Acta Metall., 19, 1379 (1971).
86. J.D. Boyd and R.B. Nicholson, Acta Metall. 19, 1101 (1971).
87. R.W. Cahn, Nature 281, 338 (1979).
88. K.Y. Liou, H.V. Smith, P. Wilkes and G.L. Kulcinski, J. Nucl. Mater. 83, 335 (1979).
89. J.W. Cahn, Private communication.
90. W. Gauding and H. Warlimont, Z.F. Metallk. 60, 488 (1969).
91. H. Warlimont and G. Thomas, Met. Sci. J. 4, 47 (1970).
92. C. Wagner, Z. Elektrochem. 65, 581 (1961).
93. I.M. Lifshits and V.V. Slyozov, J. Phys. Chem. Solids 19, 35 (1961).
94. R.K. Ham, R.H. Cook, G.R. Purdy and G. Willoughby, Met. Sci. J. 6, 203 (1972).
95. H.P. Aubauer, Scripta Metall. 14, 77 (1980).
96. G. Lorimer, Proc. 4th European Regional Conf. on Electron Microscopy, p. 491. Tipografia, Poliglotta, Vaticana, Rome (1968).
97. H.I. Aaronson, in "Decomposition of Austenite by Diffusional Processes", Interscience Publishers, New York (1962):

98. G.C. Weatherly and R.B. Nicholson, *Phil. Mag.* 17, 801 (1968).
99. H.J. Aaronson and C. Laird, *Trans. Metall. Soc. AIME* 242, 1393 (1968).
100. T.J. Headley and J.J. Hren, *Phil. Mag.* 34, 101 (1976).
101. Y. Nakada, W.C. Leslie and T.P. Churoy (Appendix, J.C.M.L1), *Trans. ASM* 60, 223 (1967).
102. W.F. Hosford and S.P. Agrawal, *Metall. Trans.(A)*, 6, 487 (1975).
103. W.M. Stobbs and G.R. Purdy, *Acta Metall.* 26, 1069 (1978).
104. J.W. Gibbs, *The Scientific Papers of J.W. Gibbs*, Dover, New York, vol. 1, p. 325 (1961).
105. F.C. Frank, *Discussions Faraday Soc.* 5, 48 (1949).
106. W.K. Burton, N. Cabrera and F.C. Frank, *Phil. Trans. R. Soc. London*, 243(A), 299 (1951).
107. J.W. Cahn, *Acta Metall.* 8, 556 (1960).
108. A.A. Chernov, *Sov. Phys. USP.* 4, 116 (1961).
109. H.I. Aaronson, in "Decomposition of Austenite by Diffusional Processes", eds. V.F. Zackay and H.I. Aaronson (Wiley, New York, 1962) p. 387.
110. W.W. Mullins and J.P. Hirth, *J. Phys. Chem. Solids* 24, 1391 (1963).
111. K.A. Jackson, D.R. Uhlman and J. Hunt, *J. Cryst. Growth* 1, 1 (1967).
112. R.L. Schwoebel, *J. Appl. Phys.* 40, 614 (1969).

113. G.J. Jones and R.K. Trivedi, J. Appl. Phys. 42, 4299 (1971).
 114. G.J. Jones and R.K. Trivedi, J. Cryst. Growth, 29, 155 (1975).
 115. J.W. Christian, The Theory of Transformation in Metals and Alloys (Pergamon 1965).
 116. C.L. Laird and H.I. Aaronson, J. Inst. Metals 96, 222 (1968).
 117. G.C. Weatherly, Acta Metall. 19, 181 (1971).
 118. R. Sankarn and C. Laird, Acta Metall. 22, 957 (1974).
 119. M. Hillert, in "The Mechanism of Phase Transformations in Crystalline Solids", The Institute of Metals, Monograph No. 33, (1969).
 120. F.S. Ham, Phys. Chem. Solids 6, 335 (1958).
 121. H. Bushhol, Z. Elektrische und Magnetische Potentialfelder (Springer-Verlag, Berlin, 1957).
 122. G. Wulff, Z. Kristallogr. 34, 449 (1901).
 123. H.I. Aaronson and C. Laird, 242, 1437 (1968).
 124. L.M. Brown and D.R. Clarke, Acta Metall. 23, 821 (1975).
 125. H.I. Aaronson, K.R. Kinsman and K.C. Russell, Scripta Metall. 4, 101 (1970).
 126. J.H. Hildebrand and R.L. Scott, The Solubility of Non-Electrolytes, Reingold, New York (1924).
- 